The Deep Space Network
Progress Report 42-38
January and February 1977

National Aeronautics and
Space Administration

Jet Propulsion Laboratory
California Institute of Technology
Pasadena, California 91103

Preface

Beginning with Volume XX, the Deep Space Network Progress Report changed from the Technical Report 32- series to the Progress Report 42- series. The volume number continues the sequence of the preceding issues. Thus, Progress Report 42-20 is the twentieth volume of the Deep Space Network series, and is an uninterrupted follow-on to Technical Report 32-1526, Volume XIX.

This report presents DSN progress in flight project support, tracking and data acquisition (TDA) research and technology, network engineering, hardware and software implementation, and operations. Each issue presents material in some, but not all, of the following categories in the order indicated.

Description of the DSN

Mission Support
- Ongoing Planetary/Interplanetary Flight Projects
- Advanced Flight Projects

Radio Science

Special Projects

Supporting Research and Technology
- Tracking and Ground-Based Navigation
- Communications–Spacecraft/Ground
- Station Control and Operations Technology
- Network Control and Data Processing

Network and Facility Engineering and Implementation
- Network
- Network Operations Control Center
- Ground Communications
- Deep Space Stations

Operations
- Network Operations
- Network Operations Control Center
- Ground Communications
- Deep Space Stations

Program Planning
- TDA Planning
- Quality Assurance

In each issue, the part entitled "Description of the DSN" describes the functions and facilities of the DSN and may report the current configuration of one of the five DSN systems (Tracking, Telemetry, Command, Monitor & Control, and Test & Training).

The work described in this report series is either performed or managed by the Tracking and Data Acquisition organization of JPL for NASA.

Contents

DESCRIPTION OF THE DSN

MISSION SUPPORT

Ongoing Planetary/Interplanetary Flight Projects

SUPPORTING RESEARCH AND TECHNOLOGY

Tracking and Ground-Based Navigation

Communications - Spacecraft/Ground

Network Control and Data Processing

NETWORK AND FACILITY ENGINEERING AND IMPLEMENTATION

Network

Deep Space Stations

OPERATIONS

Network Operations

Deep Space Stations

PROGRAM PLANNING

TDA Planning

Network Functions and Facilities

N. A. Renzetti
Office of Tracking and Data Acquisition

The objectives, functions, and organization of the Deep Space Network are summarized; deep space station, ground communication, and network operations control capabilities are described.

The Deep Space Network (DSN), established by the National Aeronautics and Space Administration (NASA) Office of Tracking and Data Acquisition under the system management and technical direction of the Jet Propulsion Laboratory (JPL), is designed for two-way communications with unmanned spacecraft traveling approximately 16,000 km (10,000 miles) from Earth to the farthest planets of our solar system. It has provided tracking and data acquisition support for the following NASA deep space exploration projects: Ranger, Surveyor, Mariner Venus 1962, Mariner Mars 1964, Mariner Venus 1967, Mariner Mars 1969, Mariner Mars 1971, and Mariner Venus Mercury 1973, for which JPL has been responsible for the project management, the development of the spacecraft, and the conduct of mission operations; Lunar Orbiter, for which the Langley Research Center carried out the project management, spacecraft development, and conduct of mission operations; Pioneer, for which Ames Research Center carried out the project management, spacecraft development, and conduct of mission operations; and Apollo, for which the Lyndon B. Johnson Space Center was the project center and the Deep Space Network supplemented the Manned Space Flight Network (MSFN), which was managed by the Goddard Space Flight Center (GSFC). It is providing tracking and data acquisition support for Helios, a joint U.S./West German project; and Viking, for which Langley Research Center provides the project management, the Lander spacecraft, and conducts mission operations, and for which JPL also provides the Orbiter spacecraft.

The Deep Space Network is one of two NASA networks. The other, the Spaceflight Tracking and Data Network, is under the system management and technical direction of the Goddard Space Flight Center. Its function is to support manned and unmanned Earth-orbiting satellites. The Deep Space Network supports lunar, planetary, and interplanetary flight projects.

From its inception, NASA has had the objective of conducting scientific investigations throughout the solar sys-

tem. It was recognized that in order to meet this objective, significant supporting research and advanced technology development must be conducted in order to provide deep space telecommunications for science data return in a cost effective manner. Therefore, the Network is continually evolved to keep pace with the state of the art of telecommunications and data handling. It was also recognized early that close coordination would be needed between the requirements of the flight projects for data return and the capabilities needed in the Network. This close collaboration was effected by the appointment of a Tracking and Data Systems Manager as part of the flight project team from the initiation of the project to the end of the mission. By this process, requirements were identified early enough to provide funding and implementation in time for use by the flight project in its flight phase.

As of July 1972, NASA undertook a change in the interface between the Network and the flight projects. Prior to that time, since 1 January 1964, in addition to consisting of the Deep Space Stations and the Ground Communications Facility, the Network had also included the mission control and computing facilities and provided the equipment in the mission support areas for the conduct of mission operations. The latter facilities were housed in a building at JPL known as the Space Flight Operations Facility (SFOF). The interface change was to accommodate a hardware interface between the support of the network operations control functions and those of the mission control and computing functions. This resulted in the flight projects assuming the cognizance of the large general-purpose digital computers which were used for both network processing and mission data processing. They also assumed cognizance of all of the equipment in the flight operations facility for display and communications necessary for the conduct of mission operations. The Network then undertook the development of hardware and computer software necessary to do its network operations control and monitor functions in separate computers. This activity has been known as the Network Control System Implementation Project. A characteristic of the new interface is that the Network provides direct data flow to and from the stations; namely, metric data, science and engineering telemetry, and such network monitor data as are useful to the flight project. This is done via appropriate ground communication equipment to mission operations centers, wherever they may be.

The principal deliverables to the users of the Network are carried out by data system configurations as follows:

- The DSN Tracking System generates radio metric data; i.e., angles, one- and two-way doppler and range, and transmits raw data to Mission Control.
- The DSN Telemetry System receives, decodes, records, and retransmits engineering and scientific data generated in the spacecraft to Mission Control.
- The DSN Command System accepts coded signals from Mission Control via the Ground Communications Facility and transmits them to the spacecraft in order to initiate spacecraft functions in flight.

The data system configurations supporting testing, training, and network operations control functions are as follows:

- The DSN Monitor and Control System instruments, transmits, records, and displays those parameters of the DSN necessary to verify configuration and validate the Network. It provides operational direction and configuration control of the Network, and provides primary interface with flight project Mission Control personnel.
- The DSN Test and Training System generates and controls simulated data to support development, test, training and fault isolation within the DSN. It participates in mission simulation with flight projects.

The capabilities needed to carry out the above functions have evolved in three technical areas:

(1) The Deep Space Stations, which are distributed around Earth and which, prior to 1964, formed part of the Deep Space Instrumentation Facility. The technology involved in equipping these stations is strongly related to the state of the art of telecommunications and flight-ground design considerations, and is almost completely multimission in character.

(2) The Ground Communications Facility provides the capability required for the transmission, reception, and monitoring of Earth-based, point-to-point communications between the stations and the Network Operations Control Center at JPL, Pasadena, and to the mission operations centers, wherever they may be. Four communications disciplines are provided: teletype, voice, high-speed, and wideband. The Ground Communications Facility uses the capabilities provided by common carriers throughout the world, engineered into an integrated system by Goddard Space Flight Center, and controlled from the communications Center located in the Space Flight Operations Facility (Building 230) at JPL.

(3) The Network Operations Control Center is the functional entity for centralized operational control of the Network and interfaces with the users. It has two separable functional elements; namely, Network Operations Control and Network Data Processing. The functions of the Network Operations Control are:

- Control and coordination of Network support to meet commitments to Network users.
- Utilization of the Network data processing computing capability to generate all standards and limits required for Network operations.
- Utilization of Network data processing computing capability to analyze and validate the performance of all Network systems.

The personnel who carry out the above functions are located in the Space Flight Operations Facility, where mission operations functions are carried out by certain flight projects. Network personnel are directed by an Operations Control Chief. The functions of the Network Data Processing are:

- Processing of data used by Network Operations Control for control and analysis of the Network.
- Display in the Network Operations Control Area of data processed in the Network Data Processing Area.
- Interface with communications circuits for input to and output from the Network Data Processing Area.
- Data logging and production of the intermediate data records.

The personnel who carry out these functions are located approximately 200 meters from the Space Flight Operations Facility. The equipment consists of minicomputers for real-time data system monitoring, two XDS Sigma 5s, display, magnetic tape recorders, and appropriate interface equipment with the ground data communications.

DSN Test and Training System, Mark III-77

H. C. T[illegible]nan
TDA Engineering Office

Implementation of the DSN Test and Training System, Mark III-77, is currently in progress. The Mark III-77 system is configured to support DSN testing and training in preparation for the Mariner-Jupiter-Saturn 1977 and Pioneer-Venus 1978 missions, in addition to the on-going in-flight missions. DSN Test and Training System capabilities include functions performed in the Deep Space Stations, Ground Communications Facility, and Network Operations Control Center.

I. Introduction

A. System Definition

The DSN Test and Training System is a multiple-mission system which supports Network-wide testing and training by inserting test signals and data into subsystems of the Deep Space Stations (DSS), the Ground Communications Facility (GCF) and the Network Operations Control Center (NOCC). The system includes capabilities for:

(1) On-site testing of the DSS portion of each DSN system.

(2) Local testing of the NOCC portion of each DSN system.

(3) End-to-end testing of each DSN system, including DSS, GCF, and NOCC functions.

Figure 1 describes the functions, elements, and interfaces of the system. The DSN Test & Training System Requirements through 1980 were published April 15, 1976.

B. Key Characteristics

Design goal key characteristics of the DSN Test and Training System are:

(1) Capability to function without alteration of DSN operational configuration.

(2) Utilization of mission-independent equipment for DSN testing and training functions.

(3) Capability to exercise NOCC, GCF and DSS simultaneously, for end-to-end testing of each DSN system.

(4) Capability to supply test data to all DSN systems simultaneously.

(5) Capability to load Network with combination of actual and simulated data streams.

(6) Accommodation of flight-project-supplied simulation data via GCF.

(7) Accommodation of other data sources, as follows:

(a) Spacecraft test data via JPL Compatibility Test Area (CTA 21).

(b) Spacecraft prelaunch data via Merritt Island, Florida, Spacecraft Compatibility-Monitor Station (STDN (MIL 71)).

C. System Usage

Major testing and training activities supported by the DSN Test and Training System are summarized below:

(1) Prepass and pretest calibrations, readiness verifications, and fault isolation.

(2) DSN implementation activities and performance testing of DSN systems, DSS subsystems, and NOCC subsystems.

(3) DSN operational verification tests to prepare for mission support.

(4) Flight project ground data system tests and mission simulations.

D. Mark III-77 System Implementation

A functional block diagram showing the data-flow and signal-flow paths of the DSN Test and Training System, Mark III-77, is shown in Fig. 2. Implementation to meet the system functional requirements (previously described in Reference 1) is currently in progress. Station-by-station implementation is coordinated with the overall reconfiguration of the Deep Space Station subsystems.

The DSN Test and Training System, Mark III-77, includes the following modifications and additions to the Mark III-75 system:

(1) Modification of the DSS Simulation Conversion Assembly (SCA) to provide capability for short-constraint-length convolutional coding of simulated MJS'77 telemetry data and long-constraint-length convolutional coding of simulated PV'78 telemetry data.

(2) Upgrade of program software for the XDS-910 processor, associated with the SCA, to control new SCA equipment, to generate simulated MJS'77 and PV'78 telemetry data patterns, and to convert MJS'77 and PV'78 project-supplied data from GCF high-speed and wideband data blocks into serial data streams.

(3) Configuring of the DSS Communications Monitor and Formatter (CMF) backup minicomputer to provide the System Performance Test Assembly (SPTA) functions of on-site closed-loop performance testing and validation of the Tracking, Telemetry, Command, and Monitor and Control Systems.

(4) Initial phase implementation of the Network Control Test and Training Subsystem in the Network Operations Control Center (Block III).

II. Deep Space Station Functions

A. DSS Test and Training Subsystem

The functions of the DSS Test and Training Subsystem and the related interfaces are shown in Fig. 3.

1. **Telemetry simulation and conversion.** The telemetry simulation and conversion functions are performed by the Simulation Conversion Assembly, which is diagrammed in detail in Fig. 4. The digital and analog capabilities of the SCA are itemized in Tables 1 and 2, respectively.

2. **System performance test functions.** The system performance test functions are performed by the System Performance Test Assembly which is diagrammed in detail in Fig. 5.

B. Receiver-Exciter Subsystem

The Receiver-Exciter Subsystem provides the following test and training functions:

(1) Generation of simulated S-band and X-band downlink carriers.

(2) Modulation of telemetry subcarriers from the SCA onto simulated carriers.

(3) Variable attenuation of simulated downlink carrier signal level under control of the Simulation Conversion Assembly.

(4) Variable control of simulated downlink carrier frequency to permit simulation of doppler shifts.

(5) Provision of a transmitter dummy load for Command System test operations.

C. Antenna Microwave Subsystem

The Antenna Microwave Subsystem provides the following test and training functions:

(1) Routing of simulated downlink carriers to masers and/or receivers.

(2) Mixing of simulated S-band downlink carriers.

D. Frequency and Timing Subsystem

The Frequency and Timing Subsystem provides the following support functions to the DSS Test and Training Subsystem:

(1) Reference frequencies inputted to the SCA.

(2) Time code and reference frequencies inputted to the SPTA.

(3) Generation and distribution of a simulated time signal which can be substituted for the true GMT input to the various DSS subsystems. This capability is provided for realistic mission simulations in support of flight project testing and training activities.

III. Ground Communications Facility Functions

The DSN Test and Training System utilizes the Ground Communications Facility Subsystems for communicating data and information between the Network Operations Control Center (NOCC) or any Mission Operations Center (MOC) and the Deep Space Stations.

A. High-Speed Data Subsystem

The High-Speed Data Subsystem provides the following:

(1) Transmission of text messages, control messages, low-to-medium-rate simulated telemetry data, and simulated command data to any DSS from the NOCC or from any MOC.

(2) On-site loop-back of test data for systems performance testing and readiness verifications in the DSS.

B. Wideband Data Subsystem

The Wideband Data Subsystem provides the following:

(1) Transmission of simulated high-rate telemetry data to the 64-m subnet, the Compatibility Test Area in Pasadena, California, and STDN (MIL-71) at Merritt Island, Florida, from the NOCC or from any MOC having wideband capability.

(2) On-site loop-back of test data for telemetry system performance testing and readiness verification in those Deep Space Stations which have wideband capability.

C. Voice Subsystem

The Voice Subsystem provides operator-to-operator communication of information for purposes of test coordination and monitoring of the DSN Test and Training System status.

IV. Network Operations Control Center Functions

A. NOCC Test and Training Subsystem

Functions and interfaces of the NOCC Test and Training Subsystem are shown in Fig. 6. Subsystem data flow details are further diagrammed in Fig. 7.

1. **Present capabilities.** Test and training capabilities presently implemented in the Network Operations Control Center are as follows:

(1) Selection of stored data blocks and output to the DSS for system readiness verification.

(2) Off-line generation of recordings of high-speed data blocks for testing of the real-time monitors in the NOCC Tracking, Telemetry, Command, and Monitor Subsystems.

(3) Selection and output of prepared Simulation Conversion Assembly text and control messages to the DSS for remote configuration and control of the Simulation Conversion Assembly in support of DSN Operational Verification Tests.

2. **Future capabilities.** Test and training functions that remain to be implemented in the Network Operations Control Center are as follows:

(1) Real-time generation of Simulation Conversion Assembly text and control messages for transmission to the DSS without need for prestorage.

(2) Real-time generation of test data patterns for support of NOCC and DSS testing, without need for prestorage.

B. DSN Test and Training System Control Console

A DSN Test and Training System Control Console in the Network Data Processing Area is planned for future implementation. The console will provide keyboards, a card reader, a magnetic tape unit, volatile displays, and a character printer, so that operation of the Test and Training System will be separate from the operations of the other DSN Systems.

Reference

1. Thorman, H.C., "DSN Test and Training System," in *The Deep Space Network Progress Report 42-30*, pp. 5-15, Jet Propulsion Laboratory, Pasadena, Calif., Nov. 15, 1975.

Table 1. DSS Simulation Conversion Assembly digital telemetry simulation capabilities

Capability	26-meter DSS, MIL 71	64-meter DSS, CTA 21
Maximum number of simultaneous real-time data streams	2 channels	Viking prime mission, 6 channels
		Viking extended mission, 4 channels
		Other missions, 3 channels
Bi-orthogonal (32, 6) comma-free block coding	Viking, 2 channels	Viking, 3 channels
	Other missions, none	Other missions, none
Short-constraint-length convolutional coding (k=7, r=1/2 or 1/3)	Mariner Jupiter-Saturn, rate = 1/2, 2 channels	Mariner Jupiter-Saturn, rate = 1/2, 3 channels
	Future missions, rate = 1/3, 1 channel	Future missions, rate = 1/3, 2 channels
Long-constraint-length convolutional coding (k=32, r=1/2)	Helios, 1 channel	Helios, 1 channel
	Pioneer 10/11, 2 channels	Pioneer 10/11, 2 channels
	Pioneer Venus, 2 channels	Pioneer Venus, 3 channels
Variable rate control	1 bps to 600 ksps on 1 channel	1 bps to 600 ksps on 2 channels
	1 bps to 190 ksps on 1 additional channel	1 bps to 190 ksps on 1 additional channel
Selection of discrete rates	8-1/3, 33-1/3 bps on each of 2 channels (for Viking)	8-1/3, 33-1/3 bps on each of 3 channels (for Viking)

Table 2. DSS Simulation Conversion Assembly analog telemetry simulation capabilities

Capability	26-meter DSS, MIL 71	64-meter DSS, CTA 21
Data and subcarrier signal conditioning, phase-shift keyed modulation	2 subcarriers	Viking prime mission, 6 subcarriers
		Viking extended mission, 4 subcarriers
		Other missions, 3 subcarriers
Subcarrier frequency output	512 Hz to 1.25 MHz, 1/4-Hz resolution	512 Hz to 1.25 MHz, 1/4-Hz resolution
Modulation-index angle control	Controllable from 0 to 89 deg on each subcarrier	Controllable from 0 to 89 deg on each subcarrier
Subcarrier mixing and downlink carrier biphase modulation	Single or dual subcarriers onto each of 2 S-band test carriers or 1 S-band and 1 X-band	Single or dual subcarriers onto each of 3 test carriers or 2 S-band and 1 X-band
Downlink carrier signal level	Attenuation of 0 to 40 dB on each test carrier output	Attenuation of 0 to 40 dB on each test carrier output

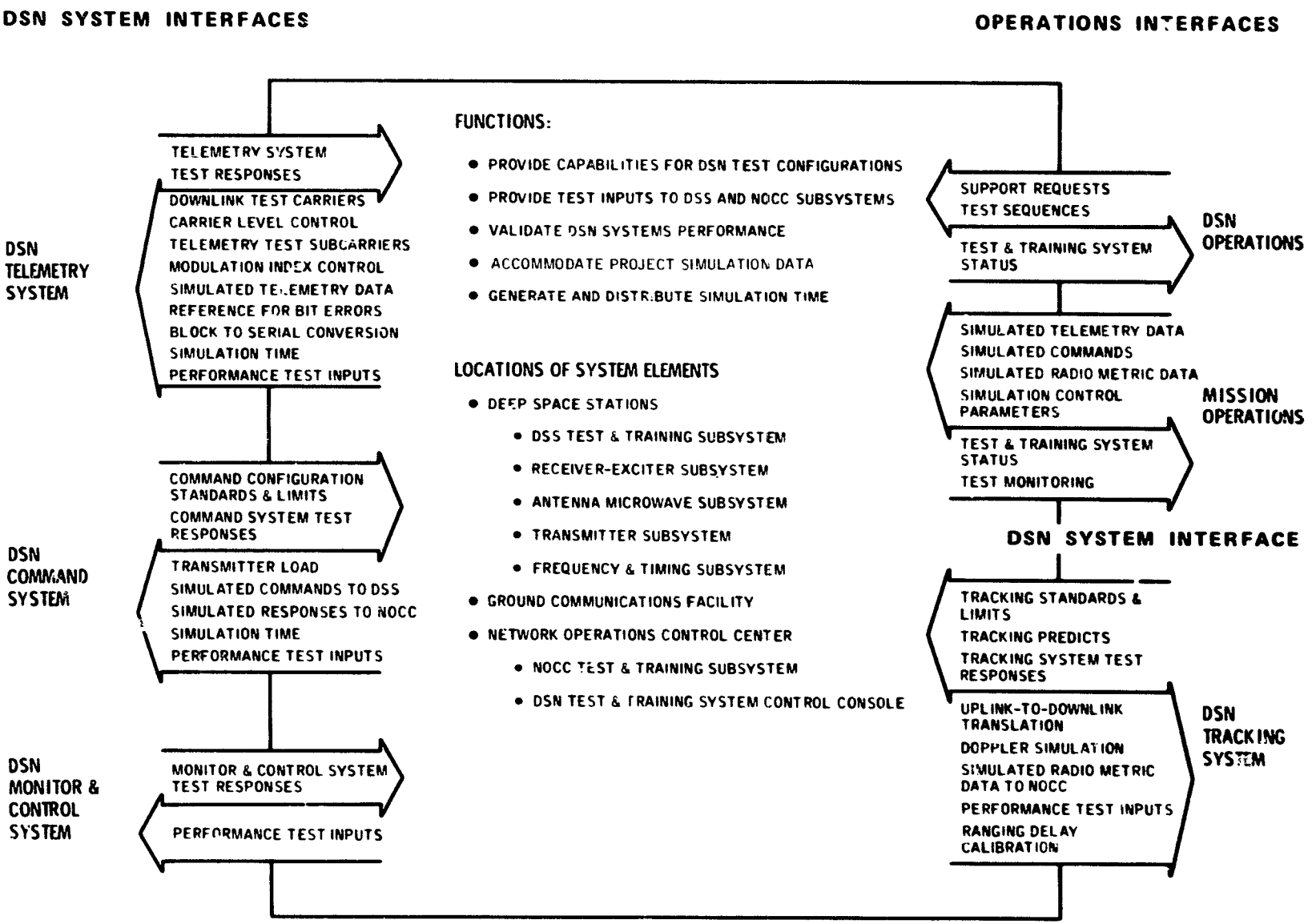

Fig. 1. DSN Test and Training System functions and interfaces

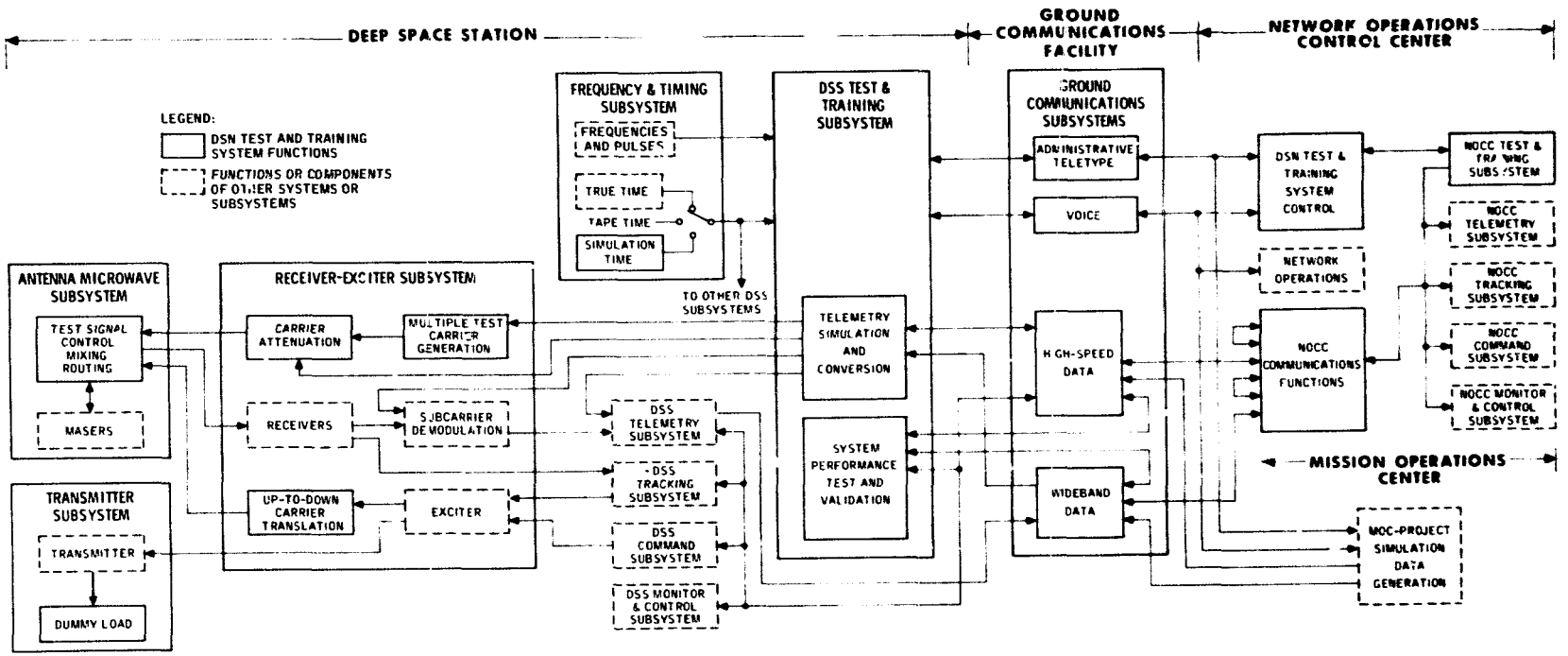

Fig. 2. DSN Test and Training System, Mark III-77, functional block diagram

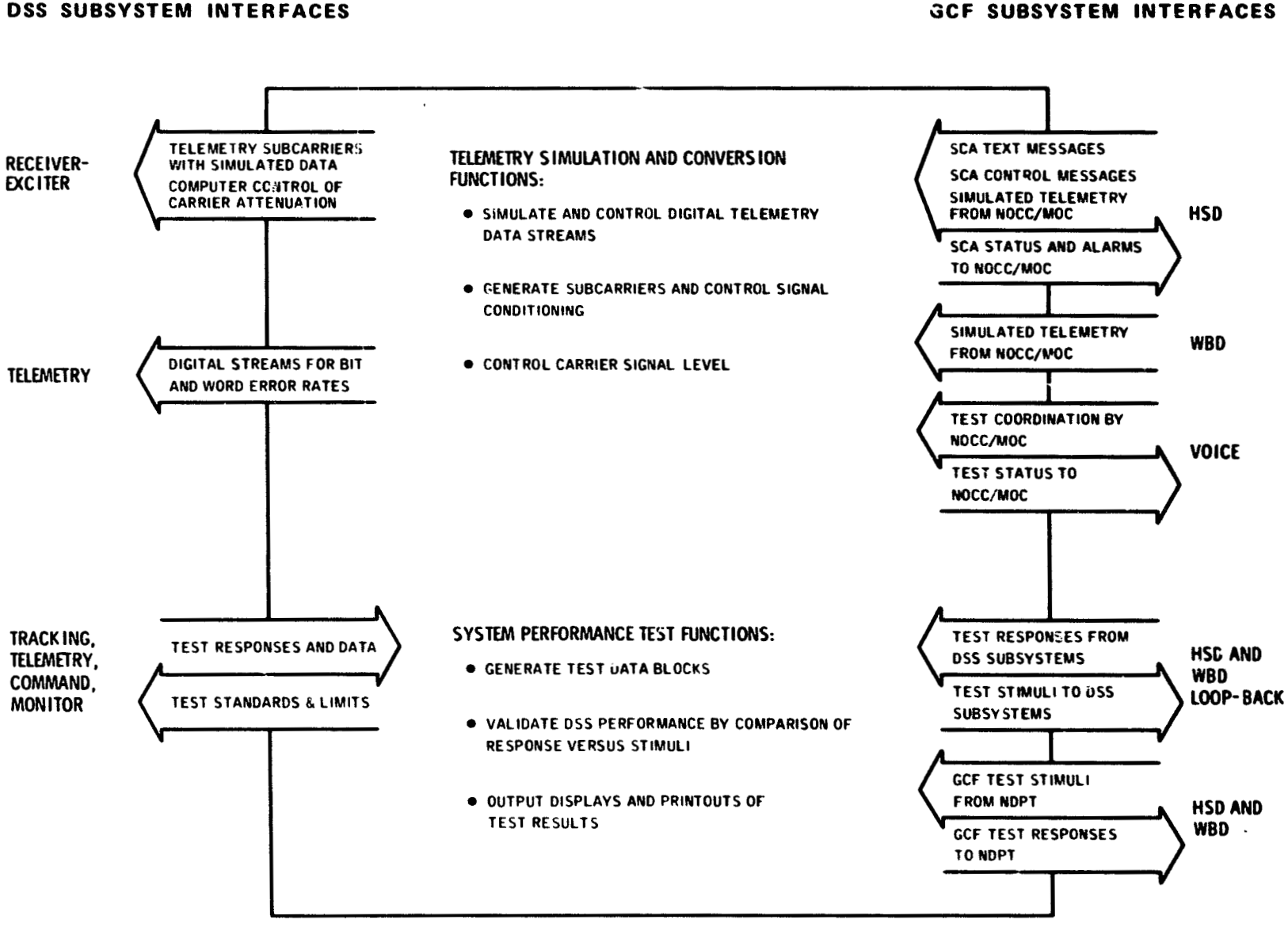

Fig. 3. DSN Test and Training Subsystem functions and interfaces

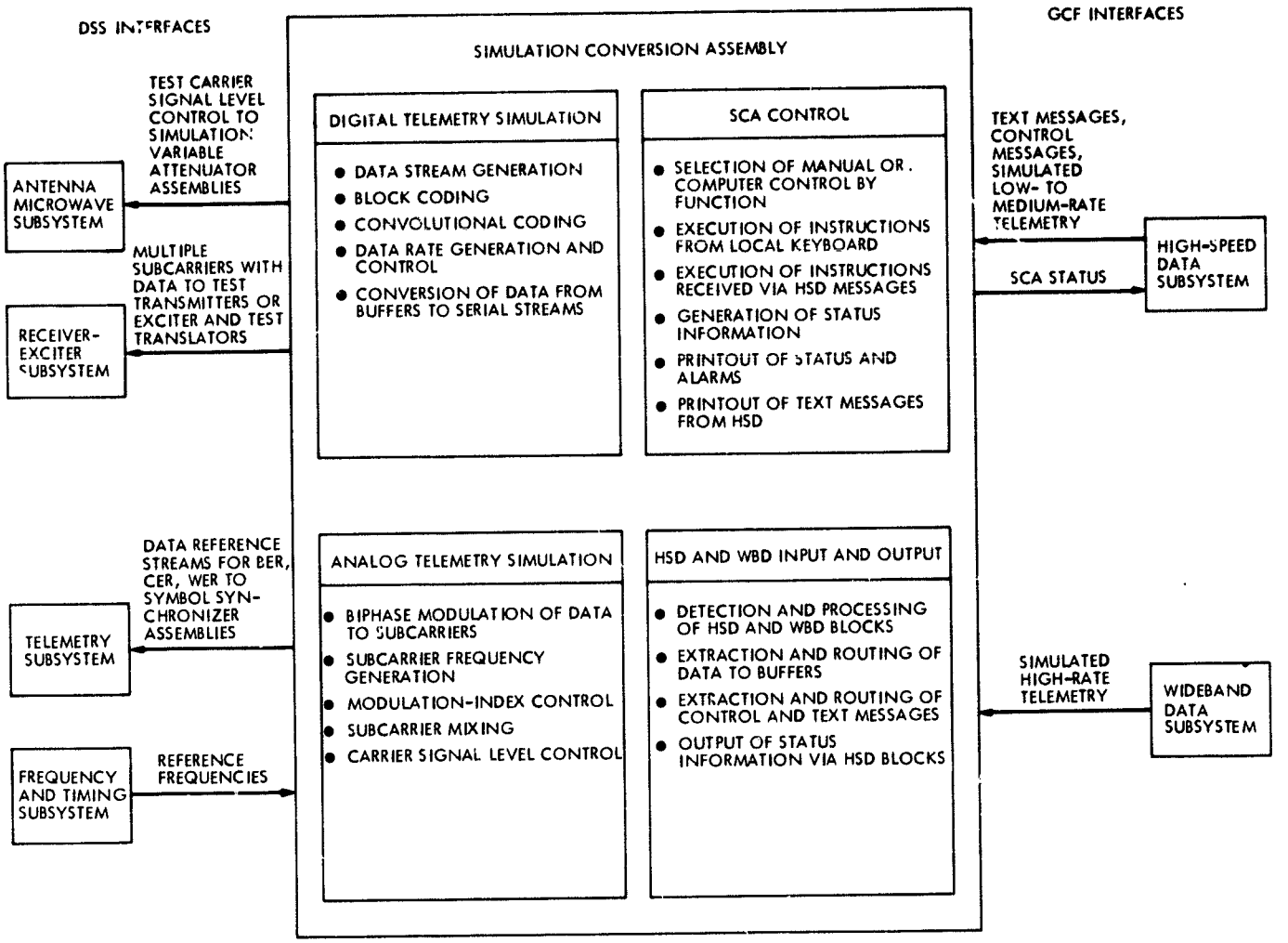

Fig. 4. Simulation conversion assembly functions and data flow

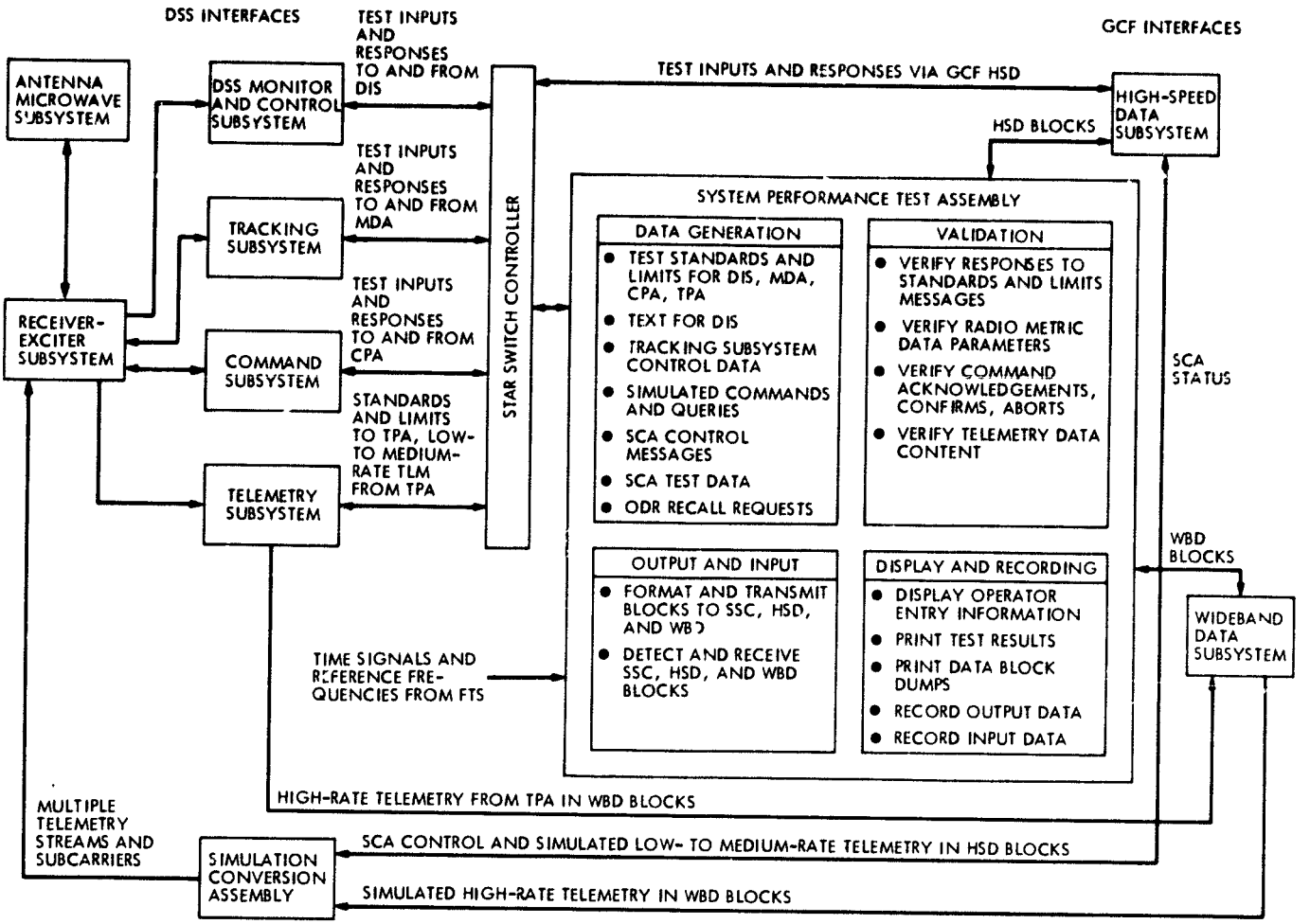

Fig. 5. System performance test assembly functions and data flow

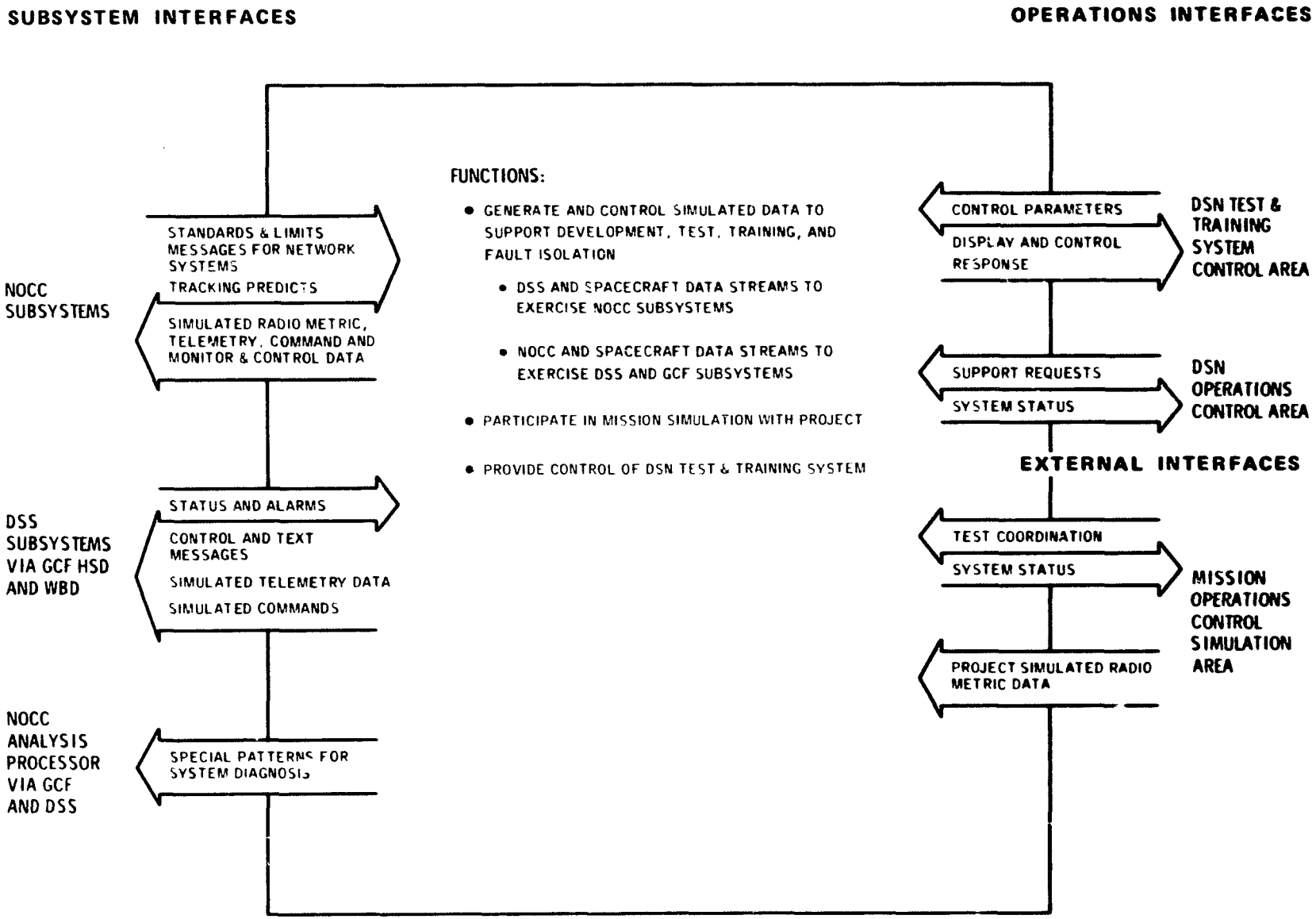

Fig. 6. NOCC Test and Training Subsystem functions and interfaces

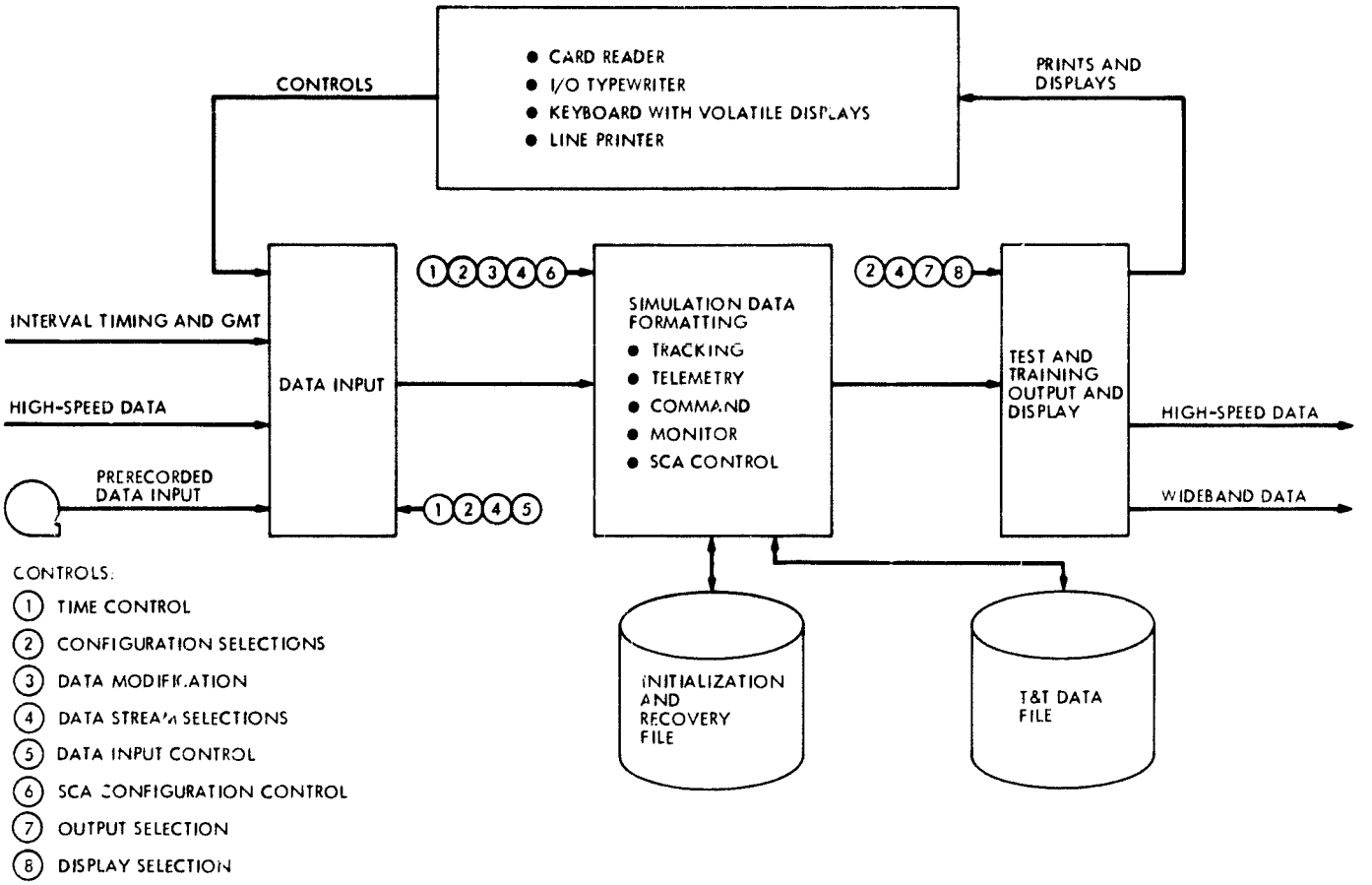

Fig. 7. NOCC Test and Training Subsystem data flow

Summary Report and Status of the Deep Space Network–Mariner Jupiter/Saturn 1977 Flight Project Telecommunications Compatibility

A. I. Bryan and R. P. Kemp
TDA Engineering Office

B. D. Madsen
Mariner Telecommunications

The DSN-Mariner Jupiter/Saturn 1977 telecommunications compatibility tests, conducted during the time periods 15–20 November 1976, 7–16 December 1976 and 5 January 1977, are an ongoing series of engineering level tests to determine the flight-ground interface compatibility and performance characteristics between these two systems. This report describes these tests in summary form and provides a status of the interface.

I. Introduction

The purpose of this report is to provide an assessment and status of telecommunications compatibility between the Deep Space Network (DSN) and the Mariner Jupiter/Saturn 1977 (MJS'77) spacecrafts. This assessment and status is derived from test results obtained between the Network, as represented in the Compatibility Test Area and the Flight-1, Flight-2 and Prototype Telecommunications Systems.

II. Test Report

The test report describes three sets of tests which were conducted between the Compatibility Test Area (CTA 21) and (1) the Flight 1 Radio Frequency and Modulation-Demodulation Subsystems, (2) the Flight 2 Radio Frequency and Modulation-Demodulation Subsystems and (3) the Prototype Spacecraft Telecommunications System.

Each of the three tests is discussed with regard to test objectives, configurations and results. In addition, Tables 1, 2, and 3 present detailed information on the DSN and MJS'77 test conditions, parameters, criteria and results. Figures 1 and 2 describe the DSN and Spacecraft operational modes. Table 4 defines the terms used in these tables.

A. DSN–MJS'77 Flight 1 Compatibility Testing

1. Test objectives. The objective of the tests was to verify the capability of the DSN to acquire and process telemetry from the spacecraft under various uplink and downlink conditions.

2. Test configuration. The MJS'77 Telecommunications System was located at the Telecommunications Development Laboratory (TDL). The hardware used was the Flight 1 Radio Frequency and Modulation-Demodulation Subsystems. The

Radio Frequency Subsystem was equipped with flight qualified X-band traveling-wave tube amplifiers (TWTAs), one S-band TWTA, and one S-band solid-state amplifier.

The DSN as represented by CTA 21 was configured to simulate a MJS'77 Flight Project committed 64-meter antenna station. The RF links between CTA 21 and the Telecommunications Development Laboratory (TDL) were provided by coax (S-band) and elliptical waveguide (X-band). These RF links were tested for amplitude and phase stability and were calibrated prior to test start.

The DSN software provided at CTA 21 to support these tests was the preliminary 64-meter MARK III Data System (MDS) telemetry software. In addition, test software was provided to enable bit error rate determination at the output of the Maximum Likelihood Convolutional Decoder (MCD).

3. **Test results.** Table 1 provides a listing of test configurations, test criteria, parameters and results. Refer to Figs. 1 and 2 for DSN and spacecraft Radio Frequency Subsystem (RFS) mode configurations.

The S- and X-band telemetry tests were run at weak signal conditions, and although the results generally met the criteria, the MCD Bit Error Rates (BER) achieved during the tests were apparently not consistent with results achieved in the Telecommunications Development Laboratory (TDL) under similar conditions. This BER measurement difference is under investigation and further tests are in progress between the Telecommunications Development Laboratory (TDL) and CTA 21 to attempt to determine the reason for the difference.

The telemetry tests, performed with command and ranging on the uplink and with the spacecraft ranging channel on, indicated a degradation of approximately 0.5 dB in the telemetry BER compared to results achieved in the tests with no modulation on the uplink and the ranging channel off.

4. **Status.** The DSN-MJS'77 Flight 1 Spacecraft Telecommunications Compatibility Tests conducted on 5 January 1977 successfully demonstrated that the telemetry interface between the DSN and the spacecraft (with X- and S-band RF amplifiers) was functional at weak signal levels and performed within specified BERs.

B. DSN–MJS'77 Flight 2 Compatibility Testing

1. **Test objectives.** The objectives of the test were to verify selected interface functions for compatibility of the DSN-MJS'77 Spacecraft Mission configuration. Compatibility is defined as satisfying the specified RF acquisition and tracking, radio metric, command, and telemetry requirements. However, the primary emphasis in this set of tests was directed toward X-band telemetry performance testing as determination of the bit error rate can be accomplished with the MJS'77 Telecommunications system in a stand-alone status in the Telecommunications Development Laboratory.

2. **Test configuration.** The MJS'77 Telecommunications System was located at the Telecommunications Development Laboratory and represented by Flight 2 Radio Frequency and Modulation-Demodulation Subsystems. The Radio Frequency Subsystem was not equipped with either S- or X-band traveling-wave tube amplifiers.

The DSN, as represented by CTA 21, was configured to simulate a MJS'77 Flight Project committed 64-meter antenna station. The S-band and X-band RF links between CTA 21 and TDL were provided by coax and elliptical waveguide. These RF links were tested for amplitude and phase stability and calibrated prior to test start.

The DSN software provided at CTA 21 to support these tests was the operational 26-meter antenna station Mark III-DSN Data Subsystems (MDS) software. In addition, test software was provided to enable operation of the DSS Telemetry Subsystem at high data rates and to enable bit error rate determination at the output of the Maximum Likelihood Convolutional Decoder (MCD).

Modulation-Demodulation Subsystem support equipment, located at the Telecommunications Development Laboratory, was utilized to determine command SNR estimates.

3. **Test results.** Table 2 provides a listing of test configurations, test criteria, parameters, results and comments. Refer to Figs. 1 and 2 for DSN and spacecraft Radio Frequency Subsystem (RFS) mode configurations. Significant test results and comments are discussed below.

a. Radio frequency acquisition and tracking. The X-band two-way phase jitter measurements verify that the DSN must provide an uplink carrier margin of 35 dB in order to provide simultaneous X-band telemetry and doppler without degradation. The two-way X-band phase jitter was measured as 64.7 degrees rms with an uplink signal level of -130 dBm and a downlink signal level of -100 dBm to the CTA 21 Block IV Receiver.

The 35-dB uplink carrier margin (Pc/No X 2 BLo) requirement translates to a carrier power level of approximately -120 dBm to the transponder. This level is approximately equivalent to what can be obtained at Saturn Encounter with a 100-kilowatt transmitter and a 64-meter antenna station (assuming 6-dB ranging and 5-dB command carrier suppres-

sion). Operation at greater distances or with a 26- or 34-meter antenna station will require noncoherent operation of the X-band link and loss of X-band doppler.

It should be noted that S-band performance of the spacecraft transponder is approximately equivalent (22 degree rms phase jitter under similar conditions) to that obtained on previous S-band transponders.

b. Telemetry. X-band telemetry performance was verified to be degraded by the two-way feed-through characteristics of the S-X transponder. Telemetry degradation due to the feed through of commands varied from 0.5 dB at low telemetry data rates to approximately 1 dB at 115.2 kbits/s. This command feed-through problem is independent of the requirement to maintain an approximate 35-dB uplink carrier margin, and the degradation noted above was obtained with 0.5-dB command suppression and 3-dB ranging suppression of the carrier. The effects of command feed through upon S-band telemetry is part of the severe operational limitations on the MJS'77 Mission due to the two-way S-X transmission characteristics of the MJS'77 transponder.

Other items verified during the telemetry tests were:

(1) The suggested procedure for adjusting the Block III SDA for the MJS'77 modulation indices of 80 degrees was verified to be operationally viable.

(2) Correlation of bit error rates and SNR readouts of the SSA and MCD was verified. Therefore, telemetry performance testing with a MJS'77 Spacecraft can utilize the DSS Telemetry Subsystem SNR indicators as a valid measure of performance.

c. Command. Command testing was performed to assure that at specified mission uplink conditions and a command modulation index of 0.5 dB, that a specified SNR ratio was observed in the Modulation-Demodulation Subsystem command loop. A modulation-Demodulation Subsystem performance problem was noted and reported as a Project PRF. If the uplink carrier is suppressed by 3 dB for command modulation, the Modulation-Demodulation Subsystem locked up to an alternate one zero command input during the bit sync acquisition. This improper operation did not occur with a 20-degree command modulation index (0.5-dB carrier suppression).

d. Radio metric. Ranging tests were not performed due to a lack of time and priority. After several false tests due to the sensitivity of the Metric Data Assembly software in detecting doppler cycle slips, it was verified that an uplink signal of −130 dBm to the Radio Frequency Subsystem is the Project stated threshold for X-band doppler performance (10 cycle slips/hour). This uplink threshold level could be altered by the additional phase jitter that would be introduced by the X-band amplifier (not available during these tests).

4. **Status.** Compatibility verification between the MJS'77 Spacecraft Telecommunication System and the DSN has been verified in only selected areas and further extensive testing is required to establish the design level compatibility of this interface. It should be noted that the final verification of the interface and determination of critical telecommunication performance parameters will depend upon testing with the S- and X-band traveling-wave tube amplifiers as part of the Spacecraft configuration.

C. DSN--MJS'77 Prototype Compatibility Testing

1. **Test objectives.** The objectives of this phase of testing was to functionally verify compatibility of the telecommunications interfaces between the DSN and the MJS'77 Prototype Spacecraft. In particular, this set of tests served as a test bed to insure that link performance between CTA 21 and the Space Simulator Facility (SSF) would support RF acquisition and tracking, radio metric, command, and telemetry requirements, at both S-band and X-band.

2. **Test configuration.** The MJS'77 Prototype Spacecraft was located at the SSF which was simulating environmental flight conditions. The Radio Frequency Subsystem was configured as follows:

(1) S-Band

(a) Receiver No. 1, Channel No. 4 (2113.312500 MHz)

(b) Receiver No. 2, Channel No. 18 (2114.676697 MHz)

(c) Ultra Stable Oscillator (USO), Channel No. 14 only (2295.000000 MHz)

(d) Exciters, Chain No. 1 and Chain No. 2, Equipped with prototype traveling wave tube (TWT) amplifiers.

(2) X-band: Exciters, Chain No 1 with no TWT capability, Chain No. 2 equipped with a prototype traveling wave tube amplifier.

The DSN, as represented by CTA 21, was configured to simulate a MJS'77 Flight Project committed 64-meter antenna station. The ground hardware included both Block III and Block IV Receiver-Exciter Subsystems and the new Mark III Data Subsystems (MDS) for telemetry, command and radio metric data.

The S-band and X-band RF links between CTA 21 and the SSF were open air links which had previously been calibrated for amplitude and phase stability. The DSN software provided at CTA 21 was the operational 26-meter antenna station software for the MDS.

In support of the new MJS'77 Flight Project Mission specifications, the following uplink modulation indices were utilized:

(1) Ranging, 45 deg (-3.0 dB carrier suppression)

(2) Command, 20 deg (-0.54 dB carrier suppression for mission nominal) and 56 deg (-5.0 dB carrier suppression for mission threshold)

3. Test results. In response to the spacecraft Flight Data Subsystem (FDS) limitations for supplying various data rates, and the provisions for only one S-band TWT equipped exciter chain, only a selected subset of the total set were performed. The majority of these tests were performed on a functional basis to insure that a viable test condition could be established with the flight model spacecrafts. However, several significant data points were observed and accumulated as a result of these tests.

Table 3, provides a listing of test configurations, test criteria, parameters and results. Refer to Figs. 1 and 2 for DSN and spacecraft RFS mode configurations. Significant test results and comments are discussed below:

a. Radio frequency acquisition and tracking. These tests were all performed at or below project mission requirements and the results were all favorable with the exception of test RF 3-2, Receiver Static Acquisition. In particular, all requirements of this test were met with the following exception:

(1) U/L signal level: -110 dBm

(2) Spacecraft Receiver No. 2: 2114.682864 MHz (-1000 Hz offset from acquisition frequency)

(3) Spacecraft would not acquire when U/L signal was applied

It is not known what the best lock frequency should have been during this test as VCO frequency versus temperature data was not available from the ground support equipment operators.

b. Telemetry. Because of limited Flight Data System configuration support, only two telemetry processing tests were performed. Both tests were performed on a functional basis to insure that the Mark III Data Subsystems hardware and software would perform satisfactorily. Results of both tests indicated proper operation. Additionally, analyses of the X-band telemetry spectrum tests are incomplete. A report on this phase of testing will be issued at a later date.

c. Command. Command testing was performed at nominal uplink signal levels and at signal levels below expected project mission conditions. Two separate, nontimed commands (2N: X-band ranging channel ON and 2 NR: X-band ranging channel OFF) were successfully sent to the Prototype Spacecraft and successfully executed. These tests were significant in that it marked the first time that the ground command system had been utilized to send actual commands to the flight command system.

d. Radio metric. Ranging tests were performed on a functional basis only. It was, however, determined that the ranging function could be performed with the new 45 degree (-3.0 dB carrier suppression) modulation index and with an uplink signal level of -130 dBm, which is 10 dB below the minimum signal level expected at Saturn encounter with a 64-meter 20-kW transmitter.

4. Status. The DSN-MJS'77 Prototype Spacecraft Telecommunications Compatibility Tests during the period 7 December through 16 December successfully demonstrated that telecommunications interfaces between the ground station and the spacecraft were viably functional at strong signal levels. It further demonstrated that telecommunications compatibility between the DSN and the MJS'77 Flight Spacecrafts can probably be achieved providing that all flight telemetry modes and flight-rated traveling wave tube amplifiers are provided.

III. Conclusions

DSN-MJS'77 telecommunications compatibility testing so far has determined that no major incompatibilities have been discovered. The series of tests have proven that the DSN Mark III Data Subsystems are performing within expectations and are compatible within the flight-ground interface structure. It can be assumed with high probability that the DSN and MJS'77 telecommunications links will satisfy mission objectives.

The formal compatibility test program developed jointly by the DSN and the MJS'77 Flight Project is progressing satisfactorily and at anticipated cost. The success of this program so far is because of the close coordination and cooperation of all participating units.

References

1. *Deep Space Network/Flight Project Interface Compatibility Test Design Handbook*, 810-8, Rev. B, DSN Standard Practice. Jet Propulsion Laboratory, Pasadena, California (JPL internal document).

2. Bryan, A. I., and Madsen, B. D., "DSN Mariner Jupiter-Saturn 1977 Prototype Radio Frequency Subsystem Compatibility Status and Test Report," *The Deep Space Network Progress Report 42-35*, pp. 4-10, Jet Propulsion Laboratory, Pasadena, California, October 1976.

3. *Mariner Jupiter-Saturn 1977 DSN-Spacecraft Compatibility Test Plan*, PD 618-258. Jet Propulsion Laboratory, Pasadena, California, September 1, 1976 (JPL internal document).

Table 1. Deep Space Network—MJS'77 Flight 1 spacecraft telecommunications compatibility test summary

Test date	Test title	Test No.	DSN mode	Spacecraft MOD	Spacecraft RM	Test conditions	Performance	Criteria	Time, min
1/5	Telemetry performance	TM-2-4	122611	6633-16		X-band DL signal level: −125.0 dBm (Pc)	MCD SNR: 2.85 dB	$<5 \times 10^{-3}$ BER	70
						X-band TLM bit rate: 44.8 kbits/s coded	SSA SNR: 0.34 dB		
						X-band Y-factor: 10.99 dB = STB/No. of 4.0 dB	BER: 8.53×10^{-3}		
						S-band UL signal level: −110 dBm			
						Command Mod. = 20 deg Ranging Mod. = 45 deg			
			002611	6633-16		Same as above	MCD SNR: 3.47 dB	$<5 \times 10^{-3}$ BER	
							SSA SNR: 0.48 dB		
							BER: 2.47×10^{-3}		
1/5	Telemetry performance	TM-2-5	002611	6630-16		X-band DL signal level: −127.5 dBm (Pc)			150
						X-band TLM bit rate: 29.9 kbits/s coded			
						X-band Y-factor: 9.43 = STB/No. of 4.0 dB			
						S-band UL signal level: −110 dBm (Pc)	MCD SNR: 3.10 dB	$<5 \times 10^{-3}$ BER	
						Command Mod. = 20 deg Ranging Mod. = 45 deg	SSA SNR: 0.21 dB		
							BER: 5.0×10^{-3}		
			122611	6631-16		Same as above	MCD SNR: 2.93 dB	$<5 \times 10^{-3}$ BER	
							SSA SNR: 0.30 dB		
							BER: 6.78×10^{-3}		
			002611	6630-14		X-band DL signal level: −127.0 dBm (Pc)	MCD SNR: 3.86 dB	$<5 \times 10^{-3}$ BER	
						X-band Y-factor: 10.3 = STB/No. of 5.0 dB	SSA SNR: 1.09 dB		
							BER: 2.27×10^{-3}		
1/5	Telemetry performance	TM-2-7	002311	6630-16		S-band DL signal level: −142.0 dBm (Pc)	MCD SNR: 6.07 dB	$<5 \times 10^{-3}$ BER	32
						S-band TLM bit rate: 2.56 kbits/s coded	SSA SNR: 2.89 dB		
						S-band Y-factor: 12.12 dB plus 10.34 dB Pad = STB/No. of 7.0 dB	BER: No bit errors		
						S-band UL signal level: −110 dBm			

Table 1 (contd)

Test date	Test title	Test No.	DSN mode	Spacecraft MOD	Spacecraft RM	Test conditions	Performance	Criteria	Time, min
1/5	Telemetry performance	TM-2-10	002311	6630-16		S-band DL signal level: -146.0 dBm (Pc)	MCD SNR: 3.95 dB	$<5 \times 10^{-3}$ BER	27
						S-band TLM bit rate: 1.2 kbits/s coded	SSA SNR: 0.49 dB		
						S-band Y-factor: 7.5 dB plus 10.34 dB Pad = STB/No. of 5.0 dB	BER: 6.64×10^{-4}		

Table 2. Deep Space Network–MJS'77 Flight 2 spacecraft telecommunications compatibility test summary

Test date	Test title	Test No.	DSN mode	Spacecraft MOD RM	Test conditions	Performance	Criteria	Time, min
11/17	Telemetry processing	TM-3-1	122612	633-16	X-band DL signal level: −120.0 dBm X-band UL signal level: −113.5 dBm X-band TLM bit rate: 89.6 kbits/s coded MCD SNR ≥ 10.175 dB	BER = 0	BER = 0	18
11/17	Telemetry processing	TM-3-2	122612	6633-16	X-band DL signal level: −120.0 dBm X-band UL signal level: −113.5 dBm X-band TLM bit rate: 67.2 kbits/s coded MCD SNR ≥ 10.175 dB	BER = 0	BER = 0	56
11/17	Telemetry processing	TM-3-3	122612	6633-16	X-band DL signal level: −120.0 dBm X-band UL signal level: −113.5 dBm X-band TLM bit rate: 21.6 kbits/s coded MCD SNR ≥ 10.175 dB	BER = 0	BER = 0	46
11/17	Telemetry processing	TM-3-4	122612	6633-16	X-band DL signal level: −120.0 dBm X-band UL signal level: −113.5 dBm X-band TLM bit rate: 19.2 kbits/s coded MCD SNR ≥ 10.175 dB	BER = 0	BER = 0	21
11/19	Telemetry processing	TM-3-5	002312	4410-10	S-band DL signal level: −120.0 dBm S-band UL signal level: −110.0 dBm S-band TLM bit rate: 1280 bits/s coded MCD SNR ≥ 10.175 dB	BER data not available	BER = 0	74
11/19	Telemetry processing	TM-3-6	002312	4410-10	S-band DL signal level: −118.0 dBm S-band UL signal level: −110.0 dBm S-band TLM bit rate: 320 bits/s coded MCD SNR ≥ 10.175 dB	BER data not available	BER = 0	26
11/19	Telemetry processing	TM-3-7	002312	4410-10	S-band DL signal level: −120.0 dBm	BER data not available	BER = 0	30

Table 2 (contd)

Test date	Test title	Test No.	DSN mode	Spacecraft MOD	Spacecraft RM	Test conditions	Performance	Criteria	Time, min
						S-band UL signal level: −110.0 dBm S-band TLM bit rate: 80 bits/s coded MCD SNR > 10.175 dB			
11/18	Telemetry performance	TM-2-5				X-band DL signal level: −128.0 dBm X-band TLM bit rate: 29.9 kbits/s coded			60
			122612	6633	16	X-band UL signal level: −113.5 dBm	BER = 8.33×10^{-4}	BER ≤ 5×10^{-3}	
			002612	6633	16	X-band UL signal level: −110.0 dBm	BER = 1.91×10^{-4}	BER ≤ 5×10^{-3}	
11/18	Telemetry performance	TM-2-6				X-band DL signal level: −128.0 dBm X-band TLM bit rate: 7.2 kbits/s coded			156
			122612	6633	16	X-band UL signal level: −113.5 dBm	BER = 6.07×10^{-4}	BER ≤ 5×10^{-3}	
			002612	6633	16	X-band UL signal level: −110.0 dBm	BER = 2.04×10^{-4}	BER ≤ 5×10^{-3}	
11/18	Telemetry performance	TM-2-7	002312	6633	16	S-band DL signal level: −152.0 dBm S-band UL signal level: −110.0 dBm S-band TLM bit rate: 2.56 kbits/s coded ST_B/N_o = 4.0 dB	BER = 7.09×10^{-4}	BER ≤ 5×10^{-3}	80
11/19	Telemetry performance	TM-2-8	002312	4410	10	S-band DL signal level: −151.5 dBm S-band UL signal level: −110.0 dBm S-band TLM bit rate: 640 bits/s coded ST_B/N_o = 4.0 dB	BER = 4.27×10^{-4}	BER ≤ 5×10^{-3}	131
11/19	Telemetry performance	TM-2-9	002312	4410	10	S-band DL signal level: −154.5 dBm S-band UL signal level: −110.0 dBm S-band TLM bit rate: 160 bits/s coded ST_B/N_o = 6.0 dB	BER = 7.58×10^{-4}	BER ≤ 5×10^{-3}	130
11/19	Telemetry performance	TM-2-10	002312	4410	10	S-band DL signal level: −151.5 dBm S-band UL signal level: −110.0 dBm	BER = 1.26×10^{-4}	BER ≤ 5×10^{-3}	51

Table 2 (contd)

Test date	Test title	Test No.	DSN mode	Spacecraft MOD	Spacecraft RM	Test conditions	Performance	Criteria	Time, min
						S-band TLM bit rate: 1.2 kbits/s coded ST_B/N_o = 5.0 dB			
11/15	Downlink RF carrier threshold (one-way) S- and X-band	RF-1-1	000100	4400-10		S-band DL frequency. 2295.001088 MHz	-157.2 dBm	-158.0 ± 1.0 dBm	118
			000600	4400-10		X-band DL frequency: 8414.960510 MHz	-152.8 dBm	-154.0 ± 1.0 dBm	
11/15 11/16	Downlink RF carrier (two-way) S- and X-band	RF-1-5				S-band UL frequency: 2113.310408 MHz S-band DL frequency: 2294.997728 MHz X-band DL frequency: 8414.990873 MHz			69
			002100	4413-10		S-band UL signal level: -100.0 dBm	S-band; -156.8 dBm	-158.0 ± 1.0 dBm	
			002500				X-band; -152.8 dBm	-154.0 ± 1.0 dBm	
						S-band UL signal level: -130.0 dBm	S-band; -156.6 dBm	-158.0 ± 1.0 dBm	
							X-band; -150.0 dBm	-154.0 ± 1.0 dBm	
			122100			S-band UL signal level: -100.0 dBm	S-band; -156.5 dBm	-158.0 ± 1.0 dBm	
							X-band; -149.4 dBm	-154.0 ± 1.0 dBm	
11/16	Spacecraft transmitter carrier phase jitter (one-way)	RF-5-1	000$\frac{1}{2}$00	4400-10		S-band DL frequency: 2294.997728 MHz	1.55 deg rms	≤3.0 deg rms	65
			000$\frac{5}{6}$00	4400-10		X-band DL frequency: 8414.991669 MHz	8.32 deg rms	≤11.0 deg rms	
	(two-way)		002$\frac{1}{2}$00	4410-10		S-band DL frequency: 2294.997719 MHz	21.8 deg rms	≤2.3 deg rms*	
			002$\frac{5}{6}$00	4410-10		X-band DL frequency: 8414.991638 MHz	64.13 deg rms	≤8.4 deg rms*	
						*UL signal level -130.0 dBm instead of -70.0 dBm for criteria shown			
11/16	Spacecraft transmitter carrier phase jitter (one-way)	RF-5-2	000$\frac{1}{2}$00	6620-16		S-band DL frequency: 2295.000992 MHz	0.76 deg rms	≤3.0 deg rms	68
			000$\frac{5}{6}$00	6620-16		X-band DL frequency: 8415.003637 MHz	7.01 deg rms	≤11.0 deg rms	
	(two-way)		002$\frac{1}{2}$00	6630-16		S-band DL frequency: 2295.008140 MHz	22.04 deg rms	≤2.3 deg rms*	
			002$\frac{5}{6}$00	6630-16		X-band DL frequency: 8414.994850 MHz	64.7 deg rms	≤8.4 deg rms*	
						*UL signal level -130.0 dBm instead of -70.0 dBm for criteria shown			

Table 2 (contd)

Test date	Test title	Test No.	DSN mode	Spacecraft MOD	Spacecraft RM	Test conditions	Performance	Criteria	Time, min
11/18	Telemetry performance	TM-2-3				X-band DL signal level: -122.0 dBm			165
						X-band TLM bit rate 115.2 kbits/s coded			
						ST_B/N_o = 4.0 dB			
			122612	6633-16		X-band UL signal level: -133.5 dBm	BER = 4.78×10^{-4}	BER < 5×10^{-3}	
			002612	6633-16		X-band UL signal level: -110.0 dBm	BER = 7.8×10^{-5}	BER < 5×10^{-3}	
			002612	6633-16		X-band UL signal level: -110.0 dBm	BER = 1.03×10^{-4}	BER < 5×10^{-3}	
						X-band UL frequency Offset: +72.5 kHz			
11/18	Telemetry performance	TM-2-4				X-band DL signal level: -126.0 dBm			65
						X-band TLM bit rate: 44.8 kbits/s coded			
						ST_B/N_o = 4.0 dB			
			122612	6633-16		X-band UL signal level: -113.5 dBm	BER = 5.5×10^{-4}	BER < 5×10^{-3}	
			002612	6633-16		X-band UL signal level: -110.0 dBm	BER = 3.97×10^{-5}	BER < 5×10^{-3}	
11/22	Command SNR verification	CM-2-2	022000	4410-10		UL carrier suppression: -0.54 dB		Special investigative tests; no criteria	186
						UL signal level: -125.5 dBm	SNR = 18.5 dB		
						UL signal level: -133.5 dBm	SNR = 7.66 dB		
						UL carrier suppression: -3.0 dB			
						UL signal level: -114.0 dBm	SNR = 36.0 dB		
						UL signal level: -124.0 dBm	SNR = 27.5 dB		
						UL signal level: -141.0 dBm	SNR = 9.0 dB		

Table 3. Deep Space Network–MJS'77 prototype spacecraft telecommunications compatibility test summary

Test date	Test title	Test No.	DSN mode	Spacecraft RFS mode	Test conditions	Criteria	Performance	Time, min
12/7	DL threshold (one-way)	RF-1-3	000300	6720-16	S-band DL frequency: 2294.999640 MHz	−159.0 ± 3.0 dBm	−159.0 dBm	55
			000600	6720-16	X-band DL frequency: 8414.998820 MHz	−150.0 ± 3.0 dBm	−149.8 dBm	
12/8	DL threshold (two-way)	RF-1-4	002300	6703-16	S-band UL frequency: 2113.315008 MHz			39
					S-band DL frequency: 2295.002600 MHz	−159.0 ± 3.0 dBm	−161.0 dBm	
			002600	6703-16	X-band DL frequency: 8415.010745 MHz	−150.0 ± 3.0 dBm	−149.5 dBm	
12/8	DL threshold (two-way)	RF-1-6	002300	6720-16	S-band UL frequency: 2114.682864 MHz			54
					S-band DL frequency: 2296.488200 MHz	−159.0 ± 3.0 dBm	−161.0 dBm	
					X-band DL frequency: 8420.456695 MHz	−150.0 ± 3.0 dBm	−149.0 dBm	
12/8	UL threshold	RF-2-1	002300	6713-16	S-band UL frequency: 2113.315008 MHz	≤−152.0 dBm	−156.0 dBm	17
					Spacecraft Receiver No. 1 high-gain antenna			
12/8	UL threshold	RF-2-2	002300	6733-16	S-band UL frequency: 2114.683872 MHz	≤−152.0 dBm	−156.0 dBm	22
					Spacecraft Receiver No. 2 low-gain antenna			
12/8	UL threshold	RF-2-3	122300	6753-16	S-band UL frequency: 2113.315008 MHz	≤−152.0 dBm	−155.0 dBm	34
					Spacecraft Receiver No. 1 low-gain antenna			
2/8	UL threshold	RF-2-4	122300	6773-16	S-band UL frequency: 2114.683872 MHz	≤−152.0 dBm	−156.0 dBm	31
					Spacecraft Receiver No. 2 low-gain antenna			
12/8	Spacecraft receiver static acquisition	RF-3-1	002300	6603-16	Spacecraft best lock frequency: 2113.312512 MHz			32
					−200 Hz OFFSET	≤15 s	Lock at 1 s	
					−400 Hz OFFSET	≤30 s	Lock at 3 s	
					−600 Hz OFFSET	≤60 s	Lock at 7 s	
					−800 Hz OFFSET	≤150 s	Lock at 16 s	
					−1000 Hz OFFSET	≤300 s	Lock at 48 s	
					+200 Hz OFFSET	≤15 s	Lock at 1 s	
					+400 Hz OFFSET	≤30 s	Lock at 3 s	
					+600 Hz OFFSET	≤60 s	Lock at 6 s	
					+800 Hz OFFSET	≤150 s	Lock at 14 s	
					+1000 Hz OFFSET	≤300 s	Lock at 18 s	

Table 3 (contd)

Test date	Test title	Test No.	DSN mode	Spacecraft RFS mode	Test conditions	Criteria	Performance	Time, min
2/8	Spacecraft receiver station acquisition	RF-3-2	002300	6733-16	Spacecraft best lock frequency: 2114 683872 MHz			64
					-200 Hz OFFSET	≤15 s	Lock at 1 s	
					-400 Hz OFFSET	≤30 s	Lock at 3 s	
					-600 Hz OFFSET	≤60 s	Lock at 6 s	
					-800 Hz OFFSET	≤150 s	Lock at 20 s	
					-1000 Hz OFFSET	≤300 s	No lock	
					+200 Hz OFFSET	≤15 s	Lock at 1 s	
					+400 Hz OFFSET	≤30 s	Lock at 3 s	
					+600 Hz OFFSET	≤60 s	Lock at 6 s	
					+800 Hz OFFSET	≤150 s	Lock at 12 s	
					+1000 Hz OFFSET	≤300 s	Lock at 25 s	
12/8	Spacecraft receiver sweep acquisition	RF-3-3	002300	6603-16	Spacecraft best lock frequency: 2113.312512 MHz			22
					UL signal level: -144.0 dBm	Acquire at Offset: +7 kHz Rate: 60 Hz/s	Acquired	
						Acquire at Offset: -7 kHz Rate: 60 Hz/s	Acquired	
12/8	Spacecraft receiver sweep acquisition	RF-3-4	002300	6623-16	Spacecraft best lock frequency: 2114.676672 MHz			
					UL signal level: -144.0 dBm	Acquire at Offset: +7 kHz Rate: 60 Hz/s	Acquired	
						Acquire at Offset: -7 kHz Rate: 60 Hz/s	Acquired	
12/8	Spacecraft receiver tracking	RF-4-1	122300	6713-16	UL signal level: -120.0 dBm Ramp rate: 100 Hz/s Offset: +72.5 kHz	≤60 deg static phase error	Maintained proper operation	57
					UL signal level: -120.0 dBm Ramp rate: 100 Hz/s Offset: -72.5 kHz	≤60 deg static phase error	Maintained proper operation	
12/8	Spacecraft receiver tracking	RF-4-2	122300	6733-16	UL signal level: -120.0 dBm Ramp rate: 100 Hz/s Offset: +72.5 kHz	≤60 deg static phase error	Maintained proper operation	44
					UL signal level: -120.0 dBm Ramp rate: 100 Hz/s Offset: -72.5 kHz	≤60 deg static phase error	Maintained proper operation	

Table 3 (contd)

Test date	Test title	Test No.	DSN mode	Spacecraft RFS mode	Test conditions	Criteria	Performance	Time, min
12/9	Spacecraft transmitter carrier phase jitter (one-way)	RF-5-2	$000\frac{1}{2}00$	6620-16	S-band DL frequency: 2296.487552 MHz	3.0 deg rms	0.4 deg rms	43
			$000\frac{5}{6}00$	6620-16	X-band DL frequency: 8420.450575 MHz	11.0 deg rms	6.62 deg rms	
12/9	Spacecraft transmitter carrier phase jitter (one-way)	RF-5-3	$000\frac{1}{2}00$	6724-16	S-band DL frequency: 2294.999648 MHz	3.0 deg rms	0.4 deg rms	54
			$000\frac{5}{6}00$		X-band DL frequency: 8414.994765 MHz	11.0 deg rms	6.08 deg rms	
	(two-way)		$002\frac{1}{2}00$	6734-16	S-band DL frequency: 2296.493756 MHz	2.3 deg rms	0.47 deg rms	
			$002\frac{5}{6}00$		X-band DL frequency: 8420.477104 MHz	8.4 deg rms	6.27 deg rms	
12/9	Spacecraft transmitter carrier phase jitter (one-way)	RF-5-4	$000\frac{1}{2}00$	6720-16	S-band DL frequency: 2294.999552 MHz	3.0 deg rms	0.55 deg rms	112
			$000\frac{5}{6}00$		X-band DL frequency: 8414.994765 MHz	11.0 deg rms	6.13 deg rms	
	(two-way)		$002\frac{1}{2}00$	6730-16	S-band DL frequency: 2296.491983 MHz	2.3 deg rms at -108 dbm UL	1.98 deg rms	
			$002\frac{5}{6}00$		X-band DL frequency: 8420.470606 MHz	8.42 deg rms at -108 dBm UL	5.34 deg rms	
12/11	Command processing	CM-1-1	121100	7513-16	S-band UL frequency: 2113.312512 MHz UL signal level, P_T: -143.0 dBm UL carrier suppression: -5.0 dB Subcarrier offset: 0.0 Hz +0.2 Hz -0.2 Hz	Proper subcarrier and bit sync acquisition; verification of command execution	 O.K. O.K. O.K.	111
12/10	Command processing	CM-1-2	022000	5772-16	S-band UL frequency: 2114.676672 MHz UL signal level, P_T: -143.0 dBm UL carrier suppression: -5.0 dB Subcarrier offset: 0.0 Hz +0.2 Hz -0.2 Hz	Proper subcarrier and bit sync acquisition; verification of command execution	 O.K. O.K. O.K.	74

Table 3 (contd)

Test date	Test title	Test No.	DSN mode	Spacecraft RFS mode	Test conditions	Criteria	Performance	Time, min
12/16	Command processing	CM-1-3	021000	2530-02	S-band UL frequency: 2114.676672 MHz UL signal level, P_T: -5.0 dB UL carrier suppression: -5.0 dB Subcarrier offset 0.0 Hz -0.2 Hz +0.2 Hz	Proper subcarrier and bit sync acquisition; verification of command execution	 O.K. O.K. O.K.	80
12/11	Command SNR verification	CM-2-1	022000	6712-16	UL signal level: -139.0 dBm, P_C UL carrier suppression: -5.0 dB	> 1.5 dB	2.5 dB SNR	45
12/10	Telemetry spectrum analysis	TM-1-1			S-band DL frequency: 2296.486976 MHz X-band DL frequency: 8420.452700 MHz	Identify all spurious spectral components greater than -30.0 dB		80
			000200	6623-12	S-band TLM: 40 bits/s		None noted	
			000600	6623-12	X-band TLM: 230.4 kbits/s S-band UL frequency: 2114.690880 MHz S-band DL frequency: 2296.496883 MHz X-band DL frequency: 8420.488572 MHz		Analysis incomplete	
			002200	6633-12	S-band TLM: 40 bits/s		None noted	
			002600	6633-12	X-band TLM: 230.4 kbits/s		Analysis incomplete	
			122200	6633-12	S-band TLM: 40 bits/s		None noted	
			122600	6633-12	X-band TLM: 230.4 kbits/s		Analysis incomplete	
12/10	Telemetry spectrum analysis	TM-1-2			S-band DL frequency: 2295.054560 MHz X-band DL frequency: 8415.189755 MHz	Identify all spurious spectral components greater than -30.0 dB		60
			000200	5703-12	S-band TLM: 230.4 kbits/s		None noted	
			000600	5703-12	X-band TLM: 230.4 kbits/s S-band UL frequency: 2113.312512 MHz S-band DL frequency: 2295.000013 MHz X-band DL frequency: 8415.000048 MHz		Analysis incomplete	

Table 3 (contd)

Test date	Test title	Test No.	DSN mode	Spacecraft RFS mode	Test conditions	Criteria	Performance	Time, min
			002200	5703-12	S-band TLM: 230.4 KSPS		None noted	
			002600	5703-12	X-band TLM: 230.4 KSPS		Analysis incomplete	
			122200	5703-12	S-band TLM: 230.4 KSPS		None noted	
			122600	5703-12	X-band TLM: 230.4 KSPS		Analysis incomplete	
12/10	Telemetry spectrum analysis	TM-1-3			S-band DL frequency: 2295.038912 MHz X-band DL frequency: 8415.189755	Identify all spurious spectral components greater than -30.0 dB		44
			000200	5703-16	S-band TLM: 40 bits/s		None noted	
			000600	5703-16	X-band TLM: 89.6 KSPS S-band UL frequency: 2113.312512 MHz S-band DL frequency: 2295.000013 MHz X-band DL frequency: 8415.000048 MHz		Analysis incomplete	
			002200	5713-16	S-band TLM: 40 bits/s		None noted	
			002600	5713-16	X-band TLM: 89.6 KSPS		Analysis incomplete	
			122200	5713-16	S-band TLM: 40 bits/s		None noted	
			122600	5713-16	X-band TLM: 89.6 KSPS		Analysis incomplete	
12/10	Telemetry spectrum analysis	TM-1-4			S-band DL frequency: 2295.004352 MHz X-band DL frequency: 8415.015957 MHz	Identify all spurious spectral components greater than -30.0 dB		40
			000200	5703-16	S-band TLM: 40 bits/s		None noted	
			000600	5703-16	X-band TLM: 14.4 KSPS S-band UL frequency: 2113.312512 MHz S-band DL frequency: 2295.000032 MHz X-band DL frequency: 8415.000290 MHz		Analysis incomplete	
			002200	5713-16	S-band TLM: 40 bits/s		None noted	
			002600	5713-16	X-band TLM: 14.4 KSPS		Analysis incomplete	
			122200	5713-16	S-band TLM: 40 bits/s		None noted	
			122600	5713-16	X-band TLM: 14.4 KSPS		Analysis incomplete	

Table 3 (contd)

Test date	Test title	Test No.	DSN mode	Spacecraft RFS mode	Test conditions	Criteria	Performance	Time, min
12/16	Telemetry spectrum analysis	TM-1-10			S-band DL frequency: 2294.999880 MHz S-band TLM: 2400 SPS	Identify all spurious spectral components greater than −30.0 dB	None noted	47
12/9	Telemetry spectrum analysis	TM-1-13			S-band DL frequency: 2296.487168 MHz X-band DL frequency: 8420.452949 MHz	Identify all spurious spectral components greater than −30.0 dB		120
			000200	6623-12	S-band TLM: 40 bits/s		None noted	
			000600	6623-12	X-band TLM: 134.4 KSPS S-band UL frequency: 2114.686368 MHz S-band DL frequency: 2296.491960 MHz X-band DL frequency: 8420.470720 MHz		Analysis incomplete	
			122200	6633-12	S-band TLM: 40 bits/s		None noted	
			122600	6633-12	X-band TLM: 134.4 KSPS		Analysis incomplete	
12/9	Telemetry processing	TM-3-2	122322	6633-12	S-band DL signal level: −120.0 dBm S-band TLM bit rate: 40 bits/s	>10.0 dB	25.0 dB SNR	69
			122612	6633-12	X-band DL signal level: −120.0 dBm X-band TLM bit rate: 67.2 kbits/s	> 2.5 dB	5.35 dB SNR	
12/16	Telemetry processing	TM-3-10	000322	4550-02	S-band DL signal level: −121.0 dBm S-band TLM bit rate: 1200 bits/s X-band DL signal level: −121.0 dBm X-band DL bit rate: 1200 bits/s	>10.0 dB >2.5 dB	19.85 dB SNR 10.18 dB SNR	46
12/11	Range delay performance test	RM-1-1			S-band UL frequency: 2113.312512 MHz UL signal level: −130 dBm DL frequency: 2295.000000 MHz DL signal level: −108.5 dBm	Functional test only. −130.0 dBm UL signal level is 10 dB below minimum signal level expected at Saturn encounter		90

Table 3 (contd)

Test date	Test title	Test No.	DSN mode	Spacecraft RFS mode	Test conditions	Criteria	Performance	Time, min
					X-band			
					DL frequency: 8415.000205 MHz			
					DL signal level: −112.0 dBm			
					0.0 Hz offset			
			$102\frac{3}{6}00$	7713-16	S-band		5434.4 RU	
					X-band		5157.0 RU	
					+72.5 kHz offset			
			$122\frac{3}{6}00$	7713-16	S-band		5436.6 RU	
					X-band		5175.8 RU	
					72.5 kHz offset			
			$122\frac{3}{6}00$	7713-16	S-band		5436.2 RU	
					X-band		5137.3 RU	
12/10	Range delay performance test	RM-1-3			S-band			163
					UL frequency: 2114.677152 MHz	Functional test only.		
					UL signal level: −130.0 dBm	−130.0 dBm UL signal level is 10 dB below minimum signal level expected at Saturn encounter		
					DL frequency: 2296.481975 MHz			
					DL signal level: −110.0 dBm			
					X-band			
					DL frequency: 8420.433908 MHz			
					DL signal level: −111.5 dBm			
					0.0 Hz offset			
			$102\frac{3}{6}00$	7733-16	S-band		5453.8 RU	
					X-band		5138.8 RU	
					+72.5 kHz offset			
			$122\frac{3}{6}00$	7733-16	S-band		5454.6 RU	
					X-band		5144.9 RU	
					72.5 kHz offset			
			$122\frac{3}{6}00$	7733-16	S-band		5452.3 RU	
					X-band		5138.4 RU	
12/10	Range delay calibration verification test	RM-2-1	$102\frac{3}{6}00$	7733-16	S-band UL frequency: 2114.677152 MHz	Functional test only		28
					S-band DL frequency: 2296.481975 MHz			
					S-band DL signal level: −108.5 dBm			

Table 3 (contd)

Test date	Test title	Test No.	DSN mode	Spacecraft RFS mode	Test conditions	Criteria	Performance	Time, min
					X-band DL frequency: 8420.433908 MHz			
					X-band DL signal level: -100.5 dBm			
					UL signal level: -112.5 dBm			
					S-band		5482.9 RU	
					X-band		5132.4 RU	
					UL signal level: -120.0 dBm			
					S-band		5468.8 RU	
					X-band		5140.0 RU	
					UL signal level: -130.0 dBm			
					S-band		5457.0 RU	
					X-band		5143.6 RU	
12/10	Range delay calibration verification test	RM-2-2	$102\frac{3}{6}00$	7773-16	S-band UL frequency: 2114.677152 MHz	Functional test only		25
					S-band DL frequency: 2296.481975 MHz			
					S-band DL signal level: -108.5 dBm			
					X-band DL frequency: 8420.433908 MHz			
					S-band DL signal level: -100.5 dBm			
					UL signal level: -113.0 dBm			
					S-band		5446.0 RU	
					X-band		5135.8 RU	
					UL signal level: -120.0 dBm			
					S-band		5447.4 RU	
					X-band		5141.6 RU	
					UL signal level: -130.0 dBm			
					S-band		5459.6 RU	
					X-band		5136.0 RU	
12/11	Range delay calibration verification test	RM-2-5	$102\frac{3}{6}00$	7513-16	S-band UL frequency: 2113.312512 MHz	Functional test only		17
					S-band DL frequency: 2295.000013 MHz			
					S-band DL signal level: -108.5 dBm			
					X-band DL frequency: 8115.000048 MHz			

Table 3 (contd)

Test date	Test title	Test No.	DSN mode	Spacecraft RFS mode	Test conditions	Criteria	Performance	Time, min
					X-band DL signal level: -112.0 dBm			
					UL signal level: -113.0 dBm			
					S-band		5430.5 RU	
					X-band		5177.3 RU	
					UL signal level: -120.0 dBm			
					S-band		5447.3 RU	
					X-band		5161.5 RU	
					UL signal level: -130.0 dBm			
					S-band		5442.3 RU	
					X-band		5151.3 RU	
12/11	Range delay calibration verification test	RM-2-6	$102\frac{3}{6}00$	7713-16	S-band UL frequency: 2113.312512 MHz	Functional		21
					S-band DL frequency: 2295.000013 MHz			
					S-band DL signal level: -108.5 dBm			
					X-band DL frequency: 8415.000048 MHz			
					X-band DL signal level: -112.0 dBm			
					UL signal level: -113.0 dBm			
					S-band		5424.8 RU	
					X-band		5188.0 RU	
					UL signal level: -120.0 dBm			
					S-band		5435.5 RU	
					X-band			
					UL signal level: -130.0 dBm			
					S-band		5438.8 RU	
					X-band		5148.5 RU	

Table 4. Definition of terms for Tables 1, 2, and 3

BER	bit error rate
BIT RATE	clock frequency of the telemetry bit information
bits/s	bits per second
CPA	Command Processor Assembly
CMF	Communications Monitor and Formatting Assembly
CTA 21	The Deep Space Network Ground Station Compatibility Test Area at JPL
dB	decibel
dBm	decibel referenced to one milliwatt
DL	RF downlink signal
DSN mode	The Deep Space Network Ground Station operational configuration
FDS	Spacecraft Flight Data Subsystem
JPL	Jet Propulsion Laboratory
MCD	Maximum Likelihood Convolutional Decoder
MDA	Metric Data Assembly
MDS	Spacecraft Modulation/Demodulation Subsystem
MDS	The DSN-MARK III Data Subsystems Implementation Project
No	noise spectral density
P_c	Power in RF carrier
P_T	Power total
PRA	Planetary Ranging Assembly
PFR	Problem/Failure Report
RDA	Ranging Demodulator Assembly
RF	radio frequency
RFS	Spacecraft Radio Frequency Subsystem
RU	range unit
SAF	Spacecraft Assembly Facility (JPL Building 179)
S/C RFS Mode	The Spacecraft Radio Frequency Subsystem operational configuration
SDA	Subcarrier Demodulator Assembly
SER	symbol error rate
SNR	signal-to-noise ratio
SPS	symbols per second
SSA	Symbol Synchronizer Assembly
SSF	Space Simulator Facility (JPL Building 150)
STb/No	signal-to-noise spectral density ratio
SYMBOL RATE	clock frequency of the telemetry symbol information
TBD	to be determined
TBS	to be supplied
TDL	Telemetry Development Laboratory
TLM	telemetry
TPA	Telemetry Processor Assembly
TWT	Traveling Wave Tube Amplifier
UL	RF uplink signal
Uplink Doppler	ramp rate of uplink RF carrier frequency
Uplink Offset	uplink RF carrier frequency displacement relative to the spacecraft receiver rest frequency
USO	ultra stable oscillator
VCO	voltage controlled oscillator

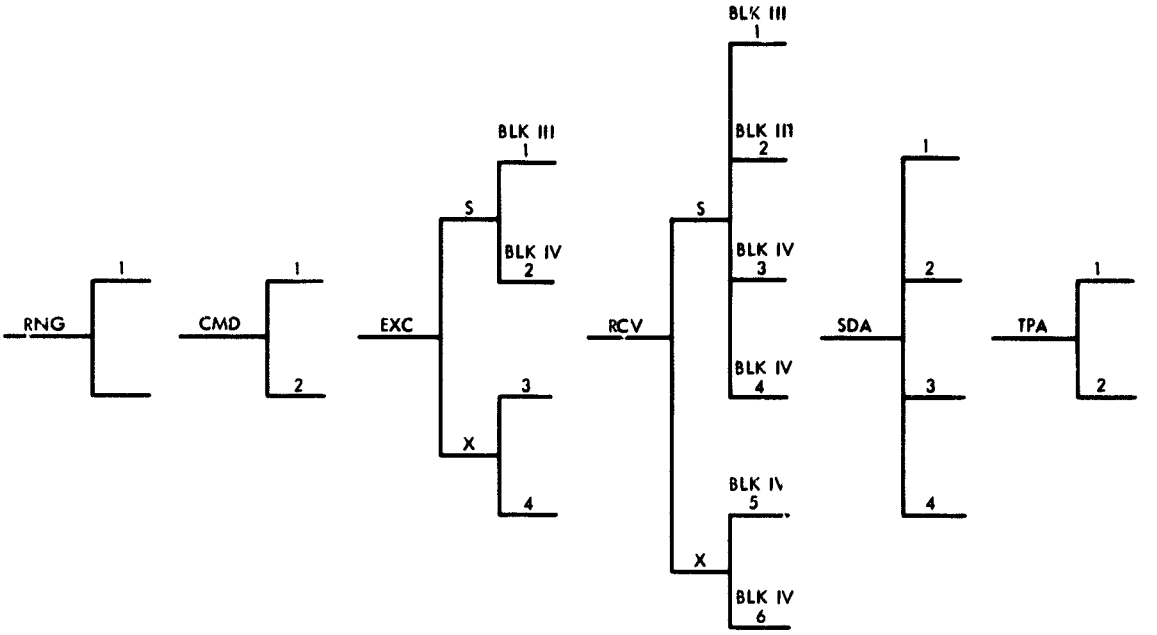

Fig. 1. DSN modes

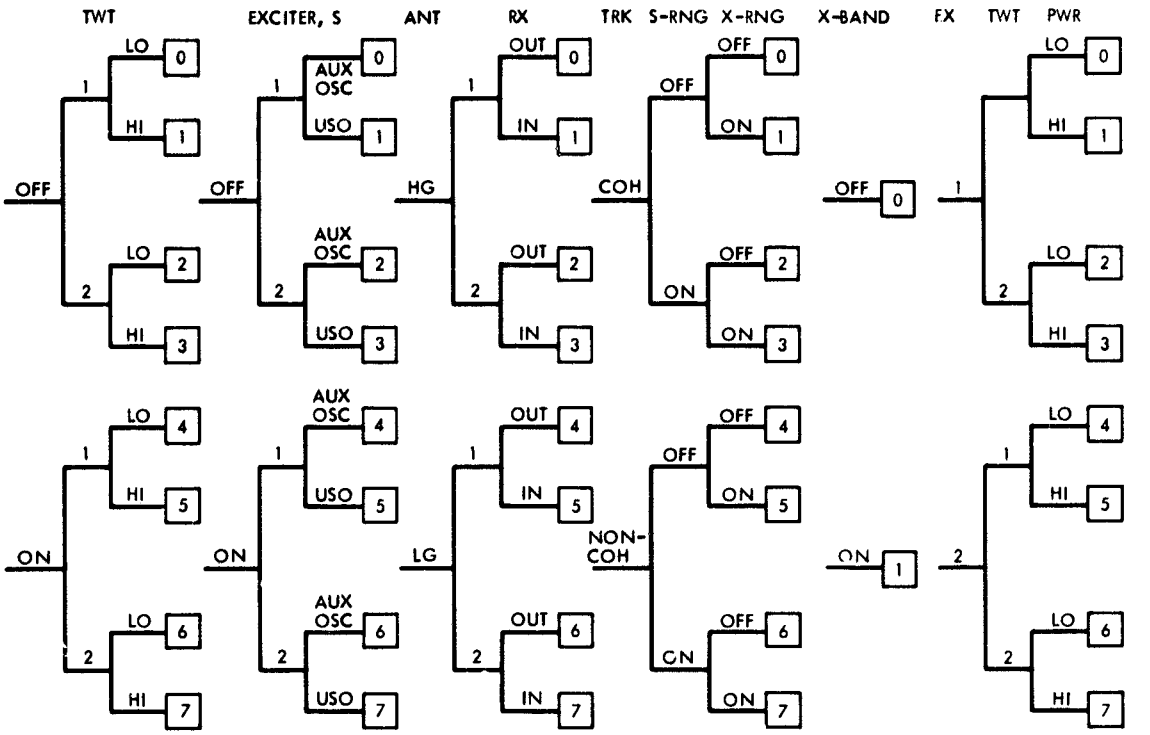

Fig. 2. MJS'77 operational RFS modes

Viking Mission Support

D. W. H. Johnston
DSN Network Operations

This report covers the relatively quiet Viking On Board Science & Telemetry period from November 15, 1976, through December 31, 1976, when Mars and the Viking spacecraft were in the Solar conjunction period. The period therefore presented the Viking Radio Science Team with a unique opportunity to utilize the DSN and Viking spacecraft to exercise their experiments with nonstandard station configurations, without the usual command and telemetry constraints.

I. Viking Operation Activities

The beginning of this reporting period (November 16, 1976) was coincident with the start of the Viking Extended Mission (VEM). At that time the Sun-Earth-Probe (SEP) angle was approximately 2.8 deg (from the center of the Sun's disc) and the degradation of the RF link caused by the proximity of the signal to the Sun was much that the Viking Orbiters were switched to a single subcarrier mode transmitting engineering telemetry only. The bit error rate was estimated at 23 in 4687 bits or 5×10^{-3}.

The 64-meter stations were using 100 kW of uplink power at this time on a daily basis to decrease the noise on the two-way doppler and ranging. The degradation of the RF links gradually increased as the SEP angle decreased, until the closed loop receivers were out of lock more than 50% of the time. Following is a summary of the events during the roughly symmetrical degradation and then improvement of the RF links through the solar conjunction period (see Figs. 1-3).

Nov. 16 DSS 61, bit error rate about 5×10^{-3}. The Sun-Earth-Probe angle (SEP) was about 2.8 deg, and decreasing 0.3 deg/day.

Nov. 18 DSS 61, bit error rate about 10^{-2}.

Nov. 22 X-band practically out of lock all the time, especially in two-way (when uplink at S-band is perturbed by Sun). SEP about 1 deg.

Nov. 23 DSS 14 could not lock closed-loop S-band receiver (about 50% out of lock) and could not lock telemetry on today's pass, beginning about 15:00 GMT (Day 76/328).

Nov. 25 Minimum SEP occurred today (Day 76/330/00:00 approximately).

Nov. 26 DSS 14 locked telemetry data (8-1/3 bps single subcarrier) on today's pass, beginning about 15:00 GMT (Day 76/331). Station also locked X-band downlink.

Dec. 1 DSS 61 was first 26-meter downlink since minimum SEP. SNR about 2.5 dB, BER not available, but data was readable.

Dec. 2 DSS 61 BER about 10^{-2}, data quality described as "very poor."

Dec. 8 First 33-1/3 bps single subcarrier (obtained at both DSS 42 and DSS 43, with even DSS 42 SNR above threshold. SNR about 7.5 dB at DSS 43, BER not available).

Dec. 13 SEP 5 deg today. First 2-kbps dual subcarrier (DSS 43).

Dec. 14 First 4-kbps playback, DSS 14, SNR 5 dB (above threshold).

Dec. 17 First 8-kbps playback, DSS 43, SNR 4 dB (above VIS threshold).

II. Viking Radio Science

Although during the solar conjunction period the Viking Orbiter and Lander uplink and downlink subcarrier data was virtually "lost in the noise," this gave the radio science team a unique opportunity to gather radio science data without the usual constraints of the normal mission operations. The radio science experiments detailed in the previous report were carried out as planned and results were as predicted or better. Following are some of the initial results of the radio science activities produced to date.

A. General Relativity Experiment

The Viking Flight Team and DSN completed the most stringent test of Einstein's General Theory of Relativity to date. A 0.5% accurate test of the relativistic time delay (Fig. 4) has already been accomplished, and it is expected that the test will achieve a 0.1% accuracy when all the lander ranging data is calibrated for solar corona effects and when sufficient long-term lander ranging and near-simultaneous orbiter ranging are obtained to correct for planetary ephemerides errors. The lander and near-simultaneous orbiter ranging will also be used as a dynamic test of the General Theory of Relativity as data is collected over the lifetime of the landers and orbiters.

B. Solar Corona Experiment

Extensive open-loop receiver analog and digital recordings were made by the DSN for the radio science solar corona experimenters at Stanford and JPL during the solar conjunction time period. X-band signals were observed and recorded within one solar radius on both entry and exit. Recordings were made when the signal passed through the chromosphere, but it has not been determined yet if any signal was detected. In any case, this is probably the deepest penetration of the solar corona by any man-made signal.

On December 29/30, 1976, a very complex set of simultaneous solar corona observations were made. DSS 14 received and recorded open-loop S-band signals from VO-1 and VO-2 and closed-loop doppler from VL-1. Simultaneously, DSS 43 received and recorded open-loop S and X-band signals from VO-1, and DSS 42 received closed-loop doppler from VO-2. These multiple-spacecraft/multiple-station solar corona observations were made during the same passes that two very successful lander and near-simultaneous orbiter ranging passes were accomplished.

C. Lander Ranging

The lander and near-simultaneous orbiter ranging are also used for various Martian planetology experiments. Preliminary results from these experiments have been published in two *Science* articles.

Preliminary results for lander locations, radii at the landing sites, the orientation of the spin axis of Mars, and the spin rate of Mars have been published (*Science* 193, 803 (1976) and 194, 1337 (1976)). Extended mission lander and simultaneous orbiter tracking data are needed to improve the accuracy of these results and, specifically, to attempt to determine spin axis precession and nutation. Spin axis motion constants, combined with low-degree gravity field parameters, would provide data for determination of constraints and models for mass and density distributions in the interior of Mars, with applications to its origin and history.

Preliminary results are available for pressure and temperature profiles in the lower atmosphere, and for radii at occultation points, for about two-thirds of the occultations observed during the primary mission (summarized in *Science* 194, 1337 (1976)). The uncertainties are somewhat larger than for previous occultation measurements because of the noise introduced by the signals passing close to the Sun. Additional and more accurate occultation data will be obtained for VO-2 starting in about 2 weeks, and for VO-1 starting in April.

D. Orbiter Doppler

Orbiter S and X-band doppler will continue to be collected and processed for the Martian gravity field experiments. Both a global gravity field analysis and a local gravity field analysis will be done. The global gravity field solutions are based on full orbits of tracking data, and the local gravity field analysis is based on the S-band/X-band doppler near periapsis.

E. Earth Occultation

The earth occultation resumed on January 14 (as planned), but unfortunately only a small percentage of the occultations will yield useful data. This is due to the limited DSN tracking coverage available and the conflicting project requirements for the limited resources available.

F. Very Long Baseline Interferometer (VLBI)

Orbiter/quasar VLBI observations will resume on February 8 and 10. However, these observations will also be limited during the Viking Extended Mission due to limited resources, particularly DSN station coverage.

III. DSN Support for Viking

The statistics listing the DSN tracking support for Viking during this reporting period are listed in Table 1. The Discrepancy Report status for this period is summarized in Table 2.

IV. DSN Major Items

Two major items related to DSN Viking support were the ball and socket bearing rework at DSS 63 and the implementation of the MK III data subsystems at DSS 12.

A. DSS 63 Support

During the solar conjunction period the scheduled rework on the DSS 63 64-meter antenna was carried out as planned. Tests during 1976 had indicated that the three 32-in.-diameter truncated steel balls, which support the entire antenna structure, had become more difficult to move in their sockets, to the point where new lubricant could no longer be forced between the ball and socket bearing surfaces. The rework, which consisted of removing the three assemblies and fitting new ball and socket assemblies, was started on November 15, 1976, and successfully completed on December 14, 1976. Examination after removal showed that the original lubricant had dried and compacted, preventing injection of fresh lubricant, and that the ball units were "out of round." A similar rework is scheduled to take place at DSS 43 during March 1977.

B. DSS 12 Support

The MK III Data Subsystem (MDS) update of the entire DSN involves the sequential modification of all Deep Space Stations, starting with DSS 12 in October 1976 and finishing with DSS 11 in early 1978. The System Performance Tests planned for the 26-meter stations include all the Viking requirements and were successfully completed at DSS 12 in December 1976. Two Operational Verification Tests, one System Integration Test with the VMCCC, and one Demonstration Pass with the Viking Orbiter spacecraft are scheduled for January 1977. These tests will be repeated with DSS 62 and DSS 44 during February and March 1977.

Acknowledgment

J. P. Brenkle and William H. Michael, Jr., contributed inputs from the Viking Radio Science Team.

Table 1. DSN tracking support for Viking

DSS	Number tracks	Hours tracked	Commands
	November 16-30		
11	3	11:18	0
12	–	–	–
14	32	179:16	0
42	2	16:14	0
43	24	143:14	0
44	–	–	–
61	8	44:20	0
62	–	–	–
63	–	–	–
Total	69	349:22	0
	December		
11	19	120:32	419
12	–	–	–
14	59	356:26	2113
42	27	278:17	3
43	63	608:41	1514
44	–	–	–
61	42	297:56	308
62	–	–	–
63	30	215:14	262
Total	240	1877:06	4699

Table 2. DSN Discrepancy Report status
November - December 1976

DRs open	=	56 as of November 15, 1976
New DRs opened	=	98
DRs closed	=	102
DRs open	=	52 as of January 1, 1977

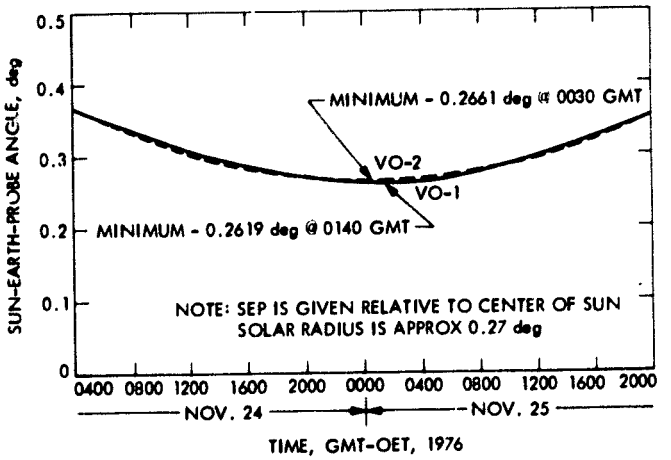

Fig. 1. Sun-Earth-Probe angle, November 24/25, 1976

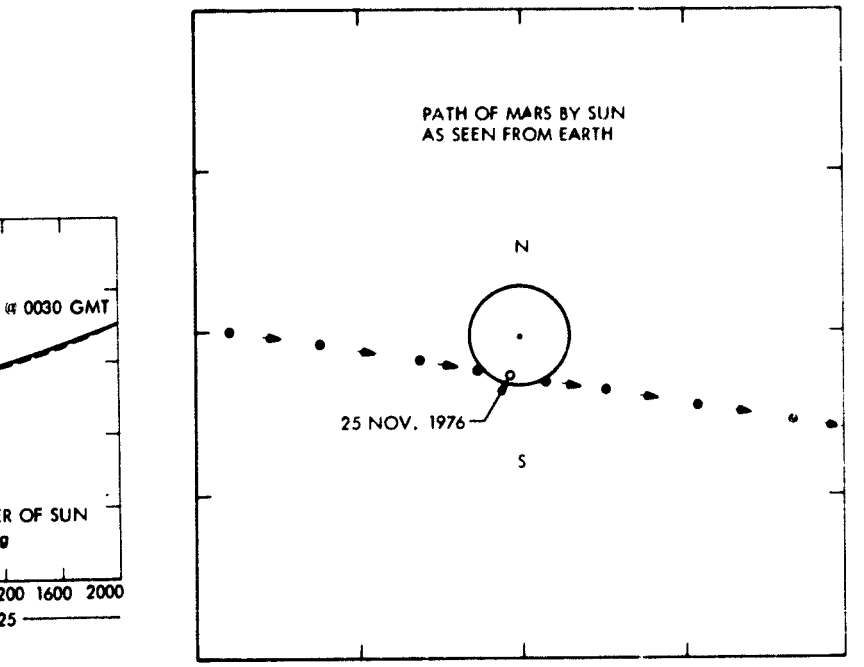

Fig. 3. Geometry of superior conjunction (Sun equator coordinate system)

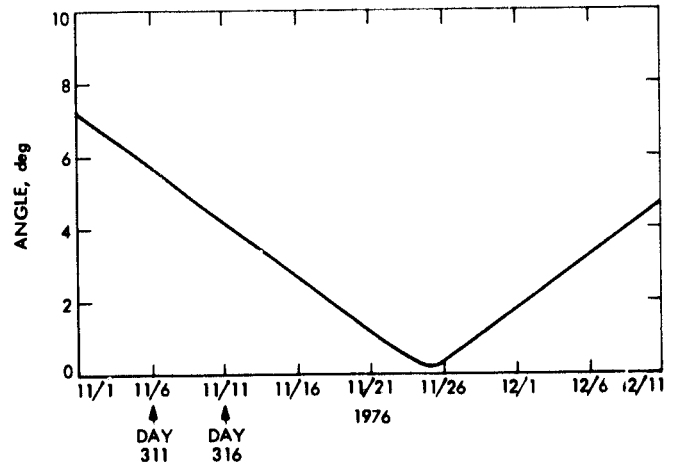

Fig. 2. Mars-Earth-Sun angle

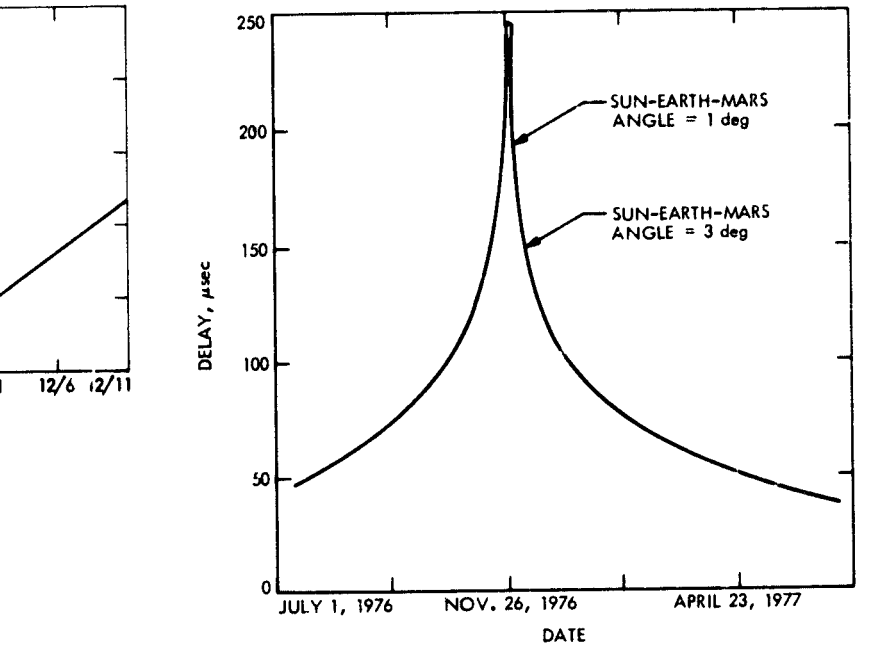

Fig. 4. Relativistic delay predicted for Viking

Pioneer Venus 1978 Mission Support

R. B. Miller
TDA Mission Support Office

The Ground Data System configuration for support of the Pioneer Venus 1978 Mission is described. Current status of the DSN portion of the Ground Data System is described.

I. Introduction

The telemetry and command portion of the Ground Data System which will be used to support the Pioneer Venus 1978 mission is described schematically in Fig. 1. Pictured is the usual telemetry and command configuration for the transit phase of the mission and for orbital operations. There will be a single telemetry stream in all transit and orbital phases of the mission, except for a brief period of Probe checkout in transit to Venus when a second subcarrier will be present containing Probe data.

The station configuration will be the standard multimission Mark III-DSN data subsystems configuration. Pioneer Venus will not, however, utilize the new "store-and-forward" mode of Command System operation. All telemetry data in the standard mission will be long constraint length, convolutionally encoded. Command and telemetry data will flow via standard NASCOM high-speed data circuits to the Pioneer Mission Operations Control Center (PMOCC) located at Ames Research Center. At Ames Research Center (ARC), real-time telemetry processing takes place in a Sigma 5 computer, and incoming high-speed data is logged. The Command System at Ames Research Center operates in a PDP-11 computer.

As the data passes through the West Coast Switching Center located at JPL in Pasadena, it will also be routed to the Network Operations Control Center where proper operation of the DSN portion of the Command and Telemetry Systems will be monitored. In addition, the DSN will be producing a log of the telemetry data and producing an Intermediate Data Record as a non-real-time deliverable to the Flight Project. The Intermediate Data Record will be shipped to Ames Research Center, where its contents can be merged with data logged in real-time in the PMOCC and where the Project will produce the Master Data Record (MDR) and with further processing produce the Experimenter Data Records (EDR) for delivery to the experimenters.

The Ground Data System interfaces between the DSN and ARC are, therefore, high-speed data circuits for the real-time data flow, voice circuits for coordination of operations, and an Intermediate Data Record of all recoverable telemetry.

The Tracking System portion of the Ground Data System does not directly involve Ames Research Center. The data flow would look identical to Fig. 1 for the path from the tracking station through the Intermediate Data Record (IDR) interface, with the navigation function at JPL being substituted for Ames Research Center as the recipient of the IDR.

There are three other elements of the Ground Data System which will be discussed separately below: the configuration for support of the Orbiter occultations, the configuration for support of telemetry recovery for the Multiprobe entry, and the configuration for support of the Multiprobe Wind Measurement Experiment.

II. Status of the DSN-GDS Interfaces: Cruise and Orbit

In December 1976, the high-speed data circuits used in support of Pioneer 6 through 11 were converted from 4800 to 7200 bits per second. This is significant for Pioneer Venus since this change gives enough margin on the high-speed data line capacity to enable making the Pioneer Venus high-speed data blocks for telemetry frame-synchronous. Each telemetry high-speed data block for Pioneer Venus will contain a single 512-bit telemetry frame. Note that all Pioneer Venus telemetry formats are the same 512-bit frame length and format changes will be transparent to the DSN.

The Ground Data System configuration being used to support Pioneer 10 and 11 looks essentially identical to that shown for Pioneer Venus in Fig. 1, except that an Intermediate Data Record is not currently produced for Pioneer 10 and 11. The current data record interface is to utilize the log tape produced by the PMOCC real-time system with Ames directly recalling missing data from the tracking stations to produce a Master Data Record of sufficient quality. It is planned to convert all previous Pioneers to the Intermediate Data Record interface in December 1977, coincident with the start of Ground Data System testing for Pioneer Venus.

Current high-speed data formats include a 33-bit error code used to detect errors in transmissions in real-time. The DSN has long-term plans to implement an error-correcting high-speed data system which will automatically retransmit high-speed data blocks found to be in error. This new system will require a new error code of 22 bits which requires a change in the high-speed data format. It was desirable to implement this change in high-speed data format prior to the start of Pioneer Venus testing in order to avoid having to implement two different formats for Pioneer Venus and changing format during the mission. Therefore, it was negotiated to convert all Pioneers to the new high-speed data format in February 1978, and to support Pioneer Venus testing starting in November 1977 in the new format. It was discovered, however, that this plan was inconsistent with the Navigation interface in that the Mission Control and Computing Center computer involved in the existing Navigation interface would not be able to handle the new high-speed data formats. There was an original plan to go to a new DSN Navigation interface for all missions in May 1978. This new DSN Navigation interface eliminates the Mission Control and Computing Center 360/75 computer from the radio metric data flow and involves the delivery of a radio metric Intermediate Data Record from the DSN directly to the Navigation computers. This scheduling incompatibility problem was solved by negotiating an earlier availability of the new interface in order to support Pioneer Venus prelaunch testing. The new interface will be operational by February 1978.

III. Configuration for Pioneer Venus Orbiter Occultation Support

Pioneer Venus will have periapsis Earth occultations on the order of the first 80 days of Venusian orbit. These occultations will be in the mutual view period of DSS 14 and 43 (Goldstone and Australian 64-meter stations). The first few occultations will be visible from only a single station until the orbit can be trimmed and synced up with the 2-station overlap period. The large number of Venusian occultations involved in Pioneer Venus made it impractical to utilize the configuration used to support all previous planetary occultations.

The usual method of supporting an occultation has been to make analog recordings of the output of an open-loop receiver whose bandwidth is wide enough to cover all the frequency changes that take place during the time span of interest. These analog recordings were then shipped to JPL, where the DSN digitized the recordings in the Compatibility Test Area. The digitized recordings were then delivered to the experimenter, who would then do a first step processing termed decimation.

The decimation process involves bandwidth reduction by multiplying the wide-bandwidth signal by an estimate of that signal and then filtering the product to remove that portion of the bandwidth which no longer contains any information. The problem in the case of Pioneer Venus is that the total shift at S-band for a Venusian occultation is on the order of 100 kHz. Pioneer Venus will also have X-band for the occultations, which would then be on the order of 400 kHz. This wide bandwidth meant that each analog recording would turn into many digitized tapes and that the processing by the experimenter to do the decimation was excessively expensive and time consuming.

A DSN team was formed in May 1976 to study ways to solve this problem as well as the problem of providing the interface with Massachusetts Institute of Technology for the Wind Measurement Experiment (described in Ref. 2). The functional concept of solving the occultation problem was accepted both by OTDA and the Project in June 1976. The resulting configuration, which will be implemented at DSS 14 and 43 for Pioneer Venus, is shown in Fig. 2.

The decimation process briefly described above can be accomplished in either a digital or analog fashion. The configuration shown in Fig. 2 is an analog approach. Instead of the open-loop receiver being driven by a fixed LO, a computer-controlled programmable local oscillator will be used to drive the first LO in the open-loop receivers to approximate the expected signal. This will enable using a much narrower bandwidth so that the signals can be analog-to-digital converted in real-time, and the resulting data rate will be low enough to be accommodated on a conventional computer-compatible recording. The configuration requires the implementation of an additional minicomputer at both stations in order to control the programmable local oscillator as well as do the formatting of the tape recording.

The operation of the system requires that an estimate of the expected signal be available for programming of the local oscillator. This requires the addition of a Venusian atmospheric model in the Navigation-to-DSN predict interface. The result will be predicted doppler, including atmospheric effects, which will be used to compute a series of linear ramps which will be programmed into the minicomputer to drive the programmable local oscillator.

It is intended that the standard interface with the experimenters will be the replay of the computer-compatible Original Data Record on-site over high-speed data lines back to the NOCC for production of an open-loop radio science Intermediate Data Record by the DSN. It will also be possible, when warranted, to directly ship the computer-compatible tapes to the NOCC for conversion to the Intermediate Data Record format.

A cost problem developed in the implementation of the occultation support system in the planned use of an integration contractor for constructing the system. The first proposal from the integration contractor was many times higher than the planned budget for the system. This problem has been negotiated by clarifying the requirements with the contractor and by pulling certain portions of the work back in-house. Although the schedule is tight, it is planned to have this configuration operable at Stations 14 and 43 by July 1, 1978, to give five months of operational system checkout and test and training. DSS 63 will also be provided with an occultation support system since some Mariner Jupiter-Saturn occultations will be visible from that station.

IV. Multiprobe Entry Configuration and Status

The Multiprobe entry operations and support strategy are described in Ref. 1. Figure 3 shows the configuration for the telemetry data recovery and the interferometry Wind Measurement Experiment for the Multiprobe entry. This is an update of the drawing which appeared in Ref 1. There are two principal changes since the time of writing of the reference. The interferometry experiment now requires a separate receiver, and the requirement for symbol recordings at the tracking stations has been deleted.

The original configuration involved sharing the Differential Long Baseline Interferometry Experiment (DLBI) function with one of the open-loop receivers which are being provided for precarrier detection telemetry recovery. Detailed design work on meeting the stringent DLBI experiment relative phase accuracy requirements led to the need for providing a separate special-purpose receiver for the experiment. The status of the DLBI experiment, including the support by two STDN tracking stations, was covered in great detail in Ref. 2. The only change in status since the writing of Ref. 2 is that a cost problem developed when the bid for the operational high-rate digital recorders came in 50% over plan. This problem was solved by deleting several desired multimission features from the recorders which do not directly affect the Pioneer Venus requirements, by delaying one of the transports for both Station 14 and 43 until FY-78, and by deleting the second recorder for CTA-21 for the tape conversion facility.

Originally it was thought that since each Telemetry Processor Assembly (TPA) contains only a single sequential decoder, there would be a capability for only two real-time probe streams from each station, and therefore a means of recording the soft decisions out of the Symbol Synchronizer Assembly would have to be provided to provide a "loss-less" digital recording for two of the four streams. It has turned out that since the sequential decoders which are provided within the main frame of the TPA computers are 4 to 5 times faster than the sequential decoders which were used for Pioneer 10 and 11 support, it will be possible to take advantage of this speed and produce software for the TPA which can handle two low-rate sequentially decoded streams simultaneously. It is, therefore, the current implementation plan to provide special software in the TPA for support of the Multiprobe entry in order to support two low-rate sequentially decoded streams simultaneously. This capability is currently scheduled for late summer of 1977.

A recent addition to the requirement for precarrier detection telemetry recovery is the requirement for the DSN to play the analog recordings backward into a closed-loop telemetry string at CTA-21 to produce a digital recording of the soft decisions out of the Symbol Synchronizer Assembly. Preliminary DSN testings make this backward playback look feasible with a minimal additional performance loss. The Project will develop "backward" sequential decoding software at Ames to process this data.

Also shown in Fig. 3 is a Multiprobe entry simulator which will be used to train the station operators for the Multiprobe entry event. This system has undergone a detailed design review and will enable simulating all four probes' signals simultaneously, including modulation changes, bit rate changes, and approximate doppler profiles. The system involves an analog tape recording of the four telemetry data streams (data plus subcarrier), which will be read into the Multiprobe entry simulator. The recorded tape will control the bit rates, and the start time on the tape will control the start of the sequencing in the Multiprobe entry simulator. The simulator will modulate the telemetry data onto a doppler realistic carrier for insertion into the station microwave system.

A detailed design still not settled is the signal presence indicator for the Multiprobe entry. There are currently two design alternatives. First, is a single signal presence indicator which would use an array processor to analyze the entire 2 MHz of interest at once. This approach would require a minicomputer to control the array processor and to generate operator displays. The second approach involves purchasing four or five separate spectrum analyzers for each station, where each analyzer would look at the output of a single open-loop receiver and therefore would be only 150- to 300-kHz bandwidth capability. Both systems would also be used to validate proper end-to-end operation of the DLBI system by operating either the array processor or one of the narrower bandwidth spectrum analyzers on the read-after-write output of the high-rate digital recorder.

References

1. Miller, R. B., Pioneer Venus Mission Support, *Deep Space Network Progress Report 42-27*, pp. 28-35, Jet Propulsion Laboratory, Pasadena, Calif., June 15, 1975.

2. Miller, R. B., Pioneer Venus Mission Support, *Deep Space Network Progress Report 42-36*, pp. 22-27, Jet Propulsion Laboratory, Pasadena, Calif., Dec. 15, 1976.

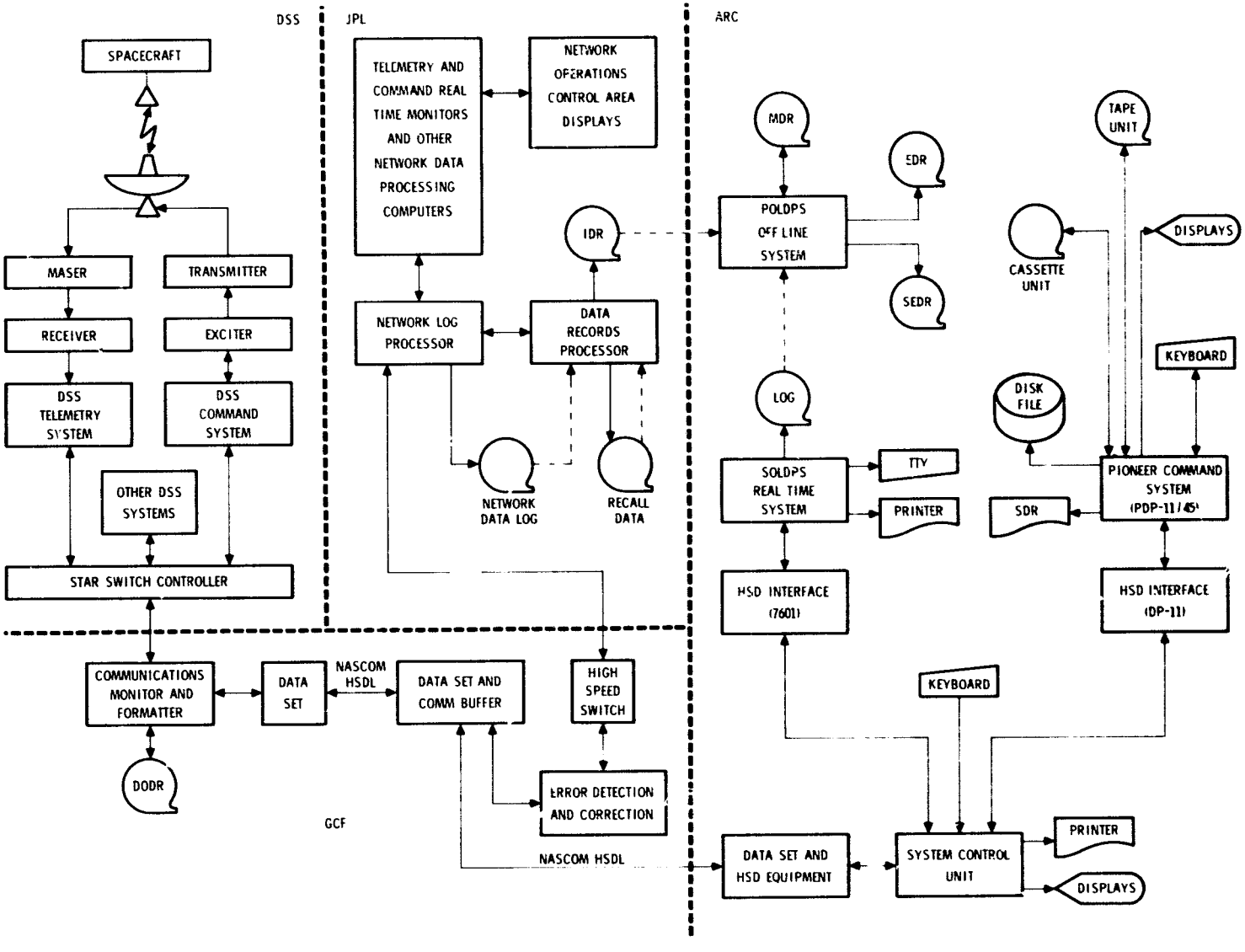

Fig. 1. Pioneer Venus telemetry and command Ground Data System configuration

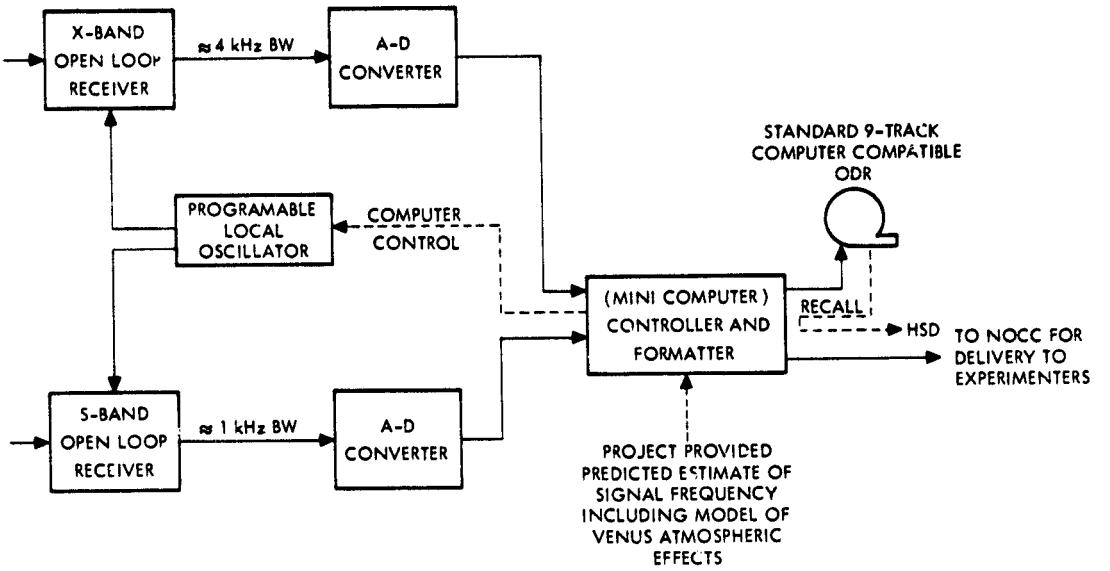

Fig. 2. DSS 14 and 43 configuration for Pioneer Venus orbiter occultation support

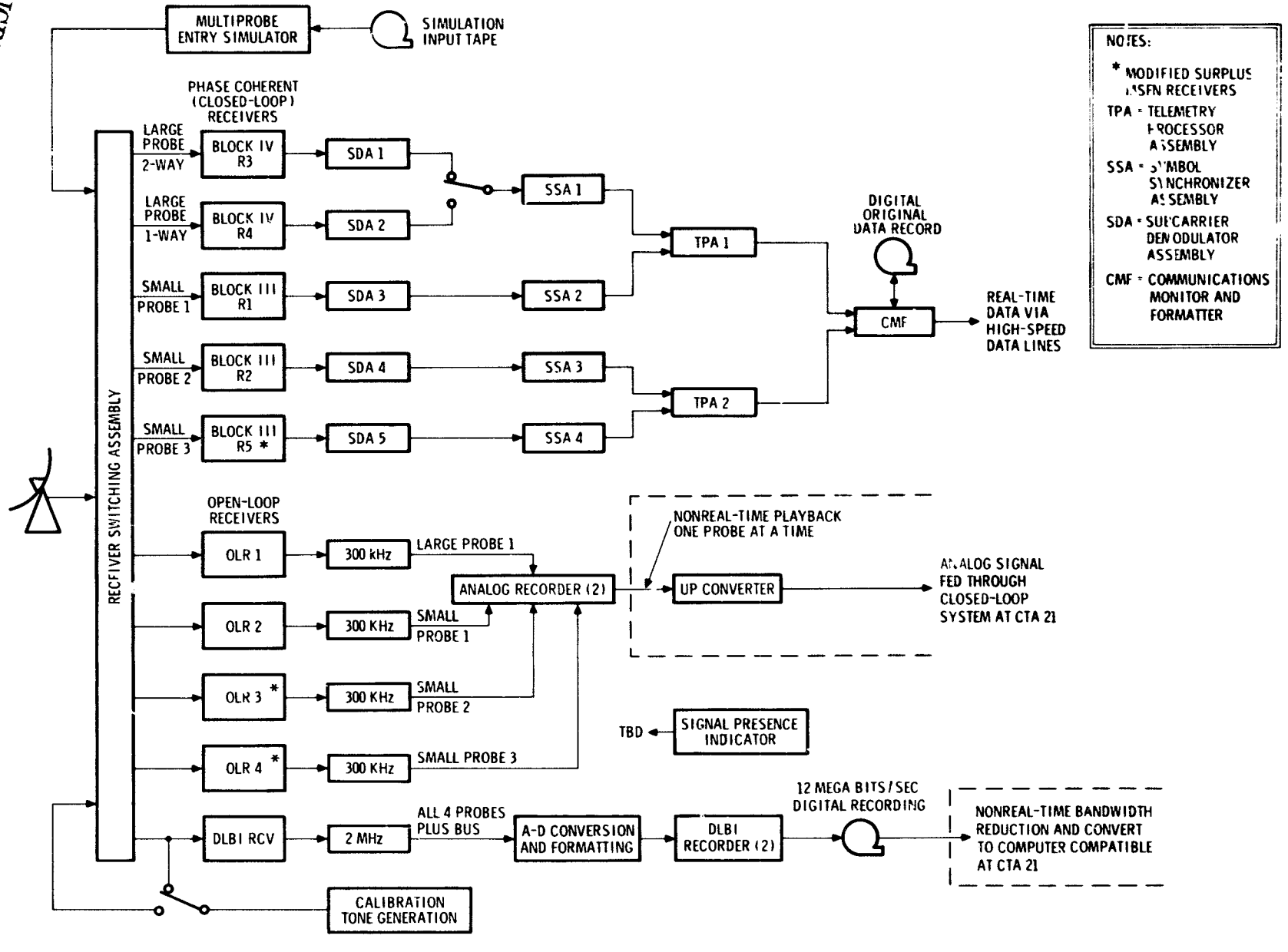

Fig. 3. Pioneer Venus 78 Multiprobe configuration for telemetry data recovery and interferometry experiment

Helios Mission Support

P. S. Goodwin
TDA Mission Support

E. S. Burke and G. M. Rockwell
DSN Network Operations Section

This article reports on activities of the Network Operations organization in support of the Helios Project during December 1976 and January 1977.

I. Introduction

This article is the fourteenth in a continuing series of reports that discuss Deep Space Network support of Helios mission operations. Included in this report is information concerning the demonstration tracks conducted over DSS 12 and DSS 62 utilizing the Mark III-DSN Data Subsystem, the Helios-2 Receiver-1 failure, the future use of the STDN-DSN telemetry and command cross-support, and other mission-oriented information.

II. Mission Operations and Status

Helios-1 continues to function normally in its extended mission. The fourth aphelion occurred on January 8, 1977, without any problems. During the aphelion, the spacecraft configuration was medium power, high-gain antenna, bit rate of 512 bps, and all experiments on. No critical spacecraft temperature exceedings occurred.

The Helios-2 spacecraft encountered some difficulty during this past period, namely, the apparent failure of its Receiver 1 on January 7, 1977. As a result, the command subcarrier has been changed to 448 Hz from 512 Hz while using Receiver 2. No problems are expected with command support on Receiver 2 using a 10-kW uplink in the near future. Receiver 1 was acquired again on January 12, 1977, only to be lost again shortly thereafter. Before the receiver failure, Helios-2 passed a greyout zone on January 1, 1977. This phase was covered by DSS 42 in Australia and later by station 67/68 in Weilheim, Germany. The Sun-Earth-Probe angle at entry was 0.38 deg and 0.46 deg at exit. The second aphelion for Helios-2

occurred on January 20. This period was not covered by a ground station, but the next data received showed no problems were encountered.

III. Special Activities

A. Mark III-DSN Data Subsystems Support of Helios

Since the report of the first demonstration track utilizing the Mark III-DSN Data Subsystem at DSS 12 for Helios (Ref. 1), 11 such passes have been conducted. As a result, DSS 12 has been committed to support Helios flight operations. Following is a brief summary of the last 10 demonstration passes and the problems encountered.

Between January 5, 1977, and January 25, 1977, 10 demonstration tracks with Helios spacecraft were conducted over DSS 12. In nearly every instance, the same problems and detrimental conditions were evident. Listed below is a brief description of each and the resulting effect on operations.

(1) The Communications and Monitor Formatter was unable to consistently provide high-speed data output to the station's communications buffer and in turn to the Network Operations Control Center. Also, data such as command and predicts going to the station were hindered due to this same condition. Since the first tests, hardware and software changes have improved operation. Work is continuing to correct the remaining problems.

(2) The Telemetry Processor Assembly (TPA), when processing sequentially coded data, was unable to interface properly with the Temporary Original Data Record (TODR), and a failure in the TPA resulted. It was found that with the addition of three modifications to the MODCOMP computer within the TPA, this problem was corrected. In the interim, the TODR has been disabled while sequentially coded data were being processed.

(3) The Star Switch Controller, which interconnects all devices to the Communications and Monitor Formatter, was found to be arbitrarily reassigning output ports without operator intervention. This problem is being worked on and a solution is expected soon.

(4) The interface between the Digital Instrumentation Subsystem and the Star Switch Controller has not been adequate. The result has been dropouts of monitor data leaving the station. This problem is also being looked into in order to correct it as soon as possible.

(5) During the early test tracks, the Network Operations Control Center was lacking adequate monitor software, and the station's monitor data could not be validated and processed. Now that the software is available, this problem no longer exists.

(6) The Communications and Monitor Formatter seems limited as to what speed data can be replayed to or received from the Network Operations Control Center. Transmission rates in excess of 1 block per second create data gaps. This problem needs correction, because a rate of 5 blocks per second is what the system should be able to accommodate.

In addition to DSS 12 at Goldstone, California, DSS 62 in Spain began its Mark III-DSN Data Subsystems test and training phase on February 2. The first Helios demonstration track was conducted with DSS 62 on February 12. On this particular pass, no problems were encountered and this test was highly successful. Although the problems listed above were not evident during this particular exercise, they have been observed on previous testing with other projects at the Madrid station.

The configuration for Helios support is the same at DSS 62 as it is at DSS 12 (see Fig. 1).

B. STDN-DSN Cross-Support

Beginning March 1, 1977, the STDN-DSN cross-support configuration (Ref. 2) will again be required for Helios operations support. Prior to this time, the cross-support configuration will be tested to ensure success. The results of this and the actual real-time support will be reported in future articles. Also, the difference in the predicted signal-to-noise ratio of Helios-2 data and the actual level received, observed during the last cross-support period (Ref. 1), may be further explained.

References

1. Goodwin, P. S., Burke, E. S., and Adamski, T. P., "Helios Mission Support," in *The Deep Space Network Progress Report 42-37*, pp. 39-42, Jet Propulsion Laboratory, Pasadena, Calif., Dec. 28, 1976.

2. Goodwin, P. S., Burke, E. S., and Morris, R. E., "Helios Mission Support," in *The Deep Space Network Progress Report 42-36*, pp. 28-34, Jet Propulsion Laboratory, Pasadena, Calif., Oct. 15, 1976.

Table 1. Helios tracking coverage

Period	Spacecraft	Station type	Number of tracks	Tracking/time, hr, min
December, 1976	Helios-1	26-meter	35	317:09
		64-meter	2	12:47
	Helios-2	26-meter	24	291:55
		64-meter	3	38:09
January, 1977	Helios-1	26-meter	27	180:59
		64-meter	4	22:13
	Helios-2	26-meter	35	208:36
		64-meter	3	11:33

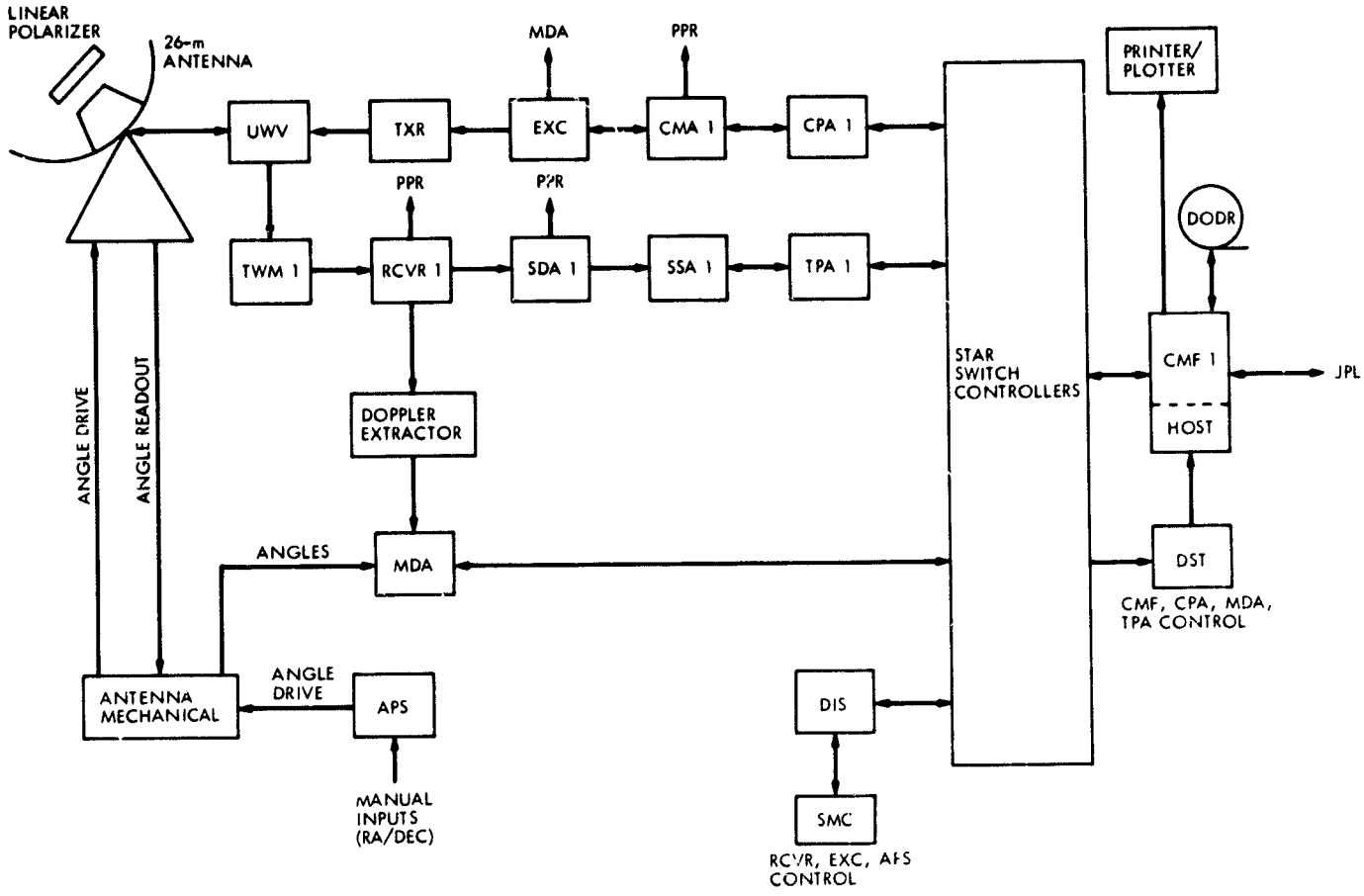

Fig. 1. DSS 12/62 support configuration

Improvements in Navigation Resulting from the Use of Dual Spacecraft Radiometric Data

C. C. Chao and H. L. Siegel
Navigation Systems Section

V. J. Ondrasik
Tracking Systems and Applications Section

When two interplanetary spacecraft lie along similar geocentric lines-of-sight, navigational advantages may be achieved by navigating one spacecraft with respect to the other. Opportunities to employ this technique will become more common as more multiprobe missions are launched. The two Viking spacecraft and the two Mariner Jupiter/Saturn '77 spacecraft will be within two and three degrees of each other, respectively, for a large portion of their missions. Results of simulated analysis as well as the processing of real tracking data from the two Viking spacecraft reveal the following advantages of the dual spacecraft navigation technique: (1) cancellation of platform parameter and transmission media modeling errors in short arc solutions, (2) accurate encounter guidance for the trailing spacecraft, (3) reduction of total tracking requirements, and (4) rapid determination of the orbit following a maneuver on either spacecraft.

I. Introduction

Many of the interplanetary missions which are likely to take place during this and the next decade involve two spacecraft. For example, both the Viking and MJS '77 missions have two spacecraft that often approach to within a few degrees of each other in the sky. For a couple of years it has been conjectured that navigational capabilities (at least for the trailing spacecraft) might be substantially improved if the radiometric data from the two spacecraft were not treated independently but somehow combined. The rationale for this is based primarily on the following two observations:

(1) Once the leading spacecraft has flown by or gone into orbit about a planet, its orbit with respect to the planet is known to within a few km.

(2) If the leading spacecraft is used as a beacon for the trailing spacecraft many of the common error sources such as ephemeris errors, transmission media, and station location errors should cancel.

When the two spacecraft are tracked simultaneously from neighboring ground sites, the common error sources may be removed by differencing the corresponding data types from the two spacecraft. The information retained by the new data types will include the differences in right ascension and declination between the two spacecraft as well as the difference in geocentric range rate (differenced doppler data) or the difference in geocentric range (differenced range data). Under certain conditions, relatively error-free determinations of these quantities should improve navigational capabilities. Results of this study obtained from real radiometric data demonstrations show that dual spacecraft data types can improve navigation capabilities by a factor of 5 to 10 under the conditions of small angular separation between spacecraft and a well determined reference spacecraft.

A couple of years ago some introductory work on dual spacecraft tracking was performed at the Jet Propulsion Laboratory (JPL) (Ref. 1). Results of that study indicate the potential advantages of the concept. Recently we have completed a fairly thorough accuracy analysis study of dual spacecraft tracking using simulated tracking data based on the trajectories of Viking and MJS '77 missions. These results, which are to be described in this paper, are extremely encouraging. For instance, the Viking B navigational errors can be reduced by an order of magnitude. It has been found that in addition to the cancellation of common errors dual spacecraft tracking can reduce the tracking time requirement and help the low declination problem.

Of course before this technique can be incorporated routinely in mission design (e.g., MJS) it is necessary to obtain sufficient tracking experience and demonstrate that the expected improvement in navigation can actually be achieved. Hopefully, the necessary data to conduct such a demonstration will be made available during the Viking mission. Results of dual spacecraft tracking conducted during the early cruise phase of Viking mission are included in this paper.

II. Information Content of Single Spacecraft Single Station Radiometric Data

Before proceeding into a discussion of the new data types of dual spacecraft tracking, it will be worthwhile to briefly review the information provided by single-station, single-spacecraft radiometric data. The range, ρ, and range rate, $\dot{\rho}$, from a tracking station to a spacecraft can be approximately given by the Hamilton and Melbourne model (Ref. 2).

$$\rho = at - b\cos\omega t + c\sin\omega t + d$$

$$\dot{\rho} = a + \omega b\sin\omega t + \omega c\cos\omega t$$

where

$a = \dot{r}$ = geocentric range rate at $t = 0$

$b = r_s\cos\delta$

$c = \omega t_\epsilon r_s\cos\delta$

$d = r - z_s\sin\delta$

and

r = geocentric range of spacecraft at $t = 0$

δ = declination of spacecraft

r_s = distance of tracking station from Earth's spin axis

z_s = distance of tracking station from Earth's equator

ω = Earth's rotation rate

t = time past meridian crossing

t_ϵ = Error in time past meridian crossing

The slowly varying geocentric term, r and $\dot{r}$, provide acceleration information, and the sinusoidal modulation, b and c, produced during each tracking pass by the spin of the earth yields geometric information on the right ascension, α, and the declination, δ, of the spacecraft. The above equations provide insight into several of the limitations of single-station, single-spacecraft range and doppler data for determining the spacecraft state. The limiting factors may be summarized as follows:

(1) Low declination singularity,

(2) Station location errors (including variations in earth spin rate-UT1-and polar motion).

(3) Transmission media effects (space plasma, atmosphere).

(4) Ephemeris errors,

(5) Unmodelled spacecraft accelerations.

(6) Tracking station availability.

Part of the above limitations may be examined from the following relations derived in Ref. 2.

$$\sigma_\alpha^2 = \frac{\sigma_c^2}{(r_s\cos\delta)^2} + \omega^2\sigma_{UT1}^2 + \sigma_\lambda^2$$

$$\sigma_\delta^2 = \frac{\sigma_b^2}{(r_s\sin\delta)^2} + \frac{\cos^2\delta}{(r_s\sin\delta)^2}\sigma_{r_s}^2$$

From the first equation, the errors in *UT1* (i.e., earth spin rate) and station longitude, λ, directly limit the accuracy of the determination of right ascension. The second equation shows the poor determination of declination at low declination and the effect from station location errors in r_s. The transmission media effects degrade the α, δ accuracy through the parameters, b and c.

The effect of unmodelled spacecraft accelerations is not included in our simplified equation for $\dot{\rho}$. However, it is clear that such accelerations add a spurious signature which, if of significant magnitude relative to ωb and ωc, can severely degrade the determination of both α and δ.

In recent years a program has been undertaken at JPL to develop new data types and estimation techniques (Ref. 3) to alleviate some of the problems discussed here. For example, simultaneous differenced doppler will remove unmodelled spacecraft accelerations; high precision simultaneous range will remedy the low declination problem, and S/X-band dual frequency doppler can be used to calibrate charged particle effects. For outer planet fly-by missions the primary limitation of conventional radiometric navigation is ephemeris uncertainties. As discussed in Ref. 3, the most promising method of reducing ephemeris problems involves the use of onboard optical data. The onboard optical data, though promising, is considered less reliable than radiometric data. For two spacecraft missions the dual spacecraft tracking has been found to be another way to reduce the effects of ephemeris uncertainties using radiometric data. In principle, the first spacecraft may be used as a beacon to guide the second spacecraft. If the two spacecraft have a small angular separation, many of the error sources will be common and will cancel. In the next two sections, we will show, through this simple model, that the dual spacecraft tracking is also insensitive to station location errors, the low declination singularity and transmission media effects.

III. Dual Spacecraft Two-Station Data

If the two spacecraft are being simultaneously tracked by two nearby ground stations, we call it dual spacecraft two-station tracking. The range and range rate to a second spacecraft (subscript 0) whose orbit is well determined and used as a beacon may be written as

$$\rho_0 = r_0 + \dot{r}_0 t_0 - r_s \cos\delta_0 \cos\omega t_0 + \omega t_{\epsilon 0} r_s \cos\delta_0 \sin\omega t_0 - z_s \sin\delta_0$$

$$\dot{\rho}_0 = \dot{r}_0 + \omega r_s \cos\delta_0 \sin\omega t_0 + \omega t_{\epsilon 0}\, \omega r_s \cos\delta_0 \cos\omega t_0$$

Where, as in Ref. 1, for mathematical simplicity the tracking station associated with the second spacecraft has been assumed to be collocated with the tracking station associated with the first spacecraft. These simultaneous range and range rate data may be differenced to form a new set of data types: dual-spacecraft two-station range and range rate. Taking the expansion with the following quantities

$$\Delta\alpha = \alpha - \alpha_0$$

$$\Delta\delta = \delta - \delta_0$$

$$\Delta r = r - r_0$$

$$\Delta\dot{r} = \dot{r} - \dot{r}_0$$

and neglecting second-order terms in $\Delta\alpha$, $\Delta\delta$, the new data type may be represented as

$$\rho - \rho_0 = \Delta r + (\dot{r}t - \dot{r}_0 t_0) - \Delta\delta z_s \cos\delta_0 + b_2 \cos\omega t_0 + c_2 \sin\omega t_0$$

$$\dot{\rho} - \dot{\rho}_0 = \Delta\dot{r} - \omega b_2 \sin\omega t_0 + \omega c_2 \cos\omega t_0$$

where

$$b_2 = r_s \Delta\delta \sin\delta_0$$

$$c_2 = r_s \Delta\alpha \cos\delta_0$$

From the above relations the differential quantities $\Delta\alpha$ and $\Delta\delta$ can be more accurately determined, since

$$\sigma^2_{\Delta\alpha} = \frac{\sigma^2_{c_2}}{(r_s \cos\delta_0)^2} + \frac{\Delta\alpha^2}{r_s^2}\,\sigma^2_{r_s} + \Delta\alpha^2 \tan^2\delta_0\, \sigma^2_{\delta_0}$$

$$\sigma^2_{\Delta\delta} = \frac{\sigma^2_{b_2}}{(r_s \sin\delta_0)^2} + \frac{\Delta\delta^2}{r_s^2}\,\sigma^2_{r_s} + \frac{\Delta\delta^2}{\tan^2\delta_0}\,\sigma^2_{\delta_0}$$

The right ascension difference $\Delta\alpha$ is no longer affected by the common errors due to *UT1* and station longitude. The small value of $\Delta\alpha$ effectively reduces the sensitivity to errors in r_s and δ_0 as shown in the first of the above two equations. The low declination problem is also solved to a large extent as shown in the second equation. The most important evidence is that the error in $\Delta\delta$ due to r_s is nearly removed since the

second term is now multiplied by the small quantity $\Delta\delta$ instead of being magnified by the inverse of sin δ as in single-spacecraft tracking. This small difference of declination also makes the last term in the second equation well behaved at low declination. The sensitivity to low declination now exists only in the first term, the observed parameter, which may be improved by increasing observations. Furthermore, for the same amount of data, the parameter b_2 should be more accurately determined than the corresponding parameter b because of the better data quality of dual spacecraft tracking due to the cancellation of the atmospheric effects.

It is interesting to have an estimate about how well the atmospheric effects cancel for small angular separations. Figures 1 and 2 show the sensitivity to errors in the calibration for tropospheric refraction (a 10% or 20-cm error is assumed at the zenith). For angular separation less than 5 degrees the 10% error is almost an order of magnitude less important in the dual-spacecraft range and doppler than in the conventional single-spacecraft data types. The presence of unmodelled accelerations from both spacecraft limits us to the use of either the sequential estimation technique (permitting the inclusion of process noise compensation) or the dual spacecraft four-station data types (so-called ΔQVLBI) which will be discussed next.

IV. Dual Spacecraft Four-Station (ΔQVLBI) Data

If the same spacecraft is simultaneously tracked from two widely separated tracking stations such as Goldstone and Australia, differencing of the corresponding data types from the two stations provides differenced range and doppler (sometimes called QVLBI range and doppler as in Ref. 2) that are free of geocentric range and range rate terms and hence relatively uncorrupted by unmodelled spacecraft accelerations. With dual-spacecraft tracking these differenced range and doppler data from both spacecraft will again be differenced. These twice-differenced new data types require the simultaneous tracking at four stations, and thus they are called the dual-spacecraft four-station data types. The differenced range and range rate observables from a single spacecraft may be written in terms of the line segment (baseline) between stations as follows

$$D\rho = z_b \sin\delta + r_b \cos\delta \sin\omega t_b - r_b \omega t_\epsilon \cos\delta \cos\omega t_b + \Delta t$$

$$D\dot{\rho} = \omega r_b \cos\delta \cos\omega t_b + \omega r_b \omega t_\epsilon \cos\delta \sin\omega t_b + \Delta f$$

where

r_b = baseline projection on equatorial plane

z_b = baseline component in the spin axis direction

λ_b = longitude of the perpendicular to r_b

Δt = error due to station clock bias

Δf = error due to station frequency bias

After performing the similar expansion and differencing, the dual spacecraft four-station (ΔQVLBI) data types may be given as

$$D\rho - D\rho_0 = z_b \Delta\delta \cos\delta_0 + b_4 \cos\omega t_{b_0} - c_4 \sin\omega t_{b_0}$$

$$D\dot{\rho} - D\dot{\rho}_0 = \omega b_4 \sin\omega t_{b_0} - \omega c_4 \cos\omega t_{b_0}$$

where

$$b_4 = r_b \Delta\delta \cos\delta_0$$

$$c_4 = r_b \Delta\delta \sin\delta_0$$

Notice that in addition to the removal of unmodelled accelerations the errors due to station clocks are not present in the above equations of four-station data types. This is due to the fact that those collocated stations are either conjoint stations which share a common station clock or the clock bias and drift can be accurately determined by short baseline data (Ref. 4). These new data types are relatively clean because of the double differencing and reduce the number of parameters to three in range observables and two in range rate observables. The uncertainties of the determination of $\Delta\alpha$ and $\Delta\delta$ may be estimated as before by

$$\sigma^2_{\Delta\delta} = \frac{\sigma^2_{c_4}}{(r_b \sin\delta_0)^2}\left(\frac{\Delta\delta}{r_b}\right)^2 \sigma^2_{r_b} + \left(\frac{\Delta\delta}{\tan\delta_0}\right)^2 \sigma^2_{\delta_0}$$

$$\sigma^2_{\Delta\alpha} = \frac{\sigma^2_{b_4}}{(r_b \cos\delta_0)^2} + \left(\frac{\Delta\alpha}{r_b}\right)^2 \sigma^2_{r_b} + (\Delta\alpha \tan\delta_0)^2 \sigma^2_{\delta_0}$$

The sensitivities to the parameters b_4, c_4, r_b and δ_0 are the same as for the dual spacecraft two-station data types

discussed in the previous section. Figure 3 shows the uncertainties of the angular position, α and δ, of the spacecraft determined from one pass of dual spacecraft doppler data. The angular position error of the reference spacecraft is independent of that of the other spacecraft and is assumed to be $\sigma_{\delta_0} = \sigma_{\alpha_0} = 1 \times 10^{-7}$ rad.

We used the relation

$$\sigma_\alpha^2 = \sigma_{\Delta\alpha}^2 + \sigma_{\alpha_0}^2$$

$$\sigma_\delta = \sigma_{\Delta\delta}^2 + \sigma_{\delta_0}^2$$

to compute the results shown in Figure 3. Data noise is assumed to be 0.2 mm/s (0.003 Hz) at 60-s integration time and $\sigma_{r_s} = \sigma_{r_b} = 1.5$ meter. It is interesting to learn that the right ascension can be determined to within 0.04-arc second compared with a 0.15-arc second accuracy from conventional data due to a 3-meter error in longitude. The declination uncertainty increases as declination decreases, and at low declination the uncertainty increases with the angular separation $\Delta\alpha$ and $\Delta\delta$. When δ_0 is 2 degrees the declination error is about 0.20 arc second as a result of dual-spacecraft, two-station tracking. The corresponding error from conventional single-spacecraft tracking is as large as 1.7 arc seconds due to the low declination problem. The results of this simple analysis clearly reveal the potential capabilities of dual-spacecraft tracking. Results of simulated analysis as well as the processing of real tracking data from the two Viking spacecraft will be discussed next.

V. An Algorithm for Processing Dual Spacecraft Data

Before we go to the discussion of the results of orbit determination (OD) based on dual-spacecraft tracking, it is worthwhile to explain the algorithm used in our analysis. Ideally speaking, the particular OD program for studying this problem should be able to handle the twelve-parameter state vector of the two spacecraft. It would have been a major effort to implement such an OD program; instead we designed and developed a special program to difference the data files obtained from the OD runs made for each spacecraft separately. After that the new data types of dual-spacecraft tracking are created with partial derivatives for the reference spacecraft included. This new data file is then ready for OD analysis.

In the OD analysis of the dual-spacecraft tracking, the covariance of the six-state parameters of the reference spacecraft which is already in orbit about or has flown-by a planet will be generated from an OD run fitting the fly-by or orbit data. Then the covariance which gives the best estimate of the state of the reference spacecraft relative to the planet will be used as a priori values for the reference spacecraft in the orbit determination of the second spacecraft. When we use dual-spacecraft, two-station data, the unmodelled accelerations from the second spacecraft are estimated sequentially. The unmodelled accelerations from the reference spacecraft which are not dynamic parameters to the second spacecraft are also estimated sequentially treating them as a random noise such as that due to the transmission media. The six-state parameters of the reference spacecraft are not estimated, but their errors are *considered* (i.e., their effect on the accuracy of the solution is taken into account). We believe that this is a valid way to process the dual-spacecraft data and study the information content of the new data types.

VI. Results of Simulated Analysis

A. The Viking Spacecraft

1. Data. Each of the three DSN (Deep Space Network) complexes has three tracking stations, i.e., stations 11, 12, 14 at Goldstone, California, 42, 43, 44 at Canberra, Australia, and 61, 62, 63 at Madrid, Spain. Thus continuous coverage of simultaneous tracking of two spacecraft is possible. In the analysis it was assumed that Viking A was tracked by stations 12, 42, and 62 and Viking B was tracked by stations, 14, 43, and 63. Doppler data was continuous and two-way range points were taken about every 3 hours. Because Viking B suffers from low declination problems nearly simultaneous range points between California and Australia were also included every day for both spacecraft. To include the information provided by the Viking A data into the solution for Viking B, two new data types, dual-spacecraft differenced doppler ($\Delta\dot{\rho}$) and differenced range ($\Delta\rho$) are formed by simply subtracting the Viking B doppler/range from the Viking A doppler/range.

2. Estimated and considered parameters. The navigation solutions solved for the state of Viking B and considered the effects of errors in station locations[1] ($\Delta r_s = 1.5$ m, $\Delta\lambda = 3.0$ m, $\Delta z = 15$ m), constant nongravitational accelerations (1.2×10^{-12} km/s^2), ephemeris of Viking A orbit (2 km at periapsis), ephemeris of Mars (≈ 30 km), and several of the primary harmonics of Mars. When the data is differenced almost all of the geocentric range, and range rate information cancels. Therefore, when differenced data is used a small amount of loosely weighted single station/single spacecraft doppler and range data will be included to retrieve the geo-

[1]The station location parameters of the two stations at the same site are highly correlated in the OD solutions so that their relative errors are small (10 cm).

centric range and range rate information without significantly degrading the declination and right ascension information.

3. Results for dual-spacecraft two-station data ($\Delta\rho$, $\Delta\dot{\rho}$). The first solutions used two-station differenced doppler and range. As expected, the degrading effects of the station location errors on the B-plane[2] solutions were reduced by an order of magnitude from similar errors resulting from the use of conventional single-spacecraft data. Unfortunately, the few km errors in the ephemeris of the Viking A orbiter produced errors in the B plane solution for Viking B which were thousands of km. This result was also expected because an error of a few km in the orbit of the orbiter will introduce 10^{-8} km/s^2 unmodelled acceleration errors into the dual-spacecraft data. It is well known that if the data of an interplanetary spacecraft is subject to unmodeiled accelerations of this size, the navigation solutions will be in error by thousands of km.

4. Results for dual-spacecraft four-station data (ΔQVLBI). It has been shown that one method of reducing the effects of large unmodelled accelerations is to take data from one spacecraft simultaneously from two widely separated stations and then subtract the first station's data from the second station's data. This type of data is commonly called QVLBI data. Based upon our experience with single spacecraft, QVLBI data, we thought that if Viking A is tracked simultaneously from two stations, (e.g., 12 and 42) and at the same time Viking B is tracked simultaneously from two other stations (e.g., 14 and 43) going through a double differencing between both the spacecraft and the stations a new data type will be generated which will be insensitive to both unmodelled acceleration errors and to station location errors. We chose to call this new data type ΔQVLBI and it does improve navigation capabilities by an order of magnitude. One of the major error sources in QVLBI doppler data is the frequency bias between the two-way and three-way data. The effect of this error source should also be substantially reduced in the ΔQVLBI data.

5. Comparison between single- and dual-spacecraft navigation. A comparison of navigational capabilities resulting from the use of single-spacecraft data with those resulting from the use of dual-spacecraft (ΔQVLBI) data is shown in Figure 4 for 10-day and 20-day data arcs. The single-spacecraft data set consists of continuous three-station doppler (1 mm/s) and nearly simultaneous range (5 m). The first dual-spacecraft data set consists of ΔQVLBI doppler (1 mm/s) during the station overlaps and single-spacecraft, three-station nearly simultaneous range (5 m). This hybrid data set is included because it may be difficult to obtain ΔQVLBI range from Viking. The second set of dual-spacecraft data consists of ΔQVLBI doppler (1 mm/s) and QVLBI range (1 m) during the overlaps. The ΔQVLBI range is weighted more tightly than the nearly simultaneous range because in the double differencing procedure many of the components of the range error will cancel.

Figure 4 clearly shows the improvement in navigational capabilities resulting from the use of dual spacecraft data. As mentioned earlier, the dual spacecraft four-station data type improves the navigational capabilities of Viking B by anywhere from a factor of five to an order of magnitude over that associated with conventional data. Furthermore the dual spacecraft data should require less total tracking time and reduce the need for station location and transmission media calibration.

In the cruise phase of the two Viking spacecraft, another simulation study was performed tying the short arc trajectory of Viking A immediately after its maneuver to the long arc of Viking B. An accurate rapid redetermination of a spacecraft orbit following a midcourse maneuver is very important for a successful planet encounter. In this analysis we assumed a midcourse maneuver of the A spacecraft at 40 days before it encountered Mars. At that time the B spacecraft had a long arc and its orbit was well determined. Based on 4 days data after the maneuver, the target errors from the conventional data were as large as 1500 km mostly due to station location errors. By performing dual spacecraft tracking (two-station doppler and range) and tying the A spacecraft to the B spacecraft, this error was reduced to 300 km with more than one third of the error due to the uncertainty of the B spacecraft's orbit. From Fig. 5 we see again a factor of 5 improvement. About 4 weeks later Viking A had a long arc and the target error based on conventional data was brought down to 200 km. This comparison indicates that the 4-day arc solution based on dual-spacecraft tracking is nearly as good as the 30-day long arc single-spacecraft solution, and it shows the potential reduction of DSN tracking time requirements. Due to the limited ground tracking facilities and the long flight time associated with many deep space missions in the future, the tracking time limitation will be a serious problem.

B. The MJS Uranus Option Mission

In 1976 the MJS mission was redesigned to include an option to target the second spacecraft for Uranus after its Saturn encounter. This situation is made to order for a dual spacecraft strategy for the following reasons:

(1) The Uranus option for the second spacecraft will not be implemented unless a successful Saturn encounter is achieved by the lead spacecraft. Thus, the assumption that the first spacecraft will be available as a reference for the Uranus-targeted spacecraft is valid.

[2]The "B-plane" is JPL terminology for the target plane or aim plane. See Ref. 3 for the defining geometry.

(2) The Uranus option trajectory design stretches propellant reserves to the limit. A precise Saturn encounter by the second spacecraft will reduce the magnitude of the post-Saturn maneuver and increase the probability of having sufficient propellant for a successful Uranus encounter. In fact, if a large injection error or other propellant-wasting event should occur, the dual spacecraft strategy might be a means of preserving the Uranus option.

We have conducted a series of simulated analyses of dual spacecraft two-station and four-station data types for the MJS Uranus option in the same manner as the Viking simulation.

1. Data. The data distribution and arc length of the conventional data types for the second spacecraft are the same as used by MJS navigation analysts (Ref. 5). The data which consist of doppler and nearly simultaneous range from DSN stations 14, 43, and 63 start at 60 days before Saturn encounter. The data distribution is rather sparse in the first 30 days, but continuous in the second 30 days. For dual spacecraft tracking analysis, we generated the same data pattern at the same time interval for the first spacecraft that has already flown by Saturn and is 9 months ahead of the second spacecraft. In this analysis only the doppler from the two spacecraft are differenced to form dual-spacecraft two-station and four-station doppler. Due to the ground tracking capability and long round-trip-light time (longer than 2 hours) it will not be possible to have four-station simultaneous two-spacecraft range data. Therefore, we did not simulate any differenced range data.

2. Estimated and considered parameters. The estimated parameters are the state of second MJS spacecraft and the constant part of the unmodelled spacecraft accelerations. In the meantime the parameters of unmodelled accelerations from both spacecraft are estimated sequentially with a two-day batch size and a one-day correlation time. The assumed a priori for these accelerations is 10^{-12} km/s^2. The considered parameters are station location uncertainties (σ_{r_s} = 1.5 m, σ_λ = 3 m, σ_z = 15 m), range bias at each station (4.37 m), and the ephemeris of the reference spacecraft (~ 300 km Saturn relative). The ephemeris of Saturn is not considered since the spacecraft is tied to the planet through the fly-by of the first spacecraft which contains the ephemeris information of the planet.

3. Results for dual-spacecraft two-station data ($\Delta\dot{\rho}$). The differenced dual spacecraft doppler is weighted at 15 mHz (1 mm/s) at 60-s integration time, and the conventional doppler is loosely weighted at 150 mHz to retain the geocentric range rate information without degrading the planet relative information. The near simultaneous range data was weighted at 10 meters in our initial attempt because of the low declination problem ($\delta \approx 2$ deg). Later we found that the tight geocentric range data increased the sensitivity to the error of the ephemeris of the reference spacecraft by a factor of 6 and thus caused the B-plane uncertainty to be unreasonably large. Once we deweight the range to 1 km, the B-plane error as shown in Fig. 6 at six days before Saturn encounter becomes less than 600 km, which is less than half the error using conventional data types.

4. Results for dual-spacecraft four-station data (ΔQVLBI). As discussed earlier the dual-spacecraft four-station doppler is not sensitive to unmodelled spacecraft accelerations. Therefore, only the constant part of the accelerations from the second spacecraft are estimated together with the state of that spacecraft. The same parameters considered in the two-station data solutions are considered here. The four-station (ΔQVLBI) doppler is weighted at 7 mHz (0.5 mm/s) because of its better data quality after double differencing. The conventional doppler and range are weighted at 150 mHz (10 mm/s) and 1 km as the previous case. With this clean data type of four-station doppler, the target (B-plane) error based on the same data arc is reduced down to only 360 km, nearly 4 times better than that of the conventional data (Fig. 6). The promising results of this simulated analysis for the MJS mission show that even under a rather unfavorable situation, i.e., low declination and large angular separation ($\Delta\alpha \approx 9$ deg), the navigation accuracy can still be improved by a factor of 2 to 4 by performing dual-spacecraft tracking. It also gives us the confidence to demonstrate this new technique with real tracking data. Next we will show a couple of examples of demonstrations conducted during the cruise phase of the Viking mission.

VII. Results of Real Tracking Data Demonstration (Viking Cruise Phase)

A. Rapid Redetermination of Viking B

We processed 4 days of dual spacecraft two-station doppler data immediately after the first maneuver of the Viking B spacecraft early in September, 1975. Viking A at that time had a long arc solution of about 40 days and was used as the reference spacecraft. The doppler data with 60-s count time received at six DSN stations located at three different complexes (California, Spain, and Australia) were first compressed to a 10-min count time using a modified JPL data editing program. This program provides simultaneous compressed doppler data from the two spacecraft during concurrent tracking. During that time, the two spacecraft were not far away from Earth and thus station location errors were not important. So we purposely introduced large errors in station locations (Δr_s = 15 m, $\Delta\lambda$ = 20 m) to magnify the effects due

to such errors. As shown in Fig. 7, the introduced station location errors moved the B-plane solution based on conventional data by as much as 10,000 km. While the dual-spacecraft two-station doppler with loosely weighted conventional data gave a solution only 1000 km away from the current best estimate. The results of this real data demonstration did indicate that short arc dual-spacecraft tracking is insensitive to station location errors.

B. A Low Declination Example

During late November of 1975, Viking B spacecraft was at a very low declination of about -2 deg. A total of seven days of dual spacecraft two-station doppler were processed. The dual-spacecraft data was weighted at 15 mHz and the conventional doppler and range loosely weighted at 150 mHz and 1 km, respectively. The resulting B-plane solution differed by only 600 km from the current best estimate. A large part of the 600-km error is believed to be due to the uncertainty from the reference spacecraft, Viking A. The conventional data with the same data arc and doppler weighted at 15 mHz and range at 1 km moved the B-plane solution by as much as 920 km mainly due to the low declination difficulty. Thus this example shows the navigation capability of the dual spacecraft tracking at an unfavorably low declination.

VIII. Concluding Remarks

As a result of this analysis, we may conclude the following:

(1) Dual-spacecraft data types, which are relatively insensitive to platform parameter errors, transmission media effects, low declination problems, and ephemeris errors, may improve navigational capabilities by a factor of 5 to a factor of 10, under the conditions of small angular separation (≤ 3 degrees of the two spacecraft) and well determined trajectory of the reference spacecraft.

(2) Dual-spacecraft tracking has the potential of significantly reducing DSN tracking time requirements.

While our results, so far, are very encouraging, the work is not yet complete. We need to develop software enchancements to be able to apply sequential filtering simultaneously to both spacecraft and we need to perform more realistic demonstrations using real tracking data, such as Viking encounter data. The increased understanding and more thorough evaluation gained will be necessary before the dual-spacecraft tracking technique can be used in interplanetary navigation.

References

1. Preston, R. A., "Dual-Spacecraft Radio Metric Tracking," *The Deep Space Network Progress Report 42-22*, Jet Propulsion Laboratory, Pasadena, Calif., May/June 1974.

2. Hamilton, T. W., and Melbourne, W. G., "Information Content of a Single Pass of Doppler Data from a Distant Spacecraft," in *The Deep Space Network, Space Programs Summary 37-39*, Vol. 3, pp. 18-23, Jet Propulsion Laboratory, Pasadena, Calif., May 31, 1966.

3. Ondrasik, V. J., et al., "Demonstration of the New Data Types For Use in Interplanetary Navigation," AIAA Paper 74-831, AIAA Mechanics and Control of Flight Conference, Anaheim, California, August 5-9, 1974.

4. Chao, C. C., et al., *Short Baseline QVLBI Demonstrations-Part I*, Technical Report 32-1526, Vol. 18, pp. 47-56, Jet Propulsion Laboratory, Pasadena, Calif., September 1973.

5. Jacobson, R. A., et al., "Navigation Accuracy Analysis for the Mariner-Jupiter-Saturn 1977 Mission," AIAA Paper 76-833, AIAA/AAS Aerodynamics Conference, San Diego, California, August 18-20, 1976.

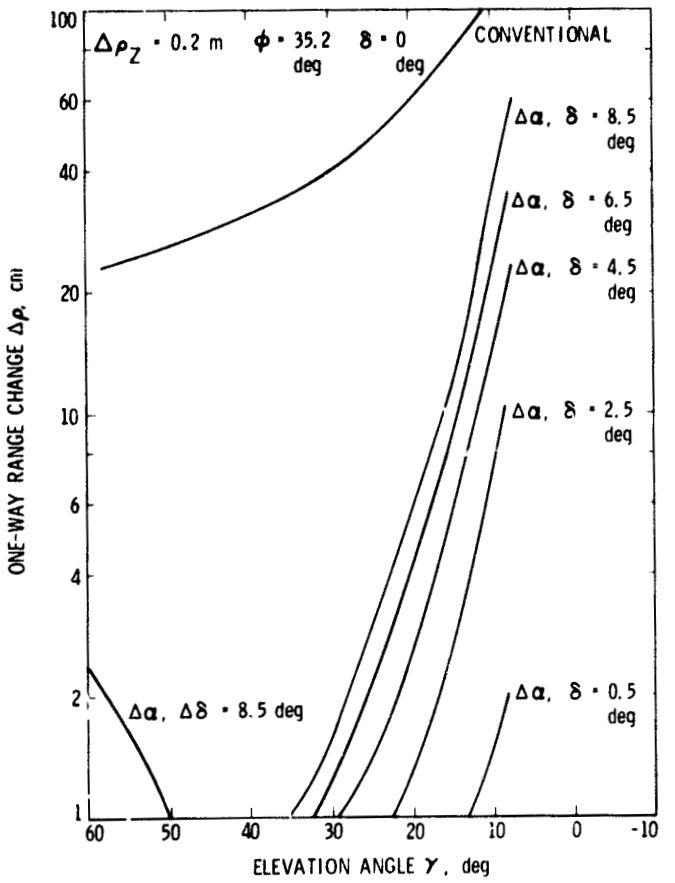

Fig. 1. Range change due to a 10% tropospheric effect

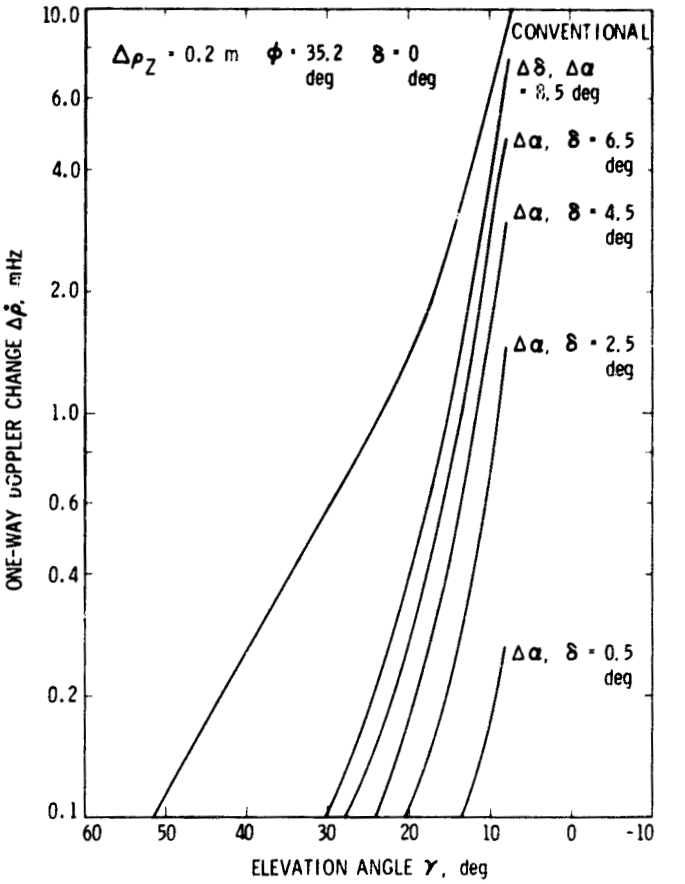

Fig. 2. Doppler change due to a 10% tropospheric effect

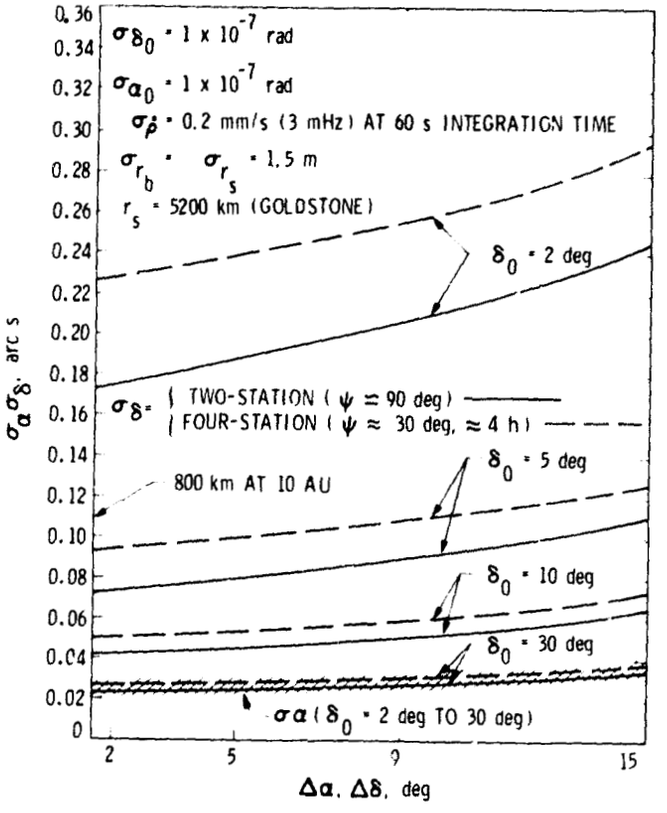

Fig. 3. Information content from a single pass of dual spacecraft doppler

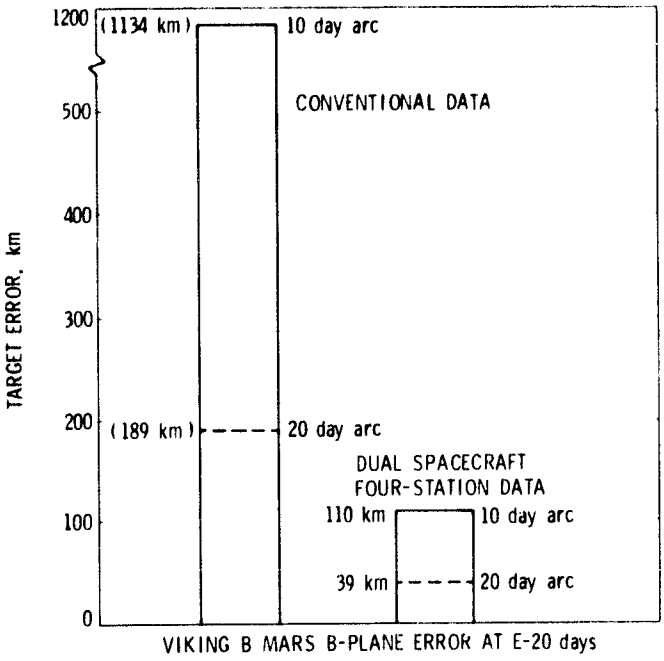

Fig. 4. Using Orbiter as a beacon

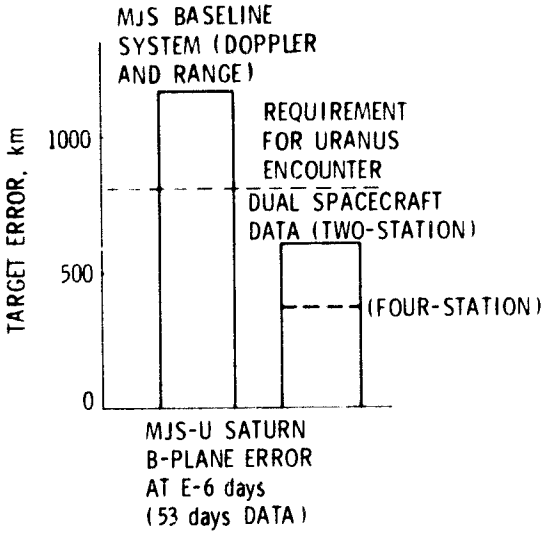

Fig. 6. Using fly-by spacecraft as a beacon

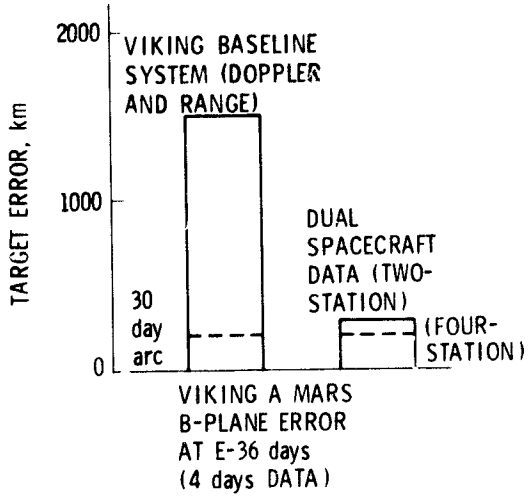

Fig. 5. Rapid determination of Viking A

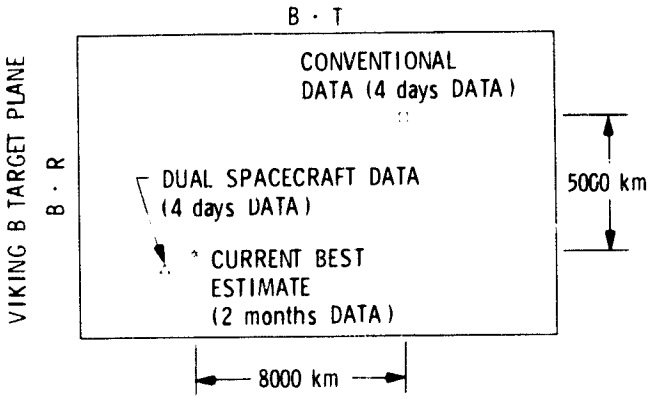

Fig. 7. Viking B target plane predictions using 4 days data with introduced errors in station locations (Δr_s = 15 m, $\Delta\lambda$ = 20 m)

A K-Band Radiometer for the Microwave Weather Project

K. Wallace, M. Reid, and H. Reilly
Radio Frequency and Microwave Subsystems Section

The design of a K-band radiometer for use in the microwave weather project is discussed. The major components of the system, such as feedhorn, waveguide switch, and receiver assembly are described. The system will be installed at DSS 13 at Goldstone, California, when completed.

I. Introduction

The Microwave Weather Project forms part of an overall Radio Systems Development Project which seeks to optimize the spacecraft-to-ground communications link. The objective is to provide a mathematical model of atmospheric transmission at X- and K-bands. This model will allow practical predictions of link performance to be made and will also form the basis of a specification of the receiving sensitivity of a Deep Space Network ground station. The model, which contains both probabilistic and deterministic elements, is based on the statistical correlations of weather and communications capability at X- and K-bands.

An X-band radiometer has been designed and constructed and has been operated at DSS 13 since August 1975 to gather data for the statistical analysis. The radiometer (Ref. 1) and the data system (Ref. 2) have been described in previous reports. This radiometer will continue operation, and statistical X-band results will be periodically reported (Ref. 3). A K-band radiometer has been designed and is presently being constructed and tested. This article describes the design of this K-band radiometer and reports on the progress of construction and testing. On completion of the construction and testing the radiometer will be installed at DSS 13 near the X-band radiometer. The data from the K-band radiometer will also be fed into the existing data acquisition system.

The K-band radiometer has been designed to operate over the frequency range of 12.75 to 13.25 GHz, centered at 13.00 GHz. The radiometer system consists of a feedhorn, waveguide switch, receiver assembly, detector, and other components required to operate the system as a noise-adding radiometer (NAR). Figure 1 is a block diagram of the system front end.

The feedhorn has been built and tested (Fig. 2). It is a standard corrugated horn, linearly polarized, with a gain of 22 dB and 10-dB beamwidth of 26 deg. The reflection coefficient is 24 dB or greater. Standard WR-62 waveguide components are used to mate with the waveguide switch. The waveguide switch has been constructed and is presently under test (Fig. 3). It is designed to be extremely reliable, with low insertion loss and high isolation. Electronic controls select from the four positions. The switch is used for calibration with an ambient termination, a cryogenic termination, or a waveguide short.

The receiver assembly has been designed for reliable low noise and stable operation in all weather conditions at Goldstone (Fig. 4). Stability is greatly enhanced by operation in a noise-adding radiometer mode. For total power stability, the assembly is temperature-controlled. The receiver is built with low insertion loss isolators of high isolation and wide bandwidth. Typical values are: 0.5 dB insertion loss, 40 dB isolation, 150 MHz bandwidth. The mixer-preamp noise figure is less than 5 dB, DSB. The local oscillator is a Gunn-effect oscillator, fixed-tuned initially to 13.050 GHz. A coaxial port is provided to monitor the local oscillator frequency and power. Noise diode 1 is used for NAR operation, and noise diode 2 is used for calibration and linearity measurements. The IF system is approximately 40 MHz bandwidth, although filters may be used to limit the operational bandwidth to a lower value.

The detector, controls, and data acquisition system are located inside a building at DSS 13. The NAR control system will eventually be a new design under development, although initially a system using a computing counter and programmer will be used.

Subsequent reports will provide test results and operational performance of this system.

References

1. Reid, M. S., Parham, O. B., and Gardner, R. A., "An X-Band Radiometer for the Microwave Weather Project," *Deep Space Network Progress Report 42-29*, Jet Propulsion Laboratory, Pasadena, Calif., pp. 54-59, Oct. 1975.
2. Reid, M. S., and Gardner, R. A., "A Versatile Data Acquisition System for Goldstone," *Deep Space Network Progress Report 42-30*, Jet Propulsion Laboratory, Pasadena, Calif., pp. 132-143, Dec. 1975.
3. Slobin, S. D., et al., "X-Band Atmospheric Noise Temperature Statistics at Goldstone DSS 13, 1975-1976," *Deep Space Network Progress Report 42-38*, Jet Propulsion Laboratory, Pasadena, Calif., (this issue).
4. Clauss, R., and Reilly, H., "Microwave Maser Development," Technical Report 32-1526, Vol. VI, Jet Propulsion Laboratory, Pasadena, Calif., pp. 118-122, Dec. 15, 1971.
5. Neff, D., Bathker, D., "DSS 14 X-Band Radar Feedcone," *Deep Space Network Progress Report 42-30*, Jet Propulsion Laboratory, Pasadena, Calif., pp. 119-131, Sept 15, 1975.

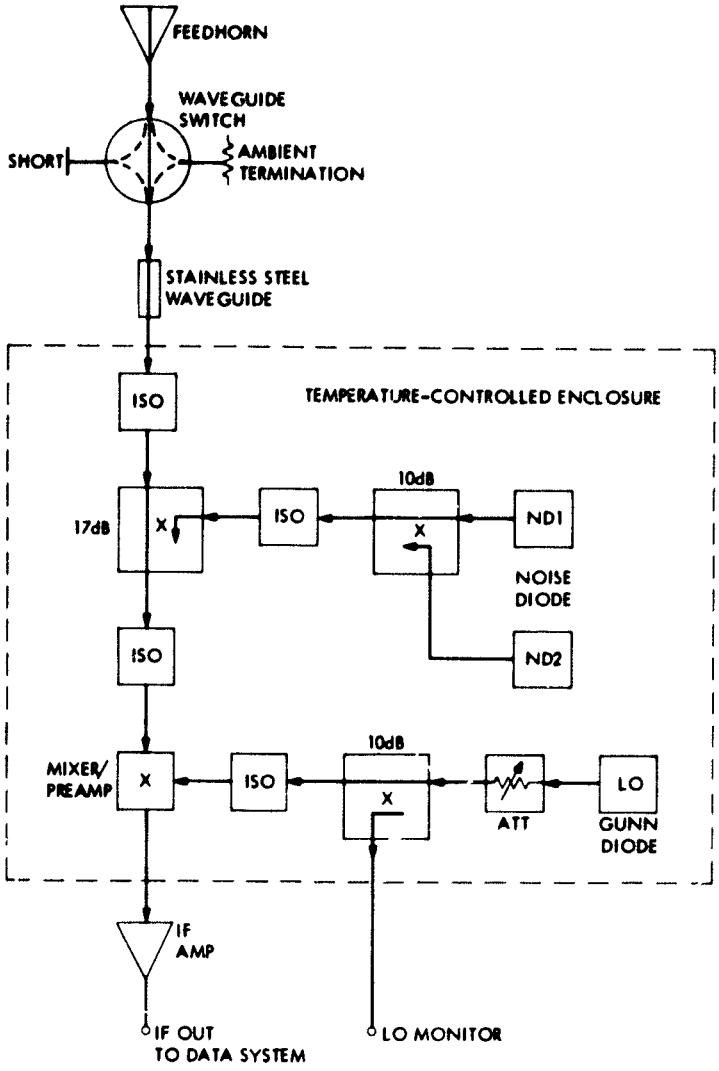

Fig. 1. K-band radiometer block diagram

Fig. 2. Feedhorn

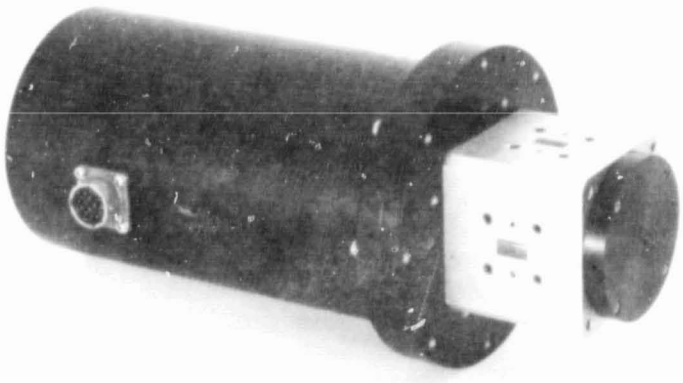

Fig. 3. Waveguide switch

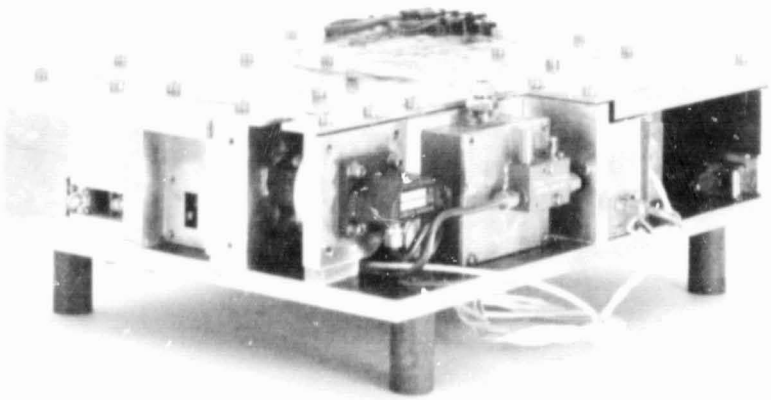

Fig. 4. Receiver assembly

X-Band Atmospheric Noise Temperature Statistics at Goldstone DSS 13, 1975–1976

S. Slobin, M. Reid, R. Gardner, and D. Cheng
Radio Frequency and Microwave Subsystems Section

X-band noise temperature data have been taken at Goldstone DSS 13 for the period August 1975 through January 1977. A description of the experiment is given along with probability density functions for zenith noise temperature increase during all year quarters and day quarters. Elevation angle modeling of the data is described along with a discussion of the problems associated with relating wide beamwidth statistics (this report) to narrow beamwidth antennas.

I. Introduction

X-band noise temperature data have been taken at the Goldstone Venus site (DSS 13) since August 1975. Instrumentation at that site consists of an X-band noise-adding radiometer and a horn antenna (no reflector) with a beamwidth of about 15 deg. Data are being taken continuously to develop X-band noise temperature statistics for the Goldstone complex. The horn is pointed at an elevation angle of 30 deg in the direction of DSS 14 (AZ = 325 deg). This tilt is necessary to keep rainwater from pooling on the aperture diaphragm during rainstorms; the azimuth direction was picked in order to look at weather which was "seen" commonly by both the X-band horn and the DSS 14 64-meter antenna.

Virtually all the data taken from August 1975 through January 1977 has been reduced and analyzed. A data point consists of the equivalent zenith noise temperature integrated over 2 minutes of time and over the 15 deg (±7 1/2 deg) 3-dB beamwidth. A total of 308,200 2-minute data points was considered "good," 7800 were "bad," and the instrument was inoperative for a total time equivalent to 67,300 data points. This amounts to an 80% "good data" return.

II. Description of Results

Data points are classified according to which year and day quarter they belonged. The year quarters are classified:

Year Quarter 1:	Dec, Jan, Feb
Year Quarter 2:	Mar, Apr, May
Year Quarter 3:	Jun, Jul, Aug
Year Quarter 4:	Sep, Oct, Nov

The day quarters are classified:

Day Quarter 1:	0000 to 0600 local time
Day Quarter 2:	0600 to 1200 local time
Day Quarter 3:	1200 to 1800 local time
Day Quarter 4:	1800 to 2400 local time

Noise temperature increases are due to atmospheric changes only, except for rare cases such as water droplets adhering to the aperture diaphragm or an airplane in the beam. The same conditions could exist for a 64-m antenna as well.

The noise temperature statistics are presented in Tables 1 through 5 and Figs. 1 and 2. The tables present the values of normalized probability density functions (percent of time ÷ 100) corresponding to *zenith noise temperature increases above the quiescent baseline* (e.g., 1 = 0 to 1 K, 2 = 1 to 2 K). The zenith X-band quiescent (lowest loss) baseline noise temperature value for Goldstone is approximately 2.3 kelvins (for oxygen and water vapor), which corresponds to approximately 0.043 dB zenith attenuation. Tables 1 through 4 present the probability density functions for each year quarter and each day quarter separately, including the sums over all day quarters. Table 5 presents pdf's for each day quarter, summed over all year quarters, plus the sum over all year and day quarters. Zenith temperature increases greater than 20 K are not shown, both for reasons of clarity and because of the fact that nearly all of the time (> 99%), increases are less than 20 K above the quiescent baseline.

Figure 1 gives a histogram presentation of the data from Table 5 (last column), which is the sum of data for all year quarters and all day quarters. Figure 2 gives the cumulative distribution for the data in Fig. 1. For example, 95.215% of the time the noise temperature increase is 1 K or less, 98.488% of the time 2 K or less, 98.878% of the time 3 K or less, and so forth. Similar figures may be drawn for any year or day quarter data. A system resolution of 1 K covers the entire cumulative distribution range of 0.0 to 0.95 for very low noise temperature increases. Thus "50% weather" at X-band is a concept that cannot be talked about with great precision.

III. Interpretation of the Results

One problem is readily apparent in analyzing the experiment. The difference in beamwidths between the test antenna (15 deg) and a 64-meter antenna (0.04 deg) results in a condition in which the test antenna sees less than or equal to the "amount" of significant weather seen by a 64-m antenna. This means that in a localized weather condition (a rainstorm, for example) which fills a very narrow beam, a wide beam may or may not be filled, resulting in a possibly lower measured antenna temperature. In the case of a widespread weather condition (complete overcast) both beams will be filled and the noise temperature increases will be equal. Data gathered by a wide-beam antenna will be biased toward lower-than-actual values.

Care must be taken in applying these statistics. Modeling techniques to apply wide beam results to narrow beam antennas are being investigated. These will depend on the physical characteristics of rain and clouds, plus associated wind conditions. Wind conditions are important because what a wide-beam antenna sees of a small high noise temperature cell in a 2-minute period as it drifts within the beam, *may* be what a narrow-beam antenna sees *on the average* over a longer *time* period as it drifts in and out of the beam. The ramifications of this are important, and the modeling will be quite difficult.

IV. Elevation Angle Modeling

Elevation angle modeling can be done (with thought and care) as follows. The zenith atmospheric attenuation *increase* may be found from

$$\Delta\text{dB} = 10 \log_{10} \left[\frac{T_P}{T_P - DELTZX} \right]$$

where

T_P = assumed average physical temperature for attenuating elements

$DELTZX$ = zenith noise temperature increase above baseline

For $DELTZX \ll T_P$, ΔdB is insensitive to the choice of T_P, although 265 K to 270 K is a reasonable range for the physical temperature of clouds.

The total zenith atmospheric attenuation becomes:

$$\text{total dB (zenith)} = 0.043 + \Delta\text{dB}$$

At an elevation angle θ the total atmospheric attenuation becomes (for *uniform* weather over the field of interest)

$$\text{total dB}\,(\theta) = \frac{\text{total dB, zenith}}{\sin\theta}$$

This approximation is valid for $\theta > 10$ deg. Note that for *scattered* rain and/or clouds, there are nonattenuating spaces between the attenuating elements, and the above expression must be altered considerably based on considerations of percent rain and/or cloud coverage.

For the uniform case, the *total atmospheric noise temperature* may be computed from

$$TX(\theta) = T_P \cdot \left[1 - \frac{1}{L_\theta}\right]$$

where

$L_\theta = 10^{(\text{total dB}, \theta)/10}$

T_P = same assumed physical temperature

Note that as the atmospheric attenuation *increases*, the cosmic background contribution *decreases*. The net cosmic contribution then becomes

$$T_{cosmic,\ \theta} = \frac{2.7}{L_\theta}$$

where L_θ is calculated above. The increase above baseline at elevation θ is *not* $TX(\theta) - T_{baseline}\ (\theta)$. The *difference* in cosmic contributions must be added back into the above difference.

V. Summary of Data

At Goldstone, there is a zenith X-band noise temperature increase of less than 1 K above the quiescent baseline 95% of the time. The "worst" (highest attenuation) year quarter and day quarter of the year appears, at present, to be the fourth year quarter (Sep, Oct, Nov) in the morning (6 a.m. to noon). The best year quarter/day quarter appears to be the third year quarter (Jun, Jul, Aug) in the morning (6 a.m. to noon). The worst year quarter is the fourth; the best is the third. The worst time of day is the afternoon (noon to 6 p.m.); the best is the evening (6 p.m. to midnight). However, one should take about 10 to 15 years of data before real long-term average statistics may be developed. (Note that 1975-1976 Southern California weather conditions were far "drier" than the long-term average.) These data will be updated quarterly.

Table 1. X-band zenith noise temperature increase — probability density functions.[a] YEAR QUARTER = 1

	Day quarter				
DELTZX[b]	1	2	3	4	All
1	.96813+00	.94814+00	.94851+00	.96614+00	.95765+00
2	.23291-01	.44679-01	.44516-01	.24970-01	.34453-01
3	.33517-02	.17120-02	.34892-02	.56056-02	.35283-02
4	.17043-02	.49705-03	.11256-02	.45298-03	.94180-03
5	.11930-02	.88364-03	.45022-03	.16987-03	.67473-03
6	.34085-03	.13255-02	.22511-03	.56622-04	.49199-03
7	.68170-03	.88364-03	.56278-04	.11324-03	.43576-03
8	.34085-03	.12150-02	.22511-03	.00000	.44982-03
9	.28404-03	.33136-03	.16883-03	.00000	.19680-03
10	.17043-03	.16568-03	.56278-04	.00000	.98398-04
11	.17043-03	.00000	.22511-03	.56622-04	.11245-03
12	.17043-03	.55227-04	.00000	.00000	.56227-04
13	.00000	.55227-04	.16883-03	.00000	.56227-04
14	.11362-03	.00000	.11256-03	.00000	.56227-04
15	.00000	.00000	.00000	.56622-04	.14057-04
16	.56808-04	.00000	.16883-03	.00000	.56227-04
17	.00000	.00000	.00000	.56622-04	.14057-04
18	.00000	.00000	.56278-04	.00000	.14057-04
19	.00000	.00000	.11256-03	.56622-04	.42170-04
20	.00000	.00000	.56278-04	.00000	.14057-04

[a]Percent of time (= 100) that noise temperature increase is in range of DELTZX (below). (e.g., .96813 + 00 = .96813 x 10^0).

[b]DELTZX = X-band zenith noise temperature increase above quiescent baseline, 1 = 0 to 1 K, 2 = 1 to 2 K, etc.

Table 2. X-band zenith noise temperature increase — probability density functions. YEAR QUARTER = 2

	Day quarter				
DELTZX	1	2	3	4	All
1	.97982+00	.98621+00	.97688+00	.98177+00	.98117+00
2	.65540-02	.77951-02	.86487-02	.52829-02	.70688-02
3	.16385-02	.18845-02	.31684-02	.18746-02	.21421-02
4	.86237-03	.77094-03	.21408-02	.10225-02	.11996-02
5	.94860-03	.77094-03	.10276-02	.51125-03	.81398-03
6	.94860-03	.17132-03	.42816-03	.42604-03	.49267-03
7	.43118-03	.85660-04	.94194-03	.42604-03	.47125-03
8	.51742-03	.17132-03	.42816-03	.59646-03	.42841-03
9	.25871-03	.00000	.42816-03	.59646-03	.32131-03
10	.25871-03	.00000	.42816-03	.34083-03	.25705-03
11	.17247-03	.00000	.34252-03	.42604-03	.23563-03
12	.34495-03	.00000	.34252-03	.34083-03	.25705-03
13	.25871-03	.85660-04	.85631-04	.34083-03	.19279-03
14	.25871-03	.00000	.85631-04	.42604-03	.19279-03
15	.25871-03	.85660-04	.25689-03	.68166-03	.32131-03
16	.25871-03	.85660-04	.42816-03	.34083-03	.27847-03
17	.00000	.00000	.85631-04	.25562-03	.85663-04
18	.17247-03	.85660-04	.85631-04	.25562-03	.14994-03
19	.25871-03	.00000	.85631-04	.85208-04	.10710-03
20	.34495-03	.17132-03	.17126-03	.85208-04	.19279-03

Table 3. X-band zenith noise temperature increase — probability density functions. YEAR QUARTER = 3

	Day quarter				
DELTZX	1	2	3	4	All
1	.97960+00	.99203+00	.97789+00	.98331+00	.98313+00
2	.10894-01	.63198-02	.11617-01	.87719-02	.94265-02
3	.19702-02	.82689-03	.35527-02	.31126-02	.23854-02
4	.75332-03	.23625-03	.19173-02	.14714-02	.11065-02
5	.69537-03	.00000	.10151-02	.56593-03	.57479-03
6	.23179-03	.59063-04	.11278-02	.73571-03	.54605-03
7	.40563-03	.00000	.33835-03	.28297-03	.25865-03
8	.40563-03	.59063-04	.22557-03	.28297-03	.24428-03
9	.57947-03	.00000	.16918-03	.11319-03	.21555-03
10	.52153-03	.59063-04	.28196-03	.16978-03	.25865-03
11	.34768-03	.59063-04	.33835-03	.56593-04	.20118-03
12	.23179-03	.00000	.22557-03	.56593-04	.12933-03
13	.11589-03	.00000	.56392-04	.56593-04	.57479-04
14	.17384-03	.00000	.56392-04	.11319-03	.86218-04
15	.17384-03	.59063-04	.56392-04	.56593-04	.86218-04
16	.34768-03	.59063-04	.00000	.00000	.10059-03
17	.23179-03	.00000	.56392-04	.11319-03	.10059-03
18	.23179-03	.00000	.00000	.00000	.57479-04
19	.23179-03	.00000	.56392-04	.00000	.71848-04
20	.34768-03	.00000	.00000	.00000	.86218-04

Table 4. X-band zenith noise temperature increase — probability density functions. YEAR QUARTER = 4

	Day quarter				
DELTZX	1	2	3	4	All
1	.92344+00	.91136+00	.91330+00	.92860+00	.91918+00
2	.55902-01	.63683-01	.51913-01	.50648-01	.55507-01
3	.35278-02	.60683-02	.84961-02	.46565-02	.56952-02
4	.18318-02	.17046-02	.31442-02	.20246-02	.21801-02
5	.61058-03	.10909-02	.21742-02	.13160-02	.13013-02
6	.61058-03	.81819-03	.17728-02	.14509-02	.11661-02
7	.61058-03	.34091-03	.14383-02	.87731-03	.81964-03
8	.50882-03	.34091-03	.10035-02	.40491-03	.56614-03
9	.57666-03	.44319-03	.12376-02	.16871-03	.60839-03
10	.57666-03	.37500-03	.10035-02	.13497-03	.52389-03
11	.44098-03	.75001-03	.50174-03	.20246-03	.47319-03
12	.37313-03	.10568-02	.26759-03	.10123-03	.44784-03
13	.78019-03	.95456-03	.23415-03	.26994-03	.55769-03
14	.54274-03	.30682-03	.20070-03	.13497-03	.29575-03
15	.27137-03	.23864-03	.16725-03	.33743-03	.25350-03
16	.20353-03	.68183-04	.10035-03	.13497-03	.12675-03
17	.27137-03	.10227-03	.13380-03	.10123-03	.15210-03
18	.23745-03	.34091-04	.13380-03	.67486-04	.11830-03
19	.23745-03	.34091-03	.23415-03	.33743-04	.21125-03
20	.20353-03	.17046-03	.66899-04	.67486-04	.12675-03

Table 5. X-band zenith noise temperature increase — probability density functions. ALL YEAR QUARTERS

	Day quarter				
DELTZX	1	2	3	4	All year and day quarters
1	.95517+00	.94957+00	.94591+00	.95798+00	.95215+00
2	.30578-01	.37807-01	.34382-01	.28148-01	.32725-01
3	.28445-02	.32218-02	.53973-02	.40937-02	.38952-02
4	.14091-02	.94681-03	.22445-02	.13820-02	.14979-02
5	.81648-03	.74956-03	.13363-02	.75616-03	.91575-03
6	.51359-03	.67066-03	.10639-02	.80831-03	.76531-03
7	.55310-03	.35505-03	.79143-03	.49542-03	.54945-03
8	.44775-03	.46025-03	.55789-03	.31290-03	.44479-03
9	.46091-03	.24985-03	.62276-03	.18252-03	.37938-03
10	.42141-03	.19725-03	.53194-03	.14341-03	.32378-03
11	.31606-03	.30245-03	.37625-03	.16949-03	.29108-03
12	.28972-03	.42080-03	.20759-03	.10430-03	.25510-03
13	.36873-03	.39450-03	.15569-03	.16949-03	.27146-03
14	.31606-03	.11835-03	.12974-03	.14341-03	.17661-03
15	.18437-03	.11835-03	.11677-03	.26075-03	.17007-03
16	.21070-03	.52600-04	.14272-03	.10430-03	.12755-03
17	.15803-03	.39450-04	.77845-04	.11734-03	.98116-04
18	.17120-03	.26300-04	.77845-04	.65187-04	.85034-04
19	.18437-03	.13150-03	.14272-03	.39112-04	.12428-03
20	.21070-03	.92051-04	.64871-04	.39112-04	.10139-03

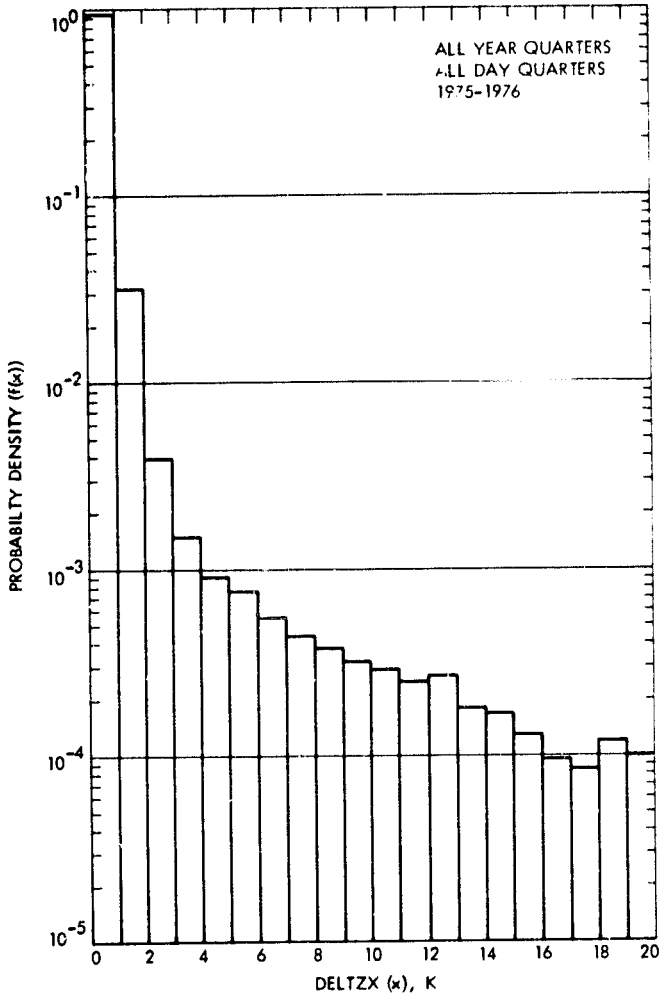

Fig. 1. Probability density histogram of zenith noise temperature increase (DELTZX)

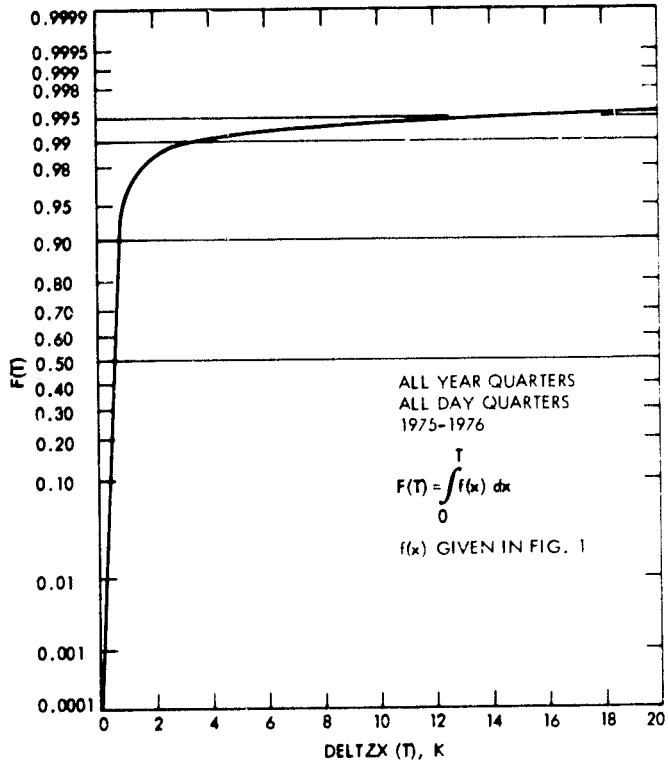

Fig. 2. Cumulative distribution function for zenith noise temperature increase (DELTZX)

Computation of Spacecraft Signal Raypath Trajectories Relative to the Sun

R. Cannon and C. Stelzried
Radio Frequency and Microwave Subsystems Section

A computer program (CTS 41B) used to determine the trajectory of a spacecraft signal raypath has been updated to increase its usefulness during solar conjunctions (CTS 41C). The closest point of approach of the raypath to the sun is projected onto the surface and the solar latitude and longitude calculated. A sample computation and plots are given for the 1976 Viking solar conjunction. Eventually it may be possible to predict the communication link performance degradation in the near sun region due to solar activity.

I. Introduction

A double-precision computer program, CTS 41B (Ref. 1), was recently developed to determine the trajectory of a spacecraft telemetry signal raypath relative to some body (e.g., the sun), with respect to which the spacecraft is undergoing a superior conjunction. Such a determination is necessary in order to assess the effects imposed on the telemetry carrier during the superior conjunction. The evaluation of relationships between the quality of the communication channel and particular features of the conjunction body is facilitated by the newest version of this trajectory program, CTS 41C. While CTS 41C has been developed specifically for solar conjunctions, the program could be adapted for conjunctions involving planets or other bodies.

It is theoretically expected that the telemetry signal from a spacecraft which is undergoing superior conjunction with the sun should be most strongly affected by the solar atmosphere in the vicinity of the point of closest approach of the signal raypath to the sun. Measurements made during the superior conjunctions of several different spacecraft (Ref. 2-7) have indicated that such generally tends to be the case. The coronal features which are actually encountered by telemetry signals during the superior conjunctions of deep space probes with the sun are difficult to observe by other available techniques. Features in the chromosphere and photosphere, however, are considerably more susceptible to the standard observational techniques and may therefore provide the best basis for the establishment of relationships between particular solar phenomena and the effects measured in the coronal communication channel.

Because the solar plasma is extended more or less radially away from the sun in the developing solar wind, the photospheric and chromospheric features that are most favorably located with respect to the signal raypath can be identified by projecting the point of closest approach of the raypath to the sun radially onto the photosphere. A finite interval of time may be required for the surface properties to be communicated to

the coronal regions traversed by the signal raypath; hence the solar longitude of the projected point must be corrected to account for the solar rotation during this time interval. Because different types of solar phenomena may be communicated through the corona at different speeds, no attempt to estimate this effect has been included in CTS 41C; it is assumed that users of this program will make the corrections that are appropriate to their specific situations.

II. Input

The location of a point on the solar surface can be specified in terms of its coordinates in solar latitude and solar longitude. The solar longitude, in turn, is specified by the Carrington solar longitude and the Carrington solar rotation number. In order to correctly compute the coordinates of a point on the surface of the sun through the program CTS 41C, it is necessary to input the Carrington solar rotation number and the Carrington solar longitude of the central meridian of the sun on the first day of the conjunction interval, unless that day also happens to be the first day of the year. These values can be found in the *American Ephemeris and Nautical Almanac* and should be entered in the program as the constants NROTZZ and CSLZZ, respectively. If the first day of the conjunction interval is the first day of the year (i.e., January 1), the correct longitude and rotation number will be automatically computed without requiring these inputs. In default of these inputs, the solar coordinates will be computed incorrectly (unless the conjunction interval begins on January 1), but all of the other computations will be done correctly; hence users who are not interested in locating the projected point of closest approach on the solar surface need not concern themselves with these inputs.

III. Computations

The basic coordinate system used in the raypath trajectory computations is a heliocentric system referred to the ecliptic plane, in which

$\hat{X}_{ec} \equiv$ direction from sun to earth

$\hat{Z}_{ec} \equiv$ normal to ecliptic plane, positive to north

The Y-axis completes the right-handed system, and the X-Y plane is the ecliptic plane.

In this coordinate system the coordinates of the point of closest approach of the telemetry signal raypath to the sun are given by (Ref. 1)

$$X_B = R \sin (SEP)$$

$$Y_B = Y_P R_{EB} / R_P$$

$$Z_B = \frac{Z_P R_{EB}}{R_P}$$

where

(X_B, Y_B, Z_B) = coordinates of point of closest approach

R = raypath offset from sun

SEP = sun-earth-probe angle

R_{EB} = distance from earth to point of closest approach

R_P = earth-probe range

(X_P, Y_P, Z_P) = coordinates of probe

Locations on the solar surface are better specified in a heliocentric coordinate system referred to the solar equatorial plane, in which

$\hat{Z}_{eq} \equiv$ direction of solar rotational axis

$\hat{X}_{eq} \equiv$ in plane of central meridian

with the X-Y plane being the solar equatorial plane.

The transformation from heliocentric-ecliptic coordinates to heliocentric-equatorial coordinates can be accomplished by a sequence of simple coordinate system rotations. The heliocentric-ecliptic coordinates are first rotated about the Z_{ec} axis (normal to the ecliptic plane) by the angle between the sun-earth line and the ecliptic-equatorial node. This angle, ϕ_n, is equal to the difference between the longitude of the sun, which is provided in record 27 of the geocentric block of coordinates on the DPTRAJ save tape read by the program CTS 41C, and the longitude of the ecliptic-equatorial node = 73 deg, 40 min + 50.25 sec × T, where T is the time in years

since 1850. This coordinate rotation is thus performed by the matrix operator

$$M_1 = \begin{pmatrix} \cos\phi_n & \sin\phi_n & 0 \\ -\sin\phi_n & \cos\phi_n & 0 \\ 0 & 0 & 1 \end{pmatrix}$$

The new X-axis then lies along the ecliptic-equatorial node and is common to both the ecliptic and solar equatorial planes. A rotation about this axis by the angle between the ecliptic and solar equatorial planes, 7.25 deg, is performed by the matrix operator

$$M_2 = \begin{pmatrix} 1 & 0 & 0 \\ 0 & \cos 7.25 & \sin 7.25 \\ 0 & -\sin 7.25 & \cos 7.25 \end{pmatrix}$$

The new Z-axis then coincides with the solar rotational axis. A rotation about this axis by the angle between the sun-earth line and ecliptic-solar equatorial node, in the opposite sense to the original rotation, is performed by the matrix operator

$$M_3 = \begin{pmatrix} \cos\phi_n & -\sin\phi_n & 0 \\ \sin\phi_n & \cos\phi_n & 0 \\ 0 & 0 & 1 \end{pmatrix}$$

The final coordinate system then has the Z-axis in the direction of the solar rotational axis, with the X-axis in the plane of the central meridian and the X-Y plane is the solar equatorial plane.

The coordinates of the point of closest approach of the signal raypath to the sun in the solar equatorial coordinate system are then given by

$$\begin{pmatrix} X_B \\ Y_B \\ Z_B \end{pmatrix}_{eq} = M_3 M_2 M_1 \begin{pmatrix} X_B \\ Y_B \\ Z_B \end{pmatrix}_{ec}$$

The point of closest approach lies at solar latitude

$$\lambda_B = \arctan\left(\frac{Z_{B_{eq}}}{\sqrt{X^2_{B_{eq}} + Y^2_{B_{eq}}}}\right)$$

and differs in solar longitude from the central meridian by the angle

$$\phi_B = \arctan\left(\frac{Y_{B_{eq}}}{X_{B_{eq}}}\right)$$

The Carrington solar longitude of the central meridian on the kth day of the conjunction interval is computed according to

$$\theta_{cm}(k) = CSLZZ - \sum_{i=1}^{k} 360\left(\frac{1}{T_{SID}} - \frac{1}{365.25\, R^2_{EAU}(i)}\right)$$

where

$CSLZZ$ = Carrington solar longitude of central meridian on first day of conjunction interval

T_{SID} = sidereal solar rotation period = 25.38 days

$R_{EAU}(i)$ = earth-sun range in astronomical units on ith day of the conjunction interval

In this computation, the Carrington solar longitude of the central meridian decreases from the initial longitude, $CSLZZ$, as a consequence of the solar rotation. Each time the longitude becomes negative the Carrington solar rotation number is increased by unity and the Carrington solar longitude is increased by 360 deg. The Carrington solar longitude of the point of closest approach of the signal raypath on the kth day of the conjunction interval is then

$$\theta_B(k) = \theta_{cm}(k) + \phi_B$$

It is convenient to define the fractional Carrington solar rotation number corresponding to the solar longitude ϕ_B as

$$\eta_{FSR} = \eta_{CSR} + \frac{\theta_B}{360 \text{ deg}}$$

where

η_{FSR} = fractional solar rotation number

η_{CSR} = integral Carrington solar rotation number.

In addition to computing the location of the projected point of closest approach on the solar surface, the program CTS 41C also computes several trajectory parameters that are of potential value to experimenters and which were not computed by the program CTS 41B. One of these is the apparent angle between the sun-probe line and the ecliptic plane, as seen from earth. This angle, PEL, is defined by the equation

$$PEL = \arctan (Z_A / Y_A)$$

where (Y_A, Z_A) = coordinates of the spacecraft relative to the sun, as described in Ref. 1.

The sign convention was chosen to make $0 < PEL < 180$ when the probe is north of the ecliptic plane, $180 < PEL < 0$ when the probe is south of the ecliptic plane, $|PEL| < 90$ when the probe is west of the sun, and $90 < |PEL| < 180$ when the probe is east of the sun.

The program CTS 41C also computes the sun-earth-probe angle (SEP), the sun-probe-earth angle (SPE), and the daily rate of change of the sun-probe-earth angle (DSPE). This latter quantity is computed from the equation

$$DSPE(k) = \frac{SPE(k+1) - SPE(k-1)}{2}$$

IV. Output

In addition to all of the output formerly provided by the program CTS 41B (Ref. 1), the program CTS 41C also provides tabular listings of the Carrington solar longitude, solar latitude, and fractional Carrington solar rotational number of the projection on the solar surface of the point of closest approach of the telemetry signal raypath to the sun. The Carrington solar longitude of the central meridian is included in this tabulation. Tabular listings of the apparent angle between the sun-probe-earth angle and the daily rate of change of the sun-probe-earth angle are also provided for each day of the conjunction interval.

The coordinates of the projected point of closest approach are plotted in a format similar to that used in the standard synoptic charts of solar features. In this plot, the solar latitude of the point of closest approach is plotted between −90 and +90 deg, as usual. However, the solar longitude is plotted in terms of the fractional number of solar rotations within the conjunction interval, rather than the usual Carrington solar longitude. This choice was inspired by the constraints imposed by the standard computer plot routine. Each integral value on this scale corresponds to an integral solar rotation, at which point the Carrington solar longitude passes through 0/360 deg. The initial Carrington solar rotation number is printed on the plot and corresponds to the first point plotted. The solar rotation numbers then increase from right to left, while the solar longitude within a given rotation increases from left to right. While this convention coincides with the standard convention used in synoptic charts of solar observations, the plotting device does not permit the solar longitude and solar rotation numbers to be printed directly on the plot; hence the method of fractional solar rotations was resorted to.

Sample plots made for the superior conjunction of the Viking spacecraft in 1976 are presented in Figs. 1 and 2.[1] Solar longitudes and solar rotation numbers have been added along the bottom of the computer plot (Fig. 2) to illustrate the manner in which they are related to the fractional rotation numbers printed by the computer. Several dates have also been added to the plots. These can be determined by referring to the printed output as described in Ref. 1.

[1] For this sample plot computed for the period Oct. 12 to Dec. 30, 1976 use for CTS 41C input data NROTZZ = 1647 and CSLZZ = 345.54 (see the 1976 *American Ephemeris and Nautical Almanac*, pages 359 and 357), for rotation number and value of L_0, respectively, for Oct. 12, 1976.

References

1. Cannon, A. R., and Stelzried, C. T., "Computation of Spacecraft Signal Raypath Trajectories Relative to the Sun," *The Deep Space Network Progress Report 42-34*, Jet Propulsion Laboratory, Pasadena, Calif., Aug. 15, 1976.

2. Goldstein, R. M., "Superior Conjunction of Pioneer 6", *Science, 166*, 1969.

3. Stelzried, C. T., et al., "The Quasi-Stationary Coronal Magnetic Field and Electron Density as Determined from a Faraday Rotation Experiment," *Solar Physics*, Vol. 14, No. 2, Oct. 1970.

4. Levy, G. S., Sato, T., Seidel, B. L., Stelzried, C. T., Ohlson, J. E., and Rusch, W. V. T., "Pioneer 6: Measurement of Transient Faraday Rotation Phenomena Observed During Solar Occultation," *Science*, Vol. 166, Oct. 31, 1969, p. 596.

5. Cannon, A. R., *Radio Frequency Probing of the Solar Corona*, Ph.D. Thesis, University of California, Berkeley, Calif., June 1976.

6. Stelzried, C. T., "A Faraday Rotation Measurement of a 13-cm Signal in the Solar Corona," *The Deep Space Network*, Technical Report 32-1401, Jet Propulsion Laboratory, Pasadena, California, July 15, 1970.

7. Cannon, A. R., Stelzried, C. T., and Ohlson, J. E., "Faraday Rotation Observations During the 1970 Pioneer 9 Solar Occultation," *The Deep Space Network*, Technical Report 32-1526, Vol. XVI, Jet Propulsion Laboratory, Pasadena, Calif., Aug. 15, 1973.

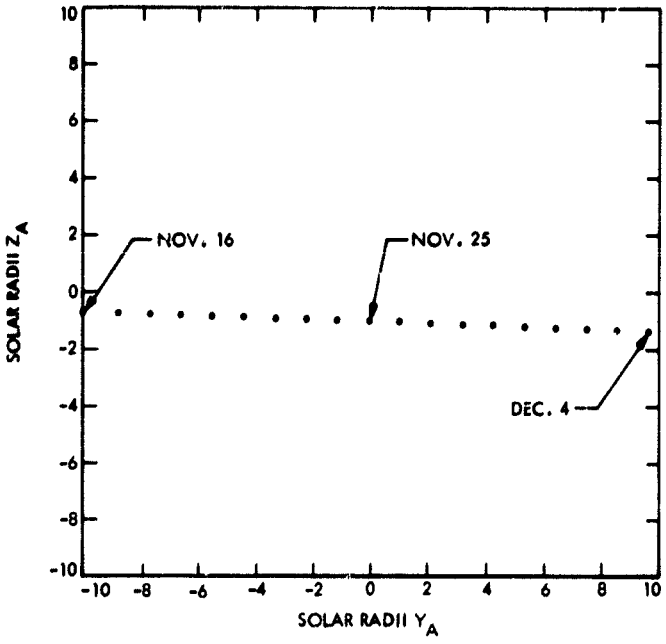

DAY 1 3.2100000+02 DAY N 3.3900000+02

Fig. 1. Plot of the Viking spacecraft ray path offset from the sun as a function of 1976 data

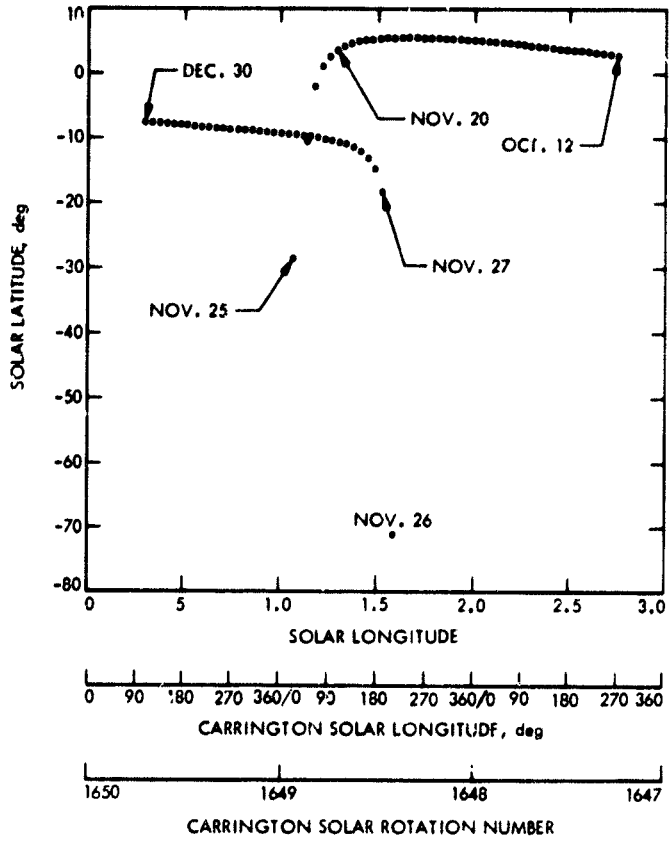

BEG. ROT. No. 1.647(000+03 YEAR 1.9760000+03

Fig. 2. Coordinates of the projected point of closest approach during the superior conjunction of the Viking spacecraft in 1976

Analysis of a Discrete Spectrum Analyzer for the Detection of Radio Frequency Interference

B. K. Levitt
Communications Systems Research Section

As the radio frequency spectrum becomes increasingly overcrowded, interference with mission-critical DSN operations is rising at an alarming rate. To alleviate this problem the DSN is developing a wideband surveillance system for on-site detection and identification of potential sources of radio frequency interference (RFI), which will complement the existing frequency coordination activities. The RFI monitoring system is based on a wideband, multi-look discrete spectrum analyzer operating on fast Fourier transform principles. This article presents an extensive general statistical analysis of such spectrum analyzers and derives threshold detection performance formulas for signals of interest. These results are then applied to the design of the RFI spectrum analyzer under development.

I. Introduction

Due to the steady increase of commercial and military users of the radio frequency (RF) spectrum, deep space telemetry and tracking can no longer expect to have dedicated, interference-free bands available all the time. DSN operations are particularly vulnerable to radio frequency interference (RFI) because of the relatively weak signals received from deep space probes. The magnitude of this problem was addressed in part by an earlier article (Ref. 1), which demonstrated the potential for an alarming number of outages in DSN reception due to RFI from a rapidly growing contingent of powerful Earth-orbiting satellites.

To alleviate this problem, the DSN is developing equipment to provide continuous, real-time surveillance of the RF environment at each complex. This monitoring system will function independent of existing DSS receivers and antennas so as to avoid interrupting normal DSN operations. By detecting and identifying potential sources of RFI in advance, and using available frequency coordination procedures, the loss of mission-critical data can be minimized.

The heart of the RFI monitoring system under development is a wideband (10-20 MHz at S-band), high-resolution (2^{17}, or about 130,000 spectral lines), digital spectrum analyzer, using fast Fourier transform (FFT) processing for real-time operation. This article determines the statistical performance of discrete spectrum analyzers corrupted by additive Gaussian noise, and applies the resulting formulas to the design of the RFI surveillance system.

Much of the detailed mathematical analysis is confined to a series of appendices. A general expression for the power in a

given spectral line is derived in Appendix A for a discrete Fourier transform (DFT) spectrum analyzer. (The FFT is simply a computationally efficient method of implementing a DFT). This is followed by an examination of the statistical characteristics of the spectral line powers for an "L-look" analyzer (in which the output powers are averages of L independent measurements), and the derivation of system performance probabilities for threshold signal-detection processing. In Appendix B, this is done for continuous spectrum bandpass Gaussian signals, while Appendix C looks at discrete spectrum signals imbedded in white Gaussian noise. Finally, Appendix D discusses aliasing effects in the DFT spectrum resulting from the finite observation window for the input signal.

II. Application to RFI Spectrum Analyzer Design

In this section, we will use some of the statistical performance formulas derived in the appendices to compute some preliminary design parameters for the RFI spectrum analyzer. This is an L-look, FFT-based system which produces an $N = 2^{17}$ line spectrum of total bandwidth $W = 10$ MHz (baseline design), so that the line width is $W/N = 76.3$ Hz. The system internal noise temperature is assumed to be 30 K in this exercise, corresponding to a thermal noise power spectral density $N_0 = -183.83$ dBm/Hz.

For RFI applications, most of the time the spectrum analyzer will see only its own thermal noise. In this case, Appendix B shows that each of the normalized spectral line powers is a central chi-square random variable with $2L$ degrees of freedom, mean 1, and standard deviation $1/\sqrt{L}$ (see Eq. B-16 with signal-to-noise ratio $\gamma = 0$). If a threshold $\eta > 1$ is used to detect the presence of an external signal component at each line frequency, the false alarm probability per line P_{FA} is given by Eq. (B-21). Since it requires T_L seconds (see Eq. B-12) to generate one entire spectrum, the probability of a false alarm on any line during 24 hours of continuous operation, $P_{FA}{}^*$, is overbounded by

$$P_{FA}{}^* < \frac{(24 \times 60 \times 60)N}{T_L} P_{FA} < \frac{86400W\left[\eta e^{-(\eta-1)}\right]^L}{\sqrt{2\pi L}\,[(\eta-1)L+1]} \tag{1}$$

which is accurate for small $P_{FA}{}^*$ (union bound argument) and $(\eta-1)\sqrt{L} \gtrsim 4$ (see Fig. B-3).[1] For reliable RFI surveillance on a round-the-clock basis, we will arbitrarily set a baseline design requirement that $P_{FA}{}^* = 10^{-3}$. The variation of L and T_L with η subject to this constraint is illustrated in Fig. 1; note that $(\eta-1)\sqrt{L}$ varies slowly over the range of η shown.

Occasionally, the RFI spectrum analyzer will receive an external signal of interest. The Consultative Committee for International Radio (CCIR) Recommendation 365-2 states that the interference from any RFI source, measured at the input to a DSN receiver, shall not exceed -190 dBm/Hz (7.25 K) for more than 5 minutes each day. As in our first RFI article (Ref. 1), we shall assume that this power spectral density is the minimum RFI level of interest, and design the spectrum analyzer to detect signals down to this level.

The interference signal spectrum can have many forms. Suppose the sidebands from a wideband (e.g., spread-spectrum) transmission lie in the DSN receive band. Then the RFI signal might look like white Gaussian noise, with one-sided power spectral density N_0' over the spectrum analyzer bandwidth W. This situation is considered in Appendix B. The probability P_M that a given spectral line power lies below the detection threshold η, referred to as a "miss," is accurately approximated by Eq. (B-20) for large L. The tradeoff between P_M and $P_{FA}{}^*$ vs η is illustrated in Fig. 2 for $L = 2100$ and $N_0' = -190$ dBm/Hz. If we select for our baseline design the balanced performance requirement $P_M = P_{FA}{}^* = 10^{-3}$, this is satisfied for the above N_0' by the system parameters

$$L = 2091 \text{ and } \eta - 1 = 0.1587 \Downarrow T_L = 27.4 \text{ s and } (\eta - 1)\sqrt{L} = 7.26 \tag{2}$$

For this design, the sensitivity of P_M to changes in N_0' is shown in Fig. 3 ($P_{FA}{}^*$ remains constant at 10^{-3}, of course, independent of N_0').

On the other hand, the interfering source might transmit a discrete, higher-order carrier or subcarrier harmonic component that falls into the DSN receive band. For example, suppose the RFI signal is a single sinusoid of power P at some frequency f_s, where f_s is a priori uniformly distributed over the spectrum analyzer bandwidth W. This is a special case of the M-sinusoid analysis in Appendix C. Consider the spectral line *nearest* in frequency to f_s, and denote this frequency separation by Δ: then Δ is uniformly distributed over $(-W/2N, W/2N)$. To properly detect the RFI signal, we want this particular spectral line power to be above the threshold η. Conditioned on Δ, the probability of this not occurring (a

[1] Note that the threshold is $(\eta-1)\sqrt{L}$ standard deviations beyond the mean normalized spectral line power in the noise-only case.

miss) is given by Eqs. (C-19) and (C-20), and (see Eq. C-17 with $M = 1$)

$$\lambda_k = \left(\frac{PN}{N_0 W}\right)\left(\frac{\sin N\Delta}{N \sin\Delta}\right)^2 \tag{3}$$

Averaging over Δ, the probability of a miss on this particular line is

$$P_M = \frac{2N}{W}\int_0^{\frac{W}{2N}} d\Delta \int_0^{\eta} dx\, e^{g_k(x)} \tag{4}$$

where $g_k(x)$ is defined by Eqs. (3) and (C-20). Since $N_0' W/N = -171.2$ dBm for the design point N_0' previously used, we will plan on a minimum detectable P in this vicinity. Thus, for $P = -170$ dBm and $T_L = 65.0$ s, the tradeoff between P_M and $P_{FA}{}^*$ as η is varied is shown in Fig. 4. To ensure that $P_M = P_{FA}{}^* = 10^{-3}$ for this P, we need

$$\begin{gathered} T_L = 64.0 \text{ s and } \eta - 1 = 0.1003 \\ \Downarrow \\ L = 4883 \text{ and } (\eta - 1)\sqrt{L} = 7.01 \end{gathered} \tag{5}$$

The corresponding sensitivity of P_M to changes in P is illustrated in Fig. 5.

The design parameters of Eq. (5) represent a good baseline to cover both types of RFI signals above with their corresponding minimum detectable levels. When this selection is made, and the white noise-like RFI signals with $N_0' = -190$ dBm/Hz is present, Eq. (B-20) yields $P_M = 7.03 \times 10^{-17}$, while $P_{FA}{}^*$ remains at 10^{-3}.

III. Conclusions

This article presented an extensive statistical analysis of a multi-look discrete spectrum analyzer based on DFT or FFT techniques. We demonstrated that the output spectral line powers are central or noncentral chi-square random variables with many degrees of freedom for continuous spectrum Gaussian signals or discrete spectrum sinusoidal components imbedded in internal Gaussian noise. We derived threshold detection probabilities for these signals, and determined accurate simple approximations for these probabilities.

These results were applied to the design of a 10 MHz, 2^{17} line FFT spectrum analyzer with a 30 K internal noise temperature, which forms the basis for an RFI surveillance system under development for the DSN. It was shown that reliable performance down to required signal detection levels can be achieved with an approximately 5000-look system, a spectrum generation time of about a minute, and a detection threshold placed 7 standard deviations beyond the mean, noise-only spectral line power.

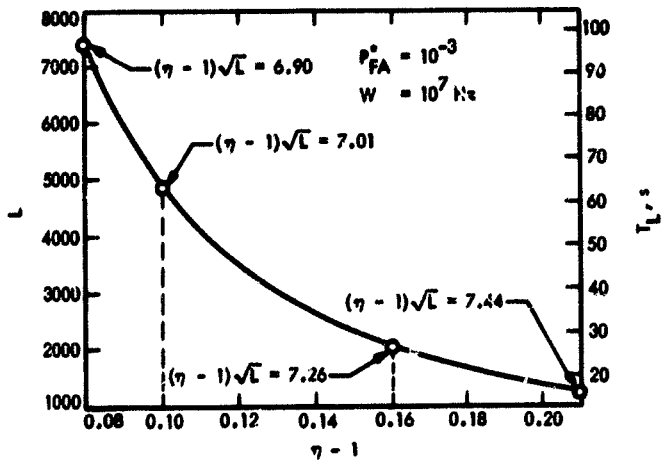

Fig. 1. Variation of number of looks L and spectrum generation time T_L with threshold η for W = 10 MHz DFT spectrum analyzer, subject to constraint that false alarm probability P_{FA}^* during 24 hours of continuous operation be 10^{-3}

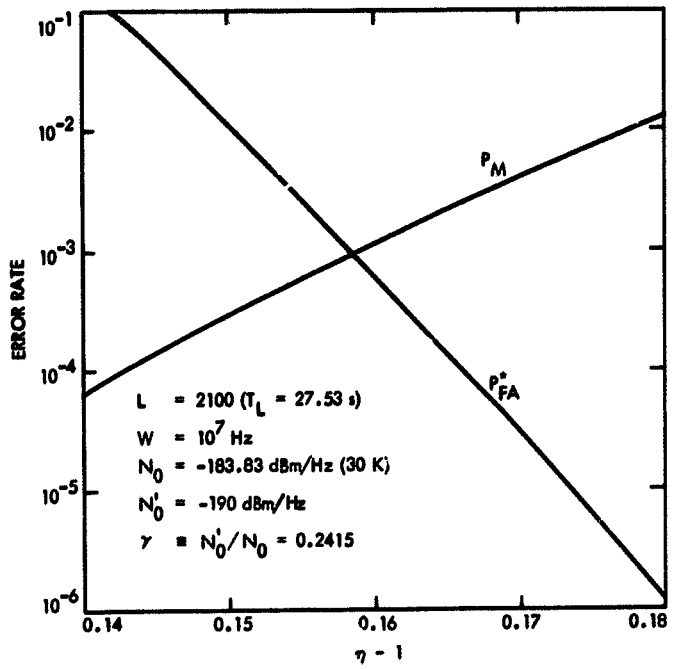

Fig. 2. Tradeoff between probability of false alarm per day P_{FA}^* and probability of a miss P_M vs threshold η for 2100-look system with spectrally white external Gaussian signal of power spectral density N'_0 = −190 dBm/Hz imbedded in internal thermal noise of power spectral density N_0 = −183.83 dBm/Hz (30 K noise temperature)

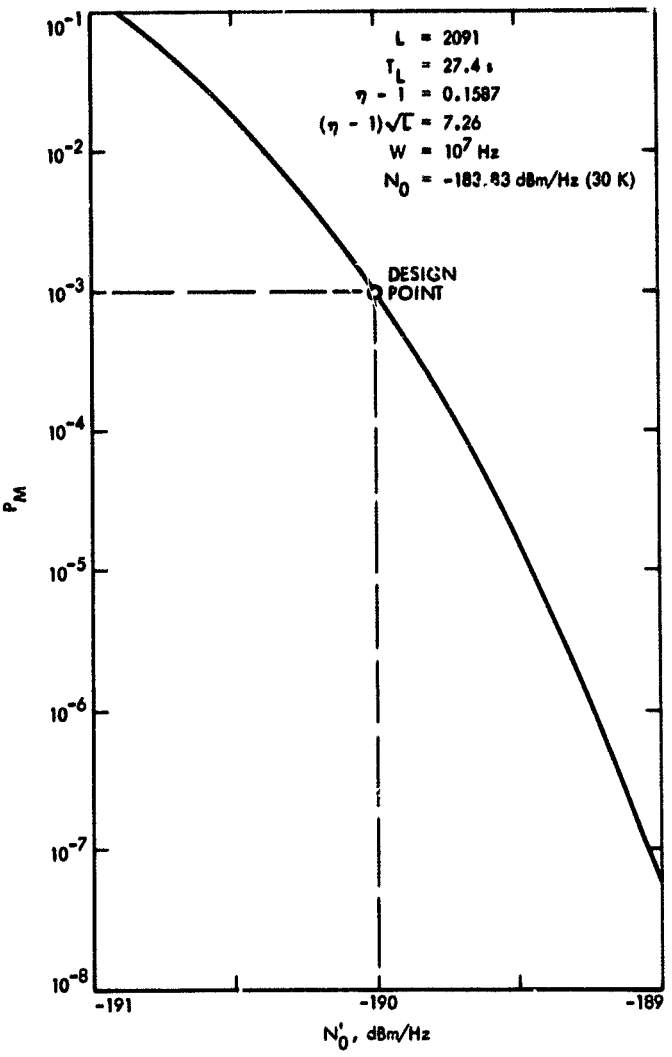

Fig. 3. Signal detection performance vs received signal power spectral density N'_0, for values of L and η selected to set $P_M = P_{FA}^* = 10^{-3}$ when N'_0 = −190 dBm/Hz

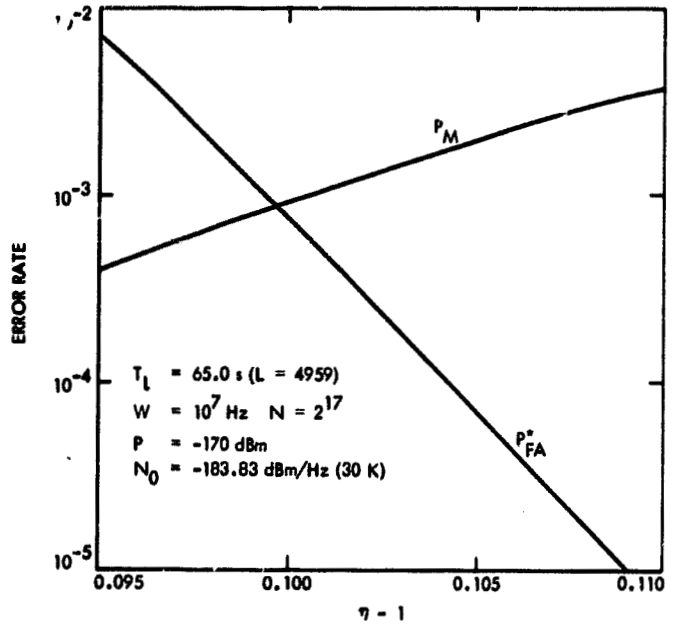

Fig. 4. DFT spectrum analyzer performance tradeoff for 65.0 s observation (4959 looks) of sinusoidal signal with power P = −170 dBm, and frequency uniformly distributed over spectral line width W/N

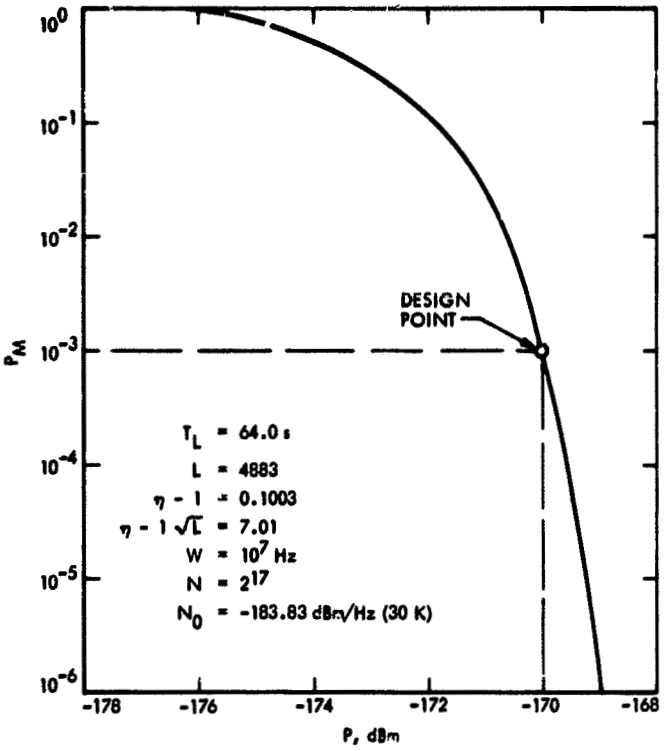

Fig. 5. Variation of probability of a miss P_M vs RFI signal power P, for values of T_L and η selected to have $P_M = P_{FA}^* = 10^{-3}$ at P = −170 dBm

Appendix A

Derivation of DFT Power Spectrum for Bandpass Signals

Consider a deterministic signal $x(t)$ with bandwidth W centered at f_c. Based on the observation of $x(t)$ over [0,T], we want to measure its power spectrum using DFT techniques.

First, $x(t)$ is reduced in quadrature to baseband, using a lowpass filter (LPF) to eliminate components near $2f_c$:

$$y(t) \equiv x(t)\ \sqrt{2}\ \cos 2\pi f_c t \Big|_{LPF}$$
$$z(t) \equiv x(t)\ \sqrt{2}\ \sin 2\pi f_c t \Big|_{LPF} \qquad \text{(A-1)}$$

In the frequency domain, the corresponding Fourier transform relations are

$$Y(f) = \frac{1}{\sqrt{2}}\ [X(f-f_c) + X(f+f_c)]\Big|_{LPF}$$
$$Z(f) = \frac{1}{j\sqrt{2}}[X(f-f_c) - X(f+f_c)]\Big|_{LPF} \qquad \text{(A-2)}$$

Solving for $X(f+f_c)$, we have

$$X(f+f_c) = \frac{1}{\sqrt{2}}[Y(f) - jZ(f)];\ |f| < \frac{W}{2} \qquad \text{(A-3)}$$

To apply the DFT approach to the determination of $Y(f)$ and $Z(f)$, it is convenient to introduce some shorthand notation:

$$\left.\begin{aligned} y_m &\equiv y\left(\frac{m}{W}\right) \\ z_m &\equiv z\left(\frac{m}{W}\right) \end{aligned}\right\} \quad m = 0,1,\ldots,N-1;\ N = WT$$

$$\left.\begin{aligned} Y_k &\equiv Y\left(\frac{kW}{N}\right) \\ Z_k &\equiv Z\left(\frac{kW}{N}\right) \end{aligned}\right\} \quad k = -\frac{N}{2}, -\frac{N}{2}+1, \ldots, \frac{N}{2}-1, \text{ for even } N \qquad \text{(A-4)}$$

$$c_{km} \equiv \cos\left(\frac{2\pi km}{N}\right)$$

$$d_{km} \equiv \sin\left(\frac{2\pi km}{N}\right)$$

Then, for sufficiently large T (or equivalently, N), we have the approximation

$$Y_k \cong \int_0^T dt\, y(t)\, e^{-j2\pi k W t/N} \cong \frac{1}{W}\sum_{m=0}^{N-1} y_m(c_{km} - jd_{km}) \qquad \text{(A-5)}$$

and Z_k is expressed similarly. Therefore

$$X\left(f_c + \frac{kW}{N}\right) \cong \frac{1}{W\sqrt{2}}\sum_{m=0}^{N-1}(y_m - jz_m)(c_{km} - jd_{km})$$
$$= \frac{N}{W\sqrt{2}}(A_k - jB_k) \qquad \text{(A-6)}$$

where

$$A_k \equiv \frac{1}{N}\sum_{m=0}^{N-1}(y_m c_{km} - z_m d_{km})$$
$$B_k \equiv \frac{1}{N}\sum_{m=0}^{N-1}(y_m d_{km} + z_m c_{km}) \qquad \text{(A-7)}$$

The one-sided power spectral density of $x(t)$ is approximated by

$$S_x(f) \cong \frac{2}{T}\left|X(f)\right|^2 \qquad \text{(A-8)}$$

It follows that the k^{th} discrete power spectral component, which approximates the power in $x(t)$ with a bandwidth W/N centered at frequency $f_c + kW/N$,[2] can be expressed as

$$\frac{W}{N}S_x\left(f_c + \frac{kW}{N}\right) \cong A_k^2 + B_k^2 \equiv S_k \qquad \text{(A-9)}$$

Although Eq. (A-9) was derived for deterministic signals $x(t)$, the DFT spectrum approach is readily extended to random signals, except that S_k is now a random variable, sometimes called a periodogram (Ref. 3).

[2] Actually, the finite observation time T causes some spectral spreading (see Appendix D), which can be reduced by appropriate data sample "windowing" (e.g., Refs. 2, 3).

Appendix B

DFT Power Spectrum Statistics for Continuous Spectrum Gaussian Signals

Suppose that $x(t)$ in Appendix A consists of a zero mean, bandpass, spectrally nonwhite Gaussian signal, plus zero mean, bandpass, white Gaussian noise:

$$x(t) = x_c(t)\sqrt{2}\cos 2\pi f_c t + x_s(t)\sqrt{2}\sin 2\pi f_c t \quad \text{(B-1)}$$

where $x_c(t)$ and $x_s(t)$ are lowpass signal-plus-noise quadrature components, each with one-sided bandwidth $W/2$. If the one-sided power spectral density of $x(t)$ is $S_x(f)$, then the auto- and crosscorrelation functions of $x_c(t)$ and $x_s(t)$ can be expressed as (Ref. 4, pp. 498-501):

$$R_c(\tau) \equiv \overline{x_c(t+\tau)x_c(t)} = R_s(\tau) = \int_0^{\frac{W}{2}} df\, S_e(f)\cos 2\pi f\tau \quad \text{(B-2)}$$

and

$$R_{cs}(\tau) \equiv \overline{x_c(t+\tau)x_s(t)} = -R_{cs}(-\tau) = -R_{sc}(\tau) = \int_0^{\frac{W}{2}} df\, S_0(f)\sin 2\pi f\tau \quad \text{(B-3)}$$

where $S_e(f)$ and $S_0(f)$ are the even and odd parts of $S_x(f+f_c)$ about $f = 0$ (see Fig. B-1):

$$S_e(f) \equiv \frac{1}{2}\left[S_x(f+f_c) + S_x(-f+f_c)\right]$$

$$S_0(f) \equiv \frac{1}{2}\left[-S_x(f+f_c) + S_x(-f+f_c)\right] \quad \text{(B-4)}$$

Now, to determine the spectral line statistics, we first note that the lowpass quadrature components of Eq. (A-1) are simply

$$y(t) = x_c(t) \qquad z(t) = x_s(t) \quad \text{(B-5)}$$

Since $x_c(t)$ and $x_s(t)$ are zero mean, jointly Gaussian random processes, the spectral components A_k and B_k of Eq. (A-7) must be zero mean, jointly Gaussian random variables. Furthermore,

$$\overline{A_k^2} = \frac{1}{N^2}\sum_{m=0}^{N-1}\sum_{j=0}^{N-1} \overbrace{\overline{y_m y_j}}^{R_c\left(\frac{m-j}{W}\right)} c_{km}c_{kj} + \overbrace{\overline{z_m z_j}}^{R_s\left(\frac{m-j}{W}\right)} d_{km}d_{kj}$$

$$- \overbrace{\overline{y_m z_j}}^{R_{cs}\left(\frac{m-j}{W}\right)} c_{km}d_{kj} - \overbrace{\overline{y_j z_m}}^{R_{cs}\left(\frac{j-m}{W}\right)} c_{kj}d_{km}$$

$$= \frac{1}{N^2}\sum_{m=0}^{N-1}\sum_{j=0}^{N-1}\left[R_c\left(\frac{m-j}{W}\right)\cos 2\pi k\left(\frac{m-j}{N}\right) + R_{cs}\left(\frac{m-j}{W}\right)\sin 2\pi k\left(\frac{m-j}{N}\right)\right]$$

$$= \frac{R_c(0)}{N} + \frac{2}{N^2}\sum_{i=1}^{N-1}(N-i)\left[R_c\left(\frac{i}{W}\right)\cos\left(\frac{2\pi ki}{N}\right) + R_{cs}\left(\frac{i}{W}\right)\sin\left(\frac{2\pi ki}{N}\right)\right] = \overline{B_k^2} \quad \text{(B-6)}$$

and similarly

$$\overline{A_k B_k} = \frac{1}{N^2}\sum_{m=0}^{N-1}\sum_{j=0}^{N-1}\left[-R_c\left(\frac{m-j}{W}\right)\sin 2\pi k\left(\frac{m-j}{N}\right) + R_{cs}\left(\frac{m-j}{W}\right)\cos 2\pi k\left(\frac{m-j}{N}\right)\right] = 0 \quad \text{(B-7)}$$

The summation in Eq. (B-7) is zero since $R_c\,[(m-j)/W]$ and $\cos 2\pi k\,[(m-j)/N]$ are even functions of $m-j$, while $R_{cs}\,[(m-j)/W]$ and $\sin 2\pi k\,[(m-j)/N]$ are odd. So A_k and B_k are

independent and identically distributed. Consequently, for a single-look system, the power spectral components S_k, defined in Eq. (A-9), are central chi-square random variables with 2 degrees of freedom, and mean

$$\overline{S_k} = 2\overline{A_k^2} \tag{B-8}$$

Let us now specialize to the case where the input Gaussian signal is white, with one-sided power spectral density N_0'. If the additive noise is independent of the input signal, and has spectral density N_0 over the bandpass region of interest, we have

$$S_e(f) = S_x(f+f_c) = N_0 + N_0'; \; 0 \leq f \leq \frac{W}{2}$$
$$S_0(f) = 0, \; \forall f \tag{B-9}$$

Then Eqs. (B-2) and (B-3) yield

$$R_c\left(\frac{i}{W}\right) = \frac{(N_0 + N_0')W}{2}\left(\frac{\sin \pi i}{\pi i}\right) = \frac{(N_0 + N_0')W}{2}\,\delta_{i0}$$
$$R_{cs}\left(\frac{i}{W}\right) = 0, \; \forall i \tag{B-10}$$

and Eqs. (B-6) and (B-8) reduce to

$$\overline{S_k} = (N_0 + N_0')\frac{W}{N}, \; \forall k \tag{B-11}$$

where W/N is the bandwidth of a spectral line.

For an L-look DFT spectrum analyzer, the k^{th} spectral component S_k^* is the average of L independent samples of S_k, which preserves the mean and reduces the variance by $1/L$. If the L measurements are made sequentially, the total observation time is (see Eq. A-4)

$$T_L = LT = \frac{LN}{W} \tag{B-12}$$

For convenience, we will scale the entire spectrum by $(N_0 W/N)^{-1}$, so that the mean spectral line power is 1 in the absence of an input signal:

$$v_k \equiv \frac{N}{N_0 W} S_k^* \tag{B-13}$$

Then the normalized spectral line power v_k is a central chi-square random variable with $2L$ degrees of freedom; its probability density function is (Ref. 5)

$$p(v_k) = \frac{1}{\Gamma(L)}\left(\frac{L}{1+\gamma}\right)^L v_k^{L-1} e^{-\frac{Lv_k}{1+\gamma}}; \; v_k > 0 \tag{B-14}$$

where we have introduced the signal-to-noise ratio

$$\gamma \equiv \frac{N_0'}{N_0} \tag{B-15}$$

and

$$\overline{v_k} = 1 + \gamma$$
$$\sigma_{v_k} = \frac{1+\gamma}{\sqrt{L}} \tag{B-16}$$

In this particular case, the input signal spectrum is flat, so the v_k's all have the same mean. However, in general, we detect the presence of a signal component at each frequency $f_c + kW/N$ by comparing v_k with a threshold η. The selection of η involves a tradeoff between the probability of incorrectly deciding a signal is not present (a "miss"), vs the probability of falsely detecting a signal (a "false alarm"): a smaller η improves the former at the expense of the latter.

The probability of a miss at the k^{th} frequency is given by (using Ref. 6, pp. 317 and 940)

$$P_M \equiv Pr[v_k < \eta] = \frac{L^L}{\Gamma(L)}\int_0^{\frac{\eta}{1+\gamma}} dx\, x^{L-1} e^{-Lx}$$
$$= e^{-\frac{\eta L}{1+\gamma}} \sum_{i=L}^{\infty} \frac{\left(\frac{\eta L}{1+\gamma}\right)^i}{i!}; \; \forall k \tag{B-17}$$

To ensure an acceptable balance between the miss and false alarm error rates, we select an η in the range $(1, 1+\gamma)$. Therefore the terms in the summation of Eq. (B-17) decrease mono-

tonically with i over the range $i \geq L$, suggesting the expansion (similar to Ref. 7):

$$P_M = \frac{1}{L!} e^{-\frac{\eta L}{1+\gamma}} \left(\frac{\eta L}{1+\gamma}\right)^L \left\{1 + \frac{\left(\frac{\eta L}{1+\gamma}\right)}{L+1} + \frac{\left(\frac{\eta L}{1+\gamma}\right)^2}{(L+1)(L+2)} + \cdots\right\}$$

$$< \frac{1}{L!} e^{-\frac{\eta L}{1+\gamma}} \left(\frac{\eta L}{1+\gamma}\right)^L \sum_{i=0}^{\infty} \left[\frac{\eta L}{(1+\gamma)(L+1)}\right]^i$$

$$= \frac{\left[\left(\frac{\eta L}{1+\gamma}\right) e^{-\frac{\eta}{1+\gamma}}\right]^L}{L!\left[1 - \frac{\eta L}{(1+\gamma)(L+1)}\right]} \qquad \text{(B-18)}$$

The upperbound in Eq. (B-18) becomes tight for large values of L, as will be shown later for a similar upperbound to the false alarm probability. Furthermore, $L!$ is bounded by (Ref. 8, p. 257):

$$\sqrt{2\pi L}\,(L/e)^L < L! < \sqrt{2\pi L}\,(L/e)^L\, e^{\frac{1}{12L}} \qquad \text{(B-19)}$$

and the lowerbound on $L!$ (called Stirling's approximation) is also accurate for large L (*e.g.*, within 1% for $L > 8$, and 0.1% for $L > 83$). Combining Eqs. (B-18) and (B-19) yields the useful approximation

$$P_M < \frac{\left[\left(\frac{\eta}{1+\gamma}\right) e^{1-\frac{\eta}{1+\gamma}}\right]^L}{\sqrt{2\pi L}\left[1 - \frac{\eta L}{(1+\gamma)(L+1)}\right]} \qquad \text{(B-20)}$$

The false alarm probability for a given spectral line is similarly expressed as

$$P_{FA} \equiv P_r\,[v_k > \eta \mid \gamma = 0] = e^{-\eta L} \sum_{i=0}^{L-1} \frac{(\eta L)^i}{i!}$$

$$< \sqrt{\frac{L}{2\pi}}\,\frac{\left[\eta e^{-(\eta-1)}\right]^L}{(\eta-1)L+1}\,;\ \forall k \qquad \text{(B-21)}$$

Another common approach to approximating the false alarm rate for large L is based on the central limit theorem (CLT):

$$p(v_k \mid \gamma = 0) \cong \sqrt{\frac{L}{2\pi}}\, e^{-\frac{L(v_k-1)^2}{2}} \qquad \text{(B-22)}$$

$$\Downarrow$$

$$P_{FA} \cong Q\left[(\eta - 1)\sqrt{L}\right] \qquad \text{(B-23)}$$

where

$$Q(\beta) \equiv \frac{1}{\sqrt{2\pi}} \int_{\beta}^{\infty} dx\, e^{-\frac{x^2}{2}} \qquad \text{(B-24)}$$

is the Gaussian error function (Ref. 4, pp. 82-83). Note that $(\eta-1)\sqrt{L}$ is $(\eta-\bar{v}_k)/\sigma_{v_k}$ conditioned on $\gamma = 0$; the larger this parameter is, the further the threshold η is into the tail of $p(v_k|\gamma = 0)$. Since the CLT approximation is only accurate near the mean, Eq. (B-23) is only useful for small $(\eta-1)\sqrt{L}$. Also, since the Gaussian probability distribution tail dies faster than the actual chi-square tail, the CLT false alarm approximation is actually a lowerbound, except for very small values of $(\eta-1)\sqrt{L}$. These comments are reinforced quantitatively in Fig. B-2.

The two false alarm approximations are compared in Fig. B-3. We see that Eq. (B-21) is accurate for $(\eta-1)\sqrt{L} \gtrsim 4$ independent of L itself, while Eq. (B-23) is only valid for $(\eta-1)\sqrt{L} \lesssim 2$ and very large $L \gtrsim 1000$.

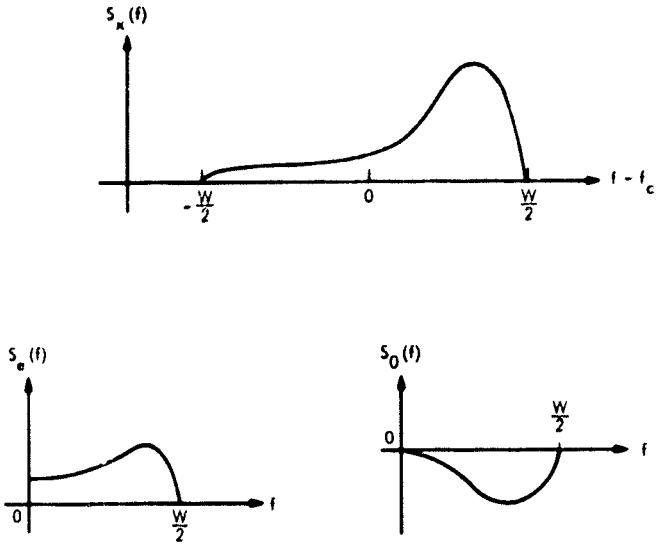

Fig. B-1. One-sided power spectral density $S_x(f)$ of colored bandpass signal $x(t)$. $S_e(f)$ and $S_0(f)$ are the even and odd parts of $S_x(f)$ about $f = 0$, for $0 \leq f \leq W/2$

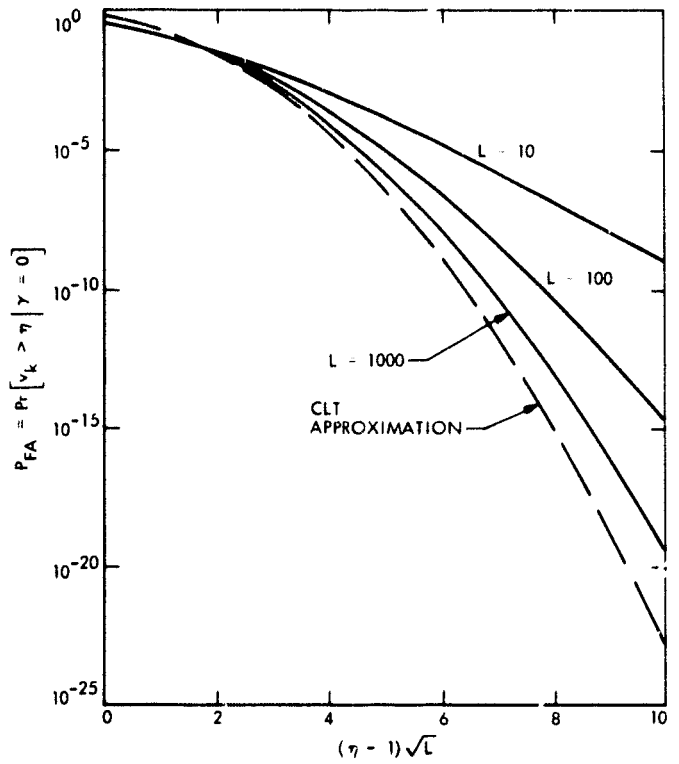

Fig. B-2. Accuracy of central limit theorem (CLT) approximation for false alarm probability P_{FA}, where v_k is a central chi-square random variable with $2L$ degrees of freedom, and $\overline{v_k} = 1$, $\sigma_{v_k} = 1/\sqrt{L}$

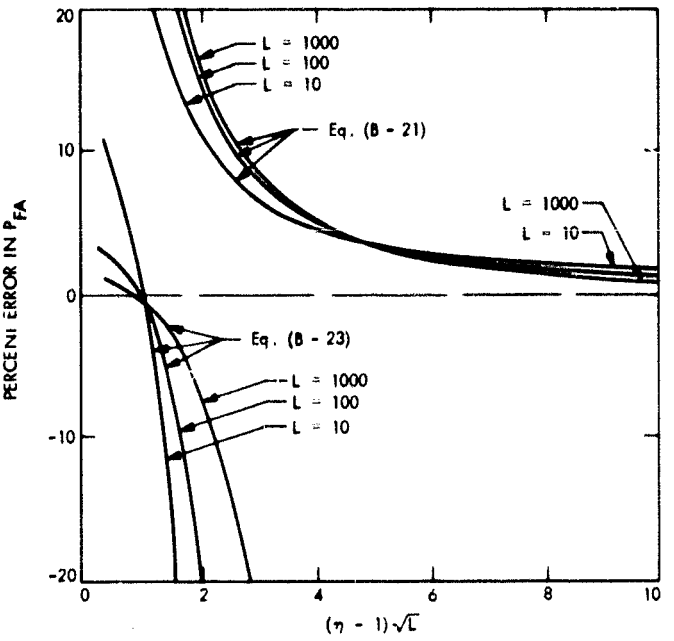

Fig. B-3. Comparison of two false alarm approximations with actual value

Appendix C

DFT Power Spectrum Statistics for Discrete Spectrum Signals

Now let $x(t)$ consist of a sum of M sinusoidal components, with the i^{th} one having power P_i, frequency $f_i \in [f_c - (W/2), f_c + (W/2)]$, and phase θ_i, plus bandpass, white Gaussian noise:

$$x(t) = \sum_{i=1}^{M} \sqrt{2P_i} \sin(2\pi f_i t + \theta_i) + \sqrt{2}\,[n_c(t)\cos 2\pi f_c t + n_s(t)\sin 2\pi f_c t] \tag{C-1}$$

The lowpass noise terms $n_c(t)$ and $n_s(t)$ are independent, zero mean, jointly Gaussian random processes (Ref. 4, Eq. 7.28), each with one-sided power spectral density N_0 over $0 \leq f \leq (W/2)$, and autocorrelation function

$$R_n(\tau) = \frac{N_0 W}{2}\left(\frac{\sin \pi W \tau}{\pi W \tau}\right) \tag{C-2}$$

The lowpass quadrature components of $x(t)$ are (see eq. A-1):

$$y(t) = \sum_{i=1}^{M} \sqrt{P_i} \sin[2\pi(f_i - f_c)t + \theta_i] + n_c(t)$$
$$z(t) = \sum_{i=1}^{M} \sqrt{P_i} \cos[2\pi(f_i - f_c)t + \theta_i] + n_s(t) \tag{C-3}$$

Combining the notation of Eq. (A-4) with the following parameters,

$$n_{cm} \equiv n_c\left(\frac{m}{W}\right) \qquad n_{sm} \equiv n_s\left(\frac{m}{W}\right)$$
$$\Delta_{ik} \equiv \frac{\pi}{W}\left(f_i - f_c - \frac{kW}{N}\right) ; \; |\Delta_{ik}| < \pi$$
$$C_{ik} \equiv \frac{1}{N}\sum_{m=0}^{N-1} \cos(2m\Delta_{ik})$$
$$D_{ik} \equiv \frac{1}{N}\sum_{m=0}^{N-1} \sin(2m\Delta_{ik}) \tag{C-4}$$
$$F_k \equiv \frac{1}{N}\sum_{m=0}^{N-1} (n_{cm} c_{km} - n_{sm} d_{km})$$
$$G_k \equiv \frac{1}{N}\sum_{m=0}^{N-1} (n_{cm} d_{km} + n_{sm} c_{km})$$

Eq. (A-7) reduces to

$$A_k = \sum_{i=1}^{M} \sqrt{P_i}\,(C_{ik}\sin\theta_i + D_{ik}\cos \quad _k$$
$$B_k = \sum_{i=1}^{M} \sqrt{P_i}\,(C_{ik}\cos\theta_i - D_{ik}\sin\theta_i) + G_k \tag{C-5}$$

Consider the random variables F_k and G_k. Since $R_n(m/W) = 0$ for $m \neq 0$, the n_{cm}'s and n_{sm}'s are independent; they are also zero mean, jointly Gaussian random variables, with variance $R_n(0) = N_0 W/2$. Because F_k and G_k are linear combinations of the n_{cm}'s and n_{sm}'s, they are zero mean and jointly Gaussian. Furthermore,

$$\overline{F_k^2} = \frac{1}{N^2}\sum_{m=0}^{N-1}\sum_{n=0}^{N-1} \Big(\overbrace{\overline{n_{cm} n_{cn}}}^{\frac{N_0 W}{2}\delta_{mn}} c_{km} c_{kn} + \overbrace{\overline{n_{sm} n_{sn}}}^{\frac{N_0 W}{2}\delta_{mn}} d_{km} d_{kn} + \overbrace{\overline{n_{cm} n_{sn}}}^{0} c_{km} d_{kn} + \overbrace{\overline{n_{sm} n_{cn}}}^{0} d_{km} c_{kn} \Big)$$
$$= \frac{N_0 W}{2N^2}\sum_{m=0}^{N-1} \overbrace{\left(c_{km}^2 + d_{km}^2\right)}^{1} = \frac{N_0 W}{2N} \tag{C-6}$$

Similarly, we can show that

$$\overline{G_k^2} = \frac{N_0 W}{2N} \qquad \overline{F_k G_k} = 0 \tag{C-7}$$

so that F_k and G_k are independent and identically distributed.

Now conditioned on $\{P_i, f_i, \theta_i\}$, A_k and B_k are independent, jointly Gaussian random variables, with identical variances, but different, nonzero means in general. Therefore, the power spectral component S_k of Eq. (A-9) is conditionally a *noncentral* chi-square random variable with 2 degrees of freedom, and conditional mean

$$\overline{S_k}^{F_k, G_k} = \mu_k + \frac{N_0 W}{N} \tag{C-8}$$

where

$$\mu_k = \sum_{i=1}^{M} \sum_{j=1}^{M} \sqrt{P_i P_j} \left[(C_{ik} C_{jk} + D_{ik} D_{jk}) \cos(\theta_i - \theta_j) \right.$$

$$\left. + (C_{ik} D_{jk} - D_{ik} C_{jk}) \sin(\theta_i - \theta_j) \right] \tag{C-9}$$

Generally, the P_i's and f_i's are fixed but unknown parameters to be resolved by the spectrum analyzer. However, the θ_i's depend on the observation period, and can be regarded as independent, uniformly distributed random variables. So, while the mean spectral line power conditioned on $\{\theta_i\}$ contains cross terms (i.e., $i \neq j$ in Eq. C-9), the unconditional mean does not:

$$\overline{S_k}^{F_k, G_k, \{\theta_i\}} = \zeta_k + \frac{N_0 W}{N} \tag{C-10}$$

where

$$\zeta_k \equiv \overline{\mu_k}^{\{\phi_i\}}$$

$$= \sum_{i=1}^{M} \sum_{j=1}^{M} \sqrt{P_i P_j} \left[(C_{ik} C_{jk} + D_{ik} D_{ik}) \overbrace{\cos(\theta_i - \theta_j)}^{\delta_{ij}} \right.$$

$$\left. + (C_{ik} D_{jk} - D_{ik} C_{jk}) \overbrace{\sin(\theta_i - \theta_j)}^{0} \right]$$

$$= \sum_{i=1}^{M} P_i \left(C_{ik}^2 + D_{ik}^2 \right) = \sum_{i=1}^{M} P_i \left(\frac{\sin N\Delta_{ik}}{N \sin \Delta_{ik}} \right)^2 \tag{C-11}$$

The last step in Eq. (C-11) follows from the series identities (Ref. 6, p. 30)

$$C_{ik} = \frac{\sin N\Delta_{ik} \cos(N-1)\Delta_{ik}}{N \sin \Delta_{ik}}$$

$$D_{ik} = \frac{\sin N\Delta_{ik} \sin(N-1)\Delta_{ik}}{N \sin \Delta_{ik}} \tag{C-12}$$

We also note that the unconditional probability density function of S_k has the form (Ref. 5)

$$p(S_k) = \frac{N}{N_0 W} e^{-\frac{N S_k}{N_0 W}} e^{-\frac{N \mu_k}{N_0 W}} I_0 \left(\frac{2N}{N_0 W} \sqrt{S_k \mu_k} \right)^{\{\theta_i\}} \tag{C-13}$$

which, in general, does not simplify to a noncentral chi-square distribution for $M > 1$.

As in Appendix B, we now extend our results to an L-look spectrum in which the k^{th} spectral component S_k^* is the average of L independent observations of S_k. Furthermore, we again use Eq. (B-13) to form the normalized discrete spectrum $\{\nu_k\}$. Let the phase of the i^{th} sinusoidal input component for the l^{th} look be denoted by θ_{il}. Conditioned on $\{\theta_{il}\}$, ν_k is a noncentral chi-square random variable with $2L$ degrees of freedom: its conditional probability density function (Ref. 5) and mean can be expressed as

$$p(\nu_k \mid \{\phi_{il}\}) = L \left(\frac{\nu_k}{\lambda_k} \right)^{\frac{L-1}{2}} e^{-L(\nu_k + \lambda_k)} I_{L-1}(2L\sqrt{\nu_k \lambda_k})$$

$$\overline{\nu_k}^{\{\theta_{il}\}} = \lambda_k + 1 \tag{C-14}$$

where

$$\lambda_k \equiv \frac{N}{N_0 W} \sum_{i=1}^{M} \sum_{j=1}^{M} \sqrt{P_i P_j} \left[(C_{ik} C_{jk} + D_{ik} D_{jk}) \alpha_{ij} \right.$$

$$\left. + (C_{ik} D_{jk} - D_{ik} C_{jk}) \beta_{ij} \right] \tag{C-15}$$

and

$$\alpha_{ij} \equiv \frac{1}{L} \sum_{l=1}^{L} \cos(\theta_{il} - \theta_{jl})$$

$$\beta_{ij} \equiv \frac{1}{L} \sum_{l=1}^{L} \sin(\theta_{il} - \theta_{jl}) \qquad \text{(C-16)}$$

Since the θ_{il}'s are independent and uniformly distributed, for large L, we can approximate Eq. (C-16) by $\alpha_{ij} \cong \delta_{ij}$ and $\beta_{ij} \cong 0$: then

$$\lambda_k \cong \frac{N}{N_o W} \zeta_k = \sum_{i=1}^{M} \left(\frac{P_i N}{N_o W} \right) \left(\frac{\sin N\Delta_{ik}}{N \sin \Delta_{ik}} \right)^2 \qquad \text{(C-17)}$$

and we can essentially remove the conditioning restriction in Eq. (C-14). (Note that all of these approximations become exact for the special case $M = 1$.)

If a threshold detection approach is used, as in Appendix B, the false alarm probability is again given by Eq. (B-21). The probability of a miss on the k^{th} line must be computed by numerical integration techniques:

$$P_{M,k} \equiv Pr\,[v_k < \eta]$$

$$\cong \frac{L\, e^{-L\lambda_k}}{\lambda_k^{\frac{L-1}{2}}} \int_0^{\eta} dx\, x^{\frac{L-1}{2}} e^{-Lx} I_{L-1}(2L\sqrt{\lambda_k x}) \qquad \text{(C-18)}$$

For large L, the Bessel function can be accurately approximated by its asymptotic formula (Ref. 8, p. 378), simplifying the task of numerically evaluating Eq. (C-18):

$$P_{M,k} \cong \int_0^{\eta} dx\, e^{g_k(x)} \qquad \text{(C-19)}$$

where

$$g_k(x) \equiv \ln L - \frac{1}{2} \ln\left[2\pi (L-1)\, a_k(x)\right]$$

$$+ \left(\frac{L-1}{2}\right) \ln\left(\frac{x}{\lambda_k}\right) + (L-1)\, b_k(x) - L(x + \lambda_k)$$

$$a_k(x) \equiv \sqrt{1 + \left(\frac{2L}{L-1}\right)^2 \lambda_k x}$$

$$b_k(x) \equiv a_k(x) + \ln\left[\left(\frac{2L}{L-1}\right) \frac{\sqrt{\lambda_k x}}{1 + a_k(x)}\right] \qquad \text{(C-20)}$$

and λ_k is given by Eq. (C-17) in terms of the P_i's and f_i's (but independent of the θ_i's).

Appendix D

Aliasing Effects in DFT Power Spectrum

In Eq. (A-5), an integral over an infinite time interval is approximated by a finite sum of N samples of the integrand spaced $T/N = 1/W$ seconds apart. Although the spacing of the samples satisfies the Nyquist rate condition for the infinite-duration integrand (one-sided bandwidth $W/2$), the finite-time integrand has a larger bandwidth and requires a correspondingly higher sampling rate. Consequently, the DFT power spectrum typically exhibits frequency foldover and spectral spreading effects known as "aliasing."

To examine this effect more closely, consider a special case of Appendix C in which the input signal $x(t)$ is a single sinusoid with power P and frequency f_s, and neglect the additive noise. The one-sided power spectral density $S_x(f)$ consists of a single impulse of weight P at $f = f_s$, as shown in Fig. D-1a. Using the results in Appendix C with $M = 1$ and $N_0 = 0$, the DFT spectrum has envelope

$$E(f) = P\left[\frac{\sin\frac{N\pi}{W}(f - f_s)}{N\sin\frac{\pi}{W}(f - f_s)}\right]^2$$

$$\approx P\left[\frac{\sin\frac{N\pi}{W}(f - f_s)}{\frac{N\pi}{W}(f - f_s)}\right]^2 ; |f - f_s| << \frac{W}{2} \qquad \text{(D-1)}$$

and the k^{th} spectral line is simply

$$S_k = E\left(f_c + \frac{kW}{N}\right) \qquad \text{(D-2)}$$

The spectral spreading of the form $(\sin af/af)^2$ in Eq. (D-1) is a consequence of the flat T-second observation "window." Other windows can be used to reduce this effect (e.g., Ref. 2,3). Also, since $E(f)$ has period W, there is some foldover in the DFT spectrum when $|f_s - f_c|$ is near $W/2$. These aliasing effects are illustrated in Figs. D-1b and D-1c.

A special case is when $f_s - f_c$ is precisely equal to kW/N for some k, say $k = k_0$. Then Eqs. (D-1) and (D-2) yield

$$S_k = P\left[\frac{\sin\pi(k - k_0)}{N\sin\frac{\pi}{N}(k - k_0)}\right]^2 = P\,\delta_{kk_0} \qquad \text{(D-3)}$$

as illustrated in Fig. D-1d. So in this case only, the DFT spectrum looks like the actual spectrum of Fig. D-1a.

Note that for any choice of f_s, the total power in all of the DFT spectral lines is exactly P. Defining $\beta \equiv (\pi/W)(f_c - f_s)$, Eqs. (D-1) and (D-2) reduce to

$$S_k = P\left[\frac{\sin(N\beta + k\pi)}{N\sin\left(\beta + \frac{k\pi}{N}\right)}\right]^2 \qquad \text{(D-4)}$$

from which it follows that

$$\sum_{k=-\frac{N}{2}}^{\frac{N}{2}-1} S_k = \frac{P}{N^2}\sin^2 N\beta \underbrace{\sum_{k=\frac{N}{2}}^{\frac{N}{2}-1} \sin^{-2}\left(\beta + \frac{k\pi}{N}\right)}_{\frac{N^2}{\sin^2 N\beta}\ \text{(Ref. 9)}} = P \qquad \text{(D-5)}$$

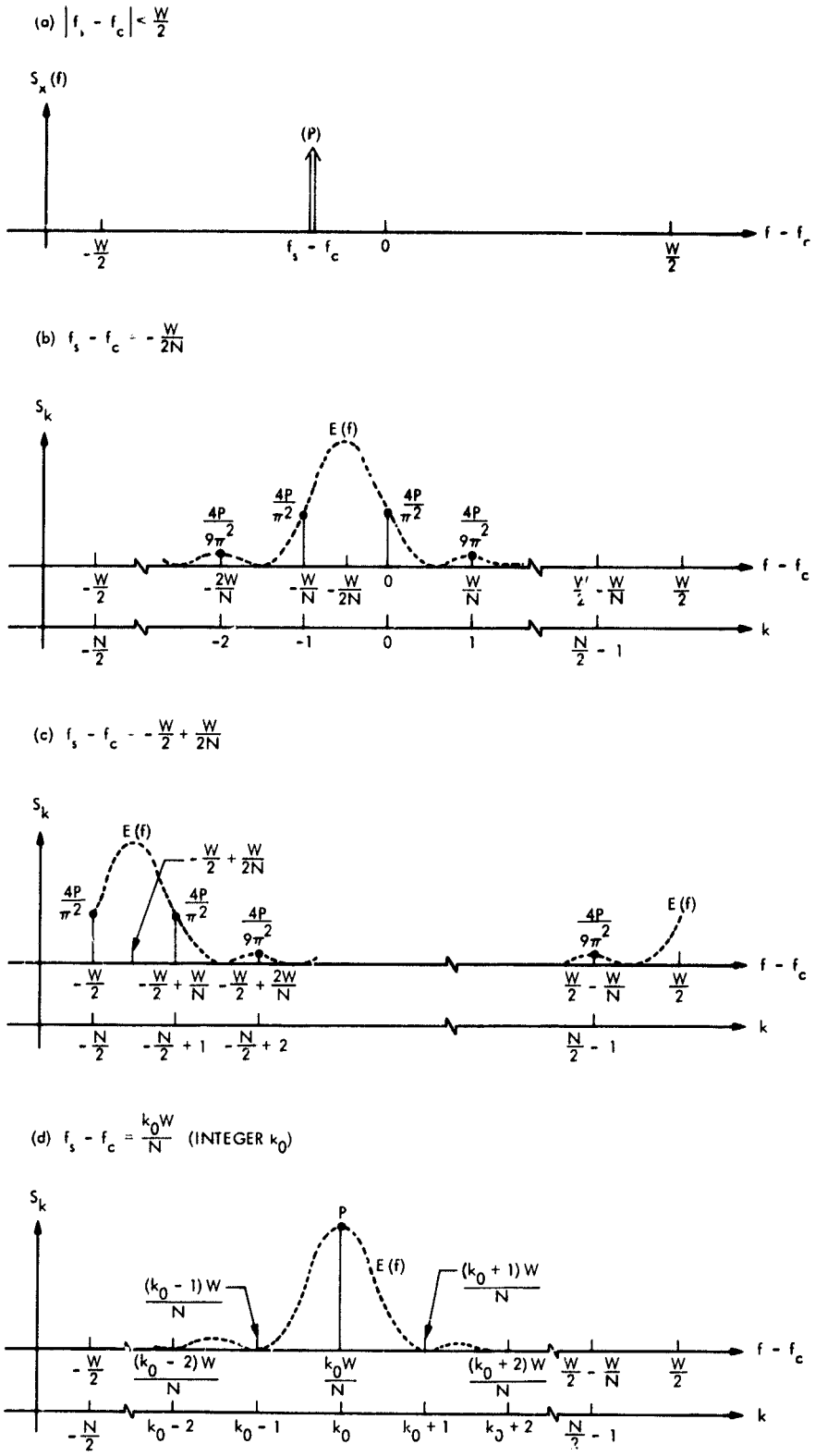

Fig. D-1. Comparison of one-sided power spectral density $S_x(f)$ of sinusoidal carrier with power P at frequency f_s and DFT spectral lines $\{S_k\}$ at frequencies kW/N

References

1. Levitt, B. K., "Radio Frequency Interference from Near-Earth Satellites," in *The Deep Space Network Progress Report 42-37*, Jet Propulsion Laboratory, Pasadena, Calif., Feb. 15, 1977.

2. Oppenheim, A. V., and Schafer, R. W., *Digital Signal Processing*, Prentice-Hall, Englewood Cliffs, New Jersey, pp. 549-553, 1975.

3. Welch, P. D., "The Use of Fast Fourier Transform for the Estimation of Power Spectra: A Method Based on Time Averaging over Short, Modified Periodograms," *IEEE Trans. Audio Electroacoust.*, Vol. AU-15, pp. 70-73, June 1967.

4. Wozencraft, J. M., and Jacobs, I. M., *Principles of Communication Engineering*, John Wiley, New York, New York, 1965.

5. Miller, K. S., *Multidimensional Gaussian Distributions*, John Wiley, New York, New York, p. 56, 1964.

6. Gradshteyn, I. S., and Ryzhik, I. M., *Table of Integrals, Series, and Products*, Academic Press, New York, New York, 1965.

7. Van Trees, H. L., *Detection, Estimation, and Modulation Theory, Part I*, John Wiley, New York, New York, p. 110, 1968.

8. *Handbook of Mathematical Functions*, U.S. Govt. Printing Office, M. Abramowitz and I. A. Stegun, ed., Washington, D.C., 1964.

9. Jolley, L. B. W., *Summation of Series*, Dover Publications, New York, New York, pp. 92-93, 1961.

A Markov Model for X-Band Atmospheric Antenna-Noise Temperatures

O. H. Adeyemi
Communications Systems Research Section

A five-state Markov model is suggested for the X-band antenna-noise temperatures based on data collected at Goldstone. The states of the model are determined by changes in the "cloud and rain" condition of the atmosphere so as to take advantage of the correlation observed between the antenna temperatures and changes in rain rates. Then an indication is given of how to obtain the estimates of the parameters of the model from the data.

I. Introduction

This report documents the progress made thus far in constructing a stochastic model for the X-band antenna-noise temperatures using data collected at Goldstone. The model suggested here is a finite-state Markov model (see Ref. 1 for a method of reproducing the data if the temperature increases follow a half-gaussian law).

Figure 1 shows the normalized X-band antenna-noise temperatures and rain rates during a tropical storm in September 1976 (days 253 through 255). This segment of the data is chosen to illustrate the rationale for the model because it is typical of the high temperature fluctuations observed during such a "cloud and rain" condition of the atmosphere. Under such a cloudy and high rain-rate condition, the DSN X-band receiver temperature can be as high as 150 K. Since the DSN receivers are operated at varying elevation angles, these temperature readings are all standardized to the zenith. For example, a temperature reading of 140 K at 30 deg elevation angle is recorded in Fig. 1 as 70 K at the zenith, the same reading at 60 deg elevation would be recorded as 121 K at the zenith.

Now because of the variation of the antenna-noise temperature with the "cloud and rain" conditions of the atmosphere, the states of the model are allowed to be determined by changes in the water content of the air (in vapor and liquid form). Thus the following are taken to represent the states of the model:

(1) Clear sky with water vapor only, no clouds.

(2) Clouds gathering – dense clouds with no rain.

(3) Dense clouds with light rain.

(4) Dense clouds with medium rain.

(5) Dense clouds with heavy rain.

The diagram of the model suggested is shown in Fig. 2.

The model is described in Section II where the proportion of the time the process spends in each of the states is also given. An indication is given of how to obtain the estimates of the parameters of the model from the data.

II. The Markov Model

Let us designate as base temperature the minimum antenna temperature (in Kelvins) recorded throughout the experiment. Thus in the following, 0 K will refer to the base temperature and 1 K is equivalent to 1 K above the base temperature.

Referring to Fig. 1, let us represent by:

(1) Clear state S_c: water vapor only, no clouds; temperature range 0 to 1 K.

(2) State S_0: clouds gather – dense clouds, no rain; temperature range 1 to 4 K.

(3) State S_1: dense clouds with light rain (0 to 1 mm/h); temperature range 4 to 16 K.

(4) State S_2: dense clouds with medium rain (1 to 5 mm/h); temperature range 16 to 40 K.

(5) State S_3: dense clouds with heavy rain (5 to 10 mm/h); temperature range >40 K.

The diagram of the transitions between these states is shown in Fig. 2.

In the diagram the direction of the arrows between any pair of states denotes the direction of the transitions between them. Let us write the transition matrix of the process as:

$$M = \begin{array}{c} \\ S_c \\ S_0 \\ S_1 \\ S_2 \\ S_3 \end{array} \begin{array}{c} \begin{array}{ccccc} S_c & S_0 & S_1 & S_2 & S_3 \end{array} \\ \begin{pmatrix} q_{cc} & q_{co} & 0 & 0 & 0 \\ q_{0c} & q_{00} & q_{01} & q_{02} & q_{03} \\ 0 & q_{10} & q_{11} & q_{12} & q_{13} \\ 0 & q_{20} & q_{21} & q_{22} & q_{23} \\ 0 & q_{30} & q_{31} & q_{32} & q_{33} \end{pmatrix} \end{array}$$

where we have represented the probability of transition from S_i to S_j by q_{ij}, *i.e.*, $P(S_j|S_i) = q_{ij}$, $ij = c, 0, 1, 2, 3$. Transitions between every pair of states are allowed except between the clear state S_c and each of S_1, S_2, S_3. This is because it is assumed that the atmospheric condition cannot go from clear sky to "dense clouds and rain" in a single step without first passing through "clouds gathering – dense clouds, no rain". Also after each rainfall, clouds linger on (state S_0) for some time before the atmosphere becomes clear (S_c).

Now let

$$p_1 = 1 - q_{00} - \frac{q_{0c}q_{cc}}{1 - q_{cc}} - \frac{q_{10}q_{01}}{1 - q_{11}}$$

$$p_2 = q_{23} + \frac{q_{13}(1 - q_{22})}{q_{12}}$$

$$p_3 = q_{30} + \frac{q_{10}q_{31}}{1 - q_{11}}$$

$$p_4 = q_{20} + \frac{q_{10}q_{21}}{1 - q_{11}}$$

$$C_1 = \frac{q_{01} + q_{21}C_2 + q_{31}C_3}{1 - q_{11}}$$

where

$$C_2 = \frac{p_3C_3 - p_1}{p_4}$$

$$C_3 = \frac{p_1p_2 + p_4\left(q_{03} - \dfrac{q_{02}q_{13}}{q_{12}}\right)}{p_2p_3 + p_4\left[1 - q_{33} + \dfrac{q_{13}q_{32}}{q_{12}}\right]}$$

Then the proportion of times spent in states S_c, S_0, S_1, S_2, S_3 (the stationary distribution) is given by u_c, u_0, u_1, u_2, u_3 where

$$u_0 = \left[1 + C_1 + C_2 + C_3 + \frac{q_{0c}}{1 - q_{cc}}\right]^{-1}$$

$$u_c = \frac{q_{0c}}{1 - q_{cc}}u_0$$

$$u_1 = C_1u_0$$

$$u_2 = C_2u_0$$

$$u_3 = C_3U_0$$

Further, let the sequence of the temperature readings be represented by $\{y_n\}$. Let N_{ij} = the number of times y_n is in state i and y_{n+1} is in state j. Then we can estimate the transition probability q_{ij} by:

$$q_{ij} = \frac{N_{ij}}{\sum_j N_{ij}}$$

III. Conclusion

As constructed, the states of this model represent the main features of the antenna-noise temperature increases shown in Fig. 1. It may however become necessary to modify the number of states when the model is fitted to the data and the appropriate goodness-of-fit test is performed. The results of that phase of the work will be reported in the future.

Reference

1. E. C. Posner and F. J. Ziegler. "A Technique for Generating Correlated X-Band Weather Degradation Statistics," in *The Deep Space Network Progress Report 42-35*, pp. 180-195, Jet Propulsion Laboratory, Pasadena, Calif., October 15, 1976.

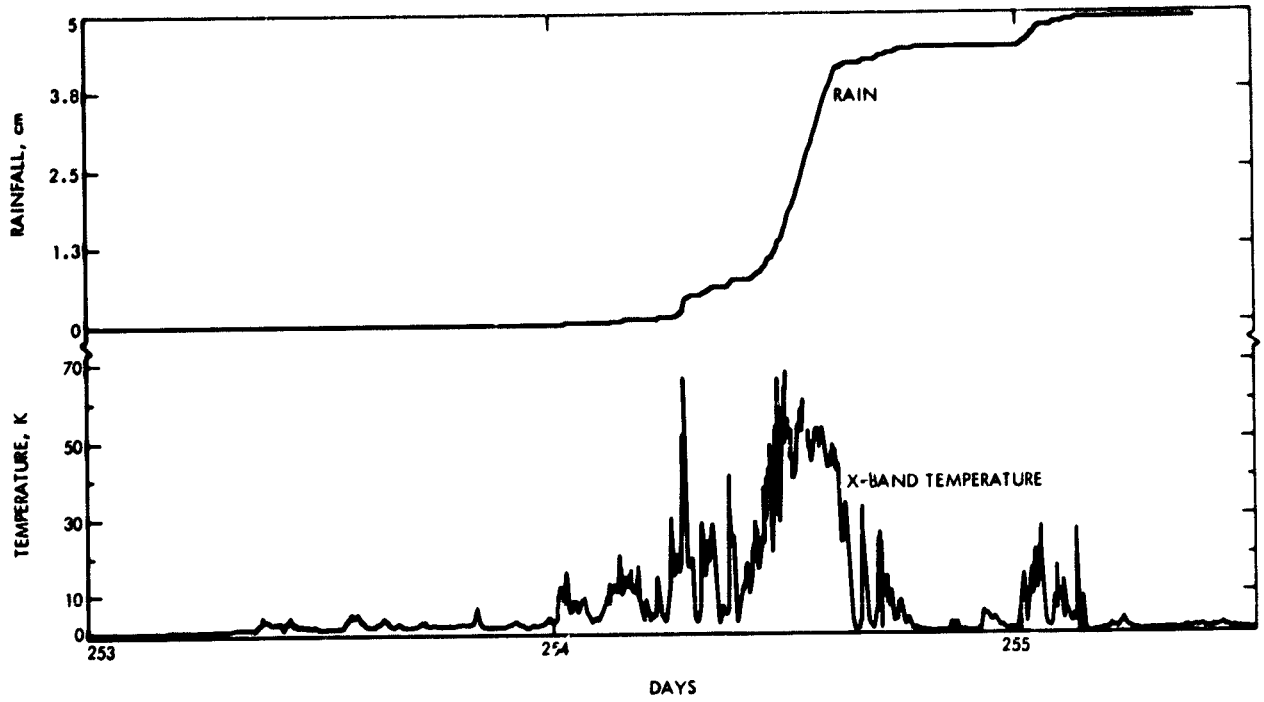

Fig. 1. Rainfall and X-band zenith noise temperatures during tropical storm (Sept. 1976)

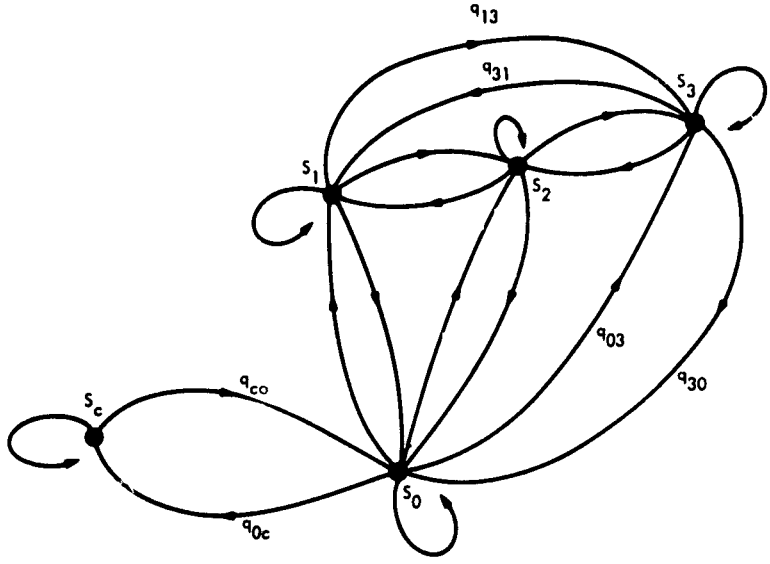

Fig. 2. Transition diagram of the Markov model

Synchronization Strategies for RFI Channels

R. J. McEliece
Communications Systems Research Section

H. van Tilborg
California Institute of Technology

S. Tung
Cornell University

In this article we define an RFI channel to be a multiple-access channel in which no sender can know when any other starts, and study the problem of determining the relative phases of the senders at the receiver. Along the way we prove a new result about binary deBruijn sequences.

I. Introduction

As the electromagnetic spectrum becomes increasingly crowded, it becomes more and more important to study the possibilities of cooperation between individuals who must share the same channel. In the information-theory literature, there is a class of channel models designed for such studies called *multiple-access* channels. Unfortunately, a basic assumption about these channels is that all senders begin transmission simultaneously. Recently (Ref. 2) we have begun to study multiple-access channels without making this assumption; we call these channels RFI (radio frequency interference) channels. We now describe the simplest kind of RFI channel, the two-input, one-output, discrete memoryless RFI channel.

Such a channel has two inputs $x^{(1)} \in A_1$, $x^{(2)} \in A_2$, and one output $y \in B$, where A_1, A_2, and B are finite sets. The transition probability $p(y|x^{(1)}, x^{(2)})$ represents the probability that y will be the output, given that $x^{(1)}$ and $x^{(2)}$ are the two inputs. Figure 1 gives the appropriate block diagram. The sources are assumed independent. Note that since the channel has only one output, there is no loss in generality in assuming a single decoder, although there may actually be two receivers located in physically different places.

We assume that the two senders may agree ahead of time on the strategies they will use, but that neither can know when the other will begin transmission. In Ref. 2 we assumed that the receiver can always determine when each sender begins transmission either by a separate synch channel or by the design of suitable synchronization prefixes. In this paper we shall study the second method of obtaining joint synchronization.

II. An Example

Consider the two-input, one-output RFI channel described in Table 1. The two inputs are labeled X_1 and X_2, and the corresponding output, Y. Notice that if $X_1 = X_2$, then $Y = X_1 = X_2$; but if $X_1 \neq X_2$, the output Y is the special erasure symbol "?". It can be shown that the capacity region of this channel is given by Fig. 2. This means that for any pair of rates (R_1, R_2) lying in the shaded region of Fig. 2, and any $\epsilon > 0$, there exists a coded communication scheme for the channel such that sender No. 1 has rate $> R_1 - \epsilon$, sender No. 2 has rate $> R_2 - \epsilon$, and the overall error probability is less than ϵ. And while it is *not* necessary to assume the two senders begin transmission simultaneously, it is necessary to assume that the receiver can determine the relative phases of the two senders, in order to prove the theorem. This section will describe a simple and generalizable technique for establishing synchronization at the receiver for this channel.

We assume sender No. 1 begins his transmission with the prefix P_1, and sender No. 2 begins with P_2, where

$$P_1 = 1\,1\,0\,0\,1\,0\,1\,1\,1\,1\,0\,1\,0\,0\,0\,0$$

$$P_2 = 1\,0\,1\,1\,0\,1\,0\,0\,1\,1\,1\,1\,0\,0\,0\,0$$

We further assume that after he sends P_1, sender No. 1 sends his information in blocks of 11 bits followed by 4-bit blocks of zeros called *windows*; ditto for No. 2. The overall transmission strategies are depicted in Fig. 3. We shall now show that if these strategies are used, then the receiver will be able to synchronize with both senders on the basis of the received sequence.

First we assume that the two senders begin transmission nearly simultaneously, say within three bits times of each other. Then the receiver will be able to synchronize with both senders on the basis of the first three received symbols, for there are only five possibilities and they all yield different initial received sequences:

P_1	110···	110···	110···	11···	1···
P_2	1···	10···	101···	101···	101···
Received	???···	?10···	1??···	??1···	?01···

(We assume that when the channel is not in use, zeros are being transmitted; by "the first three received symbols" we mean beginning with the first nonzero one.) Hence if the first three symbols are in the set {???, ?10, 1??, ??1, ?01}, synchronization is immediately established. The only other possibilities for the first three symbols are ??0, signifying that No. 1 has begun transmission, but giving no information about No. 2, or ?0?, signifying that No. 2 has begun, but giving no information about No. 1. In either of these two cases, it is more difficult but still possible to establish synchronization with the remaining sender.

Let us suppose that the first three symbols received are ??0. Synchronization with No. 1 is now established, but nothing is known about No. 2. The idea is to look through the 4-bit "windows" in No. 1's transmitted stream in order to locate No. 2. For a while, perhaps, these windows will be blank, indicating that No. 2 still has not begun transmission. But when the 16-bit prefix is finally sent, a 4-bit substring of it will appear through the window. And the prefix P_2 is a *deBruijn sequence*, which means that each of its 16 4-bit substrings taken cyclically are distinct; thus the first nonzero window will enable the receiver to synchronize with No. 2.

For example, suppose the first nonzero 4-bit window in the received stream is 000?. This must correspond to the substring 0001 of P_2, and means that No. 2 began its transmission right at the end of the window. Similarly if ??0? is received, the substring is 1101; in which case No. 2 began transmission two bits prior to the windows.

If sender No. 2 began transmission first, the procedure is the same, because the prefix P_1 is also a deBruijn sequence. Thus we have shown that joint synchronization can be established in every case. In the next section we will show that this strategy can be generalized.

III. The Generalization

In this section we will generalize only to binary, two-input, noiseless RFI channels, leaving further generalizations to a later paper. Up to obvious equivalence there are only five nontrivial such channels (Ref. 2), as given in Table 2. In the notation of Table 2, the channel discussed in Section II is channel C.

There are two problems to be solved in generalizing the approach of Section II. First, we must design the initial portion of the prefixes so that nearly simultaneous starts can be detected; and second, we must show that these initial portions can be extended to deBruijn sequences.

By trial and error we have found such pre-prefixes for each of the five channels in Table 2, as given in Table 3. The reader is invited to verify for himself that each pair of pre-prefixes has the property that if the senders start nearly simultaneously, in the sense that their pre-prefixes overlap, then joint

synchronization can be established on the basis of the first few received symbols.

The general strategy will be to extend a pre-prefix of length n to a deBruijn sequence of length $N = 2^m$ ending in $m + 1$ zeros, and then to insert windows of length $m + 1$ between data blocks of length $2^m - m - 1$. The analysis of Section II can then be extended to show that joint synchronization can be established. However, it is not obvious that an arbitrary string of length n can be extended to such a deBruijn sequence. In the next section we will show that any binary string of length n can be extended to a deBruijn sequence of length 2^m which ends with m zeros, provided only that $m \geq n + 1$. Since the "overhead" imposed on the transmission scheme by the inclusion of the windows is $(m + 1)/(2^m - 1)$, this result shows that the decrease in data rate required to establish joint synchronization can be made arbitrarily small.

IV. A Result about deBruijn Sequences

A *deBruijn sequence* of length 2^m is a sequence of 2^m 0s and 1s, such that when the sequence is viewed cyclically, each of the 2^m substrings of length m are distinct. These sequences exist for all values of $m \geq 1$; we list a few short ones below:

m	one deBruijn sequence of length m
1	0 1
2	0 0 1 1
3	0 0 0 1 0 1 1 1
4	0 0 0 0 1 0 0 1 1 0 1 0 1 1 1 1

There is a useful graphical description of deBruijn sequences which we now give.

Let G_m be the directed graph whose vertices are the 2^{m-1} binary strings of length $m - 1$. In G_m there is a directed edge going from $\mathbf{v} = v_1 v_2 \cdots v_{m-1}$ to $\mathbf{v}' = v'_1 v'_2 \cdots v'_{m-1}$ iff there is a binary string $\mathbf{e} = e_0 e_1 \cdots e_{m-1}$ of length m such that $\mathbf{v} = e_0 e_1 \cdots e_{m-2}$, $\mathbf{v}' = e_1 e_2 \cdots e_{m-1}$. This means that the edge set of G_m can be identified with the set of binary strings of length m. The graph G_3 is illustrated in Fig. 4. Any binary string $\mathbf{s} = s_1 s_2 \cdots s_M$ of length $M \geq m$ can be viewed as a closed path (circuit) of length M in G_m, viz. the path passing successively through the edges $(s_1 s_2 \cdots s_M)$, $(s_2 \cdots s_{m+1})$, $\cdots$, $(s_M \, s_{m+1} \cdots s_M)$, $(s_{M-m+2} \cdots s_M s_1)$, $\cdots$, $(s_M s_1 \cdots s_{m-1})$. In particular, $\mathbf{s}$ is a deBruijn sequence if $M = 2^m$ and the corresponding circuit uses each edge of G_m exactly once. A circuit in a graph using each edge exactly once is called an *Euler circuit*; thus there is a one-to-one correspondence between cyclically distinct deBruijn sequences and Euler paths in G_m.

The theorem we wish to prove in this section is that given any binary string $\mathbf{s}$ of length $m - 1$ (or less) beginning with a 1, there exists a deBruijn sequence of length 2^m, beginning with $\mathbf{s}$, and ending with a string of m zeros. Alternatively, since a deBruijn sequence is viewed cyclically, our assertion is that, given any such $\mathbf{s}$, there is a deBruijn sequence beginning with $0^m\mathbf{s}$. In terms of the graph G_m, our result is as follows.

Theorem: Any path $P = [\mathbf{v}_0, \mathbf{v}_1, \cdots, \mathbf{v}_{m-1}]$ of length $m - 1$ in G_m, with $\mathbf{v}_0 = (00 \cdots 0)$ and $\mathbf{v}_1 = (00 \cdots 01)$, can be completed to an Euler circuit in G_m.

Proof: Let $\mathbf{E}$ be the binary string of length $2m - 2$ obtained by concatenating $\mathbf{v}_0$ with $\mathbf{v}_{m-1}$. Then the vertices in the path P are the m substrings of $\mathbf{E}$ of length $m - 1$, and the edges of P are the $m - 1$ substrings of $\mathbf{E}$ of length m. $\mathbf{E}$ will have the general form illustrated in Eq. (1) for $m = 6$.

$$\begin{array}{c} \leftarrow m-1\rightarrow \; \leftarrow m-1\rightarrow \\ \mathbf{E} = (0\ 0\ 0\ 0\ 0\ 1\ x\ x\ x\ x) \end{array} \qquad (1)$$

From Eq. (1) it is clear that the m vertices and the $m - 1$ edges in P are all distinct. We now form a new graph G'_m by removing the $m - 1$ edges of P from G_m and replacing them with a new edge $\mathbf{e}'$ which joins $\mathbf{v}_0$ to $\mathbf{v}_{m-1}$ directly. This construction is illustrated in Fig. 5 with $m = 4$, $P = \{(000), (001), (011), (110)\}$.

The graph G'_m is clearly *balanced*, i.e. every vertex has the same number of edges going in as coming out. (This number is two except for the vertices $\mathbf{v}_1, \cdots, \mathbf{v}_{m-2}$; for these vertices it is 1.)

The graph G'_m is also *connected*. To see this, observe that for any vertex $\mathbf{v}$ in G'_m, there is always a path of length $m - 1$ from $\mathbf{w} = (111 \cdots 1)$ to $\mathbf{v}$, where edges are the $m - 1$ substrings of the string $\mathbf{F}$ formed by concatenating $\mathbf{w}$ and $\mathbf{v}$. For example in Fig. 3 if $\mathbf{v} = 101$, $\mathbf{F} = 111101$, and the path is (111), (111), (110), (101). Note that these edges are *not* among those deleted in the construction of G'_m, since the first bit in each edge is 1, whereas the first bit in each deleted edge is 0.

Since G'_m is balanced and connected, by a theorem of I. J. Good (see Ref. 1, Sec. 2.3.4.2, for example) G'_m possesses an Euler circuit, which must perforce contain the dummy edge $\mathbf{e}'$. In Fig. 3 such a path is (110), (100), (001), (010), (101), (011), (111), (111), (110), (101), (010), (100), (000), (000),

(110), the last edge corresponding to the dummy edge e'. If now we replace the dummy edge e' with the original path P in G_m, the result is an Euler circuit in G_m, which has the desired property. For example, the path so constructed in Fig. 3 is 000110010111010, which yields the prefix P_1 = 1100101111010000 of Section II. QED.

References

1. Knuth, D. E. *The Art of Computer Programming. Vol. I, Fundamental Algorithms*. Addison-Wesley, Reading, Mass., 1968.

2. McEliece, R. J. and Rubin, A. L. "Timesharing without Synchronization," in the *Proceedings of the 1976 International Telemetering Conference*, McGregory Werner, Los Angeles, 1976.

Table 1. A simple RFI channel

X_1	X_2	Y
0	0	0
0	1	?
1	0	?
1	1	1

Table 2. The five binary, two input, noiseless RFI channels

		Y				
X_1	X_2	A	B	C	D	E
0	0	0	0	0	0	0
0	1	1	1	2	1	1
1	0	2	2	2	1	1
1	1	3	2	1	0	1

Table 3. Pairs of pre-prefixes for establishing synchronization for nearly simultaneous starts

Channel	Pre-prefix 1	Pre-prefix 2
A	1	1
B	1000	1011
C	110	101
D	11011	10101
E	100011000	111000000

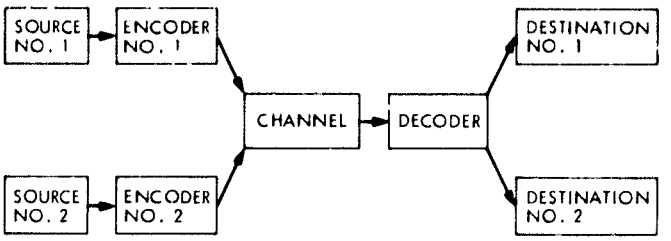

Fig. 1. An RFI channel

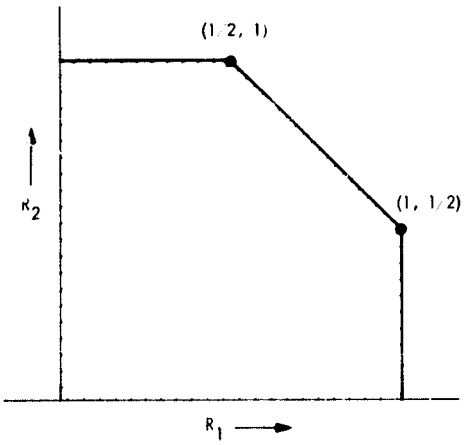

Fig. 2. The capacity region of the RFI channel described in Table 1

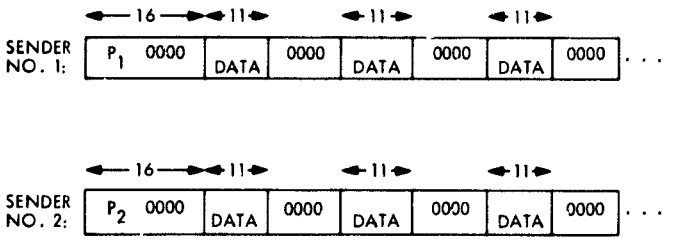

Fig. 3. The transmission strategies

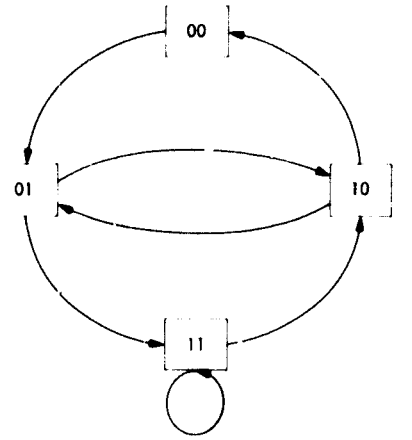

Fig. 4. The graph G_3

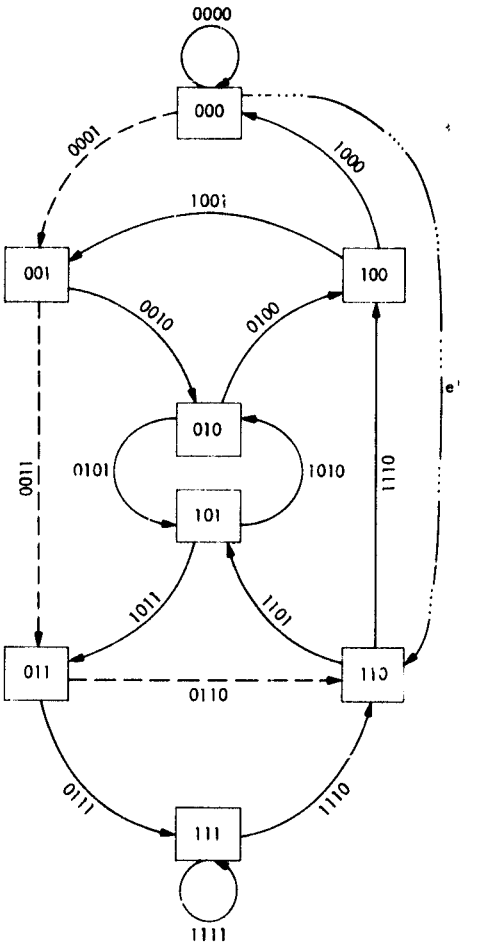

Fig. 5. The graph G'_m, with $m = 4$

A Maintenance and Operations Cost Model for the DSN

R. W. Burt
Radio Frequency and Microwave Subsystems Section

H. L. Kirkbride
Communications Systems Research Section

A cost model for the DSN is developed which is useful in analyzing the 10-year Life Cycle Cost of the Bent Pipe Project. The philosophy behind the development and the use made of a computer data base are detailed; the applicability of this model to other projects is discussed.

I. Introduction

The term "Bent Pipe" is used to describe the concept of employing high-capacity satellite and terrestrial microwave communications links to relay data streams, which now are visible only to pieces of equipment fixed at the DSN stations, between simplified antenna station installations remaining at the existing sites, and a data processing and control center where equipment from the remote stations has been relocated. It is anticipated that the increased use of satellite relay links will permit the removal and relocation of a sufficient amount of equipment from the stations to allow a reduction in maintenance, operations, support, and sustaining engineering costs to the DSN. A study is underway to assess not only the feasibility of this concept, but also the life-cycle cost to the DSN of the adoption and implementation of the Bent Pipe plan. This article discusses a technique developed for estimating the resulting long-term effects on the aforementioned costs and incorporating these estimates into a calculation of the overall life-cycle cost of the project.

This study began with an investigation of the way money is currently spent in the DSN. A rough model constructed as a result of this investigation was extended to future years to see how the DSN budget might be expected to behave without the implementation of the Bent Pipe project. The model was constructed in such a way as to pick out those parts of the total budget which are likely to be affected by the implementation of this plan, and so it becomes a relatively painless task, once the form of the model is fixed, to predict the savings which can accrue over a ten-year period during which the plan is in operation. The aim in developing this technique was to produce numbers which are accurate within 20 percent.

II. Constructing the Model

The process of constructing the model can be broken into distinct steps, which are individually detailed in the following paragraphs. These steps are almost entirely project-independent, in that the resulting model structure would be the same if any major reconfiguration of DSN equipment were used as the basis.

A. Identification of Accounts Related to Maintenance and Operations

Approximately 650 accounts registered in the WAD, JPL's Work Authorization Document, are currently funded. For each, a description of the work funded by the account is contained in a Format A Document, along with a listing of the appropriate JPL and NASA account codes. The first task in this project was to study these Format A's in sufficient detail to be able to discern which of the accounts were related to maintenance and operations and, in turn, which of these were likely to be affected by a major reconfiguration.

B. Creation of the Computer Data Base

The very large number of accounts or entries in the cost model made the process of manipulating them unwieldy and so the development of the model was aided immeasurably by the availability of an easily manipulated data base existing on the Univac 1108. Records containing extensive information from WAD 76-2, the January 4, 1977 version, about each account are contained in the WAD file on that machine. A file structure compatible with the WAD file was created by the JPL Data/Management Information/Retrieval System (JPLDIS) processor, and the WAD file, as illustrated in Fig. 1, Step 2, was appended. Abbreviations of the data fields shown in that figure have the following meanings:

ACCT:TITLE = Account Title
NASA:CODE = NASA Account Code
JPL:CODE = JPL Account Code
CTR XX = Contractor Work Years
JPL XX = JPL Work Years
OBLN XX = Obligation in thousands of dollars
COST XX = Cost in thousands of dollars

where

XX = Fiscal Year, e.g., FY77 = XX

C. Categorization of Affected Accounts

The descriptions of all accounts pertaining to maintenance or operations were studied again in order to assign each to one of five major functional categories. The decision as to how many functional categories to distribute the affected accounts among, and which set of functional categories to choose was influenced by a desire to keep the number of categories small, but at the same time find a set which would be complete in that the combination would reasonably describe all phases of operation of the network. The four functional categories chosen are: maintenance, operations, M&O support, and sustaining engineering. In addition, it can be assumed that all accounts determined to be unrelated to maintenance and operations fall under a fifth functional category called "fixed." Examples of accounts falling into each functional category are found in Table 1. Accounts that support M&O activity but are not directly related to hardware maintenance or facility operations were placed in the M&O support category.

The full complement of fields attached to each account record includes two more: location and subsystem. The four possible entries in location – JPL, GDSCC, Spain, and Australia – indicate where activity performed under the auspices of the account took place. Accounts used in direct operational support of existing equipment were tagged GDSCC, Spain, or Australia, as appropriate; most other accounts were labeled with a JPL location. The addition of this field lent to the model the ability to register a modest increase in the operations funds spent at JPL along with the anticipated decrease in operations funding at the stations. In addition, this field is necessary to give the model sufficient flexibility to handle cases in which the final project plan will affect each geographical location differently.

The subsystem field contains an entry only where appropriate. Accounts in the support functional category are assumed to have an impact on all subsystems. Most sustaining engineering accounts, however, are specific to one or more subsystems. This data field is particularly important in the Bent Pipe Project since each configuration will affect a different set of subsystems, and so some accounts will be touched by some configurations and not by others. For example, the telemetry Bent Pipe configuration would result in the relocation of telemetry equipment while command subsystem equipment would remain unaffected. In this case it is expected that half of the displaced telemetry equipment could be deimplemented, while half is transported to the central processing site. Table 2 presents two accounts with their associated functional category, location, and subsystem fields.

The point at which this data was entered into the data base is illustrated in Fig. 1, Step 3.

D. Creation of the Cost Model

At this point there was sufficient information in the modified WAD File to create a file suitable for estimating future costs. A new file structure, COST MODEL, was created as shown in Step 4 of Fig. 1. The entries in this file were created

by subtotaling the cost columns in the modified WAD file by location, category and subsystem. This reduced the data base to a very manageable form where the resulting 28 subtotal groups were treated as the smallest individual entities to be entered in the model. Some of these groups contained well over 100 accounts, some contained only one. The result of this JPLDIS sort and subtotal operation is displayed in Table 3, which details the contents of COST MODEL as displayed at the 1108 terminal. The subsystem acronyms used in that table are those prescribed for use by JPL Standard Practice. Since WAD 76-2 did not contain M&O cost entries for FY81 and FY82, these years were dropped from the cost model at this point. These data points are subsequently filled with estimates. At this point, the number of file records had been reduced from 650 to 28, greatly reducing the data handling effort, and setting the stage for a reasonable and hopefully well-reasoned cost modeling effort.

E. Extension of Cost Entries to FY86

The calculation of a ten-year life-cycle cost requires, of course, ten data points not four, and so a program was developed on the Sigma 5 computer to fill in the future cost blanks for the 28 subtotal groups in the model from FY81 through FY86. A least squares fit was performed on the available cost data to the optimum exponential curve passing through the FY80 point. These extended cost estimates were added to the data base as shown in Fig. 1, Step 5. It is important to note that extensions were not made for individual accounts, but rather for subtotals belonging to logical groups of accounts, for it is only when the data is collected and treated in this form that FY77 through FY80 cost figures are sufficiently well behaved to allow this curve fit.

F. Bent Pipe Reduction Factors

Figure 1, Step 5, also shows the addition of a field labeled COEF to each record, now in its final form. Obviously, the model has been constructed in such a way that adding the FY77 cost figures from all 28 subtotal groups will yield the total current M&O and sustaining engineering budget for the DSN; the estimated FY86 budget can be obtained similarly. However, if each of the 28 sets of 10 cost figures is multiplied by a factor which reflects how much that entry can be expected to change due to the Bent Pipe project, the sum then yields the estimate of a particular year's budget after implementation. The ten-year life-cycle cost of the project is then easily derived.

It is central to the usefulness of this model to make valid and well reasoned estimates of these reduction factors; it is also very difficult. In preliminary findings for a telemetry Bent Pipe configuration the following are exemplary of the techniques used to determine these factors:

(1) Sustaining Engineering – utilized percentage breakdown of the total number of Engineering Change Orders (ECRs) written in 1976 by subsystem.

(2) Maintenance – utilized percentage breakdown of work orders at stations or Equipment Event Reports (EERs) at CMF and DMC by subsystem.

III. Conclusion

In the course of the Bent Pipe feasibility study, a valuable tool has been developed for estimating maintenance, operations, support, and sustaining engineering cost savings resulting from this proposed major reconfiguration of DSN equipment. The model was developed in such a way as to facilitate its use in rapidly evaluating savings from several different versions of an implementation plan, especially since much thought was given to creating a computer data base in an easily manipulated form. With some modification this tool can prove useful to the life-cycle costing effort in the planning stages of other projects.

Acknowledgements

The authors thank Chuck Koscielski and Tim Scheck of the Jet Propulsion Laboratory for their contribution to this work.

Table 1. Functional categories and FY77 totals

Category	Account title	JPL: code	FY77 cost
Maintenance (MNT)	M&O CONTR GDSCC MAINT FAC	451-38120-377	393k
Operations (OPS)	M&O CONTR DSS-11 OPS	411-38102-377	517k
M&O support (SUP)	GDSCC ENERGY	411-38112-377	578k
Sustaining engineering (SUS)	RCV-EXC ECC ENG	411-70153-333	39k
Fixed (FXD)	DSN RFI ANALYSIS	411-72922-339	125k

Table 2. Functional category, location and subsystem examples

ACCT: TITLE	Cost 77	Cost 78	Cost 79	Cost 80	CAT	LOC	SUBSYSTEM
RCV-EXC ECO ENG	39k	41k	42k	45k	SUS	JPL	RCV
GDSCC ENERGY	578k	619k	680k	760k	SUP	GDSCC	ALL

Table 3. Contents of cost model file

LOC	CAT	SUBSYSTEM	Cost 77	Cost 78	Cost 79	Cost 80
AUST	OPS		4933	5316	5728	6172
SPAIN	OPS		5076	5470	5894	6351
GDSCC	FXD		605	654	694	732
GDSCC	MNT	ALL	4313	4780	5314	5554
GDSCC	OPS	ALL	1887	1987	2058	2181
GDSCC	SUP		3439	3828	4019	4274
JPL	FXD		32182	42591	45956	52528
JPL	MNT	ALL	217	85	89	94
JPL	MNT	GCF/NOCC/CTA	284	300	317	334
JPL	MNT	NOCC	839	887	939	989
JPL	OPS	ALL	1341	1438	1529	1633
JPL	OPS	NOCC	54	57	59	62
JPL	SUP		1105	1105	1156	1185
JPL	SUP	GCF/NOCC/CTA	79	81	85	88
JPL	SUS	ALL	5911	6301	6642	7029
JPL	SUS	DMC/FTS/PPR/DTT	295	328	363	365
JPL	SUS	DTK	80	86	51	54
JPL	SUS	DTK/APS	92	103	110	118
JPL	SUS	DTK/RCV/FTS	109	104	89	81
JPL	SUS	DTM	205	234	296	299
JPL	SUS	DTM/DCD	208	165	173	190
JPL	SUS	DTM/DCD/DTK/GHS/NCS	29	128	142	152
JPL	SUS	DTM/DCD/DTK/NCS/DMC/DTT/GHS	522	555	579	614
JPL	SUS	NOCC	211	354	552	576
JPL	SUS	PGM LIB	375	345	361	379
JPL	SUS	RCV	106	106	92	85
JPL	SUS	RCV/UWV/TXR/PPR/FTS	214	225	239	250
JPL	SUS	SMC	71	103	106	110
GRAND TOTALS			64782	77716	83632	92479

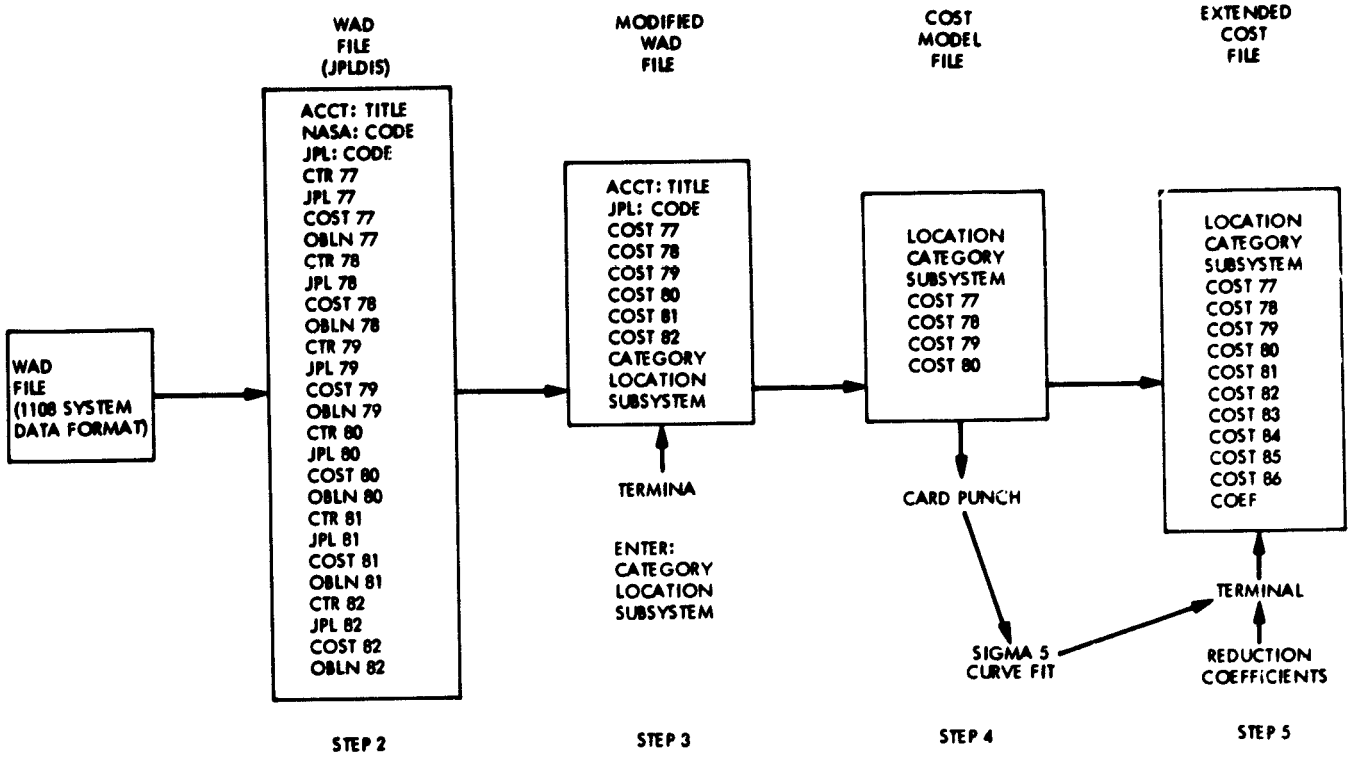

Fig. 1. Bent pipe cost model file evolution

Encoding and Decoding a Telecommunication Standard Command Code

B. Benjauthrit and T. K. Truong
TDA Engineering Office

This paper describes a simple encoder/decoder implementation scheme for the (63,56) BCH code which can be used to correct single errors and to detect any even-number of errors. The scheme is feasible for onboard-spacecraft implementation.

Recently, it was shown in Ref. 1 that a Bose Chaudhuri and Hocquenghem (BCH) code (Ref. 2) may be used to improve command coding for future planetary exploration missions. A block of command data of 64 bits is shown as follows:

$I_0 I_1$ ... I_{55}	$P_0, P_1, \ldots P_6$	F_1
56 information bits	7 parity check bits	1 filler bit

The first 56 bits, I_0 through I_{55}, are command information, $P_0, P_1, \ldots, P_6$ are parity check bits of the (63,56) BCH code, and F_1=0 is a filler bit. This code (which may also be referred to as an extended Hamming code, Ref. 3) will be shown to give a single-error correcting, even-number-error detecting capability advantage over the uncoded scheme, and simple linear switching circuits can be used to improve the encoding and decoding efficiency of it.

In order to generate the parity-check matrix of the (63, 56) BCH code, it is necessary to find the generator polynomial $g'(x)$ for this code. By Ref. 2, Appendix C, an irreducible polynomial in $GF(2^6)$ is $g^*(x) = x^6 + x + 1$. However, since the reciprocal polynomial is also a primitive polynomial, the reciprocal of $g^*(x)$, $g(x) = x^6\, g^*(1/x) = x^6 + x^5 + 1$, may also be used. Further, since the code requires 7 parity check bits, the parity check matrix generating polynomial $g(x) = x^6 + x^5 + 1$ will give one fewer parity check. To obtain one additional parity check, one must find $g'(x)$ of degree seven. One possible such $g'(x)$ is of the form:

$$g'(x) = (x + 1)(x^6 + x^5 + 1) = x^7 + x^5 + x + 1 \qquad (1)$$

Since the sequence generated from the equation

$$x^7 = x^5 + x + 1 \qquad (2)$$

has period 63[1], the period of the sequence generated from $g'(x)$, then the parity check matrix generated from Eq. (2) is given in Table 1. Note that α^j is obtained by substituting α for x in Eq. (2) and reducing modulo $\alpha^7 + \alpha^5 + \alpha + 1$. Also $\alpha^{63} = 1$.

The parity check matrix H generates a (63, 56) code which is capable of correcting single errors and detecting any even-number errors in a code block of 63 bits. To show this, let $C = (C_{62}, C_{61}, \cdots, C_0)$ denote the codeword. Then the syndrome of C is

$$S = HC^t = \sum_{j=0}^{62} C_{62-j}\alpha^j = 0, \text{ for all } \alpha^j \epsilon H,$$

where C^t designates the transpose of C. Let the received codeword with an error be

$$R = (R_{62}, R_{61}, \cdots, R_{62-j}, \cdots, R_0) = C + E$$

$$= (C_{62}, C_{61}, \cdots, C_{62-j}, \cdots, C_0) + (0, 0, \cdots, E_{62-j}, \cdots, 0)$$

where E represents the error code word. Then the syndrome S_1 of R is

$$S_1 = E_{62-j}\alpha^j = \alpha^j$$

Hence j is the error location of the received codeword, and an error is corrected.

Now observe that every column of H contains an odd number of 1's.[2] If a double error occurs in locations i and j, then

$$S_1 = E_{62-i}\alpha^i + E_{62-j}\alpha^j = \alpha^i + \alpha^j = \alpha^k, \alpha^k \epsilon GF(2^7)$$

Since α^i and α^j each has an odd number of 1's, α^k must have an even number of 1's (i.e., $(2M + 1) + (2N + 1) = 2(M + N + 1)$) and is thus not contained in H. Hence, the double error is detected. In fact, any number of double errors can be detected by this code because the field element of the resulting syndrome contains the number of 1's equal to $(2N_1 + 1) + (2N_2 + 1) + (2M_1 + 1) + (2M_2 + 1) + \cdots = 2(N_1 + N_2 + 1 + M_1 + M_2 + 1 + \cdots)$, which is even. Therefore, any double errors or even number of errors are detectable by this code.

Once the desired parity check matrix generating polynomial is determined, the encoder/decoder implementation scheme is similar to that discussed by Berlekamp [Ref. 4, Chapter 5]. The encoder and decoder derived from $g'(x)$ in Eq. (2) for the code are depicted in Fig. 1. This indicates that only a 7-cell shift register and 3 modulo-two adders are required for the implementation of the encoder. To implement the decoder, a 77-cell shift register, 6 modulo-two adders and one OR gate are needed. Any double errors can be monitored at the output of the 7-input modulo-two adder.

The encoder operates this way: First, the shift register is initialized to zero, and the three switches are posed in the up positions. When the message source is turned on, a block of 56 information bits, $I_0, I_1, \ldots, I_{55}$, is shifted down the channel and into the feedback shift register. Then the three switches are placed in the down positions, but the shifting is continued eight more times to generate the 7 parity check bits and one filler bit (to make a 64-bit word). At this point, the feedback shift register contains all zeros. Finally, all the switches are toggled back up again, ready for encoding the next block of information bits. The decoder operates as follows: After the entire received codeword $R = (R_0, R_1, \ldots, R_{63})$ has been buffered into the top register, discarding the filler bit at the end, the middle register contains the syndrome S_1 of R. The field elements S_1 are then transferred to the bottom register, while the middle register is reset to zero as indicated by the dashed lines. This yields $S_1\alpha$ in the bottom register. (The contents of this register are multiplied by α for each shift). Hence the input leads to the OR gate carry $1 + S_1\alpha^i$ as the digit at location α^{-i} deserts the buffer, $i = 1, 2, \cdots, 63$. If $1 + S_1\alpha^i \neq 0$, then $S_1 \neq \alpha^{-i}$, so the digit at location α^{-i} leaves the buffer unchanged. However, if $1 + S_1\alpha^i = 0$, then $S_1 = \alpha^{-i}$, and

[1] To prove this, one first recalls from Theorem 2.3 of Golomb (Ref. 3) that the period of the sequence I generated from the characteristic polynomial $f(x)$ is the smallest positive integer p for which $f(x) | 1 + x^p \bmod 2$. Now let $f'(x) = (x + 1) f(x)$. We must show that the sequence generated by $f'(x)$ also has period p. It is evident that $x + 1 | x^p + 1$. Since also $f(x) | x^p + 1$, then $lcm\ (x + 1, f(x)) | x^p + 1$. Now since $gcd(x + 1, f(x)) = 1$ implies $lcm(x + 1, f(x)) = f'(x)$; hence $f'(x) | x^p + 1$. Further, assume that $f'(x) | x^r + 1$ for all positive integer $r < p$. This then implies that $x^r + 1 = f'(x)\, a(x) = f(x)\, b(x)$ and $f(x) | x^r + 1$. Hence $f'(x) | x^r + 1$ for $f(x) | x^r + 1$.

[2] This is because Eq. (2) has 3 terms (or, in general, an odd number of terms, say equal to $2M + 1$ terms) on the right-hand side. Hence any column in H generated from Eq. (1) contains the number of 1's of the form $(2L + 1) - 1 + (2M + 1) - 2N = 2(L + M - N) + 1$, which is always odd.

the error is corrected as it departs the buffer. To monitor the occurrence of an even number of errors, a 7-input modulo-two adder is connected to the output of the bottom register. Since an even number of errors will result in a field element syndrome having an even number of 1's, a zero appearing at the output of this modulo-two adder will indicate an uncorrectable error.

Since the implementation and its principle of operations suggested above are simple, the (63,56) code is feasible for onboard-spacecraft implementation. The code with the above implementation scheme is suitable for incorporation into the NASA telemetry command coding standard. This would result in gaining a single-error correcting, even-number error detecting capability advantage over the uncoded system.

Acknowledgement

The authors express their thanks to B. D. L. Mulhall for first directing their attention to this coding problem and Prof. L. R. Welch of USC for his many helpful suggestions on the subject of coding.

References

1. Truszynski, G. M., and Hinners, N. W., "NASA Planetary Program Flight/Ground Telecommunications Standards — Command Coding Standard," Memorandum to distribution, NASA Headquarters, Sep. 20, 1976.

2. Peterson, W. W., and Weldon, E. J., Jr., *Error-Correcting Codes*, 2nd ed., MIT Press, Massachusetts Institute of Technology, 1972.

3. Golomb, S. W., *Shift Register Sequences*, Holden, Inc., 1967.

4. Berlekamp, E. R., *Algebraic Coding Theory*, McGraw-Hill, 1972.

Table 1. Parity check matrix generated from $x^7 = x^6 + x + 1$

$$
H = \begin{bmatrix}
1000000101010011001000100101101100011101000011010111001111101111 & \alpha^0 \\
0100000111111010101100110111011010010011100010111100101000110000 & \alpha^1 \\
0010000011111101010110011011101101001001110001011110010100011000 & \alpha^2 \\
0001000001111110101011001101110110100100111000101111001010001100 & \alpha^3 \\
0000100000111111010101100110111011010010011100010111100101000110 & \alpha^4 \\
0000010101001100100010010110110001110100001101011100111101111100 & \alpha^5 \\
0000001010100110010001001011011000111010000110101110011111011111 & \alpha^6
\end{bmatrix}
$$

$\alpha^0 \alpha^1 \alpha^2 \alpha^3 \alpha^4 \alpha^5 \ldots \alpha^{61} \alpha^{62}$

0123456789012345678901234567890123456789012345678901234567890123456789012

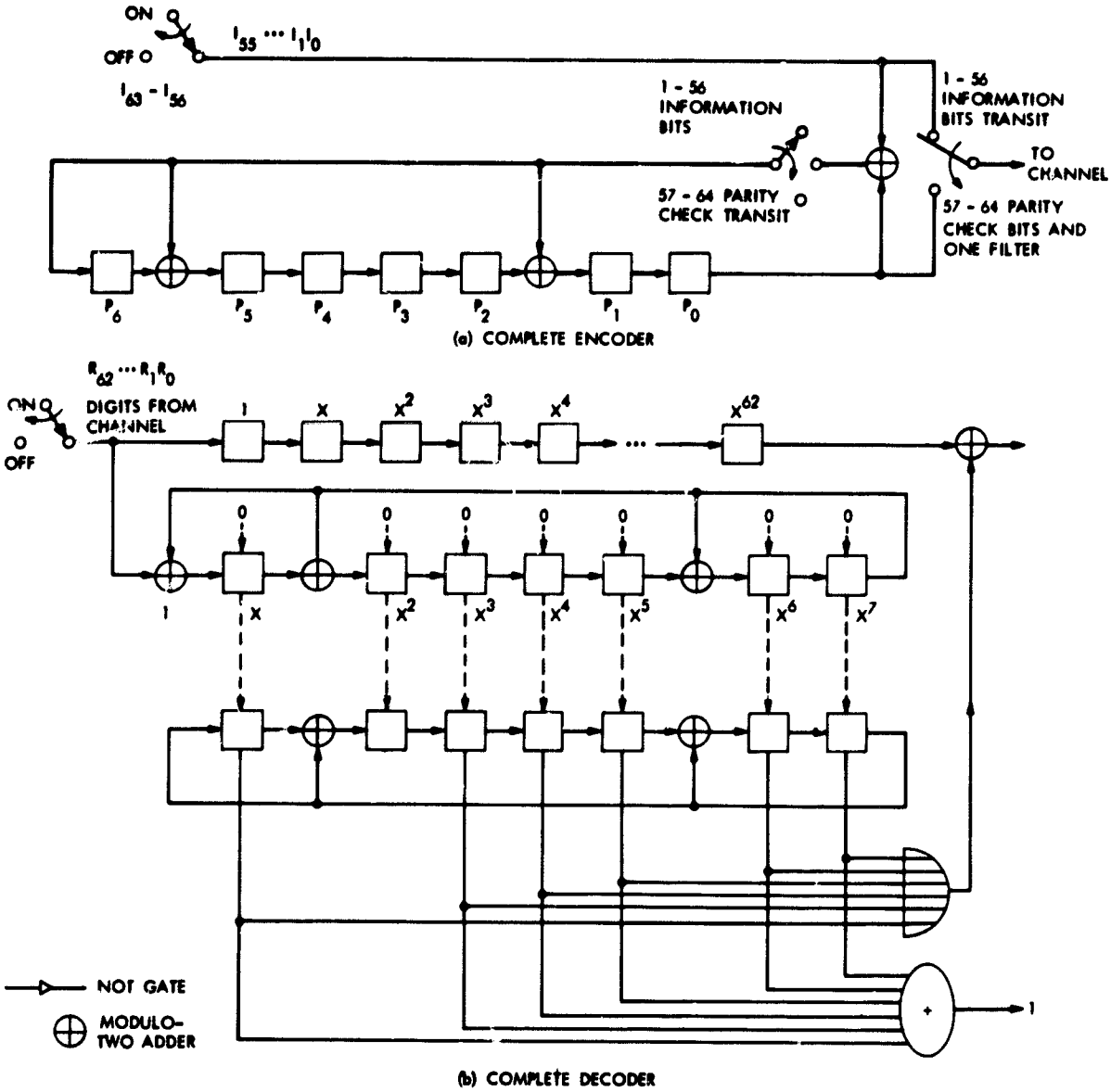

Fig. 1. Encoder/decoder for (63, 56) extended Hamming codes

Status of Goldstone Solar Energy System Study of the First Goldstone Energy Project

F. L. Lansing
DSN Engineering Section

This article summarizes the results reached by the DSN Engineering Section and private consultants in the review of the initial plan of the Goldstone Energy Project. The main objectives were in the areas of energy conservation and the application of solar-driven systems for power and hydrogen generation. This summary will provide background data for management planning decisions both to the DSN Engineering Section and other organizations planning a similar program. The review showed that an add-on solar driven absorption refrigeration unit with its associated changes to the existing system was not cost-effective, having a payback period of 29 years. Similar economically unattractive results were found for both a solar-hydrogen and a wind-hydrogen generation plant. However, cutting the hydrogen generation linkage from this plant improved its economic feasibility.

I. Introduction

As part of a broad program to conserve energy at government installations, the Jet Propulsion Laboratory examined the concept of operating one or more of its installations on clean, renewable gaseous fuels such as hydrogen or methane. The sun would be the primary source of energy in addition to other sources such as wind and municipal waste. The project was called "Goldstone Energy Project," and the goals were set to provide a system which would (1) save a significant amount of fossil fuel or commercial electric power, (2) be economically competitive with existing energy sources, and (3) minimize harmful effects to the environment and be architecturally attractive.

The installation under investigation was the Goldstone Deep Space Communication Complex (DSCC) at Goldstone, California. Six separate tracking stations and a Microwave Test Facility (MTS) were included in the complex. The Goldstone installation has some unique characteristics which made it appropriate for consideration, such as:

(1) The site is located in the Mojave Desert, which receives abundant sunshine and significant wind currents.

(2) The tracking stations are surrounded by a large land area (approximately 80 km^2), with potential for collecting solar energy while not interfering with space communications.

(3) Existing diesel engine generating capacity (12.4 MW_e) is operated only during a critical phase of space flight missions or during emergencies such as failure of commercial power. The Goldstone facility has an average electric demand of 3.5 MW_e, which is normally purchased from a utility company, and the concept of running the engine generators on a continuous basis instead of purchasing power presents a possible saving to be studied.

The original objectives of the energy program, to support the national goal of energy independence, were set in the initial stages of the project to (1) reduce the DSCC energy consumption by 30 to 40 % over a 5-year period starting in 1974, (2) reduce the fossil fuel consumption by 70 to 90 % over a 5-year period starting in 1976, and (3) attain a high degree of energy self-sufficiency during the period of energy utilization nationwide.

The original Goldstone Energy Project was a path-seeking study which could be identified as a "hydrogen based study." Later on, the project objectives were changed and the title became the "DSN Energy Conservation Project," a change that was made to express in more specific terms the new project goals brought on by the conclusions drawn from the first path-seeking study. The above phases are explained as follows:

A. Hydrogen Based Study

A baseline configuration had been proposed whose main objective was the production of hydrogen gas by water electrolysis. The electric power needed for electrolysis would be provided by a combination of a wind power plant and a solar-thermal-to-electric power plant. The generated hydrogen was to be used as a fuel for either heating purposes or for driving the standby diesel engines. During the early stages of the project and the development of the baseline configuration, a joint study effort had started between the DSN Engineering Section at JPL and Cornell University in Ithaca, New York. This study effort looked into the changes that would be required to the existing diesel fueled engines provided that the implementation of hydrogen gas became economically feasible.

Another addition to the baseline configuration which was made late in the program, was the solar driven heating, ventilation and air conditioning (HVAC), using the absorption refrigeration method. This report ties together this last addition to the Project and reports on its status.

Two different private consultants (Refs. 1-3) were selected to assist in answering the questions raised during the study. First, Keller and Gannon Consulting Engineers were assigned the task of estimating the heating and cooling loads for Goldstone buildings and evaluating many potential money-saving energy conservation ideas. Second, Burns and Roe, Inc., Consulting Engineers, followed the Keller and Gannon work and gave their own input to the Projects as a whole with a more detailed analysis.

This first phase of the Goldstone Energy Project ended with a set of technical recommendations that contributed to the scope of a broad energy project now called "DSN Energy Conservation Project".

B. DSN Energy Conservation Project

The DSN Energy Conservation Project embodies the Energy Conservation Awareness and Recognition Program (ECARP), Building Modification Program, and Utility Control System (UCS). These programs are underway and the status of their progress will be the subject of other articles to come.

II. Solar Energy System Outline

The proposed Goldstone solar energy baseline system outline is presented in detail in Refs. 4 and 5, and briefly stated in this report for convenience. It consists mainly of the following alternate subsystems: (1) "central complex" for all tracking stations, (2) "central site" for each tracking station, or (3) "distributed" units for each installation. The common outline is shown in Fig. 1 and is composed of the following:

(1) *Solar Energy Collection Subsystem.* This subsystem consists simply of a set of solar collectors and heat storage tank(s) which would supply most of the thermal energy required to operate a power generation subsystem and a solar heating and cooling subsystem.

(2) *Solar Heating and Cooling Subsystem.* This subsystem, added late in the baseline configuration, takes in a large percentage (85%) of its thermal energy requirement from the solar-energy collection subsystem; the rest is supplied by another energy source such as propane gas heating. This subsystem supplies water heating and space-air heating for the facility and provides all the air conditioning requirements through absorption refrigeration units.

(3) *Power Generation Subsystem.* This consists of both a solar-power subsystem and a wind-power subsystem. The solar-power subsystem includes a heat engine working with a technically advanced power cycle, a cooling tower, and a device for energy storage. The

wind-power subsystem consists of a set of air turbines connected to electric generators, and a device for energy storage. This subsystem would provide direct current (dc) electric power to the electrolysis subsystem and other system accessories.

(4) *Electrolysis (or Hydrogen) Subsystem.* This consists of a set of electrolyzers, hydrogen storage tanks, and an electric distribution system. The electrolysis subsystem is a combination of a wind-hydrogen subsystem and a solar-hydrogen subsystem, as shown in Fig. 1. Hydrogen was to be used directly for heating purposes and/or considered as a fuel for the engine-generators.

(5) *Waste Heat Utilization Subsystem.* This subsystem makes use of the direct waste of energy such as hot flue gases, exhaust steam or hot streams of water from cooling systems, and the energy from municipal waste incineration. The waste heat utilization subsystem assists in providing the thermal energy for the power generation subsystem. The present report considers only the efforts made to convert the existing diesel-generators to a total energy system using waste heat recovery and generated electric power to heat, cool and power the Goldstone facilities.

III. Bases for Evaluation

The following is a list of criteria considered for evaluating each candidate subsystem configuration:

(1) Minimum life-cycle cost.

(2) Maximum personnel safety.

(3) Minimum environmental impact.

(4) Ability to support the national goal of energy independence.

(5) A system whose performance can be predicted fairly accurately.

(6) Minimum use of land area with no interference with tracking and data acquisition functions.

(7) Minimum manpower requirements for maintenance and operation.

(8) Long operational life.

(9) Flexibility to relocate individual modules.

(10) Minimum replacement cost in case of destruction by natural hazards.

IV. Solar Energy Collection Subsystem

The performance and cost analysis of the following five types of solar collectors were studied (Ref. 1):

(1) A flat plate collector.

(2) A compound parabolic (Winston type) collector.

(3) A tubular collector (Corning type).

(4) A parabolic trough collector.

(5) A paraboloid dish collector.

The cost ranged from $\$60/m^2$ for a low-performance flat plate collector to $\$293/m^2$ for the paraboloid dish type. The annual thermal output for the Goldstone location ranged from 900 kWh_t/m^2 for the low-performance flat plate collector to 1470 kWh_t/m^2 for the compound parabolic type. In this study, nontracking, high-performance solar collectors which would be commercially available by 1980 were selected. However, it was later found that no collector presently available or in an advanced state of development could support an energy-on-demand system on an economically attractive basis when compared to fossil fuels at current prices.

V. Solar Heating and Cooling Subsystem

The economic evaluation of a conceptual solar heating and cooling design serving the four major buildings at DSS 12, namely, Administration and Cafeteria (G-21), Control Building (G-26), Engineering and Communications (G-33), and Network Laboratory and Maintenance (G-38), was performed. The results indicated that solar heating and cooling of these four major buildings, using an add-on absorption refrigeration unit, was not economically feasible, having a payback period of 29 years as will be shown later in Table 1. The estimate is dominated by the piping and valve cost needed both for the collectors and the cost of new fan-coil units. The collectors would be less costly if they were located near, or on top of, the buildings they serve. Also, solar heating, ventilation and air conditioning (HVAC) would be less costly if they were considered for existing buildings that do not have a predominant daytime load and would only be attractive for buildings requiring complete replacement of HVAC equipment. The rationale of these findings is described below.

A. Subsystem Criteria

Presently the above four buildings at DSS 12 are air conditioned by conventional systems, utilizing gas-fired boilers for heating and electric driven vapor compression refrigeration units for cooling (with "direct expansion" from the evaporator coils to the air handlers). The proposed solar-assisted HVAC system was designed as a "centralized" unit. Hot water for

heating and chilled water for cooling are produced in a central station on-site and then distributed to the different buildings. The following criteria are the bases of the study:

(1) System component selection is based on current technology production. Cost estimates are based on 1976 prices with 10% annual escalation.

(2) Solar collectors are of the nontracking type.

(3) The solar energy contribution to the total annual heating and cooling requirement for the four major buildings at DSS 12 is 85%. This percentage was chosen since it is not economical to size the solar collection subsystem to provide 100% of the load.

(4) Solar collectors are not to be located on the roofs of buildings but on the ground.

(5) Existing HVAC systems are to remain intact and serve as backup for the solar-assisted types.

(6) An auxiliary hot water heater is operated when the solar collector system is unable to meet the load. This heater has to be sized to meet the peak load to allow full operation without solar input.

A schematic of the system is shown in Fig. 2.

B. Heating and Cooling Load

The existing heating and cooling systems for the four major buildings at DSS 12 are multizone systems which require simultaneous heating and cooling. Two main classes of HVAC loads were considered:

(1) Loads that are associated with comfort areas such as offices and conference rooms.

(2) Loads that have a continuous demand such as electronic rack cooling in the communication and the control rooms.

The load analysis was originally made by Keller and Gannon (Ref. 3) using a computer program called ECUBE.[1] The daily heating and cooling loads for each building were updated and calculated for typical weekdays[2] of each month. The existing heating load was later planned to be reduced by 97% to become 40,300 kWh_t/year, and the buildings cooling requirement to be reduced by 45% to become 1,146,000 kWh_t/year. These reductions, claimed by Burns and Roe following the Keller and Gannon study, can be achieved if separate fan-coil units were used instead of multi-zone units. Regarding peak loads, the claimed energy conservation measures would also reduce the peak heating load by 77% of the existing system to become 97.3 kW_t and the peak cooling load by 33% to become 380 KW_t. The cooling demand for the four major buildings was then estimated as 100 tons of refrigeration.

[1] Energy Conservation Utilizing Better Engineering.

[2] The heating and cooling loads were based on (1) weekend daily requirement = 60% weekday daily requirement, and (2) 22 weekdays/month and 8 days weekends/month.

C. Solar Radiation Model

This study was developed using the ASHRAE clear day model with corrections for unclear day effects from climatic Atlas data and from actual measurements (Ref. 6). A collector tilt angle of 35 deg to the horizontal and facing south was selected based on optimization of the maximum annual solar radiation at the Goldstone area.

D. Sizing the Solar Collector

The selection of the solar collector was made from those units which are (1) commercially available or very near to the production stage, (2) able to produce relatively high fluid temperature around 100°C at good efficiency (this requirement is essential to drive an absorption type air conditioner), and (3) of low first cost with a minimum maintenance.

In the studies made by Burns and Roe, the high-performance NASA-Honeywell flat-plate collector with a black nickel selective coating and a double glass cover and anti-reflective coating was selected. The annual average energy collected per day is 5 kWh_t/m^2 or 1800 kWh_t/m^2 per year. The calculated collector field area, based on solar assistance of 85% of the total heating and cooling energy consumption, was found to be 1600 m^2.

E. Energy Storage

There are basically two approaches to sensible heat storage, one uses two separate hot and cold storage tanks and the other a single stratified storage tank. The primary advantage of the first approach is that the hot and cold fluids are separated. However, its disadvantage is that each of the two tanks must be sized to hold the full storage capacity. In the case of a stratified tank, mixing can be prevented by using a separator such as a piston or a floating membrane, and this type costs approximately one half that of the first approach. However, Burns and Roe (Ref. 1) used the two tank approach. Each tank was sized at 156 m^3 to carry a net volume of fluid of 139 m^3. An alternate configuration is described under paragraph H below.

F. Refrigeration and Air Conditioning Units

Five 25-ton LiBr/water absorption refrigeration units were selected to provide a total of 125 tons (440 kW_t) of cooling

capacity, which is a little more than needed to meet the peak cooling load of 380 kW_t. The cooling water necessary to operate the condenser and the absorber sections is provided by two wet cooling towers with a continuous supply of cooling water at 23.9°C (75°F). The chilled water produced in the evaporator is supplied to the chilled water storage tank and is kept at 7.2°C (45°F).

G. Flow Control — Solar Collector Loop

Since water alone is used as the working fluid, it was suggested that an auxiliary system be provided to drain the collector into an insulated tank at sunset to prevent nighttime freezing. Other alternatives such as circulation of a slow flow of warm water from the storage tank were eliminated since this results in some loss of the energy collected during the day. Also, the use of an ethylene glycol/water mixture was not recommended due to high cost. The flow control mechanism was very complicated due to the introduction of an anti-corrosion gas (nitrogen) in a pressurized loop which is drained by gravity. The loop is equipped with temperature sensing devices to monitor the flow rate vs the collector exit temperature through control valves so that the storage tanks always receive the fluid at a uniform pre-assigned temperature (107°C), irrespective of any variations that might occur due to ambient or solar radiation conditions.

H. Alternate Configuration

An alternative to the solar heating and cooling subsystem was presented, utilizing the same absorption refrigeration units but with a solar collector other than the NASA-Honeywell flat-plate type. A tubular collector, recently manufactured by Owens-Illinois Corp., was selected as the candidate.[3] The collector possesses a higher accumulated thermal efficiency per day (about 45%) and a lower heat loss rate to the surroundings than the comparative flat-plate type. The steady-state behavior of this collector was given in Ref. 7. Also, its unsteady-state (transient) thermal response to the time-changing input parameters was analyzed by two different methods; an analytical method (Ref. 8) and a finite difference numerical method (Ref. 9). The results indicated that with a 50/50 mixture of ethelyne glycol/water solution as a working fluid, the instantaneous collector efficiency can reach 60% and an accumulated daily efficiency[4] of 43% under a typical Goldstone weather spectrum (Ref. 9).

A lithium bromide/water absorption refrigeration unit was selected for the study based on its higher coefficient of performance relative to other absorption refrigeration types and on the current manufacturer's efforts to mass-produce small-size units at a low cost. A detailed computer model for such a unit was reported in Ref. 10. The coefficient of performance ranged from 0.6 (at peak cooling load) to 0.8 (at average load). With a solar energy share of 85% of the total demand and an average cooling capacity of 100 tons of refrigeration, the collector area was found to be 1460 m^2.

A stratified tank was considered as a part of this alternative study with a semifloating separator between the hot and cold fluids. The energy fluctuations for one-day storage (approximately 8 hours of hot fluid charging and 16 hours of discharging) indicated that the necessary tank volume should be at least 120 m^3. Also, it was found that about three times this tank capacity would be required if the tank was designed for double the collector area and a two-day storage (approximately 8 hours of hot fluid charging and 40 hours of discharging) wherein one of the two days was assumed fully cloudy with zero input solar energy.

Regarding cost, this alternate configuration was not analyzed separately since it requires the same costly alterations and additions to the existing HVAC systems as the previously mentioned configuration.

I. Conclusions of the Solar Heating and Cooling Subsystem

The cost estimates of the proposed solar heating and cooling system at DSS 12, as presented in Table 1, are shown to have a long payback period (29 years). Therefore, it is concluded that a solar assisted system, with the components and alterations as outlined in this study, is not an economically feasible alternate to the existing system.

The principal capital cost items, as shown in Table 1, are the new piping, fan-coil units and ducts which represent 40% of the total installation cost. As a result of adopting the absorption refrigeration technique, these items are needed to convert the existing system, which utilizes direct expansion of refrigerant (R-22) in the cooling coils, to a new system with a chilled water circuit. Accordingly, if an economically viable air conditioning system has to be installed, a new direction of efforts has to be followed excluding the absorption refrigeration method, wherein the existing mechanically driven air conditioners, ducts, pipes, etc., are kept intact to save a considerable amount of new installation costs.

It should not be concluded that a solar-assisted HVAC system would be uneconomical in all situations. Since we are keeping the existing HVAC systems intact, a new and different approach must be considered to reduce the new add-on

[3] This was considered the best collector commercially available at time of initial study.

[4] Manufacturer recommended fluid exit temperature not more than 120° C for coating protection.

installation cost. However, for a newly constructed system, the application of solar-assisted absorption technique may result in an economically feasible case.

VI. Wind-Hydrogen Subsystem

A. Wind Turbines

A detailed technical review about wind power and air turbines design was presented in Ref. 1. It included two general categories: the horizontal axis wind turbine and the vertical axis type.

(1) *Horizontal Axis Turbine.* This consists of a number of blades (2-12) of an airfoil shape radially distributed around a horizontal shaft with the blades rotating in a vertical plane. The blade pitch may be fixed or variable. The maximum rotor efficiency is reached during intermittent operation only if the blade tip speed is kept proportional to the wind speed. In practice, each turbine-generator is designed for a specific cut-in speed and a cut-out speed.[5] The optimum blade tip-to-wind speed ratio ranges from 2.5 (for slow speed multibladed propellers) to 6 (for high speed types).

(2) *Vertical Axis Turbine.* This offers several advantages over the horizontal axis turbine such as: (1) the ability to accept winds from any direction, (2) suitability for low range of wind velocities, (3) the generator and controls can be set on the ground for simpler tower construction, and (4) lower cost. Examples of this design are the "Savonius" rotor (a modified S-shape rotor) and the "Darrieus" rotor (consists of 3 airfoil blades having a common chord on a vertical shaft transverse to the wind currents).

A two-blade propeller rotor (horizontal axis) and a three-blade Darrieus rotor (vertical axis) are analyzed and their cost determined.[6]

In the process of evaluating and selecting the components of the wind subsystem, the relationship between the turbine design and cost projection was made. The feasibility of using batteries or flywheels as a means of leveling wind power generated during intermittent unsteady wind durations was studied. The selection of the best configuration was based on the one that possesses the lowest 10-year life cycle cost. The results indicated that the vertical axis turbines meet all the technical and cost effectiveness requirements.

The baseline wind subsystem configuration was set as an array of the "Darrieus" type coupled with a small "Savonius" type wind turbine as an auxiliary device to provide self-starting.[7] Each wind turbine drives an electric generator directly or through gearing. The self-starting device is a small generator-motor to start the big wind turbine which can operate as a low capacity generator during low wind speed periods with an overall conversion (from wind to shaft power) efficiency of 35%. The generators operate at rated capacity when the wind velocity reaches or exceeds the maximum design value. The wind subsystem is proposed to be modular, with each module having an output of 300 kW_t of hydrogen when connected to the electrolyzer.

B. Electrical Generators for Wind-Subsystem

The wind turbine generator may be classified as follows:

(1) *Constant speed generator (synchronous generator or induction generator).* The speed of the turbine rotor is controlled by means of a speed governor which changes the pitch of the propeller blades. The power generated is ac with a constant frequency (60 Hz). The generator is disconnected from the load by using a circuit breaker when it is no longer possible to regulate the speed or frequency.

(2) *Variable frequency/speed generator.* This is either: (a) A dc generator: the output may be used directly to supply a dc load or through an inverter to supply an ac load (b) An ac generator: the output is variable frequency ac. To supply a constant frequency load, a frequency converter is used. Also, to supply a dc load, a rectifier has to be used such as silicon controlled rectifiers (SCR).

Regarding cost, ac generators were recommended for economic and efficient electric power transmission for the proposed wind turbines at the Goldstone site. The vertical axis Darrieus-type rotor connected to two induction generators of squirrel-cage type appeared to be practical and cost effective.

The above selection of the candidate turbine-generator module was based on the relationship between the

[5] The cut-in speed is the minimum wind speed for energy conversion and the cut-out speed is the maximum speed allowed due to structural limitation.

[6] The 1977 installation cost of a 300-kW_e-capacity propeller wind turbine with 73.5 m (241 ft) rotor is estimated at $715,000 or $2383/$KW_e$. It produces 720,000 kWhr/year at Goldstone with an energy cost of $0.11/$kW_e$h based on 10-year operation. On the other hand, the installation cost of a 200-kW_e-capacity vertical axis wind turbine of the Darrieus type with a 27.4 m (90 ft) rotor is estimated at $110,000 or $550/$kW_e$. It produces 120,000 kWhr/yr at Goldstone with an energy cost of $0.10/$kW_e$h.

[7] Darrieus type blades stall at low blade tip-to-wind speed ratio approx 3; the optimum ratio for maximum power ranges from 4.75 to 6.

fundamental design features of the two main turbine types: vertical and horizontal axis, and the appropriate projections of their installed cost, energy cost, operation and maintenance cost, together with the effects of Goldstone wind requirements on performance. According to the rough wind data taken at Goldstone, the average wind speed is very low to be exploited as a source of energy. Since the energy cost can be lowered substantially should the average wind speed data be improved, it is recommended that additional site data be gathered over longer periods of time and neighboring locations to establish a more accurate wind velocity map.

C. Electrolyzers for Hydrogen Generation Subsystem

The following three types of electrolyzers were considered:

(1) *Tank-type electrolyzer.* Acts as one reversible cell consisting of two alternate polarity electrodes (anode (+) and cathode (-)) made of flat sheets of steel welded to the bus bars. A diaphragm, usually made of asbestos is used to separate the hydrogen generated at the cathode from the oxygen generated at the adjacent anode. The system can operate at atmospheric pressure as well as low or high pressure.

(2) *Filter-press electrolyzer with alkaline electrolyte.* This unit is constructed from a set of alternate bipolar electrodes and asbestos diaphragms. One side of the electrode is the cathode of one cell while the opposite side is the anode of the adjacent cell. The set may operate at pressures above atmospheric (~ 30 atm).

(3) *Filter press electrolyzer with solid polymer electrolyte.* The electrolyte in this case is not liquid but rather a 10-mil sheet of a polymeric structure coated with a thin film of catalyst (a form of Teflon) to form a barrier between the generating oxygen and hydrogen as well as providing a high ionic conductivity.

These different types of commercial electrolyzers under study have conversion efficiency (defined as the ratio of low heating value of hydrogen production rate/electrical energy supplied) ranging from 60 to 90%; the installation cost for every pound of hydrogen/hr ranges from $4000 to $7500, respectively.

D. Wind-Hydrogen Subsystem Configuration and Cost

Two wind-subsystem module configurations were studied for comparison, both technically and economically: (1) a centralized module having a nominal capacity of 300 kW_t of hydrogen, (2) a distributed module consisting of 10 isolated submodules, each having a nominal capacity of 30 kW_t of hydrogen. Their components were selected as follows:

(1) The "centralized" wind-subsystem includes an array of 10 vertical-axis wind turbines of 200 kW_e each (a Darrieus turbine coupled with a self-starter Savonius for each), a high-voltage ac transmission system, and four electrolyzer units of the tank type working at atmospheric pressure. Each electrolyzer unit has a full load capacity of 78.5 kW_t of hydrogen.

(2) The "distributed" wind-subsystem consists of 10 isolated vertical axis turbines (same as centralized configuration) and 10 electrolyzer units of the tank type with a capacity of 31.4 kW_t each.

The cost estimates for each configuration is presented in Tables 2 and 3.

The tank type electrolyzer was chosen since it is simple in construction, requires less maintenance and can be operated at low partial loads down to 5% of full capacity. In the centralized plant, four electrolyzer units of 78.5 kW_t full load capacity each, consume 138 kW_e/unit of electric power (a thermal conversion efficiency of 57%) or a total electric consumption of 552 kW_e and produces 314 kW_t of hydrogen (equivalent to a hydrogen production rate[8] of 9.43 kg/hr). For a typical day at Goldstone, the on-site data indicates that the periods during which the wind speed exceeds the minimum cut-in speed is about 25% of the time as an annual average (i.e., 6 hours per day). Accordingly, the electrolysis plant will require an annual electric input of 1.209×10^6 kWh_e/yr, and 10 wind turbines of 120,000 kWh_e/yr capacity are needed. Each turbine-generator is rated at 200 kW_e each at 35 mph rated velocity. Provision for storing mechanical energy for leveling the power fluctuations can be accomplished in different ways, such as high-speed flywheels or batteries.

In the "distributed" plant, the accumulated cost of 10 electrolyzers of 31.4 kW_t capacity each (replacing the 4 larger units for the "centralized" plant), the cost increase brought by using dc generators instead of ac, and the cancellation of electrical transmission system, will yield a minor difference in the 10-year life cycle cost per kW_t of hydrogen as shown in Tables 2 and 3. Although the "distributed" subsystem configuration is slightly higher in cost than the centralized subsystem, it was selected in view of its adaptability to be relocated to alternate windy sites and the suitability of the small size units to mass production.

[8]This is based on the lower heating value of hydrogen, which is 28,900 kcal/kg. The reversible (minimum) work necessary to produce 1 kg of hydrogen by electrolysis at 25°C is 27,320 kcal or 31.77 kWh_e.

It should be pointed out that it would not be economical to consider a wind-hydrogen plant without energy storage and leveling devices. Without this storage, four times the capacity of the electrolyzers would have been installed in order to meet the peak power possibly generated by the turbines (about 6 hours/day) as determined by the Goldstone wind spectrum.

VII. Solar-Hydrogen Subsystem

The solar-hydrogen subsystem is composed of solar collectors, heat engine, dc generator, and an electrolysis unit. This subsystem was assumed modular, with each module producing an output of 300 kW_t of hydrogen. Two approaches to solar thermal-to-electric power generation were studied (Ref. 1) as follows:

(1) Using a large thermal storage, one heat engine and one electrolysis unit to generate 300 kW_t of hydrogen on a continuous basis for 24 hours a day.

(2) No thermal storage is used and three heat engines and electrolysis units rated at 300 kW_t of hydrogen each are used to provide 900 kW_t of hydrogen for only 8 hours/day (sunshine period).

In the two approaches, the collector area used would be equal if the average fluid temperature was kept the same. The main difference between approaches (1) and (2) is that approach (1) utilizes a large storage tank and approach (2) adds two heat engines and two electrolyzers, as shown in Fig. 3.

The result of the analysis showed that approach (1) is less expensive than approach (2). However, *neither of the above two approaches is economically viable* due to the repetitive energy conversion from solar thermal to electrical to thermal again in the form of hydrogen. The design and cost of each component was analyzed as follows:

(1) *Solar Collectors.* Two nontracking collectors (a high-performance flat plate collector and the compound parabolic (Winston) type) were compared in performance and cost. The two collectors were selected among a list of commercially available types (Ref. 1). The high-performance flat plate collector was then recommended based on its minimum 10-year life cycle cost. The collector size was found to be 16,250 m^2 for a module producing 300 kW_t of hydrogen with an electrolyzer conversion efficiency of 57%, a heat engine generator efficiency of 21% (based on a uniform storage of fluid at 205°C), and a yearly average of the collector output per day of 3.70 kWh_t/m^2 (annual output of 1350 kWh_t/m^2). The total daily collector output will then be 60,120 kWh_t.

(2) *Thermal Storage.* Only thermal energy storage in the form of sensible heat of water is recommended. By selecting different hot storage temperatures, the amount of stored water was calculated based on a ratio of 2/3 of the collector output per day, i.e., to store 40,080 $kWhr_t$ per day. The number of tanks, tank dimensions, weight, insulation, pumping power and cost were calculated, and the selection was based on the least cost configuration. For a set of tanks partially buried underground, the cost per kWh_t stored ranged from $21.9 to $31.2 for different pressurized fluid circuits. The analysis was repeated using other storage media such as "Dowtherm A" fluid instead of water, or using solid material beds such as cast iron or rocks. The storage cost for these schemes was found more expensive than the first scheme using the sensible heat of water, and accordingly, they were not discussed further.

(3) *Thermal Conversion Cycle.* Several thermal conversion schemes have been studied, including dual cycles with two different fluids, combined Brayton/Rankine cycle, and heat pipes. The selected scheme is a dual cycle composed of (1) a primary loop with pressurized water as the circulating fluid and consists of the collectors, storage tanks and a heat exchanger acting as a boiler, and (2) a secondary loop consisting of a conventional steam Rankine-cycle with a steam turbine, a pump, a condenser, and a cooling tower. The collectors will operate in two modes, one during sunshine hours (approximately 8 hr) and one during nighttime hours (approximately 16 hr). The flow is regulated during sunshine hours so that approximately 1/3 of the flow is delivered to the steam heat exchanger of the secondary loop and 2/3 is delivered to the thermal storage tanks. During nighttime hours, the hot water is delivered from thermal storage to the steam generator.

(4) *Cost Comparison.* Table 4 shows an estimate of the costs for both approaches. Approach (1) was found less expensive than approach (2) and was selected for comparison with the wind-hydrogen subsystem previously studied. However, *neither of the approaches is acceptable* since they possess very long payback periods (~ 30 years) at very low overall efficiency of energy conversion. A cost comparison between the wind-hydrogen subsystem module and the solar-hydrogen subsystem module producing a nominal hydrogen capacity of 300 kW_t is listed in Table 5. A comparison between the 10-year life cycle

cost and the amount of fuel savings in each scheme shows very clearly that neither is acceptable. Future efforts should be addressed to the direct utilization of either solar or wind power conversion to electrical or mechanical forms.

VIII. Waste Heat Utilization Subsystem

A. Subsystem design

Assuming that the existing diesel generator power plant at Goldstone runs on a continuous basis, a feasibility study was made to convert the plant to a total energy-system to heat, cool and power the facilities. The present system utilizes power from commercial sources and burns fuel for heating and cooling. Waste heat in the cylinder jacket cooling water and in the exhaust gases would be utilized in the form of hot water or steam to provide cooling for the major-load buildings via an absorption refrigeration unit. Electric power would be used to heat and cool minor-load buildings and to power all lights, fans, etc. It was found that it is impractical to modify the existing diesel engine units to accommodate for steam formation in the cylinder jackets. Therefore, only the hot water utilization was studied and costs determined for the DSN stations (DSS 11, DSS 12, DSS 14) and the Mojave and Apollo stations. The energy consumption data for each station is listed in Tables 7 and 8. These data were used as a rough basis for sizing the new components even though the present loads were reduced due to the current energy conservation efforts. The estimated cost includes the capital investment of the absorption refrigeration units, heat exchangers, cooling tower, new chilled water and hot water lines. Comparison of the 10-year life-cycle cost between the existing system with its electric and fuel power purchased from commercial sources and the proposed system, which is continuously operated for electric power production and utilizing the waste heat for HVAC support, showed that the second system is more expensive than the first one by 26 to 73%.

B. Evaluation of Dual Fuel Operation of Diesel Engines

Should a hydrogen economy be implemented at the Goldstone site, it may be advantageous to convert the existing diesel-engine generators from diesel oil to hydrogen fuel. The use of gaseous hydrogen as a fuel for internal combustion engines was first used by Erren in the 1930's in Germany, using hydrogen injection in an engine following the diesel cycle. Development work is continuing today, based on the current national energy situation. A study was initiated by the DSN Engineering Section at JPL and performed at Cornell University, Ithaca, N.Y., to demonstrate the feasibility of this concept. The test results (Ref. 11) from an experimental CFR diesel engine, were generally favorable and the following comparisons were made between hydrogen and diesel oil as fuels: (1) the indicated and brake horsepower were comparable, (2) the cycle efficiency was comparable, and (3) the peak cylinder pressure was almost the same for both cases. A newly designed hydrogen injector, controlled and activated by the pressure pulse of the diesel fuel injection system, was successful and provided a rapid fuel changeover capability. Very high compression ratios (25.7:1) were used in the tests without knock problems. Despite the questions of reliability, crankcase explosion hazards, modifying the cooling system, and life of different components, the study has proven that it is technically feasible. Regarding cost, the dual fuel operation of diesel engines appears to be more expensive as a result of several modifications to the existing units, such as special turbocharging system, new cylinder heads, and hydrogen fuel safety system controls. The estimated cost of converting one unit to dual fuel is about $30,000 and the recommendation of its implementation is totally dependent on whether or not a hydrogen economy is implemented in the first place.

IX. General Conclusions

The following general conclusions have been reached:

(1) The subsystems and their components of Goldstone solar energy system, as illustrated in Fig. 1, have been studied sufficiently to enable the evaluation of their performance and cost effectiveness.

(2) In the solar collection subsystem, five types of commercially available solar collectors were evaluated. It was then generalized that no collector presently available or in an advanced state of development can support a thermal load on an economically attractive basis as compared to fossil fuels at current prices. However, the current research for an economic solar-assisted HVAC system will continue, as this system will become economically feasible with the rising prices of fossil fuel.

(3) The first concept of a solar heating and cooling subsystem configuration, as described in Fig. 2, was selected based on its current adoption nationwide and on the fact that all of its components are commercially available. The conceptual system would serve the four major load buildings at DSS 12. The results were not favorable since the payback period is 29 years. The cost is dominated by the alterations to the existing systems piping, ducts, fan coil units, etc., to convert to a system with underground chilled water transmission line. These costs will be in addition to the cost of new foundations and connections

for the central collector field near the Station entrance. Distributed refrigeration units utilizing the large roof area of each major load building may save some of the above cost, but it is still not economical.

(4) An alternate study of the solar heating and cooling subsystem using the Owens-Illinois tubular collector instead of NASA-Honeywell flat-plate type was made. The collector area and cost were found comparable and in the range of 15% of the total project cost.

(5) The power generation subsystem presented in Fig. 4, utilizing solar or wind power, was found economically unacceptable and it is recommended that a hydrogen generation linkage be dropped from the Goldstone solar energy system objectives. The payback period of a distributed wind-hydrogen subsystem was found to be 31 years and has an overall wind-to-hydrogen to diesel power conversion of less than 5%, as shown in Fig. 4. The payback period will be reduced to 14 years if the hydrogen linkage is deleted and a direct conversion from wind-to-electric energy is made, providing an overall conversion efficiency of 29%. Similar improvements can be made for the solar-hydrogen subsystem. The payback period is reduced from 25 years with water electrolysis to 11 years when the hydrogen link is deleted, and the corresponding overall conversion efficiency is increased from less then 1 to 4.5%.

The high cost of converting valuable electric energy (by solar-Rankine power cycles and wind turbine generators) into thermal energy (in the form of hydrogen production), then burning the hydrogen as a fuel in the diesel engines to reconvert it into electric energy (as a power output from the diesel-generator), is a highly inefficient method of energy conversion. A sequence of the energy losses in each step is presented in Fig. 4, and the effect on the payback period of the project if the hydrogen generation is eliminated is given in Tables 2-4. The effect of high cost and low efficiency of the intermediate components would preclude the economic viability even with the most advanced techniques. Future solar or wind electric power production will be limited to the direct use of electric energy instantly as generated or through energy storage and leveling devices. Meanwhile, if the need for a continuous operation of the standby diesel engines prevails, the alternate to fossil fuel would be alcohol, methane or even hydrogen brought about by the utilization of solid waste and organic residues through catalytic chemical reactions only.

(6) Dual fuel operation of diesel engines using both diesel oil and hydrogen appears to be technically feasible, but more costly. Several modifications to the existing engines have to be made with an estimated cost of $30,000/engine. Its use depends essentially on whether or not a hydrogen economy is feasible at Goldstone.

References

1. "Goldstone Energy System Study", a report prepared by Burns and Roe, Inc., as A&E service and consulting work for the DSN Engineering Section of the Jet Propulsion Laboratory. JPL/Burns and Roe Solar Position Paper, Vols. I, II, III, 1975.

2. "Hydrogen Fuel Generation" prepared by Burns and Roe, Inc., for DSN Engineering Section of JPL as part of Goldstone Energy System Study (Ref. 1).

3. Keller and Gannon Consulting Engineers, "Energy Audit and Conservation Study-Stage I," a consulting work for the Jet Propulsion Laboratory for Goldstone Energy System Study, 1974.

4. Hamilton, C. L., "A Dynamic Model for Analysis of Solar Energy Systems," *Deep Space Network Progress Report 42-27*, pp. 41-51, Jet Propulsion Laboratory, Pasadena, Calif., June 15, 1975.

5. Hamilton, C. L., "An Experiment in Dynamic Modeling for a Complete Solar-Powered Energy System," *Deep Space Network Progress Report 42-31*, pp. 137-143, Jet Propulsion Laboratory, Pasadena, Calif., Feb. 15, 1976.

6. Reid, M. S., Gardner, R. A., and Parham, O. B., "Goldstone Solar Energy Instrumentation Project: Description, Instrumentation and Preliminary Results," *Deep Space Network Progress Report 42-26*, pp. 133-144, Jet Propulsion Laboratory, Pasadena, Calif., Apr. 15, 1975.

7. Lansing, F. L., "Heat Transfer Criteria of a Tubular Solar Collector – The Effect of Reversing the Flow Pattern on Collector Performance," *Deep Space Network Progress Report 42-31*, pp. 108-114, Jet Propulsion Laboratory, Pasadena, Calif., Feb. 15, 1976.

8. Lansing, F. L., "The Transient Thermal Response of a Tubular Solar Collector," NASA Technical Memorandum 33-781, Jet Propulsion Laboratory, Pasadena, Calif., July 15, 1976.

9. Lansing, F. L., "A Two-Dimensional Finite-Difference Solution for the Transient Thermal Behavior of a Tubular Solar Collector," *Deep Space Network Progress Report 42-35*, Jet Propulsion Laboratory, Pasadena, Calif., Oct. 15, 1976.

10. Lansing, F. L., "Computer Modeling of a Single-Stage Lithium Bromide/Water Absorption Refrigeration Unit," *Deep Space Network Progress Report 42-32*, pp. 247-257, Jet Propulsion Laboratory, Pasadena, Calif., Apr. 15, 1976.

11. Reynolds, R., "Hydrogen Gas-Fueled Diesel Engine Feasibility Demonstration," *Deep Space Network Progress Report 42-27*, Jet Propulsion Laboratory, Pasadena, California pp. 199-203.

Table 1. Cost analysis of the solar heating and cooling subsystem

	Cost, $	Percent of Total
Solar collectors, 1600 m^2 supports and foundation @ $150/$m^2$	240,000	15
5 absorption refrigeration units 25 ton each @ $11,200 each	56,000	3
2 stratified storage tanks (hot and cold) of 156 m^3 each	87,000 (hot) 60,000 (cold)	5 4
Fan-coil units and duct work	295,000	18
Piping, valves and insulation (50% of that is associated with collector loop)	727,000	45
Pumps, motors, controls, accessories, house equipment	167,000	10
Total installed cost (1976 prices)	$1,632,000	100
Annual fuel cost (15% of total demand $1.8X10^6$ kWh_t) @ $0.015/$kWh_t$	4,000	
Annual electric power savings (382,000 kWh_e/yr)[a] @ $0.0384/$kWh_e$	14,600	
Annual fuel savings for heating (40,300 kWh_t/yr) @ $0.015/$kWh_t$	600	
Net annual savings	11,200	
Payback period (@ 10% energy escalation rate) and based on zero maintenance cost differential between existing and new system	29 years	

[a]Based on a cooling load of 1.146×10^6 kWh_t and coefficient of performance of the existing air-cooled unit of 3.

Table 2. Cost of a "centralized" wind-hydrogen subsystem (for 314 kW_t of hydrogen delivered)

Installation cost	Cost, $
4 electrolyzers (atm tank type) of 138 kW_e/78.5 kW_t capacity each @ $95,000 each.	380,000
10 units of wind-turbine generator (ac) (vertical axis-type) each rated at 200 kW_e and a local annual output of 120,000 kW_e hr/yr each @ $110,000 each	1,100,000
Power storage cost (flywheels, batteries, etc.) estimated @ $50/$kW_e$ for the whole plant (2000 kW_e)	100,000
Electrical transmission network (transformers, transmission lines, etc.) 2000 kW_e capacity, 13.2 kV	94,000
	$1,674,000
Operation and maintenance cost	
10-year O&M cost @ 10% of installation cost	167,400
10-yr life cycle cost	$1,841,400
Annual Fuel Savings	
(314 kW_t for 6 hr/day @ $0.015/$kWh_t$)	10,315
Payback period @ 10% energy escalation	30 years
Total installation cost of a centralized wind-turbine power plant with no hydrogen production	1,294,000
Annual electrical energy savings (120,000 kWh_e per turbine @ $0.0384/$kWh_e$)	46,080
Payback period @ 10% escalation rate	14 years

Table 3. Cost of a "distributed" wind-hydrogen subsystem (for 314 kW_t of hydrogen delivered)

Installation	Cost, $
10 electrolyzers (atm tank type) of 55 kW_e/31.4 kW_t capacity each @ $56,000 each	560,000
10 units of wind-turbine generator (dc) (vertical axis type) each rated at 205 kW_e and a local annual output of 120,000 kWh_e/yr each @ $130,000 each (increased cost for dc generation)	1,300,000
Power storage cost (estimated at $50/$kW_e$) for a plant 2000 kW_e capacity	100,000
Total installation cost	$1,960,000
10-year operation and maintenance cost @ 10% of installation cost	196,000
10-yr life cycle cost	$2,156,000
Annual fuel savings (314 kW_t for 6 hr/day @ $0.015/$kWh_t$)	10,315
Payback period @ 10% escalation rate	31 years
Total installation cost of a distributed wind turbine power plant without hydrogen production	1,400,000
Annual electric energy savings (120,000 kWh_e per turbine @ $0.0384/$kWh_e$)	46,080
Payback period @ 10% escalation rate	14.6 years

Table 4. Cost of a solar-hydrogen subsystem producing 300 kW_t of hydrogen

Approach (1)	Cost, $
Collectors cost: 16,250 m^2 @ \$127.7/m^2	2,075,000
Storage cost: storing 40,080 kWh_t/day @ \$21.9/kW_thr	877,000
One complete Rankine-cycle engine (heat exchanger, turbine generator, condenser, cooling tower, control and piping). Net output 526 kW_e	300,000
One electrolyzer (composed of 10 small units of 30.0 kW_t each)	560,000
Total installation cost	3,812,000
10 year operation and maintenance cost @ 10% of installation cost	381,000
Ten-year life cycle cost	4,293,000
Approach (2)	
Collectors cost: 16,253 m^2 @ \$127.7/m^2	2,075,000
3 installed Rankine-cycle engines (complete with heat exchanger, turbine-generator, condenser, cooling tower, etc.) Net output 526 kW_e each. Each @ \$300,000	900,000
3 electrolyzer units complete with accessories @ \$560,000 each	1,680,000
Total installation cost	4,655,000
10-yr operation and maintenance cost @ 10% of installation cost	466,000
Ten-year life cycle cost	5,121,000
Annual fuel savings (300 kW_t for 24 hr/day @ \$0.015/kWh_t)	39,420
Payback period of Approach (1)	24.8 years
Payback period of Approach (2)	26.8 years
If the solar power subsystem is installed without electrolyzers or hydrogen production	
Annual electrical savings (526 kW_e for 24 hr/day @ \$0.0384/kWh_e)	176,940
Approach (1)	
Installation cost	3,252,000
Payback period	10.9 years
Approach (2)	
Installation cost	2,975,000
Payback period	10.4 years

Table 5. Cost comparison between a wind-hydrogen subsystem module and a solar-hydrogen subsystem module each having 300 kW_t nominal capacity of hydrogen

A.	Wind-hydrogen subsystem[a]	Cost, $
	Total installation cost (10 electrolyzers, 10 wind-turbine dc generators, power storage), actual output = 314 kW_t hydrogen.	1,470,000
	10-yr operation and maintenance cost @ 10% of installation cost as in Table 3	196,000
	Ten-year life cycle cost	$1,666,000
	Annual fuel savings @ $0.015/$kWh_t$	10,315
	10-yr fuel savings	103,200
	Payback period @ 10% escalation	31 years
B.	Solar-hydrogen subsystem[b]	
	Total installation cost (collectors, thermal storage tanks, Rankine power cycle, 10 electrolyzers)	3,812,000
	10-yr operation and maintenance cost @ 10% of installation cost	381,000
	Ten-year life cycle cost	4,293,000
	Annual fuel savings @ $0.015/$kWh_t$	39,420
	10-yr fuel savings	394,200
	Payback period @ 10% escalation	24.8 years

[a]This is the "distributed" wind-hydrogen subsystem presented in Table 3. A discount of 25% of the installation cost is superimposed provided that this configuration is mass produced.

[b]This is the solar-hydrogen subsystem of approach (1) presented in Table 4.

Table 6. Annual energy consumption at Goldstone (1973 data)

Site	Load								
	Total gas heating, kWh_t	Total electrical heating, kWh_t	Total heating energy (gas and electrical), kWh_t	Electric consumption (excluding heating), 10^6 kWh_e	Average electric load (excluding heating), kW_e	Cooling load consumption, kWh_t	Average cooling load, kW_e	Peak cooling load, tons	Average electric load (excluding heating and cooling), kW_e
DSS 11 (Pioneer)	522,100	74,400	596,500	2.91	332	921,300	45	89	287
DSS 12 (Echo)	3,098,300	122,400	3,330,700	5.20	594	2,255,400	120	188	474
DSS 13 (Venus)	333,900	66,700	400,600	2.17	248	718,300	27	62	221
MW test facility	116,400	--	116,400	0.20	23	106,600	4	10	19
DSS 14 (Mars)	--	538,200	538,200	8.06	920	1,744,800	69	122	851
Apollo	--	1,116,800	1,116,800	6.42	732	3,314,000	136	151	596
Mojave	--	678,100	678,000	3.04	347	1,555,700	74	95	273
Total	4,070,700	2,596,600	6,667,300	28.00	3196	10,616,100	475	717	2721

Table 7. Annual heating and cooling requirements of major load buildings of GSCC

Station	Pioneer		Echo			Mars			Mojave/Apollo		
Major Load Building	G-1	G-18	G-21	G-26	G-33	G-38	G-80	G-86	MS-8	A-1	A-2
Annual heating requirement, kWh_t	48,200 (gas)	194,200 (gas)	308,800 (gas)	234,600 (gas)	201,800 (gas)	685,700 (gas)	282,200 (elec)	186,800 (elec)	397,500 (elec)	769,600 (elec)	287,700 (elec)
Annual cooling requirement, kWh_t	713,800	81,000	181,300	835,900	302,300	765,000	357,000	1,261,000	1,356,000	2,880,000	349,600
Percentage of station heating requirement, %	15.2	61.3	16.55	12.57	10.81	36.75	52.42	34.69	58.6	68.89	25.75
Total percentage of station heating	76.5			76.68			87.11		58.6	94.64	
Percentage of station cooling requirement, %	77.49	8.79	8.04	37.06	13.4	33.92	20.47	72.27	[illegible]	[illegible]92	10.55
Total percentage of station cooling	86.28			92.42			92.74		87.15	97.47	
Peak cooling load of major buildings, tons	69.3			163			106			193	
Peak heating load of major buildings, kW_t	200			460			168			–	
Installed cooling capacity, tons	191 (DX type)			353 (DX type)			(260) total w. chilled DX			323	
Installed heating capacity, kW_t	483 (gas-fired)			678 (gas-fired)			250 (elec)			389 (elec)	

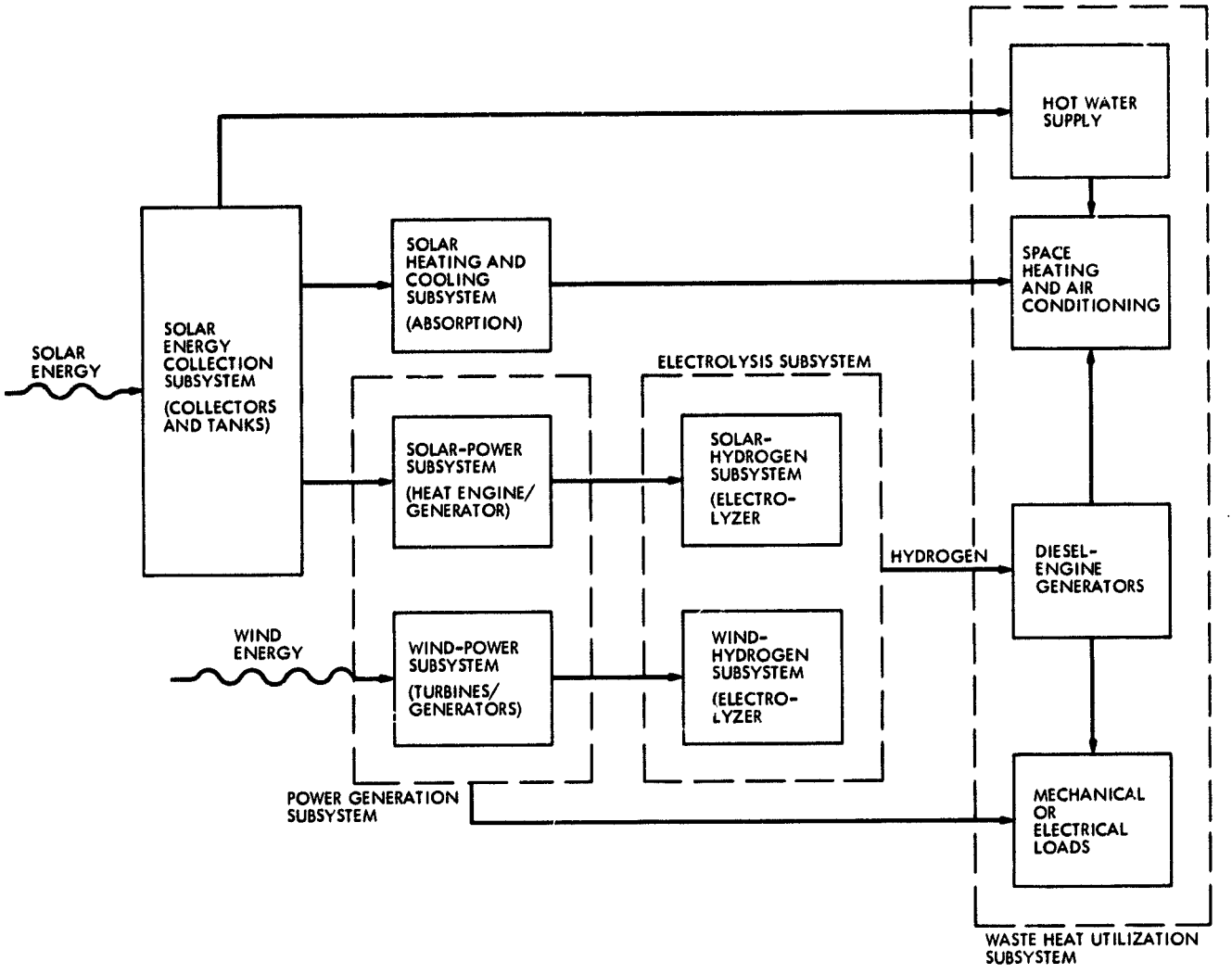

Fig. 1. Outline of Goldstone solar energy system

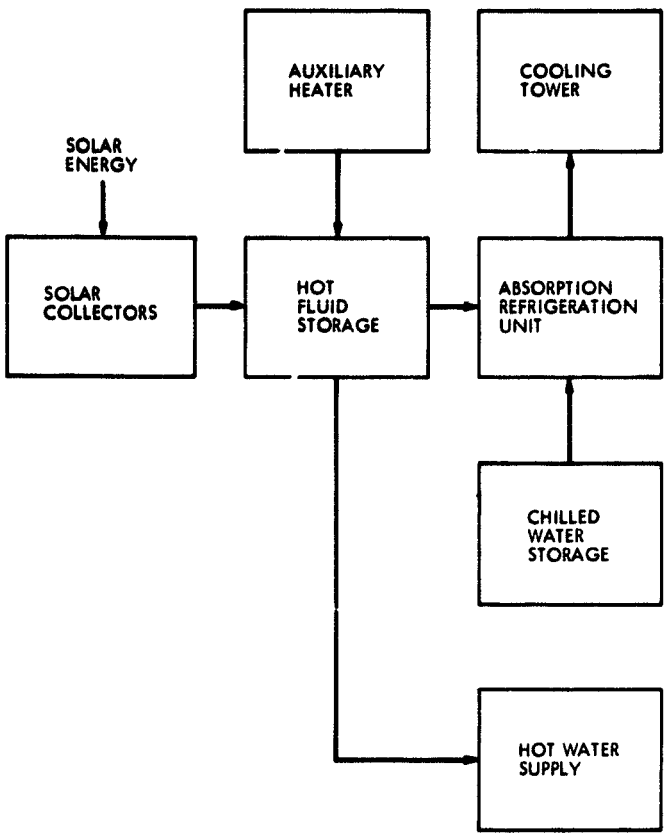

Fig. 2. Solar heating and cooling subsystem

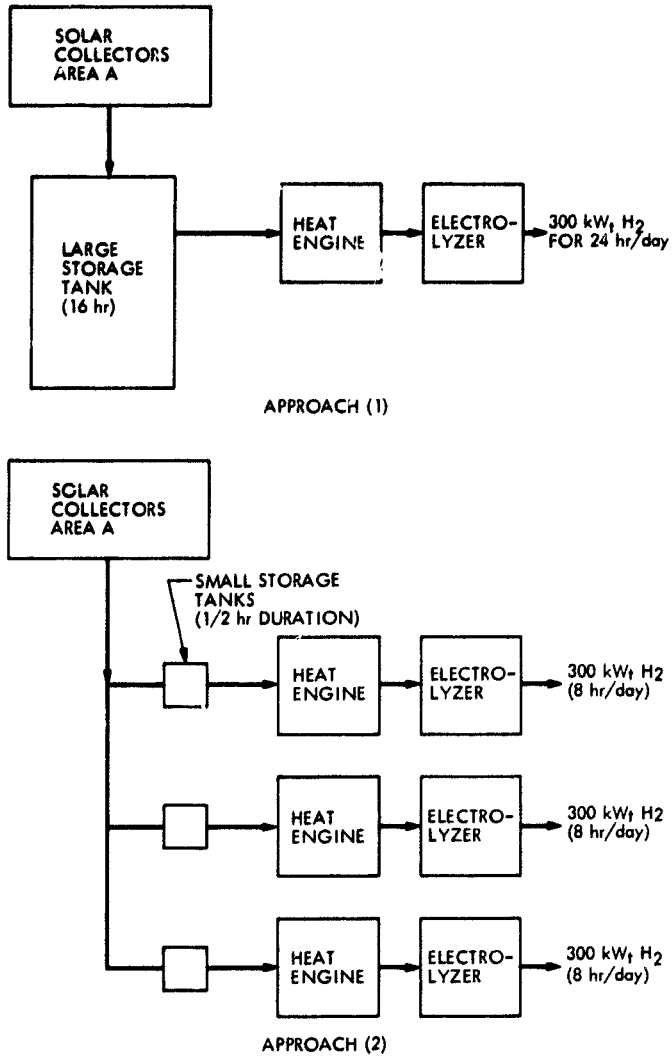

Fig. 3. Comparison of Approaches (1) and (2) of the solar hydrogen subsystem

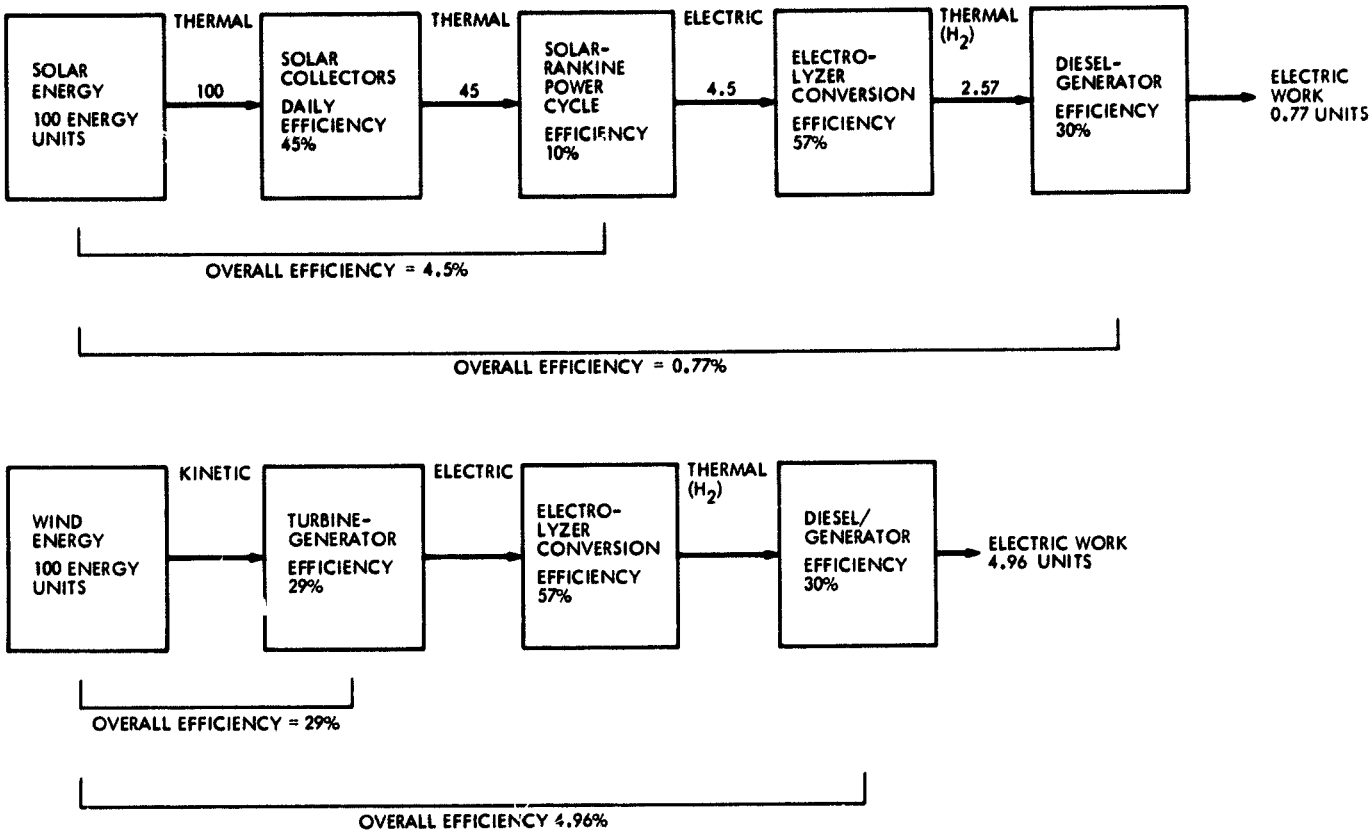

Fig. 4. Efficiency of cascaded energy systems; solar and wind to hydrogen conversion

Pioneer Venus Wind Experiment Receiver

H. Nishimura
Radio Frequency and Microwave Subsystems Section

The final design of the Pioneer Venus Wind Experiment Receiver and Phase Calibrator is discussed from the block diagram viewpoint. Measured phase data are shown to derive the predicted performance. The STDN receiver implementation is also discussed.

I. Introduction

The Pioneer Venus 1978 (PV 78) project consists of an orbiter and a multiprobe Mission. The orbiter will be inserted into a Venusian orbit with a mission lifetime of 243 Earth days. The multiprobe portion consists of a bus and four aerodynamic probes which are delivered into the Venusian atmosphere (Ref. 1). One of the experiments to be conducted by the probe descent phase consists of relative wind drift measurements. The five signals from the probes and bus will be received by open-loop receivers located at DSS 14 and DSS 43 and STDN receivers located on the island of Guam and in Santiago, Chile. This article will concentrate on the design requirements and characteristics of the DSN Wind Experiment Receiver plus a short discussion of the modification of the existing STDN receivers for use in the wind experiment.

II. Requirements

The electrical requirements for the DSN receiver are shown in Table 1. Included are the requirements for the phase calibrator which is used to measure and correct receiver phase variations. The receiver will be connected to the output of the traveling wave maser (TWM) amplifier.

III. Description

A. Overall Block Diagram

Figure 1 shows the simplified block diagram of the overall DSN receiver including the calibrator. Isolators, attenuators, and most of the amplifiers and filters have been deleted from the diagram to facilitate the overall description.

The Wind Experiment Receiver is an open-loop, constant-gain receiver which accepts the S-band carriers of the Pioneer Venus probes. The information bandwidth of 2 MHz was selected on the basis of the predicted doppler excursion of the four descending probes and bus – including the spare probe and the redundant bus frequencies, if required. Also included in this passband are the phase calibration signals which are located at the outer edges of the band. Wind drift measure-

ments will be accomplished by long baseline differential interferometry (DLBI) and the conventional doppler frequency spacecraft tracking methods. The DLBI method is an earth-based observation for obtaining the probes' and bus's relative velocities. Three velocity components are obtained for these measurements: (1) An angular velocity component relative to the earth-based two-station baseline, (2) another angular velocity component orthogonal to the first due to the additional two-station baseline, and (3) the radial velocity component relative to the earth. The first component is determined by measuring the differential time delay of a given probe's signal received and recorded by two tracking stations (DSN receivers). The second is determined by two orthogonally located baseline stations (STDN receivers) which receive and record the signal in a similar manner. The angular velocities are determined after cross-correlating the recorded data of the two-station pairs. The radial velocity component is determined by the doppler shift of the recorded probes' and bus frequencies after processing. The bus's relative velocity to the planet Venus is obtained by the conventional two-way doppler utilizing closed loop receivers.

Hence, the resultant information obtained is the relative velocities of the probes and the bus to each other and to the planet Venus as a function of time.

Basically, the receiver is a double conversion device capable of accepting an input between 2245 and 2345 MHz and an output in the 100-kHz to 2-MHz frequency range. In order to provide accurate determinations of the two angular velocity components, two differentially phase stable calibration signals are injected into the front end of the receiver. These signals, which are stable with respect to each other to within one degree of phase, provide a measurement of the phase delay variations from one edge of the band to the other.

The composite signal, consisting of the carriers and the calibration tones, is recorded. For an additional calibration of phase of the overall ground tracking system before and after tracking, provision is made for the injection of the calibration signals into the system before the TWM.

In Fig. 1, the antenna and control room portions of the receiver are shown separately and interconnected by low-loss coaxial cables. In general, the higher frequency S-band sections are located in the antenna to minimize the front end losses. The IF and lower frequency circuits are in the control room.

B. Main Signal Channel

The block diagram shows the S-band probe carriers entering the TWM. At its output the S-band signals are distributed to the telemetry receivers and to the Wind Experiment Receiver's first mixer (MIX) input. The signals are down-converted by a 2000-MHz phase-stable first LO to an intermediate frequency of 292 MHz. The first IF amplifier (IF AMP) provides enough gain to drive the single sideband mixer (SSB MIX) located in the control room. The band pass filter (BPF) is designed for a 100-MHz bandwidth and assures a linear phase delay at the probe carrier frequencies. SSB MIX has a 30-dB image rejection and 2-deg peak-to-peak phase ripple. SSB MIX is driven by a 291-MHz second LO, which is derived by multiplying the synthesizer output frequency. Output rejection is provided by a Tchebycheff low-pass filter (LPF) which is phase-equalized to within 10% of linearity.

C. First Local Oscillator

For the purpose of achieving a significant improvement in phase stability, the times-20 frequency multiplier (X20) and the coaxial 100-MHz cable connected at the reference input of the X20 are both phase-stabilized. The X20 is a commercial phase-locked design driven by an external reference frequency of 100 MHz. Like most multipliers, the long-term phase stability is a function of the ambient temperature. The overall phase drift is lowered from 60 to 2.5 deg of phase by placing the unit within a temperature-controlled component oven with an internal temperature of 60 ± 0.12°C. The coaxial cable employs a cable stabilizer circuit at each end of its length to minimize its phase variations. Measurements of long lengths of uncompensated cables which are exposed to external station environment have shown that phase changes at radio frequencies are particularly severe during the night-day and day-night transitions as the cables are heated or cooled. The stabilizer circuit reduces the expected phase variations from 76 to 5 deg of phase. The circuit consists of a phase-locked loop which senses phase variations at the terminating end of the cable and appropriately corrects a voltage-controlled phase shifter at the source end of the cable.

D. Calibrator

The calibrator generates the differentially phase stable calibration signals at S-band. The circuit is based on the Haystack Observatory method of generating a broadband of pulses from a tunnel diode generator. The diode is driven by a phase-stable 5.4-MHz square wave. As the pulses emerge from the diode, a diode switch gates the output at 1.8 MHz, the approximate frequency spread required for the calibration signals at S-band. At S-band, these signals, which are positioned at the extremities of the overall bandwidth, are at 2291.1 and 2292.9 MHz. During track, the calibrator switch is placed in the operational mode and calibration signals are injected into the S-band line after the microwave distribution assembly, but before the receiver's first mixer. This method prevents interfering phase calibration pulses from being coupled into the telemetry receivers.

The 5.4-MHz square wave is derived from the output of a divide-by-8 (÷8) circuit. The ÷8 is driven from synthesizer SYNTH 1 at 43.2 MHz, which is referenced to the 100-MHz hydrogen maser.

E. Pre/Post Tracking Calibration

As shown in Fig. 1, the pre/post calibration circuits utilize the original calibration drive frequency of 43.2 MHz and compare its phase after frequency division to the phase of the calibration signals recovered at the receiver output. The result gives a measure of the phase stability of the overall ground system before and after tracking. Note that the calibration switch is placed in the PRE/POST CAL position during the tests to permit calibration signals to be injected ahead of the TWM.

The 43.2 MHz from SYNTH 1 is divided by a factor of 24 to obtain 1.8 MHz, the same pulse repetition rate of the two calibration signals. The 1.8 MHz is applied to the reference input of the phase meter.

At the receiver output, the calibration signals are recovered, then mixed, to obtain the difference product at 1.8 MHz. This second 1.8-MHz signal is also applied to the phase meter for a phase comparison with the reference.

F. Phase Stability

Table 2 shows phase stability data of the major components within the receiver. Except where indicated as estimated, the data were measured at the expected operating frequencies. The calibrator data was obtained from a Haystack report (Ref. 2).

The table is divided essentially into two areas. The left two columns contain phase information under assumed room temperature variations, ±3°C, and with no first LO cable stabilization. The right two columns are with ±0.12°C oven temperature control on the first LO and with cable stabilization of the first LO cable. The columns headed "2-hr" and "4-hr" refer, respectively, to mission duration and to the interval between calibrations.

G. STDN Receiver

The existing STDN S-band receivers (Fig. 2) are being modified to satisfy the requirements of the wind experiment. Since STDN is not committed to providing probe telemetry, the calibration signals will be injected into the S-band signal line before the parametric amplifier. Operational and pre/post calibration measurements will be conducted from a single injection point. The first LO and mixer of the STDN receivers remain unchanged. An output from the STDN distribution coupler provides a 492-MHz IF to the added-on wind experiment receiver. This signal is amplified by amplifier IF AMP and down-converted by a single-sideband mixer, the same unit as used in the DSN receivers. The composite output signal is sent to the A-D converter. The output can also be phase-compared for pre/post tracking as in the DSN receivers.

IV. Conclusion

The design is expected to meet the PV 78 requirements for phase stability and calibration. The prototype is presently under construction using commercial parts wherever possible. The stations are expected to be operational by the middle of March 1978.

References

1. Miller, R. B., "Pioneer Venus 1978 Mission Support," in *The Deep Space Network Progress Report 42-20*, pp. 17-19, Jet Propulsion Laboratory, Pasadena, Calif., Apr. 15, 1974.

2. "VLBI Phase and Group Delay Calibration System," Technical Note 1975-1, Haystack Observatory, Massachusetts Institute of Technology, Boston, Mass.

Table 1. Electrical requirements

Parameter	Requirement
Input signal frequency range for probe and calibration signals	2291.1 to 2292.9 MHz
Receiver noise figure	≤8.0 dB
Phase calibrator	
Phase stability (over four hours)	≤1 deg phase variation between calibration signals
Signal level	≥94 dBm into receiver front end via coupler
Frequencies	2291.1 to 2291.15 MHz lower calibration signal; 2292.9 to 2292.95 MHz upper calibration signal
Receiver composite output signal	
Frequency range	0.1 to 1.9 MHz
Phase ripple	2 deg peak-to-peak
Phase linearity	9-pole Tchebycheff response. Phase equalized to within 10% of linear
Amplitude response	≥10 dB down at 2.26 MHz

Table 2. Receiver phase stability

	No temp. control, ±3°C, no cable stabilization		1st LO temp. control ±.12°C with cable stabilization	
	2-hr	4-hr	2-hr	4-hr
Main signal channel				
Phase variation of one signal in passband				
H_2 maser, 10^{-14}	60	120	60	120
Cable, 100 MHz	76	152	5	10
X20 freq. mult.	60	60	2.5	2.5
S-band mixer (est.)	2	2	2	2
IF amp and BPF	4.2	4.2	4.2	4.2
Cable, IF	6.4	12.8	6.4	12.8
Synthesizer	3.6	3.6	3.6	3.6
Freq. mult. (est.)	3	3	3	3
SSB mixer and LPF	0.6	0.6	0.6	0.6
Video amp.	0.4	0.4	0.4	0.4
Total	215°	357.4°	87.7°	159.1°
Differential phase variation between two signals in passband				
S-band mixer (est.)	0.2	0.2	0.2	0.2
IF amp and BPF	8.4	8.4	8.4	8.4
Cable, IF	0.1	0.2	0.1	0.2
SSB and LPF	1.2	1.2	1.2	1.2
Video amp.	0.8	0.8	0.8	0.8
Total	10.7°	10.8°	10.7°	10.8°
Calibrator and pre/post cal				
Differential phase variation between two calibration signals				
Synthesizer	0.03	0.03	0.03	0.03
Cable, 1.8 MHz	0.06	0.12	0.06	0.12
Calibrator (est.)	0.04	0.04	–	–
Mixer, BPF (est.)	0.1	0.1	0.1	0.1
Phase meter (est.)	0.05	0.05	0.05	0.5
Total	0.28	0.34	0.24	0.30
Differential phase variation between the two calibration signals				
Calibrator (est.)	0.04	0.04	–	–
BPF and mixer (est.)	0.1	0.1	0.1	0.1
Phase meter (est.)	0.05	0.05	0.05	0.05
Total	0.2°	0.2°	0.15°	0.15°

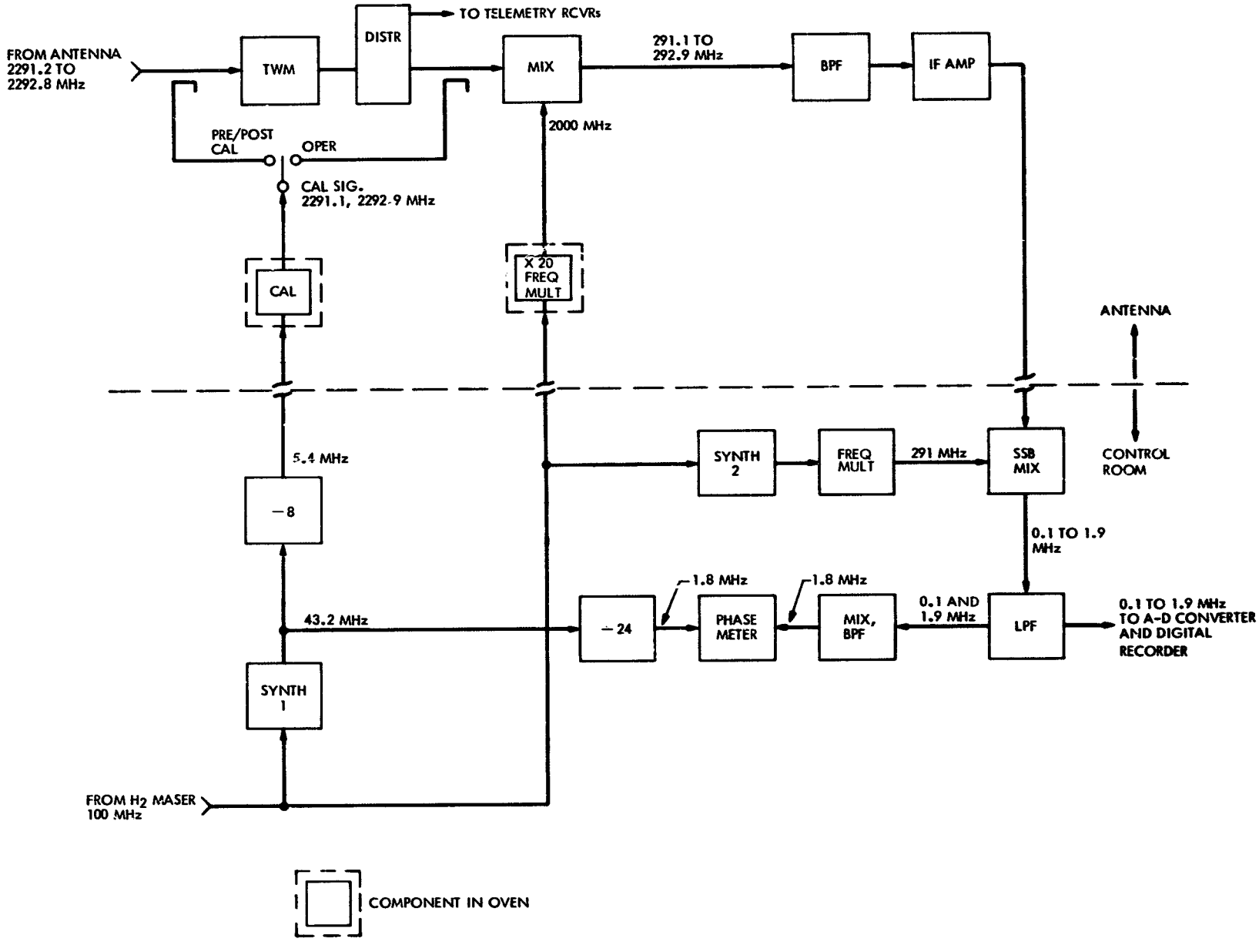

Fig. 1. DSN Wind Experiment Receiver

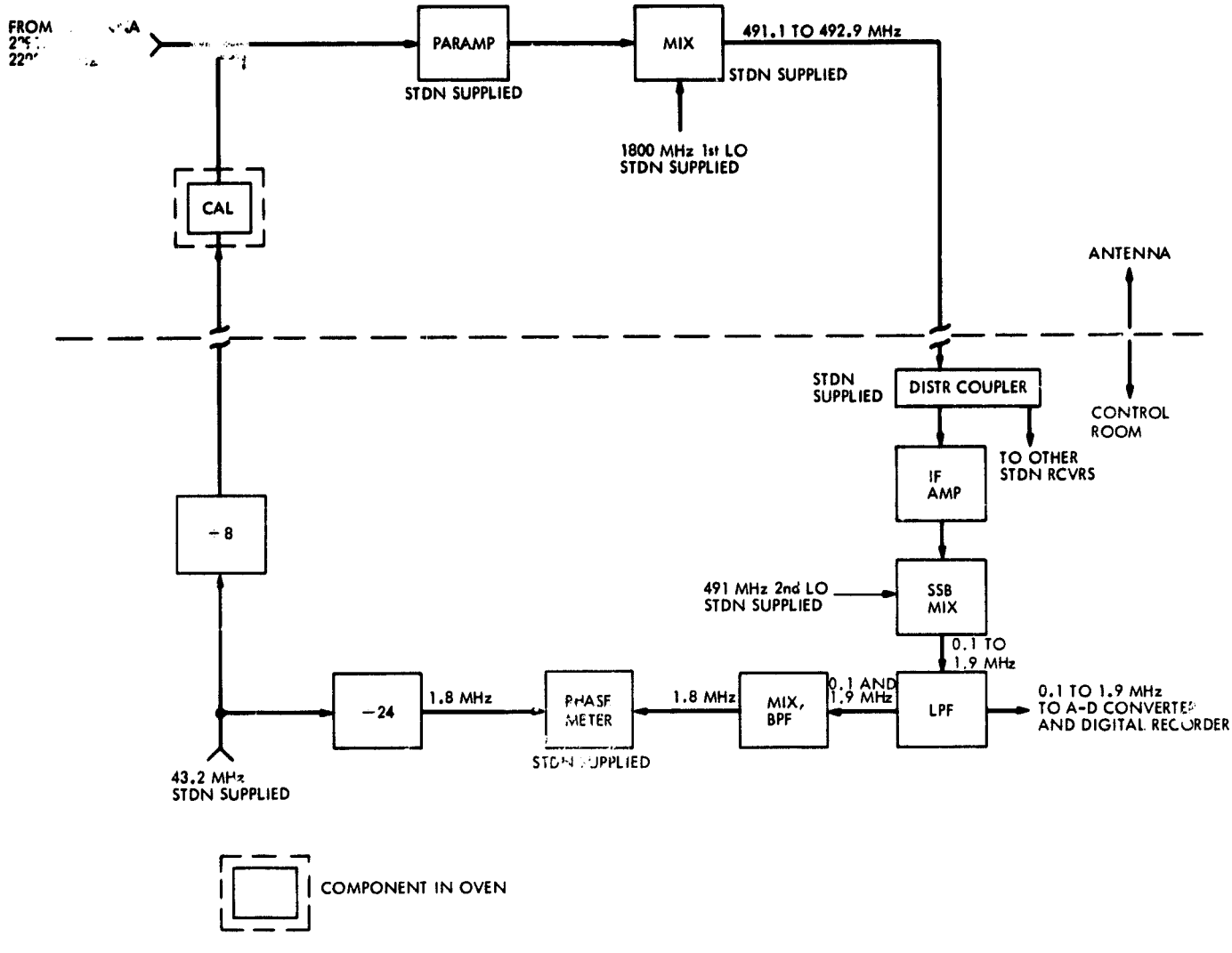

Fig. 2. STDN Wind Experiment Receiver

Pioneer Venus 1978 Multiprobe Spacecraft Simulator

S. E. Friedenberg
Radio Frequency and Microwave Subsystems Section

A test which duplicates the signals of the four probes to be deployed by the PV 78 multiprobe spacecraft has been developed. It will be used for receiver operator training prior to the mission. This article describes the operation and characteristics of the test set.

I. Introduction

The Pioneer Venus 1978 project will consist of two missions: an orbiter and a multiprobe mission. This article deals with the latter. In the multiprobe mission the spacecraft will deploy four probes, each of which will be active for a period of two hours. Only *one* opportunity exists to successfully track the probe signals, and it is necessary therefore that adequate operator training be provided before the mission takes place. To facilitate this training, a multiprobe simulator has been designed to duplicate the signal characteristics of all four probes in their proper deployment sequence. The method of simulating and timing these signals is discussed in this article.

Reference 1 describes the multiprobe mission, its scientific payload, entry sequence and associated telecommunications aspects. Reference 2 describes plans for the configuration of the Deep Space Stations in support of the multiprobe mission.

II. Multiprobe Simulator

The multiprobe simulator provides four S-band test signals, simulating the doppler, modulation and signal level of each of the four probes. Each of the S-band test signals (Fig. 1) consists of an oscillator, modulator and frequency multiplier. A voltage-controlled oscillator is used with the doppler frequency changes being simulated by varying the control voltage to the oscillator. The timings of the various events that occur with each test signal (RF turn-on, doppler, etc.) are controlled by the probe event timer. The turn-on sequence for each test signal is controlled by the probe sequence timer. These functions are discussed in the following paragraphs.

A. Doppler

Figure 2 shows a typical doppler curve of one of the probe signals. It also shows the sequence of events and their times, with reference to RF carrier turn-on, that are expected to take place. The four probe signals will be turned on sequentially at 6-minute intervals, and each will last about 90 minutes.

Telemetry modulation is not applied when the RF carrier is turned on to permit easier acquisition of the signal by receiver operators. After 5 minutes, a timer in the spacecraft turns the modulation on. The carrier decreases in frequency over the next 22 to 24 min as the spacecraft approaches the planet. At an altitude of about 200 km (entry) the probe encounters Venus's dense atmosphere and very rapid deceleration and atmospheric ionization occur, resulting in a temporary loss (blackout) of the spacecraft signals for up to 40 sec after entry. When the signal and modulation return, the probe velocity is decreased and is relatively constant. The doppler shift then becomes relatively constant and the carrier frequency is increased approximately 80 kHz above entry frequency. Impact occurs in approximately 1 hr after entry. Reference 3 describes the method of simulating the doppler profile of the signals from the probes.

B. Timing Sequence

The start of each signal source is controlled by the probe sequence timer. The timer consists of four cascaded BCD counters, driven by the station 1-second time pulse, which provide an elapsed time in seconds. A reset button is provided on the control panel (Fig. 3) to set all timing circuits to zero. The probe sequence timer is started when the large probe modulation signal is applied and detected by a level detector in this timer. The output signals are then applied to the inputs of each probe event timer, in sequence, at the required elapsed time intervals. The event timer output signals are then used in the relay control circuitry to drive the event relays.

Concurrent with the starting of each event timer, the doppler profile generator is activated. The profile generator develops the analog voltage which controls the frequency of the voltage-controlled crystal oscillator (VCXO) to closely duplicate the expected doppler profile of the received signals.

The VCXO output is coupled through a phase modulator which modulates the carrier after an elapsed time of 5 min.

The VCXO frequency is then multiplied to S-band by a X50 frequency multiplier. A signal combiner is used to combine all four sources linearly and supplies them to the station antenna.

C. Modulation

Four prerecorded modulation signals are supplied to the phase modulators from the Test and Training Subsystem. These provide modulation index and telemetry bit rate changes that occur at predetermined intervals. The phase modulators automatically apply the correct modulation indices and telemetry to each signal.

D. Signal Level

Two S-band attenuators are provided. AT-1 (Fig. 1) is a fixed attenuator that sets the signal level at the antenna input to correspond to the maximum expected signal level to be received from each probe. AT-2 is adjustable to lower the signals to near threshold levels for operator training purposes.

E. Manual Controls

Manual controls are also provided (Fig. 3). Under manual operation, the start of doppler frequency profile, turn-on of the RF signal and modulation can be controlled manually. These events can be started earlier or later than the normal start time that occurs with the sequence timer. This provides the capability of creating an abnormal sequence of events in one of the small probe signals for receiver operator training purposes.

III. Conclusion

A test set for duplicating the signals of the probes from the PV 78 Multiprobe mission has been designed. Lab measurements of a bread board unit verify that the design is adequate to simultaneously simulate the expected signals from all four probes and can be used for DSS receiver operator training, required to assure the successful collection of data from this mission.

References

1. Miller, R. B., "Pioneer Venus 1978 Mission Support," in *The Deep Space Network Progress Report 42-23*, pp. 37-40, Jet Propulsion Laboratory, Pasadena, Calif., Oct. 15, 1974.

2. Miller, R. B., "PV-78 Mission Support," in *The Deep Space Network Progress Report 42-27*, pp. 28-35, Jet Propulsion Laboratory, Pasadena, Calif., June 15, 1975.

3. Johns, C. E., "Pioneer Venus Entry Simulator," in *The Deep Space Network Progress Report 42-33*, pp. 155-158, Jet Propulsion Laboratory, Pasadena, Calif., June 15, 1976.

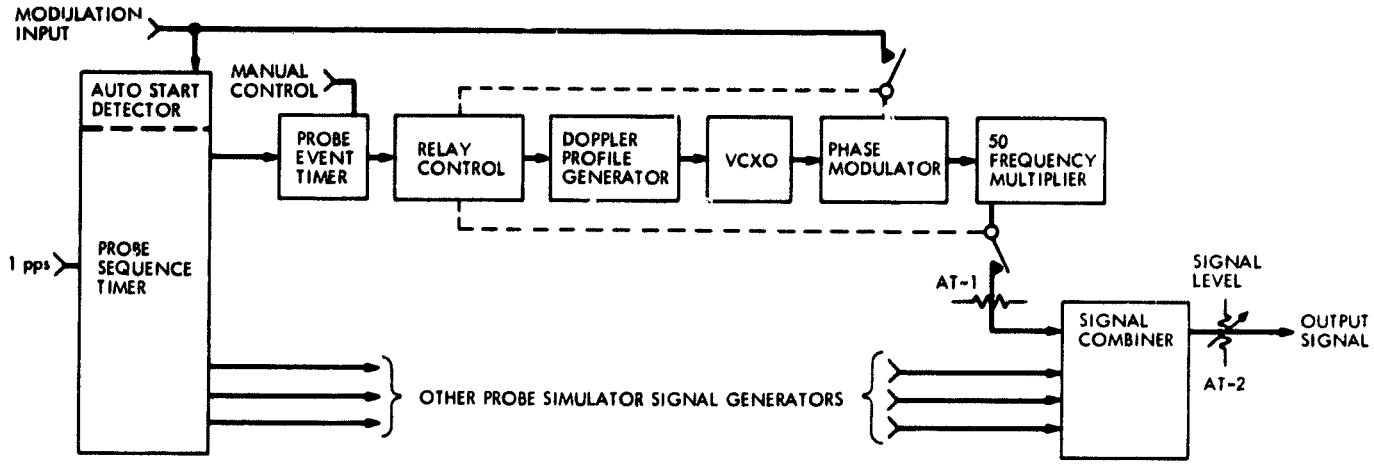

Fig. 1. Block diagram of probe simulator

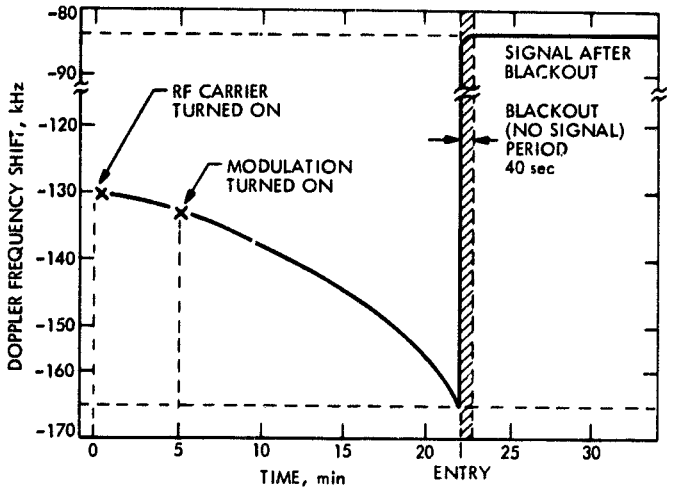

Fig. 2. Typical probe doppler profile

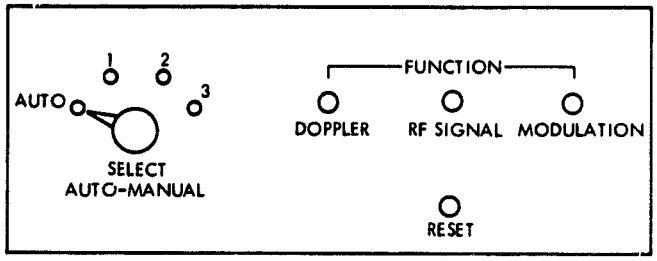

Fig. 3. Manual control panel

N77-21129

Viking S-Band Doppler RMS Phase Fluctuations Used to Calibrate the Mean 1976 Equatorial Corona

A. L. Berman
TDA Engineering Office

J. A. Wackley
DSN Network Operations Section

Viking S-band doppler rms phase fluctuations (noise) and comparisons of Viking doppler noise to Viking differenced S-X range measurements are used to construct a mean equatorial electron density model for 1976:

$$N_e(r) = \frac{2.39 \times 10^8}{r^6} + \frac{1.67 \times 10^6}{r^{2.30}}$$

where N_e is in electrons/cm^3 and r is heliocentric distance in solar radii. The model yields at 1 AU:

$$N_e(214) = 7.3 \text{ electrons/cm}^3$$

Using Pioneer doppler noise results (at high heliographic latitudes, also from 1976), an equivalent nonequatorial electron density model is approximated as:

$$N_e(r,\phi_s) = \left\{ \frac{2.39 \times 10^8}{r^6} + \frac{1.67 \times 10^6}{r^{2.30}} \right\} 10^{-0.9(|\phi_s|/90)}$$

where ϕ_s is the heliographic latitude in degrees.

I. Introduction

Since early 1975, doppler noise (rms phase fluctuations) from the Pioneer and Helios spacecraft has been shown (Refs. 1 through 9) to be well represented functionally by integrated signal path electron density. Recently, a large data base of Viking doppler noise data has been accumulated and, as expected, is also well represented functionally by integrated signal path electron density. In companion articles in this volume, the radial dependence of electron density in the extended corona is refined (Ref. 1), and the actual numerical relationship between doppler noise and integrated signal path electron density is calculated via comparison of doppler noise to concurrent measurements of differenced S-X range (Ref. 2). In this article, a combined data set of all pass-average doppler noise values (from Helios 1, Helios 2, and Viking) computed

for impact parameters of between 2 and 4 solar radii is used to refine the coefficient of the inner corona electron density term ($\sim 1/r^6$). Combining this result with those of the companion articles, a newly calibrated mean equatorial electron density model is constructed for the last half of 1976. In addition, the topics of correlation of electron density with Earth-observed solar activity and functional dependence of electron density with heliographic latitude are briefly examined.

II. The Data Base

871 points of "pass-average" Viking two-way S-band doppler noise were accumulated during the following time period:

$$168 \leq \text{Day of Year (DOY), } 1976 \leq 355$$

and for the following range of Sun-Earth-Probe (SEP) angles:

$$00.58 \leq \text{SEP, degrees} \leq 54.13$$

The data were collected from all DSSs and for all (4) Viking spacecraft. "Pass-average" doppler noise is abstracted from the output of the Network Operations Control Center (NOCC) Pseudo Residual Program. The process used in computing the noise is a "running" standard deviation about a least squares linear curve fit to the most recent 15 samples. Doppler data sample intervals in effect during the period when noise data were accumulated are listed below:

(1) 1 second

(2) 2 seconds

(3) 10 seconds

(4) 60 seconds

Normalization of the noise data to account for different sample intervals is described in detail in Refs. 2 and 3.

III. Evaluation of the Coefficient of the Outer Coronal Density Term

The term in the "ISEDC" doppler noise model (Ref. 1) that describes the noise, hence density, in the outer corona is:

$$A_0 \left[\frac{\beta}{(\sin \alpha)^{1.30}} \right] F(\alpha, \beta)$$

Residuals (in "dB") for the data base are formed between observed and predicted (ISEDC) noise as follows:

$$\Delta(\text{"dB"}) = 10 \log_{10} \left\{ \frac{\text{observed noise}}{\text{ISEDC noise}} \right\}$$

These residuals are then used to produce a standard deviation for the data base of:

$$\sigma = \left\{ \frac{1}{N} \sum_{i=1}^{N} \Delta_i^2 \right\}^{1/2}$$

Computer runs were initiated to obtain the condition:

$$\frac{\partial \sigma}{\partial A_0} = 0$$

This process yielded a value for A_0 of:

$$A_0 = 1.182 \times 10^{-3}$$

and a standard deviation for the data set of

$$\sigma = 1.617 \text{ dB}$$

Figures 1, 2, and 3 present the Viking noise data and the ISEDC model versus DOY or SEP for $A_0 = 1.182 \times 10^{-3}$. Figure 4 is a scatter diagram of observed noise and the ISEDC model for (the same) A_0.

IV. Evaluation of the Coefficient of the Inner Coronal Density Term

The term in the ISEDC model that describes the noise and density in the inner corona is:

$$A_1 \left[\frac{1}{(\sin \alpha)^5} \right]$$

The region of influence of this term is:

$$\text{impact parameter} < 4 \text{ solar radii}$$

All "pass-average" doppler noise values from Helios 1, Helios 2, and Viking which were obtained at impact parameters smaller than 4 solar radii (20 values in all) were compiled in a special data set, and computer runs were performed to obtain the condition:

$$\frac{\partial \sigma}{\partial A_1} = 0$$

This process yielded a value for A_1 of:

$$A_1 = 4.75 \times 10^{-10}$$

and a standard deviation for the data set of

$$\sigma = 1.037 \text{ dB}$$

Figure 5 is a plot of σ versus A_1 while Fig. 6 displays the fit of the observed data to the ISEDC model for $A_1 = 4.75 \times 10^{-10}$.

V. Calibration of the Mean 1976 Equatorial Corona

The functional form of the original ISED model was obtained by integrating the following electron density function:

$$N_e(r) = \frac{A}{r^6} + \frac{B}{r^{2.3}}$$

with

r = heliocentric distance

along the signal path. It is now desired to obtain electron density in the form:

$$N_e(r) = \left\{ \frac{A}{r^6} + \frac{B}{r^{2.30}} \right\} \text{ electrons/cm}^3$$

with

r = heliocentric distance, in solar radii

From Refs. 2 and 6 it is seen that (with r_0 = solar radius, meters):

$$A = \frac{r_e^5}{r_0^6}\left[\frac{8}{3\pi}\right]\left[A_1 \text{ Hz}\right]\left[\frac{7 \times 10^3 \text{m}}{\text{Hz}}\right]$$

$$\times\left[\frac{1.31 \times 10^{17} \text{ electrons/m}^2}{\text{m}}\right]$$

$$= \frac{(214)^5}{(6.95 \times 10^8)}\left[\frac{8}{3\pi}\right][4.75 \times 10^{-10}]$$

$$\times [7 \times 10^3][1.31 \times 10^{17}]$$

$$= 2.39 \times 10^{14} \text{ electrons/m}^3$$

$$= 2.39 \times 10^8 \text{ electrons/cm}^3$$

and

$$B = \frac{r_e^{1.3}}{r_0^{2.3}}\left[A_0 \text{ Hz}\right]\left[\frac{7 \times 10^3 \text{ m}}{\text{Hz}}\right]$$

$$\times \left[\frac{1.31 \times 10^{17} \text{ electrons/m}^2}{\text{m}}\right]$$

$$= \frac{(214)^{1.3}}{(6.95 \times 10^8)}[1.182 \times 10^{-3}]$$

$$\times [7 \times 10^3][1.31 \times 10^{17}]$$

$$= 1.67 \times 10^{12} \text{ electrons/m}^3$$

$$= 1.67 \times 10^6 \text{ electrons/cm}^3$$

so that the 1976 mean equatorial model becomes:

$$N_e(r) = \frac{2.39 \times 10^8}{r^6} + \frac{1.67 \times 10^6}{r^{2.30}}$$

with

N_e = electrons/cm^3

r = heliocentric distance, solar radii

The model yields at 2 solar radii:

$$N_e(2) = 4.1 \times 10^6 \text{ electrons/cm}^3$$

and at 1 AU:

$$N_e(214) = 7.3 \text{ electrons/cm}^3$$

The repeatability of coronal solutions derived from doppler noise is demonstrated via results obtained earlier with Pioneer and Helios data. In Ref. 4, 443 "pass-average" doppler noise values from the 1976 solar conjunctions of Pioneer 10, Pioneer 11, Helios 1, and Helios 2 were combined into a single data set. For the extended corona solution, a signal path integration of $r^{-2.3}$ was assumed, and, as in this article, computer runs were effected to obtain the condition:

$$\frac{\partial \sigma}{\partial A_0} = 0$$

This process yielded (p. 122 of Ref. 4):

$$A_0 = 0.1121 \times 10^{-2}$$

which corresponds to a solution for the extended corona of:

$$N_e = \frac{1.58 \times 10^6}{r^{2.3}} \text{ electrons/cm}^3$$

This solution yields a value for N_e at 1 AU of:

$$N_e(214) = 6.9 \text{ electrons/cm}^3$$

The difference in the coefficient of the $r^{-2.3}$ term (B) between the Viking solution and the Helios/Pioneer solution is thus seen to be 5%.

Table 1 compares this model to various other determinations made in the last decade or so. The critical parameter utilized in this article (7000 meters/Hz, from Ref. 2) was only approximately determined, and a more careful comparison of Viking differenced S-X range to Viking doppler noise could be expected to change the scaling of the density model by up to 10%. The ratio of the coefficients A and B would not change, however, and thus this parameter is included in Table 1 for comparison.

VI. Correlation of Viking Doppler Noise With Heliographic Latitude

In Ref. 5, Pioneer doppler noise obtained for impact parameters at very high heliographic latitudes (up to 80 degrees) was used to indicate a functional dependency of noise and hence density upon heliographic latitude of:

$$F(\phi_s) \sim 10^{-0.9(|\phi_s|/90)}$$

with

ϕ_s = heliographic latitude, degrees

The Viking impact parameter was only at a significant heliographic latitude shortly before and after solar conjunction, and even so, the highest (impact parameter) heliographic latitudes for which pass-average doppler noise was obtained were less than 30 degrees (on DOY 228 and 331). A heliographic latitude of 30 degrees produces a reduction of about 50% according to the results of the Pioneer study. This is typical of the magnitude of routine weekly fluctuations in observed doppler noise (due to solar activity), hence, it is difficult to either corroborate or refute the finding of Ref. 5. Figure 7 compares Viking noise residuals with and without the heliographic latitude correction from DOY 322 to DOY 340.

Using the functional relationship from Ref. 5, one can construct a nonequatorial model for electron density as (approximately):

$$N_e(r) = \left\{\frac{2.39 \times 10^8}{r^6} + \frac{1.67 \times 10^6}{r^{2.30}}\right\} \left[10^{-0.9(|\phi_s|/90)}\right]$$

with

N_e = electrons/cm^3

r = heliocentric distance, solar radii

ϕ_s = heliographic latitude, degrees

VII. Correlation of Viking Doppler Noise With Earth Observed Solar Activity

By way of brief review, Ref. [illegible] sumed that doppler noise could be correlated with Ea[illegible]ed sunspot activity (R_Z) by rotating $R_Z \pm 6$-3/4 day[illegible] (subtract for signal paths east of the Sun and add for signal paths west of the Sun) so as to put the "observed" region on the solar limb and propagating

towards the signal closest approach point. Then a finite propagation time was considered:

$$t_\tau \text{ (days)} = A_2 \sin \alpha$$

$$\cong A_2 \alpha$$

A_2 was varied to minimize the noise residuals, resulting in:

$$A_2 = 12 \text{ days/rad}$$

which was subsequently seen to be an "averaged" velocity of propagation of:

$$V \sim 120 \text{ km/s}$$

Callahan (Ref. 17), in a similar fashion rotated R_Z ±7 days, but did not allow for a finite propagation time. He found "moderate" correlation between spectral amplitudes and R_Z for 6 days (east of the Sun) and 10 days (west of the Sun), both results being entirely consistent with the assumption of a finite propagation time. A possibly better assumption in any future attempts of this type would be:

$$t_\tau \approx \int_0^a \frac{dr}{V_W(r)}$$

where:

a = closest approach distance

$V_W(r)$ = solar wind speed

Figure 8 presents Viking doppler noise residuals versus XR_Z (Ref. 6), which is the smoothed, phased Sunspot Index. Some regions such as that from DOY 270 to 315, appear to show some correlation. On the other hand, the region surrounding DOY 264 evidences a very strong negative correlation.

VIII. Conclusions

The authors believe that this article demonstrates the feasibility of using S-band doppler rms phase fluctuations from any (or all) spacecraft in solar conjunction phases to (more or less) continuously calibrate electron density in the solar corona. In addition, doppler rms phase fluctuations would appear to be a very useful tool in probing the time scale of electron density fluctuations (Ref. 2) and correlating electron density and density fluctuations with Earth-observed solar activity.

References

1. Berman, A. L., Wackley, J. A., Rockwell, S. T., and Kwan, M., "Viking Doppler Noise used to Determine the Radial Dependence of Electron Density in the Extended Corona," in *The Deep Space Network Progress Report 42-38* Jet Propulsion Laboratory, Pasadena, California, April 15, 1977 (published in this volume).

2. Berman, A. L., "Proportionality Between Doppler Noise and Integrated Signal Path Electron Density Validated by Differenced S-X Range," in *The Deep Space Network Progress Report 42-38* (this volume), Jet Propulsion Laboratory, Pasadena, California, April 15, 1977 (published in this volume).

3. Berman, A. L., "A Comprehensive Two-Way Doppler Noise Model for Near-Real-Time Validation of Doppler Data," in *The Deep Space Network Progress Report 42-37*, Jet Propulsion Laboratory, Pasadena, California, February 15, 1977.

4. Berman, A. L., Wackley, J. A., and Rockwell, S. T., "The 1976 Helios and Pioneer Solar Conjunctions – Continuing Corroboration of the Link Between Doppler Noise and Integrated Signal Path Electron Density," in *The Deep Space Network Progress Report 42-36*, Jet Propulsion Laboratory, Pasadena, California, 15 December 1976.

5. Berman, A. L., Wackley, J. A., Rockwell, S. T., and Yee, J. G., "The Pioneer 11 1976 Solar Conjunction: A Unique Opportunity to Explore the Heliographic Latitudinal Variations of the Solar Corona," in *The Deep Space Network Progress Report 42-35*, Jet Propulsion Laboratory, Pasadena, California, 15 October 1976.

6. Berman, A. L., and Wackley, J. A., "Doppler Noise Considered as a Function of the Signal Path Integration of Electron Density," in *The Deep Space Network Progress Report 42-33*, Jet Propulsion Laboratory, Pasadena, California, 15 June 1976.

7. Berman, A. L., "Analysis of Solar Effects Upon Observed Doppler Data Noise During the Helios 1 Second Solar Conjunction," in *The Deep Space Network Progress Report 42-32*, Jet Propulsion Laboratory, Pasadena, California, 15 April 1976.

8. Berman, A. L., and Rockwell, S. T., "Correlation of Doppler Noise During Solar Conjunctions with Fluctuations in Solar Activity," in *The Deep Space Network Progress Report 42-30*, Jet Propulsion Laboratory, Pasadena, California 15 December 1975.

9. Berman, A. L., and Rockwell, S. T., "Analysis and Prediction of Doppler Noise During Solar Conjunctions" in *The Deep Space Network Progress Report 42-30*, Jet Propulsion Laboratory, Pasadena, California, 15 December 1975.

10. Weisberg, J. M., Rankin, J. M., Payne, R. R., and Counselman III, C. C., "Further Changes in the Distribution of Density and Radio Scattering in the Solar Corona," *The Astrophysical Journal*, 209, October 1, 1976.

11. Anderson, J. D., et al., "Experimental Test of General Relativity Using Time Delay Data from Mariner 6 and Mariner 7," *The Astrophysical Journal*, August 15, 1975.

12. Muhleman, D. O., Anderson, J. D., Esposito, P. B., and Martin, W. L., "Radio Propagation Measurements of the Solar Corona and Gravitational Field: Applications to Mariner 6 and 7," in *Proceedings of the Conference on Experimental Tests of Gravitational Theories*, California Institute of Technology, Pasadena, California, November, 1970.

13. Dutcher, G. L., *A Communication Channel Model of the Solar Corona and the Interplanetary Medium*, CSRT-69-1, Center for Space Research, Massachusetts Institute of Technology, 1969.

14. Saito, Kuniji, "A Non-Spherical Axisymmetric Model of The Solar K Corona of The Minimum Type," *Annals of The Tokyo Astronomical Observatory*, University of Tokyo, Second Series, Volume XII, Number 2, Mitaka, Tokyo, 1970.

15. Newkirk, G., "Structure of The Solar Corona," in The *Ann. Rev. Astron. Astrophys.*, 1967.

16. Stelzreid, C. T., "A Faraday Rotation Measurement of a 13 CM Signal in the Solar Corona," Technical Report 32-1401, Jet Propulsion Laboratory, Pasadena, California, July 15, 1970.

17. Callahan, P. S., "Observations of The Solar Wind Turbulence Near The Sun," Doctoral Thesis, 1975, California Institute of Technology, Pasadena, California.

Table 1. Coronal model comparisons

Source	Ref.	$A \times 10^{-8}$	$B \times 10^{-6}$	A/B	ξ	$N_e \times 10^{-6}$ at $2r_0$	N_e at 1 AU	Solar Cycle
Berman & Wackley[a]		2.39	1.67	143	0.30	4.1	7.3	Min
Berman & Wackley[b]			1.58		0.3		6.9	Min
Weisberg, et al.	10		1.60		0.3		7.0	Min
Weisberg, et al.	10		0.94		0.1		12.1	Min
Anderson, et al.	11	0.69	0.54	127	0.05	1.2	9.0	
Muhleman, et al.	12	1.92	1.41	136	0.41	3.3	3.4	Max
Muhleman, et al.	12	1.30	1.15	113	0.3	2.3	5.0	
Muhleman, et al	12	0.80	0.51	156	0.3	1.4	2.2	Max
Dutcher	13						6	
Saito	14	1.58	2.51	63	0.5	2.9	3.8	
Blackwell, et al.	11	2.62	2.07	126	0.33	4.5	7.7	Max
Blackwell, et al.	11	1.01	2.01	50	0.33	2.0	7.5	Min
Blackwell & Petford	11	1.18	1.46	81	0.3	2.1	6.4	Min
Newkirk	15					5.6	5.0	Max
Newkirk	15					2.8	2.5	Min
Allen – Baumbach	16	1.55	1.00	155	0.0	2.7	21.6	

[a]Viking data.

[b]Pioneer and Helios data.

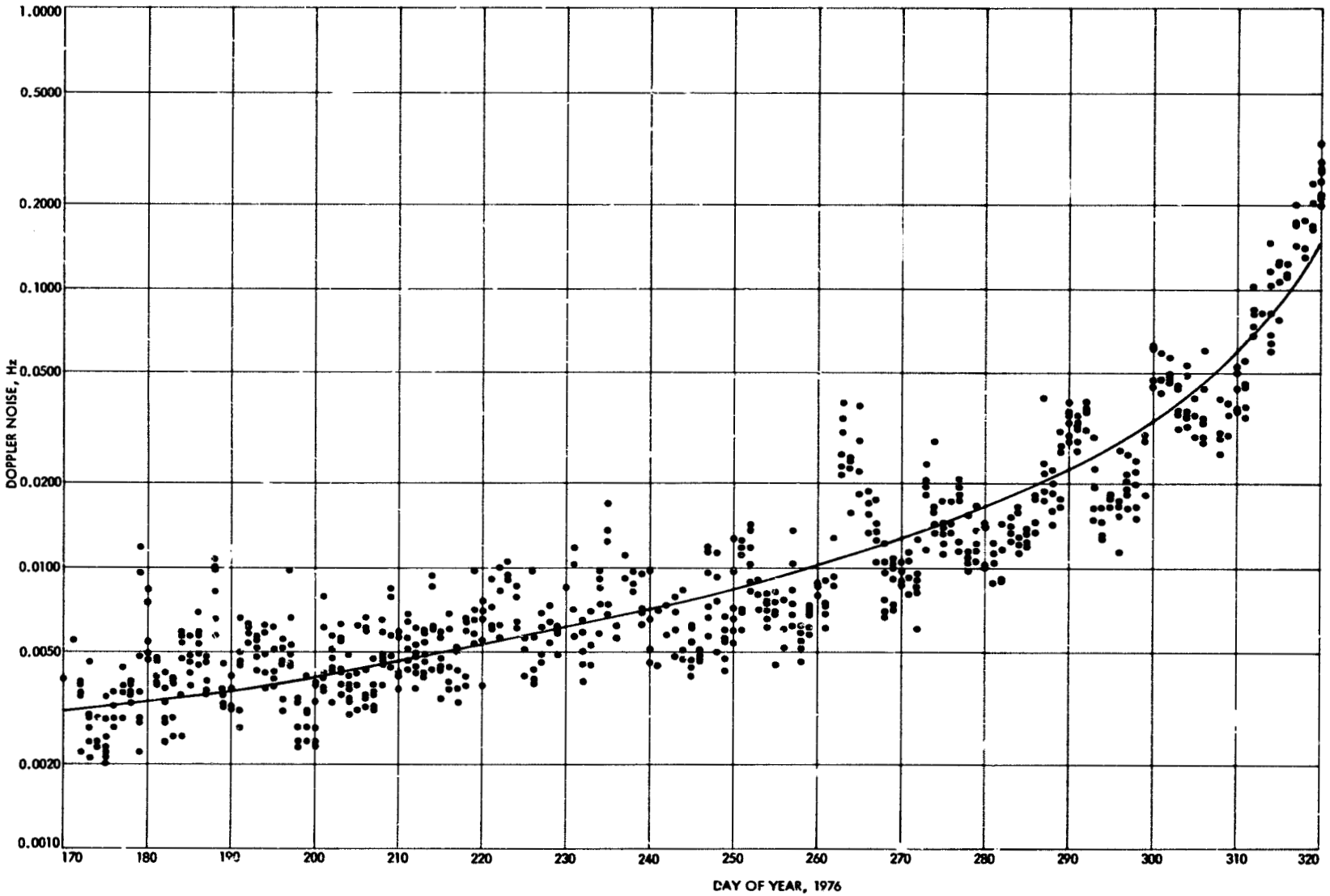

Fig. 1. Viking doppler noise and the ISEDC model vs day of year (170 to 320)

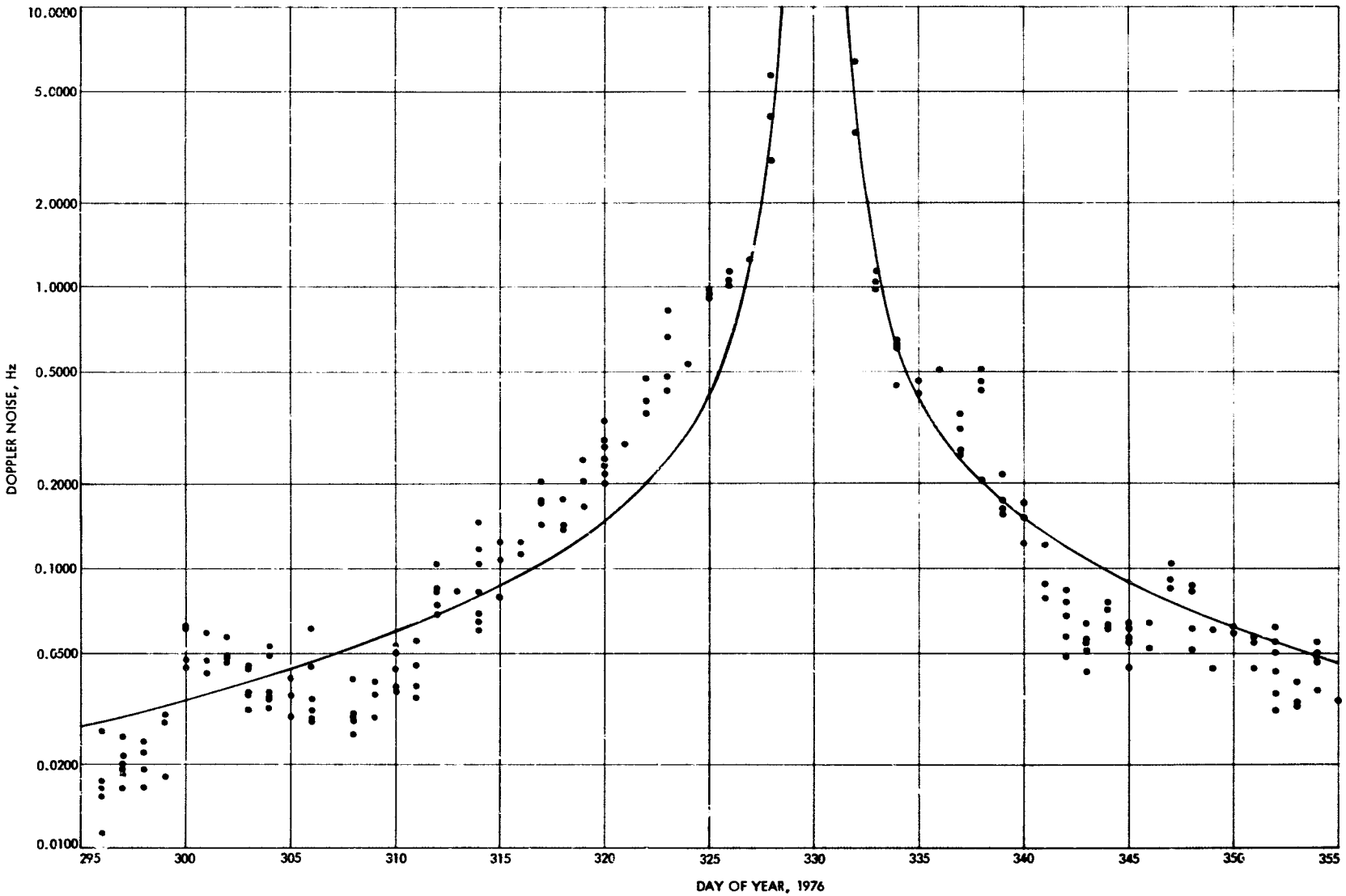

Fig. 2. Viking doppler noise and the ISEDC model vs day of year (295 to 355)

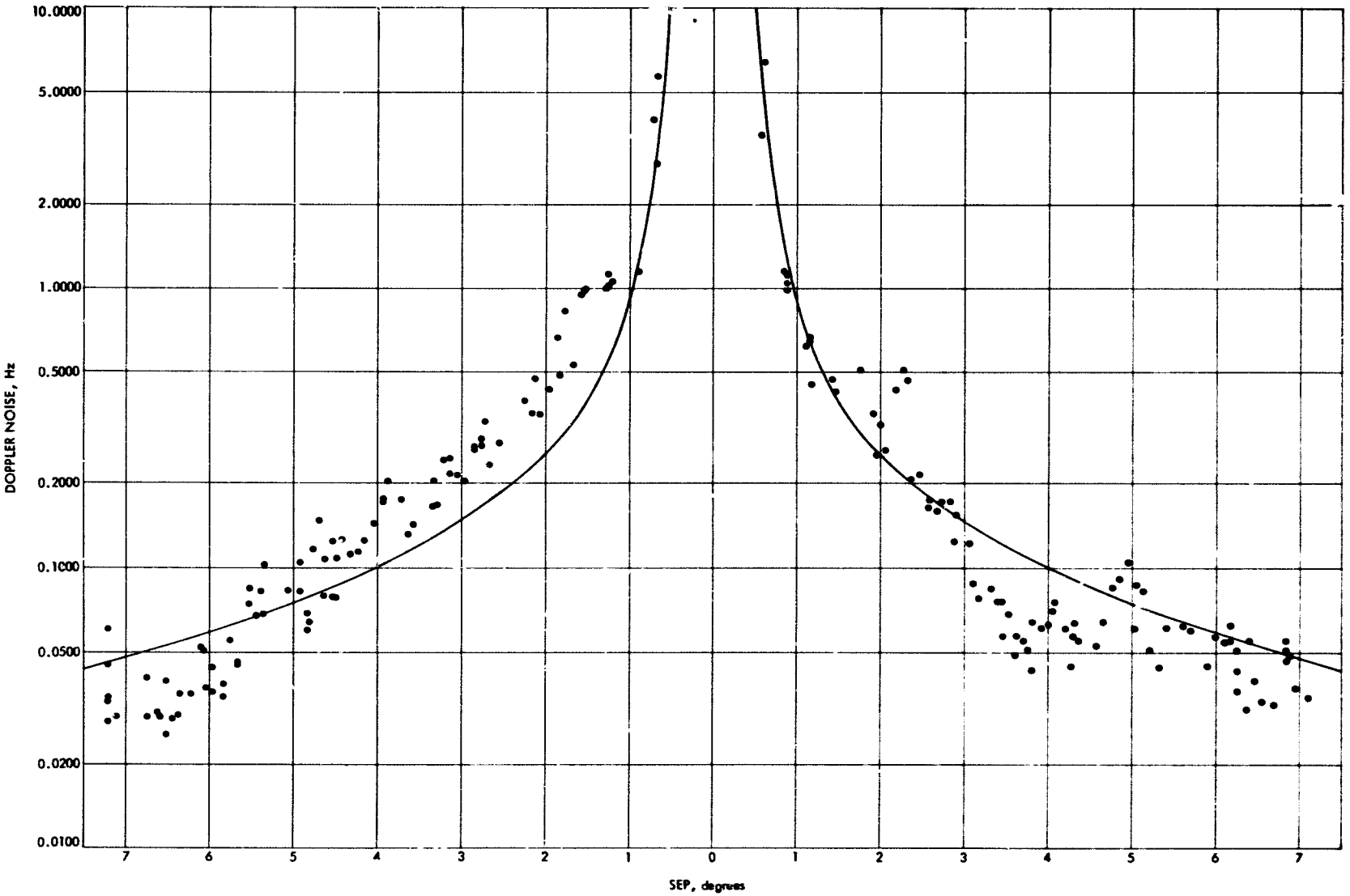

Fig. 3. Viking doppler noise and the ISEDC model vs SEP angle

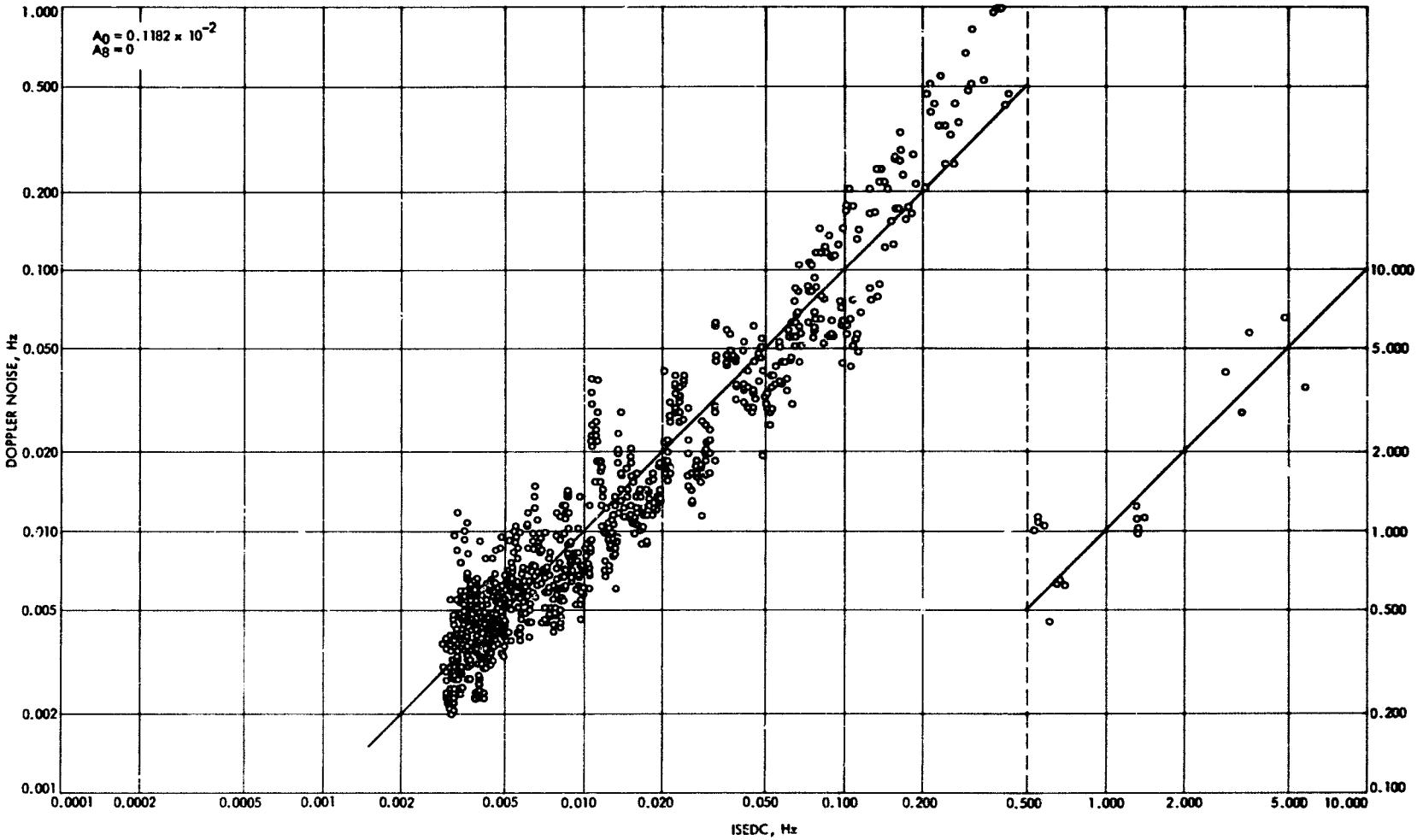

Fig. 4. Viking doppler noise vs the ISEDC model

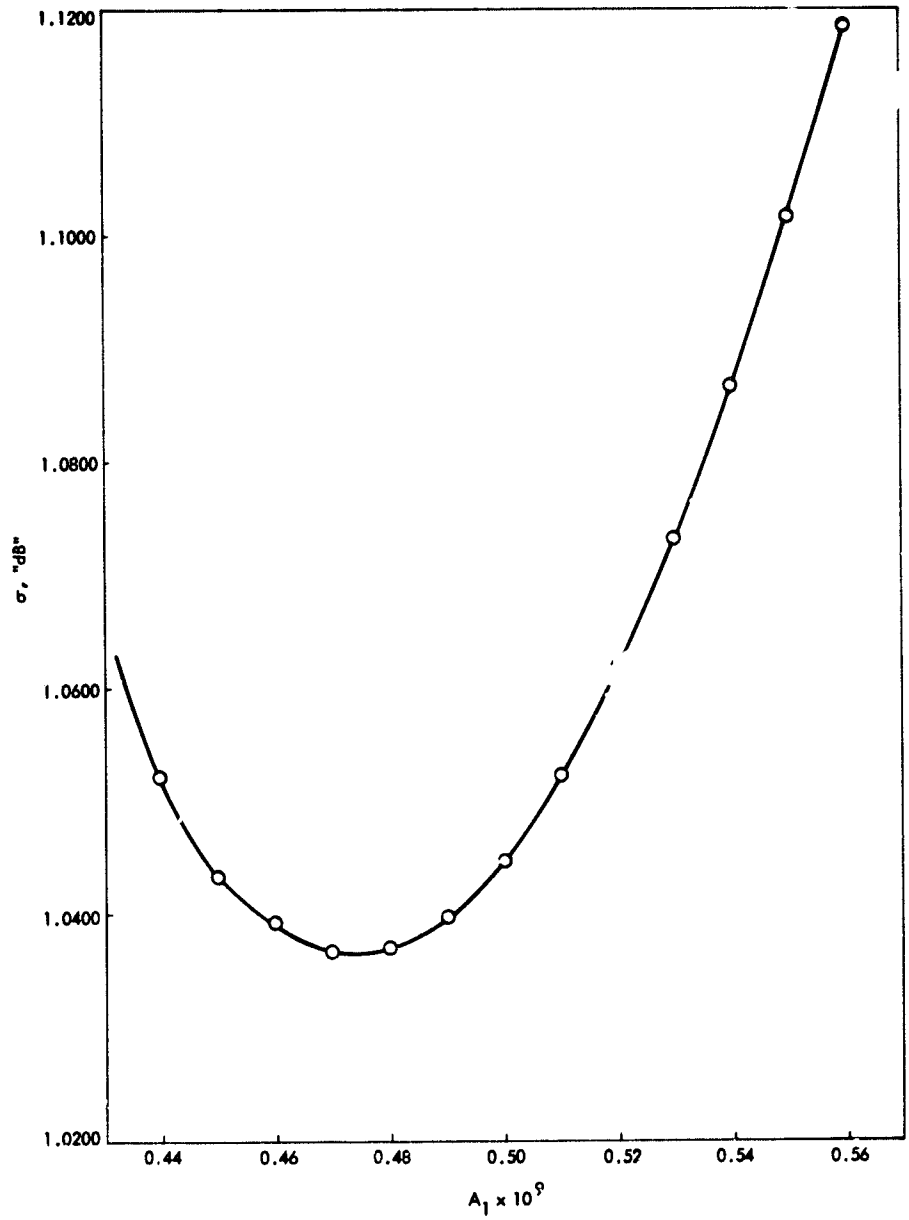

Fig. 5. Low SEP Viking and Helios doppler noise fit vs A_1

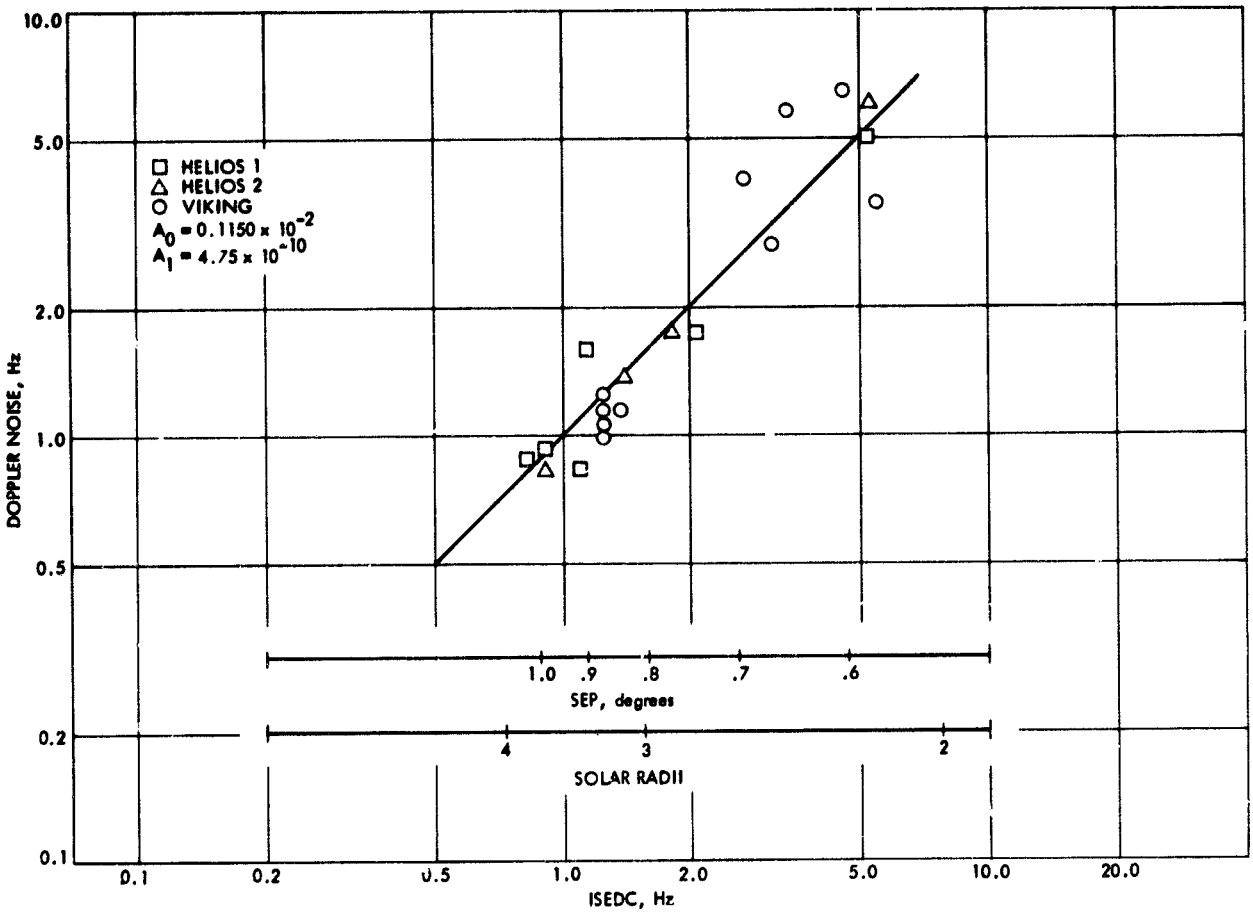

Fig. 6. Viking and Helios doppler noise fit to ISEDC between 2 to 4 solar radii

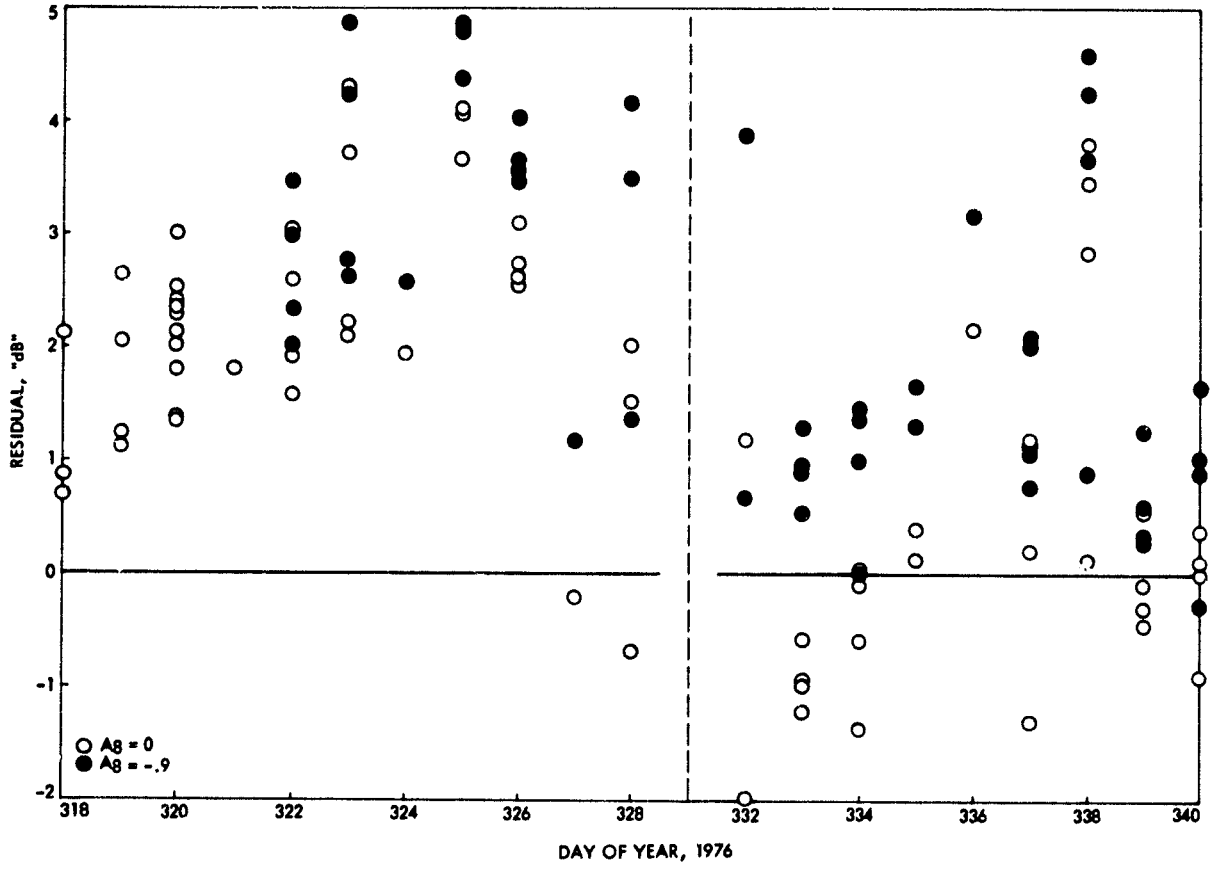

Fig. 7. ISEDC residuals with and without heliographic latitude correction

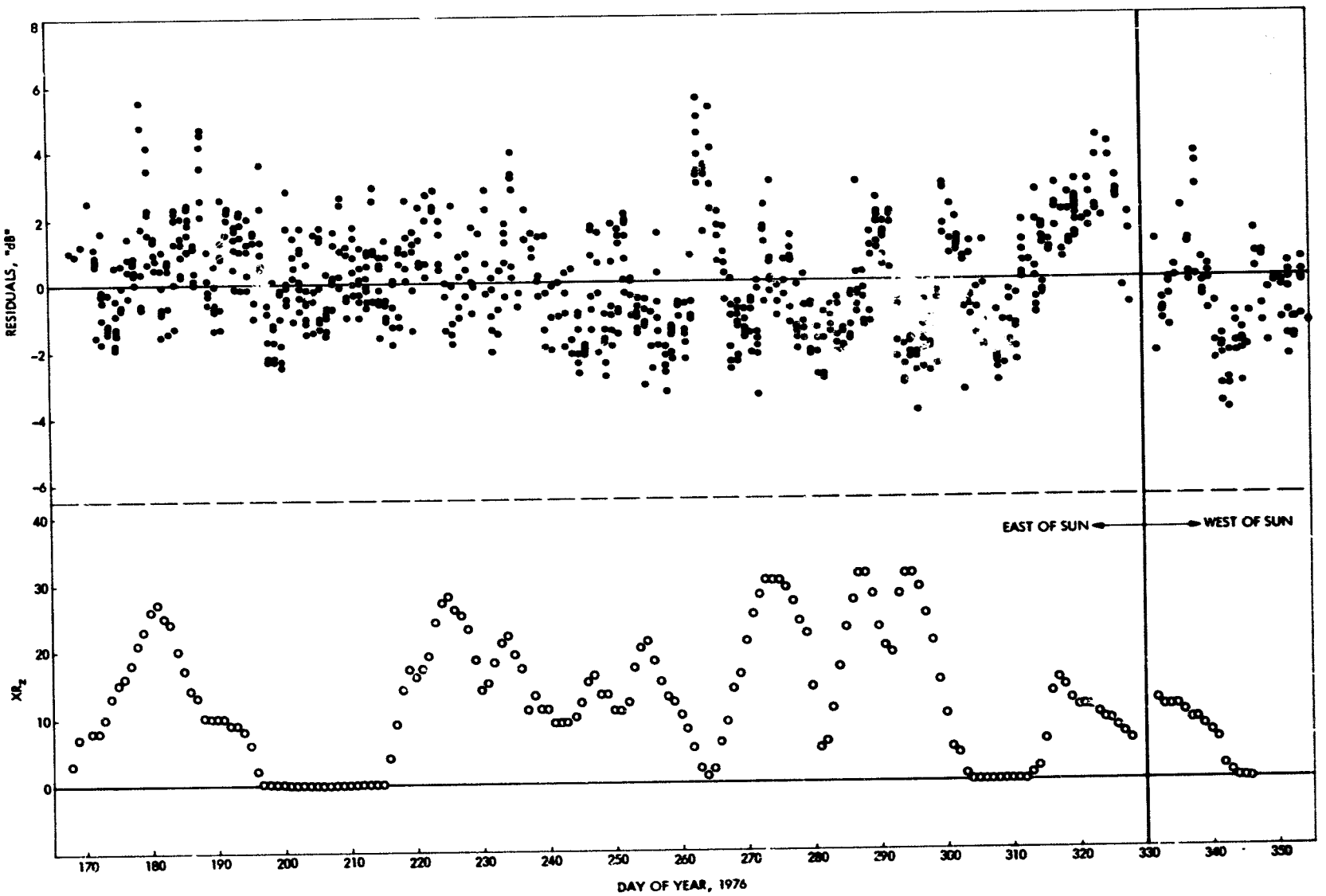

Fig. 8. Viking doppler noise residuals and phased/smoothed sunspots vs day of year

Viking Doppler Noise Used to Determine the Radial Dependence of Electron Density in the Extended Corona

A. L. Berman
TDA Engineering Office

J. A. Wackley, S. T. Rockwell, and M. Kwan
DSN Network Operations Section

The common form for radial dependence of electron density in the extended corona is:

$$N_e(r) \sim \frac{B}{r^{2+\xi}}$$

By assuming proportionality between doppler noise and integrated signal path electron density, Viking doppler noise can be used to solve for a numerical value of ξ. This process yields:

$$\xi = 0.30$$

I. Introduction

The general form of electron density for a spherically symmetric, static corona is:

$$N_e(r) = \frac{A}{r^6} + \frac{B}{r^{2+\xi}}$$

where

r = heliocentric distance

The value of ξ is either assumed from theory ($\xi = 0$) or experimentally determined; the range of ξ is usually considered to be:

$$0 \lesssim \xi \lesssim 0.5$$

Examples of values of ξ adopted or determined by various investigators are:

$\xi = 0.0$ Hollweg, Ducher (Refs. 1, 2)

$= 0.05$ Anderson (Ref. 3)

= 0.3 Blackwell, Muhleman (Ref. 4)

= 0.4 Muhleman (Ref. 4)

= 0.5 Saito, Van DeHulst (Ref. 5, 6)

Using the "ISEDC" doppler noise model (Ref. 7) and a large data base of pass average Viking S-band two-way doppler noise, ξ has been solved as follows:

$$\xi = 0.30$$

Somewhat conveniently, this determined value for ξ agrees rather well with the value adopted from the (earlier) work of D. Muhleman:

$$\xi = 0.3$$

II. The Data Base

871 points of "pass-average" Viking S-band doppler noise were accumulated during the following time period:

$$168 \leqslant \text{DOY (1976)} \leqslant 355$$

and for the following range of Sun-Earth-Probe (SEP) angles (in degrees):

$$00.58 \leqslant \text{SEP} \leqslant 54.13$$

The data were collected for all DSSs and for all (Viking) spacecraft and converted (via the ISEDC model) to "equivalent" 60-second sample interval data.

III. Reestimation of ξ

The ISEDC model follows:

$$\text{ISEDC, Hz} = \left[\left(\left\{ A_0 \left[\frac{\beta}{(\sin\alpha)^{1.3}} \right] F(\alpha, \beta) + A_1 \left[\frac{1}{(\sin\alpha)^5} \right] \right\} 10^{-A_8 (|\phi_s|/90)} \right)^2 \times (K(f_{dn}))^2 \left(\left\{ \frac{60}{\tau} \right\}^{0.3} \right)^2 + (D'_0)^2 + \left(D'_1 \left\{ \frac{60}{\tau} \right\}^{D'_2} \right)^2 \right]^{1/2}$$

where:

f_{dn} = downlink frequency (S- or X-band)

$$K(f_{dn}) = \begin{cases} 1.0 & f_{dn} = \text{S-band} \\ 0.7 & f_{dn} = \text{X-band} \end{cases}$$

τ = doppler sample interval, s

$$D'_0 = \begin{cases} 0 & \text{Pioneer} \\ 0.0014 & \text{Helios} \\ 0.0015 & \text{Viking} \end{cases}$$

$$D'_1 = \begin{cases} 0.0029 & \text{Pioneer} \\ 0.0019 & \text{Helios} \\ 0 & \text{Viking} \end{cases}$$

$$D'_2 = \begin{cases} 0.9 & \text{Pioneer} \\ 0.8 & \text{Helios} \\ & \text{Viking} \end{cases}$$

$$F(\alpha, \beta) = 1 - 0.05 \left\{ \frac{(\beta - \pi/2 + \alpha)^3 - (\alpha - \pi/2)^3}{\beta} \right\} - 0.00275 \left\{ \frac{(\beta - \pi/2 + \alpha)^5 - (\alpha - \pi/2)^5}{\beta} \right\}$$

α = Sun-Earth-Probe (SEP) angle, radians

β = Earth-Sun-Probe (ESP) angle, radians

and

ϕ_s = heliographic latitude, degrees

$= \sin^{-1} [\cot\alpha (-\cos\delta_d \sin\alpha_{ra} \sin\epsilon + \sin\delta_d \cos\epsilon)]$

α_{ra} = right ascension

δ_d = declination

ϵ = obliquity of the ecliptic (23.445 deg)

with:

$A_0 = 0.1182 \times 10^{-2}$

$A_1 = 5 \times 10^{-10}$

$A_8 = 0$

Residuals (in "db") between observed and predicted noise are formed as follows:

$$\Delta(\text{"db"}) = 10 \log_{10} \left\{ \frac{\text{observed noise}}{\text{ISEDC noise}} \right\}$$

These residuals are then used to produce a standard deviation for a particular data set:

$$\sigma \equiv \left\{ \frac{1}{N} \sum_{i=1}^{N} \Delta_i^2 \right\}^{1/2}$$

To solve for ξ, one makes the following assumptions:

(1) Doppler noise is proportional to integrated signal path electron density.

(2) The best fit of the model to the data will yield the best estimate of ξ.

The terms in ISEDC which are a function of ξ are:

$$\frac{\beta}{(\sin \alpha)^{1.3}} , \qquad F(\alpha, \beta)$$

After the fashion of Ref. 8, $(\cos w)^{\xi}$ is expanded as follows:

$$(\cos w)^{\xi} \cong 1 + \frac{w^2}{2!}(-\xi) + \frac{w^4}{4!}(3\xi^2 - 2\xi)$$

and $F(\alpha, \beta)$ becomes:

$$F(\alpha, \beta, \xi) = 1 - (\xi/6)\left\{\frac{(\beta - \pi/2 + \alpha)^3 - (\alpha - \pi/2)^3}{\beta}\right\}$$

$$+ (\xi/120)(3\xi - 2)\left\{\frac{(\beta - \pi/2 + \alpha)^5 - (\alpha - \pi/2)^5}{\beta}\right\}$$

one thus replaces:

$$\frac{\beta}{(\sin \alpha)^{1.3}}$$

with

$$\frac{\beta}{(\sin \alpha)^{1+\xi}}$$

and

$$F(\alpha, \beta)$$

with

$$F(\alpha, \beta, \xi)$$

These modifications were made and computer runs were initiated to obtain the conditions:

$$\frac{\partial \sigma}{\partial A_0} = 0$$

$$\frac{\partial \sigma}{\partial \xi} = 0$$

Figure 1 presents the σ achieved over the entire data base for various A_0 and ξ; Figure 2 presents the lowest σ achieved for each ξ. As is readily apparent from examination of Figure 2, $\sigma(\xi)$ has a well defined minimum at:

$$\xi = 0.30$$

with a resolution of ≈ 0.005; hence, a form is assumed for electron density in the extended corona of:

$$N_e(r) \sim \frac{B}{r^{2.30}}$$

References

1. Stelzried, C. T., *A Faraday Rotation Measurement of a 13 cm Signal in the Solar Corona*, Technical Report 32-1401, Jet Propulsion Laboratory, Pasadena, California, July 15, 1970.

2. Dutcher, G. L., *A Communication Channel Model of the Solar Corona and the Interplanetary Medium*, CSRT-69-1, Center for Space Research, Massachusetts Institute of Technology, 1969.

3. Anderson, J. D., et. al., "Experimental Test of General Relativity Using Time Delay Data from Mariner 6 and Mariner 7," *The Astrophysical Journal*, August 15, 1975.

4. Muhleman, D. O., Anderson, J. D., Esposito, P. B., and Martin W. L., "Radio Propagation Measurements of the Solar Corona and Gravitational Field; Applications to Mariner 6 and 7," in *Proceedings of the Conference on Experimental Tests of Gravitational Theories*, California Institute of Technology, Pasadena, California, November 1970.

5. Saito, Kuniji, "A Non-Spherical Axisymmetric Model of the Solar K Corona of the Minimum Type," *Annals of the Tokyo Astronomical Observatory*, University of Tokyo, Second Series, Volume XII, Number 2, Mitaka, Tokyo, 1970.

6. Van De Hulst, J. C., "The Electron Density of the Solar Corona." *Bulletin of the Astronomical Institutes of the Netherlands*, Volume XI, Number 410, February 2, 1950.

7. Berman, A. L., "A Comprehensive Two-way Doppler Noise Model for Near-Real-Time Validation of Doppler Data," in *The Deep Space Network Progress Report 42-37*, Jet Propulsion Laboratory, Pasadena, California, February 15, 1977.

8. Berman, A. L., and Wackley, J. A., "Doppler Noise Considered as a Function of the Signal Path Integration of Electron Density," in *The Deep Space Network Progress Report 42-33*, Jet Propulsion Laboratory, Pasadena, California, June 15, 1976.

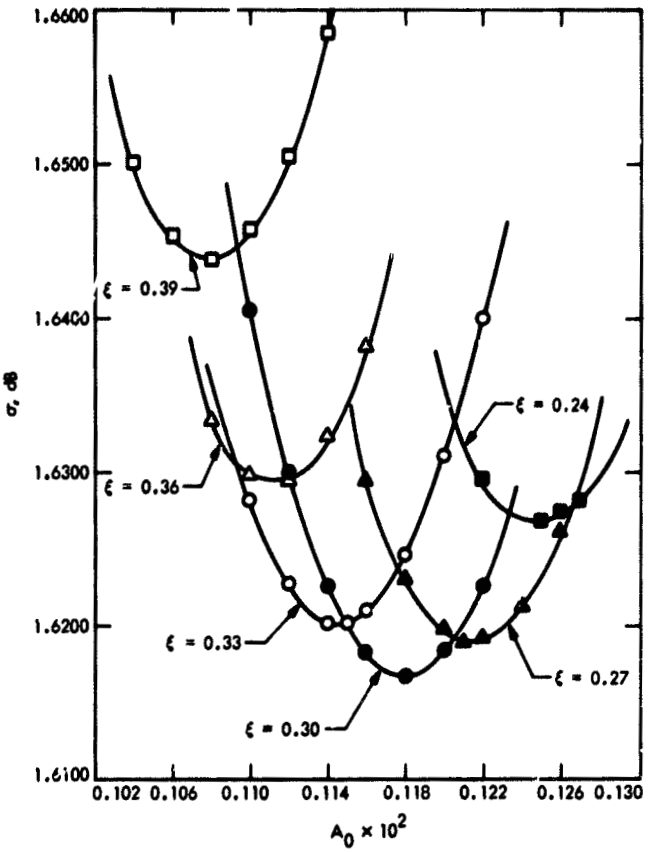

Fig. 1. Viking doppler noise fit vs A_0 and ξ

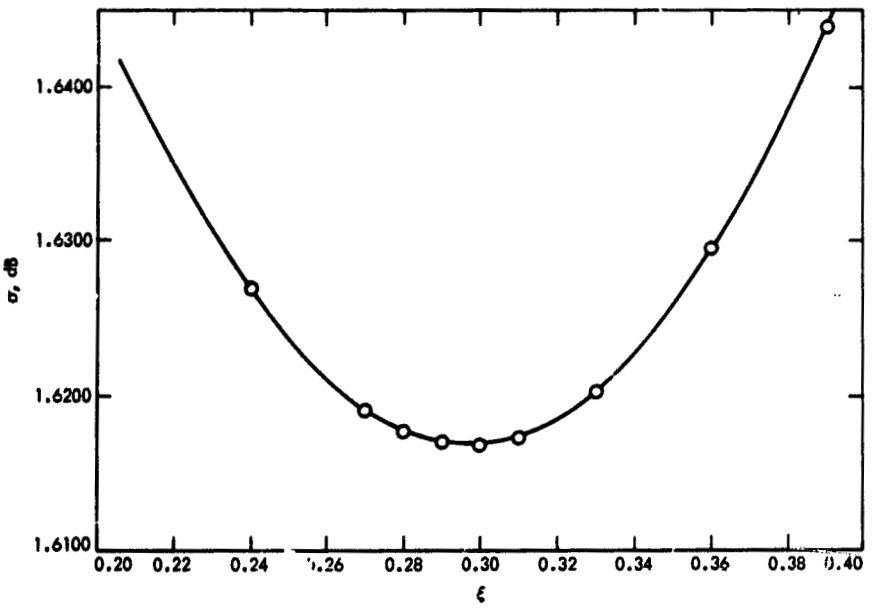

Fig. 2. Viking doppler noise best fit vs the parameter ξ (with $\partial\sigma/\partial A_0 = 0$)

N77-21131

Proportionality Between Doppler Noise and Integrated Signal Path Electron Density Validated by Differenced S-X Range

A. L. Berman
TDA Engineering Office

Previous articles have hypothesized that doppler rms phase jitter (noise) is proportional to integrated signal path electron density. In this article, observations of Viking differenced S-band/X-band (S-X) range are shown to correlate strongly with Viking doppler noise. A ratio of proportionality between downlink S-band plasma-induced range error and two-way doppler noise is calculated as:

$$\frac{\text{Downlink S-band plasma range error}}{\text{2-way S-band doppler noise}} \approx 7 \frac{\text{meters}}{\text{mHz}}$$

A new parameter (similar to the parameter ϵ which defines the ratio of "local" electron density fluctuations to mean electron density) is defined as a function of observed data sample interval (τ):

$$\epsilon'(\tau) = 7.9 \times 10^{-4} \left[\frac{\tau}{60}\right]^{0.7}$$

where the time-scale of the observations is 15τ. This parameter is interpreted to yield the ratio of "net" observed phase (or electron density) fluctuations to integrated electron density (in rms meters/meter). Using this parameter and the "thin phase-changing screen" approximation, a value for the scale size L is calculated:

$$L = a \left[\frac{7.9 \times 10^{-4}}{\epsilon}\right]^2 \left[\frac{\tau}{60}\right]^{1.4}$$

To be consistent with Doppler noise observations, it is seen necessary for L to be proportional to closest approach distance a, and a strong function of the observed data sample interval, and hence the time-scale of the observations.

I. Introduction

Previous articles have presented empirical evidence which suggests that doppler noise (rms phase jitter) is proportional to integrated signal path electron density. Strong as this hypothesis may have been, it was strictly circumstantial in that independent measurements of total columnar electron content were not available for comparison to doppler noise data. With the advent of the first Viking Solar Conjunction, *differenced* S-X range (S-band range minus X-band range) provided a readily accessible measurement of total columnar electron content for comparison to doppler noise. This report utilizes preliminary Viking differenced S-X range (provided by T. Komarek, Ref. 1) and Viking doppler noise to demonstrate a strong correlation between S-band plasma range error and S-band plasma induced doppler noise. Using these two data types, values have been calculated which relate S-band two-way doppler noise to S-band downlink plasma range error and total columnar electron content. Using the relationship between doppler noise and differenced S-X range, a new parameter is defined which is interpreted as yielding the ratio of "net" observed phase (and hence electron density) fluctuations to total columnar electron density. Utilizing this new parameter, various observations are made in reference to the "thin phase-changing screen" theory.

II. Comparison of Differenced S-X Range to Doppler Noise

Figure 1 presents differenced S-X range from Ref. 1 and Fig. 2 presents Viking two-way S-band doppler noise; in addition, the range values from Fig. 1 have been plotted on Fig. 2. Inspection of Fig. 2 discloses an immediate and very strong similarity in the range and noise signatures between DOY 261 and DOY 306, 1976. The conversion value which (arbitrarily) causes the range data to overlie the doppler noise data in Fig. 2 was calculated to be approximately:

$$\frac{23\ \text{RU}}{\text{mHz}}$$

The differenced S-X range in RU is converted to downlink S band plasma range error in meters as follows:

$$\text{S-band } \Delta R, \text{ meters} = \frac{1}{3.53}\left\{\frac{1}{1-(3/11)^2}\right\}\text{S-X } \Delta R, \text{ RU}$$

$$= \left\{\frac{1.08}{3.53}\right\}\text{S-X } \Delta R, \text{ RU}$$

$$= 0.306\ \text{S-X } \Delta R, \text{ RU}$$

and

$$\text{one-way S-band noise} = \frac{1}{\sqrt{2}}\ \text{two-way S-band noise}$$

Therefore, the conversion between meters and mHz is:

$$\frac{23\ \{1.08/3.53\}\ \text{meters}}{\{1/\sqrt{2}\}\ \text{mHz}} = 10\ \frac{\text{meters}}{\text{mHz}}$$

From Ref. 2 one has the conversion between columnar electrons and meters of range error for downlink S-band:

$$\frac{1.31 \times 10^{17}\ \text{electrons/m}^2}{\text{meter}}$$

which yields

$$\frac{1.31 \times 10^{18}\ \text{electrons/m}^2}{\text{mHz}}$$

Table 1 provides a variety of additional conversion factors between plasma range error and plasma induced doppler noise.

As a further example of the proportionality between plasma range error and doppler noise, a range acquisition performed by DSS 14 on DOY 331 while tracking Viking Orbiter 1 (at an SEP $\approx$ 0.58 deg; information provided by A. Zygielbaum (Ref. 3)) produced an S-X range error[1] of:

$$61\ \mu\text{s} \times 300\ \frac{\text{meters}}{\mu\text{s}} = 18\ \text{km}$$

During the same pass, a two-way pass average doppler noise value of 3533 mHz was recorded, or:

$$3533\ \text{mHz} \times 6.5\ \frac{\text{meters}}{\text{mHz}} = 23\ \text{km}$$

This agreement is quite good, particularly if one considers that the constant of proportionality between plasma range error and doppler noise (23 RU/mHz) was determined at approximately 35 mHz, or at a plasma level two orders of magnitude different (less) than the plasma level in this example.

[1] This value is a preliminary estimate and the range acquisition(s) is still subject to final determination of validity.

III. Calculation of a New Electron Density Fluctuation Parameter: $\epsilon'(\tau)$

From Ref. 4 one has the following expression for rms (temporal) phase error:

$$\Delta\phi\,(\text{rad}) = 2.8 \times 10^{-15}\ \{\lambda\} n \Delta R$$

where:

λ = wavelength, meters

= 0.131

n = electron density fluctuation

ΔR = distance along the signal path

if one defines:

$N_e(R, t)$ = instantaneous electron density, electron/m^3

then the mean electron density becomes:

$$N_e(R) = \frac{1}{t}\int_0^t N_e(R, t)\,dt$$

and the (rms) electron density fluctuation is:

$$n(R) = \left[\frac{1}{t}\int_0^t \{N_e(R, t) - N_e(R)\}^2\,dt\right]^{1/2}$$

The ratio of "local" electron density fluctuation to mean electron density is frequently defined as:

$$\epsilon \equiv \frac{n(R)}{N_e(R)}$$

With respect to doppler noise observations, there are two difficulties with the parameter ϵ. First, this ratio is frequently treated as a constant in the literature, whereas it should more correctly be considered as a function of the pertinent time-scale, as electron density fluctuations are well known to span a wide range of time-scales, from fractions of a second to hours, days, weeks. Second, there is no way of explicitly knowing[2] the value of ϵ from received doppler noise. Instead, a new parameter:

$$\epsilon'(\tau)$$

where

τ = data sample interval, seconds

and[3]

15τ = time-scale

will be defined, and which will be expected to yield the ratio of net observed columnar electron density fluctuation to (total) columnar electron density (in rms meters/meter).

Suppose, then, by extrapolation of the previously detailed phase error expression from Cronyn (Ref. 4), that observed phase fluctuations can be obtained by taking the rms value of local electron density fluctuation along the signal path times the signal path distance, but also times a ratio which expresses the proportionality between net observed electron density fluctuation and local electron density fluctuation. In terms of $\epsilon'(\tau)$, this ratio becomes:

$$\left\{\frac{\epsilon'(\tau)}{\epsilon}\right\}$$

$\epsilon'(\tau)$ is anticipated as a function of time-scale but *not* of geometry, and as previously mentioned, ϵ should also be considered as a function of time-scale. RMS phase fluctuation (observed) is then *defined* as:

$$\phi_{rms} \equiv 2.8 \times 10^{-15}\ [\lambda] \left\{\frac{1}{R}\int_0^R \{n\}^2\,dR\right\}^{1/2} R\left[\frac{\epsilon'(\tau)}{\epsilon}\right]$$

[2] Deducing the value of ϵ from Earth observations of scintillation, phase fluctuation, etc, has evoked much theoretical analysis during the past decade, but no definitive, widely accepted solutions have been produced.

[3] The doppler noise utilized in this study is the output from the Network Operations Control Center (NOCC) Psuedo Residual program. Pass average doppler noise is abstracted from a "running" standard deviation calculated about a least squares linear curve fit to the most recent 15 samples. Hence the time scale is considered to be 15 times the data sample interval, or 15τ.

By using this definition for observed phase fluctuations *in conjunction with* the observed relationship between phase fluctuations (doppler noise) and integrated signal path electron density (S-X range) from Section II, information will be obtained about $\epsilon'(\tau)$ and the ratio $\epsilon'(\tau)/\epsilon$.

It is easy to show (see the Appendix) that:

$$\left[R\int_0^R \{n(R)\}^2\,dR\right]^{1/2} \approx \epsilon\int_0^R N_e(R)\,dR \approx \epsilon I$$

where

$$I = \int_0^R N_e(R)\,dR$$

so that if:

$$\phi_{rms} \equiv 2.8\times10^{-15}\,[\lambda]\left\{R\int_0^R \{n\}^2\,dR\right\}^{1/2}\left[\frac{\epsilon'(\tau)}{\epsilon}\right]$$

then:

$$\phi_{rms}\,(\text{rad}) = 2.8\times10^{-15}\,[\lambda]\,\{\epsilon I\}\left[\frac{\epsilon'(\tau)}{\epsilon}\right]$$

$$= 2.8\times10^{-15}\,[0.131]\,\{\epsilon'(\tau)I\}$$

$$= 3.66\times10^{-16}\,\epsilon'(\tau)I$$

$$\phi_{rms}\,(\text{cycles}) = 3.66\times10^{-16}\,\epsilon'(\tau)I\left[\frac{\text{cycle}}{2\pi\text{ rad}}\right]$$

$$= 5.8\times10^{-17}\,\epsilon'(\tau)I$$

$$\phi_{rms}\,(\text{Hz}) = 5.8\times10^{-17}\,\epsilon'(\tau)I\left[\frac{1}{60\text{ s}}\right]$$

$$= 0.97\times10^{-18}\,\epsilon'(\tau)I$$

$$\phi_{rms}\,(\text{mHz}) = 0.97\times10^{-15}\,\epsilon'(\tau)I$$

now:

$$\text{S-band }\Delta R,\text{ meters} = \frac{I}{1.31\times10^{17}}$$

so that:

$$\frac{\Delta R,\text{ meters}}{\phi_{rms},\text{ mHz}} = \frac{I}{(1.31\times10^{17})(0.97\times10^{-15})\,\epsilon'(\tau)I}$$

$$= \frac{0.0079}{\epsilon'(\tau)}\ \frac{\text{meter}}{\text{mHz}}$$

using the expression found in Section II, one has for 60-s sample interval doppler noise:

$$\frac{0.0079}{\epsilon'(60)}\ \frac{\text{meter}}{\text{mHz}} = 10\ \frac{\text{meter}}{\text{mHz}}$$

or:

$$\epsilon'(60) = 0.00079$$

This value for $\epsilon'(\tau)$ is about 1/25th the value commonly assigned to ϵ(no time-scale specified) in the literature:

$$\epsilon \approx 0.02$$

An interpretation of these two parameters is made as follows:

$\epsilon'(\tau)$: the ratio of observed electron density fluctuation to total columnar electron density (rms meters/meter).

$\epsilon'(\tau)/\epsilon$: the ratio of observed electron density fluctuation to local electron density fluctuation.

If the above interpretation proves correct, then the usefulness of these two parameters in concert would be:

If one has in situ measurements of ϵ (really $\epsilon(\tau)$) and Earth observed measurements of $\epsilon'(\tau)$, then theory should be able to correctly predict the correspondence between the two.

This author has recently determined (Ref. 5) the dependence between doppler sample interval and doppler noise to be:

$$\text{noise}(\tau) = \{\text{noise}(60\text{ s})\}\left[\frac{60}{\tau}\right]^{0.3}$$

or

$$\text{rms phase}(\tau) = \{\text{rms phase}(60)\}\left[\frac{\tau}{60}\right]\left[\frac{60}{\tau}\right]^{0.3}$$

where:

τ = doppler sample interval, s

One therefore obtains for the relationship between $\epsilon'(\tau)$ and τ:

$$\epsilon'(\tau) = \epsilon'(60)\left[\frac{\tau}{60}\right]\left[\frac{60}{\tau}\right]^{0.3}$$

$$= 0.00079\left[\frac{\tau}{60}\right]^{0.7}$$

This relationship is seen in Fig. 3, as well as in the tabulated values below:

τ, s	$\epsilon'(\tau)$
1.0	4.5×10^{-5}
10.0	2.3×10^{-4}
60.0	7.9×10^{-4}
600.0	4.0×10^{-3}
1800.0	8.5×10^{-3}
3600.0	1.4×10^{-2}

IV. Doppler Noise Observations Compared to Results Derived From the Thin Phase-Changing Screen Approximation

Derivations using the thin phase-changing screen approximation (for instance Salpeter, Ref. 6, and Ducher, Ref. 7) produce an expression for rms phase as follows:

$$\phi_{rms} = \left\{L\int_0^R n^2\,dR\right\}^{1/2}(2\pi)^{1/4}\,r_e\,\lambda$$

$$\propto \left\{L\int_0^R N_e^2\,dR\right\}^{1/2}$$

$$\propto \frac{1}{a^{1.8}}$$

where.

L = "correlation length", "irregularity scale size", etc.

$r_e = 2.8 \times 10^{-15}$ meters

a = closest approach distance

Obviously, considering L as a constant produces an rms phase fluctuation ($\propto 1/a^{1.8}$) which is inconsistent with the radial dependence of the observed data ($\propto 1/a^{1.3}$). Considered values of L range from 100 km (Ducher, Ref. 7) to 10^6 km or larger (Jokipii and Hollweg, Ref. 8, Callahan, Ref. 9).

However, some investigators have proposed that L is a function of closest approach distance

$$L \propto a$$

Examples are Cohen and Gundermann, Ref. 10, where:

$$L \propto a^{1.05}$$

and Houminer and Hewish, Ref. 11, where:

$$L \propto a^{1.0}$$

L proportional to a would be exactly the condition required to bring doppler noise observations into correspondence with rms phase derivations from the thin phase-changing screen approximation.

The thin phase-changing screen expression can be compared to the expression for phase fluctuation presented in Section II,

but with the integration limited to $\pm a$ (as performed in the Appendix):

$$\phi_{rms} = \left\{2a \int_{-a}^{a} n^2 \, dR\right\}^{1/2} r_e \lambda \left[\frac{\epsilon'(\tau)}{\epsilon}\right]$$

ignoring the difference between $\sqrt{2\pi}$ and 2, one obtains for the scale size L:

$$\sqrt{L} = \sqrt{a}\left[\frac{\epsilon'(\tau)}{\epsilon}\right]$$

or

$$L = a\left[\frac{\epsilon'(\tau)}{\epsilon}\right]^2$$

Hence one concludes that the thin phase-changing screen scale size must be proportional to closest approach distance and is strongly effected by the time-scale over which observations are taken. Using the expression for $\epsilon'(\tau)$, one obtains for L:

$$L = a\left[\frac{7.9 \times 10^{-4}}{\epsilon}\right]^2 \left[\frac{\tau}{60}\right]^{1.4}$$

Figures 4, 5, 6, and 7 present plots of L versus a for various conditions.

It has been previously suggested that, like $\epsilon'(\tau)$, the local fluctuation to density ratio ϵ should be considered as $\epsilon(\tau)$. If one speculates that $\epsilon(\tau)$ has approximately the same dependence upon time-scale (hence τ) as does $\epsilon'(\tau)$, one would write:

$$\epsilon(\tau) = \epsilon(60)\left[\frac{\tau}{60}\right]^{0.7}$$

and thus the scale size L would simply become a function of closest approach distance:

$$L = a\left[\frac{\epsilon'(\tau)}{\epsilon(\tau)}\right]^2$$

$$= a\left[\frac{7.9 \times 10^{-4}}{\epsilon(60)}\right]^2$$

This (postulated) relationship for various values of $\epsilon(60)$ is seen in Fig. 8 as well as in the tabulated values below (L in km, a in solar radii):

$\epsilon(60)$	L
10^0	$4.3 \times 10^{-1}\, a$
10^{-1}	$4.3 \times 10^{1}\, a$
10^{-2}	$4.3 \times 10^{3}\, a$
10^{-3}	$4.3 \times 10^{5}\, a$
10^{-4}	$4.3 \times 10^{7}\, a$

V. Summation

It has been periodically suggested by this author that observed doppler noise is proportional to integrated signal path electron density. The comparison of differenced Viking S-X range to Viking S-band doppler noise has lent added weight to this conviction and has resulted in the approximate determination of the constant of proportionality between the two. Incorporating this result with the observed functional dependance of doppler noise upon data sample interval allows the ratio of net observed rms phase fluctuations to integrated electron density to be explicitly exhibited as a function of time-scale (here 15 times the data sample interval). These results are then applied to define the condition necessary to bring thin phase-changing screen theory into agreement with observed doppler rms phase fluctuations:

$$L \propto a$$

and to establish the relationship between scale size, time-scale, and the ratio of local electron density fluctuation to electron density.

Table 1. Plasma range error and plasma induced doppler noise conversion factors

Plasma/noise combinations	Conversion Value
Downlink S-band plasma range error / Downlink S-band doppler noise	10.0 meters/mHz
Downlink S-X plasma range error / Downlink S-band doppler noise	9.2 meters/mHz
Downlink S-band plasma range error / 2-way S-band doppler noise	7.0 meters/mHz
Downlink S-X plasma range error / 2-way S-band doppler noise	6.5 meters/mHz

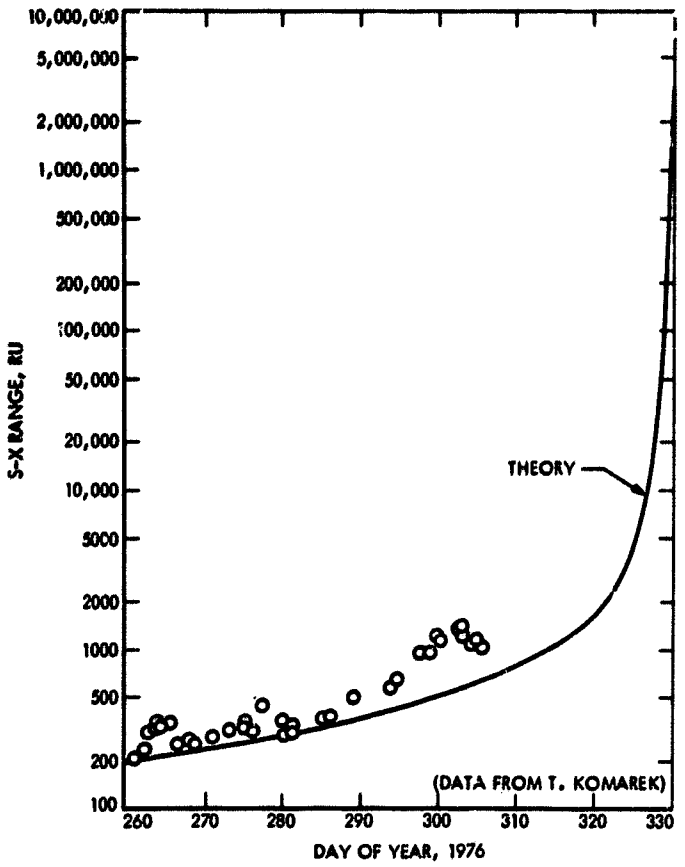

Fig. 1. Viking S-X range vs day of year

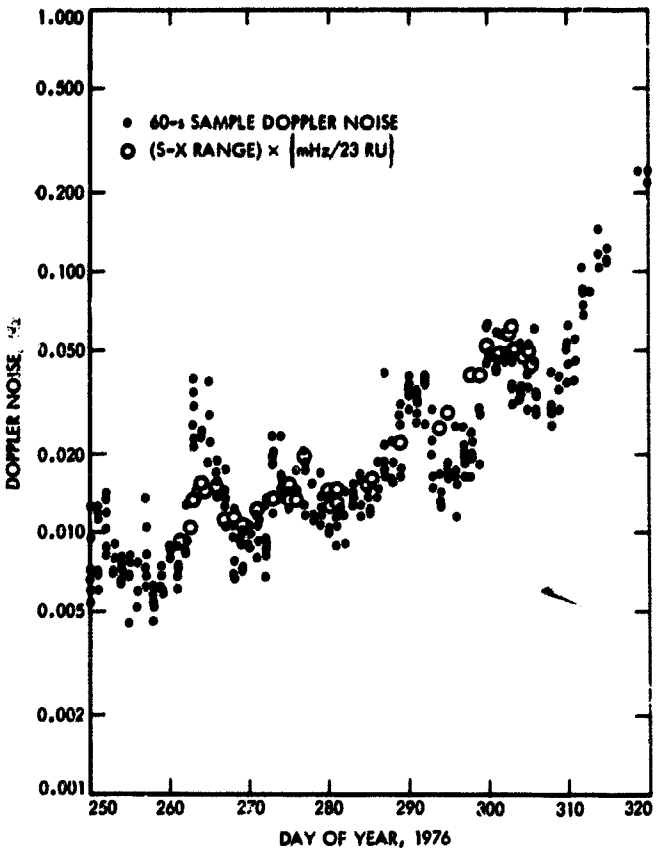

Fig. 2. Viking two-way S-band doppler noise and S-X range vs day of year

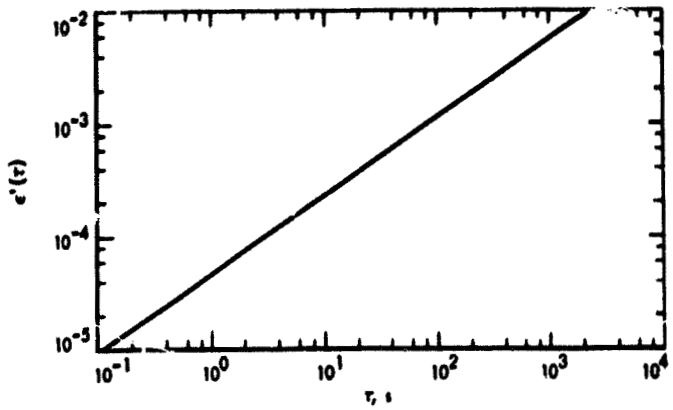

Fig. 3. $\epsilon'(\tau)$ vs τ

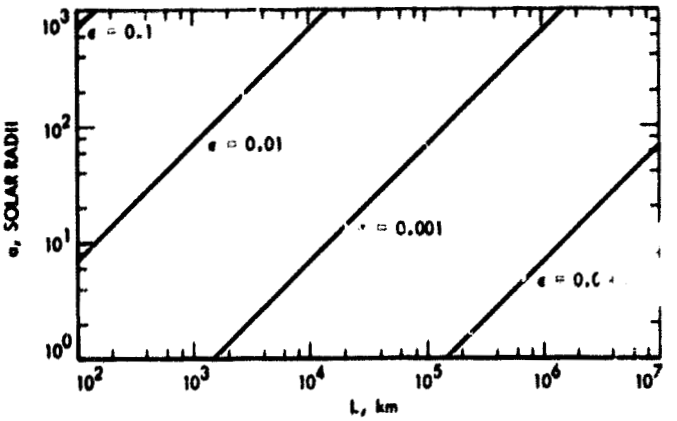

Fig. 6. Scale size for τ = 1 s vs closest approach distance

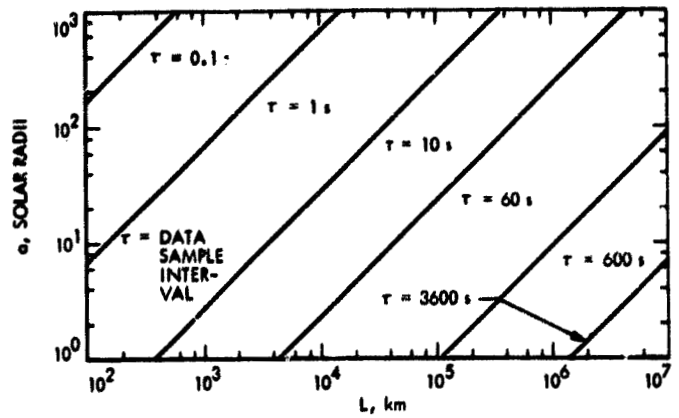

Fig. 4. Scale size for ϵ = 0.01 vs closest approach distance

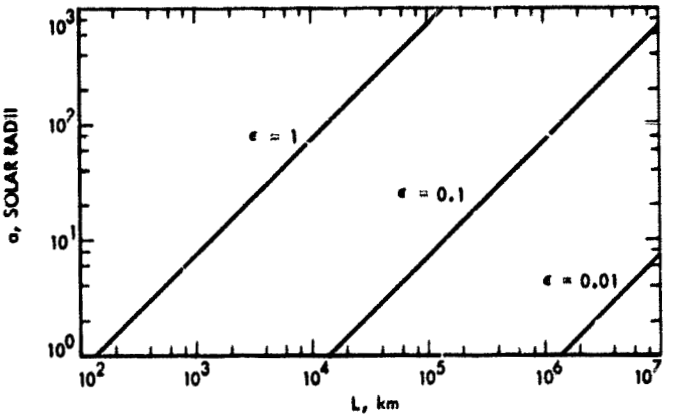

Fig. 7. Scale size for τ = 3600 s vs closest approach distance

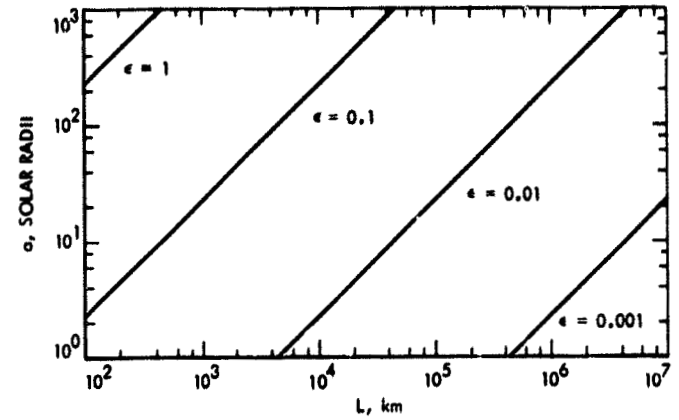

Fig. 5. Scale size for τ = 60 s vs closest approach distance

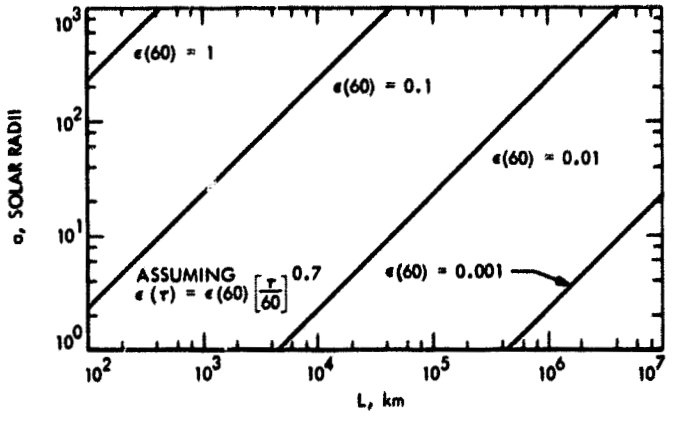

Fig. 8. Scale size vs closest approach distance, assuming $\epsilon(\tau) = \epsilon(60)\left[\frac{\tau}{60}\right]^{0.7}$

Appendix

Proportionality Between Signal Path RMS Phase Fluctuation and Integrated Signal Path Density

Proof that if :

$$\epsilon \equiv \frac{n}{N_e}$$

then:

$$\left\{R \int_0^R n^2 \, dR \right\}^{1/2} \approx \epsilon l$$

Let the interval of integration be $-a \leq R \leq a$ as in diagram below:

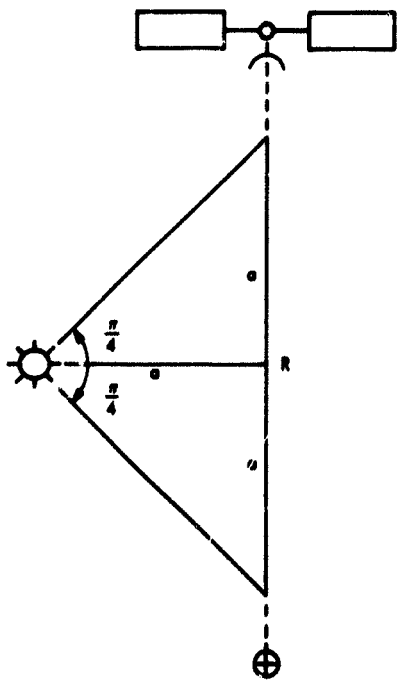

where:

$a = r_e \sin \alpha$

r_e = Earth-Sun Distance

α = Sun-Earth-Probe Angle

The signal path rms phase fluctuation is then:

$$R \int_{-a}^{a} n^2 \, dR = 2a \int_{-a}^{a} (\epsilon N_e)^2 \, dR$$

$$= 2a \epsilon^2 \int_{-a}^{a} N_e^2 \, dR$$

now (assuming):

$$N_e \cong K/r^{2.3}$$

so that:

$$R \int_{-a}^{a} n^2 \, dR = 2a \epsilon^2 K^2 \int_{-a}^{a} \frac{1}{r^{4.6}} \, dR$$

after the fashion of Ref. 12:

$$R \int_{-a}^{a} n^2 \, dR = 2a \epsilon^2 K^2 \int_{-a}^{a} \frac{dx}{(x^2 + a^2)^{2.3}}$$

$$= \frac{2a \epsilon^2 K^2}{a^{4.6}} \int_{-\pi/4}^{\pi/4} \frac{a \sec^2 w \, dw}{(\tan^2 w + 1)^{2.3}}$$

$$= \frac{2a^2 \epsilon^2 K^2}{a^{4.6}} \int_{-\pi/4}^{\pi/4} (\cos w)^{2.6} \, dw$$

$$\cong \frac{2\epsilon^2 K^2}{a^{2.6}} \int_{-\pi/4}^{\pi/4} \cos^2 w (1 - 0.3w^2) \, dw$$

$$= \frac{2\epsilon^2 K^2}{a^{2.6}} \left[\int_{-\pi/4}^{\pi/4} \cos^2 w \, dw \right.$$

$$\left. - 0.3 \int_{-\pi/4}^{\pi/4} w^2 \cos^2 w \, dw \right]$$

$$= \frac{2\epsilon^2 K^2}{a^{2.6}} \left[\left\{ 1/2\, w + 1/4 \sin 2w \right\}_{-\pi/4}^{\pi/4} \right.$$

$$-0.3 \left\{ \frac{w^3}{6} + \left(\frac{w^2}{4} - \frac{1}{8} \right) \sin 2w \right.$$

$$\left. \left. + \frac{w \cos 2w}{4} \right\}_{-\pi/4}^{\pi/4} \right]$$

$$= \frac{2\epsilon^2 K^2}{a^{2.6}} \left[\frac{\pi}{4} + \frac{1}{2} \right.$$

$$\left. -0.3 \left\{ \frac{1}{3} \left(\frac{\pi}{4} \right)^3 + \frac{1}{4} \left(2 \left[\frac{\pi}{4} \right]^2 - 1 \right) \right\} \right]$$

$$= \frac{2\epsilon^2 K^2}{a^{2.6}} [1.22]$$

$$= 2.44 \left[\frac{\epsilon^2 K^2}{a^{2.6}} \right]$$

or

$$\left\{ R \int_{-a}^{a} n^2 \, dR \right\}^{1/2} = 1.56 \left[\frac{\epsilon K}{a^{1.3}} \right]$$

Now

$$\int_{-a}^{a} N_e \, dR = \int_{-a}^{a} \frac{K}{r^{2.3}} \, dR$$

$$= K \int_{-a}^{a} \frac{dx}{(a^2 + x^2)^{1.15}}$$

$$= \frac{K}{a^{2.3}} \int_{-\pi/4}^{\pi/4} \frac{a \sec^2 w \, dw}{(\tan^2 w + 1)^{1.15}}$$

$$= \frac{K}{a^{1.3}} \int_{-\pi/4}^{\pi/4} (\cos w)^{0.3} \, dw$$

$$\cong \frac{K}{a^{1.3}} \left[w (1 - 0.05\, w^2) \right]_{-\pi/4}^{\pi/4}$$

$$= \frac{K}{a^{1.3}} \left[\frac{\pi}{2} \left(1 - 0.05 \left\{ \frac{\pi}{4} \right\}^2 \right) \right]$$

$$= 1.52 \left[\frac{K}{a^{1.3}} \right]$$

Finally,

$$\frac{\left\{ R \int_{-a}^{a} n^2 \, dR \right\}^{1/2}}{\int_{-a}^{a} N_e \, dR} = \frac{1.56 \left[\frac{\epsilon K}{a^{1.3}} \right]}{1.52 \left[\frac{K}{a^{1.3}} \right]}$$

$$= 1.03\epsilon$$

hence

$$\frac{n}{N_e} \equiv \epsilon \approx \frac{\left\{ R \int_{0}^{R} n^2 \, dR \right\}^{1/2}}{\int_{0}^{R} N_e \, dR}$$

References

1. Brunn, L., "Minutes of the Eleventh Ranging Accuracy Team Meeting", IOM 33RA-76-012, Jet Propulsion Laboratory, Pasadena, Calif., 9 December 1976. (JPL internal document).

2. Efron, L. and Lisowski, R. J., "Charged Particle Effects to Radio Ranging and Doppler Tracking Signals in a Radially Outflowing Solar Wind", in *The Space Programs Summary 37 – 56, Volume II: The Deep Space Network*, Jet Propulsion Laboratory, Pasadena, California, 31 March 1969.

3. Private communication with A. Zygielbaum.

4. Cronyn, Willard M., "The Analysis of Radio Scattering and Space-Probe Observations of Small-Scale Structure in the Interplanetary Medium" *Astrophysical Journal*, 161, pp. 755-763, 1 August 1970.

5. Berman, A. L. "A Comprehensive Two-way Doppler Noise Model for Near-Real-Time Validation of Doppler Data" in *The Deep Space Network Progress Report 42-37*, Jet Propulsion Laboratory, Pasadena, California, 15 February 1977.

6. Salpeter, E. E., "Interplanetary Scintillations. I. Theory", *Astrophysical Journal*, 147, 1967.

7. Dutcher, G. L., *A Communication Channel Model of the Solar Corona and the Interplanetary Medium*, CSRT-69-1, Center for Space Research, Massachusetts Institute of Technology, 1969.

8. Jokipii, J. R., and Hollweg, J. V., "Interplanetary Scintillations and the Structure of Solar Wind Fluctuations", *Astrophysical Journal*, 160, May 1970.

9. Callahan, P. S., "Columnar Content Measurements of the Solar Wind Turbulence Near the Sun", *Astrophysical Journal*, 199, July 1, 1975.

10. Cohen, M. H., and Gundermann, E. J., "Interplanetary Scintillations IV. Observations Near the Sun", *Astrophysical Journal* 155, February 1969.

11. Houminer, Z., and Hewish, A., "Long-Lived Sectors of Enhanced Density Irregularities in the Solar Wind", *Planetary Space Science*, Volume 20, 1972.

12. Berman, A. L., and Wackley, J. A., "Doppler Noise Considered as a Function of the Signal Path Integration of Electron Density", in *The Deep Space Network Progress Report 42-33*, Jet Propulsion Laboratory, Pasadena, California, 15 June 1976.

Modification of the DSN Radio Frequency Angular Tropospheric Refraction Model

A. L. Berman
TDA Engineering Office

The previously derived DSN Radio Frequency Angular Tropospheric Refraction Model contained an assumption which was subsequently seen to be at a variance with the theoretical basis of angular refraction. The modification necessary to correct the model is minor in that the value of a constant is changed. The accuracy of the modified model is now considered to be:

Elevation angle range	*Maximum error*
90 deg ≥ el ≥ 5 deg	*0.003 deg*
5 deg ≥ el ≥ −3 deg	*0.010 deg*

I. Modification of Refraction Model

In References 1 and 2, an assumption was made that is at a variance with the theoretical basis[1] of angular refraction. It was assumed in translating from optical frequency to radio frequency that (as in range refraction):

$$\text{refraction} \propto \int N(h)\, dh$$

where:

$N(h)$ = total refractivity at radio frequencies

h = height

so that:

$$R_{RF}(P,T,Z,RH) \approx R_{OP}(P,T,Z)\left\{1 + \frac{\int NW(h)\,dh}{\int ND(h)\,dh}\right\}$$

where:

$R_{OP} = R_{OP}(P,T,Z)$ = optical refraction model

$R_{RF} = R_{RF}(P,T,Z,RH)$ = radio frequency refraction model

P = pressure

T = temperature

Z = zenith angle

[1] Private communication with V. J. Slabinski, COMSAT Corporation.

RH = relative humidity

$N(h) = ND(h) + NW(h)$

$ND(h)$ = dry, or optical component, of refractivity

$NW(h)$ = wet component of refractivity

However, in fact, one has for angular refraction (in *contrast* to range refraction):

$$\text{refraction} \propto \int dN(h)$$

so that:

$$R_{RF}(P,T,Z,RH) \approx R_{OP}(P,T,Z)\left\{1 + \frac{NW_s}{ND_s}\right\}$$

Because it was empirically determined that:

$$\frac{\int_0^\infty NW(h)\,dh}{\int_0^\infty ND(h)\,dh} \approx 0.3224\left(\frac{NW_s}{ND_s}\right)$$

s = parameter surface value

the correction of the model requires a change in only one constant.

The full modified model is:

$$R = F_p F_t F_w \left(\exp\left\{ \frac{\sum_{j=0}^{8} K_{j+3}\,[U(Z)]^j}{1 + \Delta_3(Z)} \right\} - K_{12} \right)$$

$$F_p = \left(\frac{P}{P_0} \left\{ 1 - \frac{\Delta_1(P,Z)}{1 + \Delta_3(Z)} \right\} \right)$$

$$F_t = \left(\frac{T_0}{T} \left\{ 1 - \frac{\Delta_2(T,Z)}{1 + \Delta_3(Z)} \right\} \right)$$

$$F_w = \left(1 + \frac{W_0 RH}{TP} \left\{ \exp\left[\frac{W_1 T - W_2}{T - W_3} \right] \right\} \right)$$

$$\Delta_1(P,Z) = (P - P_0)\,\{\exp[A_1(Z - A_2)]\}$$

$$\Delta_2(T,Z) = (T - T_0)\,\{\exp[B_1(Z - B_2)]\}$$

$$\Delta_3(Z) = (Z - C_0)\,\{\exp[C_1(Z - C_2)]\}$$

where

R = refraction, s

Z = actual zenith angle, deg

EL = elevation angle

$EL = 90 \text{ deg} - Z$

$$U(Z) = \left\{ \frac{Z - K_1}{K_2} \right\}$$

$K_1 = 46.625$

$K_2 = 45.375$

$K_3 = 4.1572$

$K_4 = 1.4468$

$K_5 = 0.25391$

$K_6 = 2.2716$

$K_7 = -1.3465$

$K_8 = -4.3877$

$K_9 = 3.1484$

$K_{10} = 4.5201$

$K_{11} = -1.8982$

$K_{12} = 0.89000$

P = pressure, mm Hg

$P_0 = 760.00$ mm Hg

$A_1 = 0.40816$

$A_2 = 112.30$

T = temperature, K

$T_0 = 273.00$ K

$B_1 = 0.12820$

$B_2 = 142.88$

$C_0 = 91.870$

$C_1 = 0.80000$

$C_2 = 99.344$

RH = Relative humidity (100% = 1.0)

$W_0 = 2.2 \times 10^4$

$W_1 = 17.149$

$W_2 = 4684.1$

$W_3 = 38.450$

Note that only the value of W_0 has changed, from

$$W_0 = 7.1 \times 10^3$$

to:

$$W_0 = \frac{7.1 \times 10^3}{0.3224} = 2.2 \times 10^4$$

II. Evaluation of Modified Model Accuracy

The major source of inaccuracy was a 1%, 1σ uncertainty due to the approximation of the ratio of integrated wet refractivity to integrated dry refractivity by 0.3224 times the ratio of surface wet refractivity to surface dry refractivity. Thus the modification of the model eliminates the known 1% uncertainty in the wet refractivity term, as well as a systematic, and (previously) unknown error which ranged from 2 to 20%. The accuracy of the modified radio frequency angular tropospheric refraction model is now considered to be of the same order as the optical angular tropospheric refraction model presented in Table 2 of Ref. 2, but enlarged by 50% to account for the increased size of radio frequency refraction when compared to optical refraction:

Zenith angle range	Maximum error, deg
0 deg ≤ zenith ≤ 85 deg	0.003 deg
85 deg ≤ zenith ≤ 93 deg	0.010 deg

References

1. Berman, A. L., and Rockwell, S. T., "A Proposal for a New Radio Frequency Angular Tropospheric Refraction Model For Use Within the DSN," in *The Deep Space Network Progress Report 42-25*, pp. 142-153. Jet Propulsion Laboratory, Pasadena, California, February 15, 1975.

2. Berman, A. L., and Rockwell, S. T., *New Optical and Radio Frequency Angular Tropospheric Refraction Models for Deep Space Applications*, Technical Report 32-1601, Jet Propulsion Laboratory, Pasadena, California, November 1, 1975.

A Model of SNR Degradation During Solar Conjunction

S. T. Rockwell
DSN Network Operations Section

The downlink signal from spacecraft in solar conjunction phases suffers a drastic reduction in signal-to-noise ratio (SNR). Responsible in large part for this effect is the increase in system noise temperature (SNT) in the ground antenna-receiver system. This article presents an empirical model of SNR degradation due to increasing SNT during solar conjunction phases.

I. Introduction

One of the most important parameters in a telecommunication signal processing and detection system is the signal-to-noise ratio or SNR. When a spacecraft undergoes either a superior or inferior solar conjunction this parameter becomes greatly reduced, the reduction spanning several orders of magnitude for small Sun-Earth-Probe (SEP) angles. This change in the SNR, called the SNR degradation, results from several different causes.

During superior conjunctions the signal transmitted by the spacecraft will pass close to the Sun, traversing dense regions of the solar corona. Under these conditions, complicated plasma effects corrupt the signal and degrade the SNR. Additionally, just pointing the antenna in the vicinity of the Sun causes an increase in the system noise temperature (SNT) in the ground antenna-receiver system. Since the noise power is proportional to the SNT, the SNT increase will cause a decrease in the SNR.

In an inferior conjunction, the coronal plasma effects are minimized, leaving most of the SNR degradation due to the increasing SNT. This report is concerned with the modelling of the SNR degradation during inferior solar conjunction, the assumption being made that all of the degradation can be attributed to increases in the SNT. Although the model will be developed using data from an inferior conjunction, it should be clear that the results obtained can be used in estimating that portion of the SNR degradation due to the increasing SNT during superior conjunction.

In order to develop a model of SNR degradation, we first obtain an expression for this quantity. Begin with the definition of the symbol *SNR*:

$$SNR \equiv \frac{ST_S}{kT} \tag{1}$$

where

S = data power

T_S = symbol time

k = Boltzmann constant

T = system noise temperature

Furthermore, when the Sun is neglected, T is the sum of the zenith system noise temperature and an antenna elevation angle correction:

$$T = T_Z + T_{EL} \tag{2}$$

T is known completely since T_Z is a measured quantity and T_{EL} is readily computed from the empirical formula:

$$T_{EL} = A' e^{-B'(EL)} \tag{3}$$

where A' and B' are antenna-dependent constants (see Appendix A) and EL is the antenna elevation angle.

If the antenna is tracking a spacecraft near inferior conjunction, the Sun can be considered an additional noise source. In this case the *SNR* would be written as:

$$SNR' = \frac{ST_S}{kT'} \tag{4}$$

where T' includes the increase in *SNT* due to the Sun. The total *SNT* is now written:

$$T' = T + T_{SUN} \tag{5}$$

where T_{SUN} is to be interpreted as the increase in system noise temperature due to the Sun.

From Eqs. (1) and (4) we can obtain an expression for the SNR degradation. If ΔSNR is the *SNR* degradation in dB due to the increase in SNT during inferior conjunction, then:

$$\Delta SNR = 10 \log_{10}\left(\frac{SNR}{SNR'}\right) = 10 \log_{10}\left(\frac{T'}{T}\right)$$

$$\Delta SNR \text{ (dB)} = 10 \log_{10}\left(\frac{T + T_{SUN}}{T}\right) \tag{6}$$

It is important to note that the Δ_{SNR} is a function of two variables, T and T_{SUN}.

II. T_{SUN} – The Ambiguous Parameter

When tracking a spacecraft near solar conjunction, the ΔSNR increases as the *SEP* angle decreases. It seems reasonable, then, to try to model the ΔSNR as a function of *SEP*. However, in attempting to model the ΔSNR, we will have to find a related parameter that depends solely on the *SEP* angle. The reason for this becomes apparent if we remember that the ΔSNR varies with both T_{SUN} and T. We assume T_{SUN} depends on the *SEP* angle and, as stated, T depends on the system and antenna elevation angle. It is important to note at this point that if T_{SUN} could be determined as a function of *SEP*, constructing a model of ΔSNR would be simplified.

Before investigating the T_{SUN} parameter further, it is worth mentioning another parameter related to the ΔSNR and varying with *SEP*. This is the total operating system noise temperature T_{OP}. This quantity is measured on a strip chart at the site and is written as

$$T_{OP} = T_Z + T_{ELOP} + T_{SUNOP} \tag{7}$$

T_{SUNOP} is the increase in operating system noise temperature due to the Sun and T_{ELOP} is the actual elevation effect. Since T_{OP} and T_Z are measured and T_{ELOP} is approximated by T_{EL} it would, at first, appear that T_{SUNOP} is an attractive modelling parameter. Unfortunately in addition to measuring the changes in the *SNT*, the strip chart recording also reflects variations in maser gain and atmospheric conditions. This then renders the T_{SUNOP} parameter unusable for our purposes.

Now, continuing with the investigation of T_{SUN}, solve Eq. (6) for T_{SUN}. Some rearranging yields:

$$T_{SUN} = T\left(10^{\frac{\Delta SNR}{10}} - 1\right) \tag{8}$$

One method of developing our model would be to try to construct a set of ΔSNRs from actual measurements and then calculate a corresponding set of T_{SUN} values. The actual data will also yield a corresponding set of *SEP* angles. An empirical model could then be constructed providing the desired T_{SUN}, *SEP* relationship. We will adopt this approach in building the model. However, before calculating the ΔSNR set it will first be necessary to take a closer look at the system.

Before the spacecraft's signal reaches the ground antenna it has associated with it an incoming *SNR* (denoted SNR_{IN}). In a conjunction situation, with the Sun introduced as an extra noise source, the incoming *SNR* is degraded by an amount ΔSNR, producing a degraded incoming *SNR* (denoted $DSNR_{IN}$). See Fig. 1.

Mathematically, the above quantities are related as:

$$DSNR_{IN} = SNR_{IN} - \Delta SNR \tag{9}$$

Once in the system the $DSNR_{IN}$ undergoes the usual system losses (L_S) with a still more degraded *SNR* emerging (denoted $DSNR_{OUT}$). The L_S is estimated from the Telemetry Analysis Program (TAP) using an iterative method. The losses in the degraded SNR due to the system are expressed mathematically by the equation:

$$DSNR_{IN} = DSNR_{OUT} + L_S \tag{10}$$

The $DSNR_{OUT}$ is a quantity measured by the telemetry system and, therefore, $DSNR_{IN}$ can be determined.

With the above interpretation it is possible to calculate ΔSNR and hence T_{SUN} by starting with the measured quantity $DSNR_{OUT}$ and working backwards through the system. The only quantity unaccounted for is the SNR_{IN}. This can be estimated using the formula (see Appendix B):

$$SNR_{IN} = P_C + 20 \log \tan \phi - 10 \log k + 10 \log T_S - 10 \log T \tag{11}$$

where

P_C = downlink carrier power (dBm)

ϕ = modulation index

k = Boltzmann constant $\left(\frac{\text{mW - s}}{\text{K}}\right)$

T_S = symbol time

Putting the above ideas together, we can compute T_{SUN} as follows. Starting with the measured value of $DSNR_{OUT}$, Eq. (10) can be iterated to yield an approximate value of $DSNR_{IN}$. Combining Eqs. (11) and (9) gives for ΔSNR:

$$\Delta SNR = P_C + 20 \log \tan \phi + 10 \log T_S - 10 \log k - 10 \log T - DSNR_{IN} \tag{12}$$

Finally, substitution of this into Eq. (8) yields T_{SUN}:

$$T_{SUN} = T\left(10^{\frac{\Delta SNR}{10}} - 1\right) \tag{8}$$

This parameter, T_{SUN}, will be used as the modelling parameter. It is ambiguous inasmuch as it is subject to the interpretation of how the Sun actually affects the signal and the antenna-receiver system. One interpretation (the one used here) is to consider the Sun as an external noise source. Another would be to consider the system performance degradation by the Sun. In this latter case a more complicated set of equations would have been needed to find T_{SUN}. The interpretation adopted here is that illustrated in Fig. 1.

III. The Data

The data used in this study were obtained during the inferior conjunctions of Helios-1 and Helios-2 in early 1976. Specifically, the data span the following time periods:

Helios-1 DOY 066 – DOY 083 1976

Helios-2 DOY 074 – DOY 098 1976

Helios-1 achieved a SEP = 0 on DOY 074

Helios-2 achieved a SEP = 0 on DOY 084

Data were taken at both 26 and 64-meter-diameter antenna sites, each treated as an independent data set. Identical modelling methods were used on both sets of data to produce two separate models.

The data actually collected were the parameters needed to calculate T_{SUN}. These parameters include the downlink signal strength, modulation index, symbol rate, zenith noise temperature, elevation angle, *SEP* angle and $DSNR_{OUT}$. The working data base consisted of the two T_{SUN} sets and corresponding

SEP angles and was calculated from the actual data. A listing and a semilogarithmic plot of T_{SUN} vs *SEP* for both 26-m and 64-m data (Figs. 2, 3) are found in Appendix C.

IV. The Fit

In the previous sections we have seen how the T_{SUN} parameter will be used to model the *SNR* degradation during inferior conjunctions. Now what is needed is the relation between T_{SUN} and *SEP*. To obtain this relation it was decided to fit the data empirically, concentrating on the region spanned from 0 to 5 deg *SEP*.

Upon inspection of the graphical data (semilogarithmic plot) it was observed that T_{SUN} and *SEP* might be inversely proportional. It was, therefore, decided to try fitting a function of the form:

$$\ln T_{SUN} \propto \frac{1}{SEP}$$

Guided by the above functional form, we can construct the function:

$$T_{SUN} = A \exp\left\{\frac{B}{SEP + C}\right\} \qquad (13)$$

where A, B, and C are coefficients to be determined. Note that each of the coefficients affects a different characteristic of the curve. A scales the curve along the vertical axis, and B and C scale and translate the curve along the horizontal axis, respectively.

In fitting the curve, the coefficient C was set to zero and A and B were determined by a least squares fit. C was then varied through a range of values until a minimum standard deviation was found. With this new value of C, A and B were redetermined by least squares.

Because of the spread in the data (several orders of magnitude), the residuals and the standard deviation were expressed in logarithmic form:

$$\Delta(\text{dB}) = \text{residual in dB} = 10 \log\left(\frac{ACTUAL\ T_{SUN}}{PREDICTED\ T_{SUN}}\right)$$

$$\sigma(\text{dB}) = \text{standard deviation in dB} = \sqrt{\sum_{i=1}^{N} (\Delta_i)^2 / N}$$

The values of the coefficients yielding the best fit in each case are presented in the following table:

ANT	*A*	*B*	*C*
26	2.75	8.97	0.90
64	5.60	4.57	0.28

The standard deviation and maximum residual for these fits are:

ANT	σ (dB)	Δ_{MAX} (dB)	SEP(°)
26	1.737	-6.118	2.89
64	2.383	+5.571	0.74

By way of comparison, the following statistics are offered from a previous study utilizing a least squares curve fit of the function:

$$\ln T_{SUN} = A + B(SEP) + C(SEP)^2 + D(SEP)^3$$

$$\sigma\ (\text{dB}) = 2.7813$$

$$\Delta_{MAX}\ (\text{dB}) = -10.228$$

This maximum residual occurred at $SEP = 4^\circ.37$.

In their final form, the equations relating T_{SUN} and *SEP* are:

$$T_{SUN} = 2.75 \exp\left\{\frac{8.97}{SEP + .90}\right\} \quad \text{26-m case} \qquad (14a)$$

$$T_{SUN} = 5.60 \exp\left\{\frac{4.57}{SEP + .28}\right\} \quad \text{64-m case} \qquad (14b)$$

where *SEP* is in degrees.

V. T_{SUN} vs T_{SUNOP}

In an effort to obtain T_{SUN} more easily than by the method of Section II, the T_{SUN} data were plotted against the T_{SUNOP} data (obtained from T_{OP} strip chart measurements). Both the 26-m and 64-m data were plotted (see Figs. 4 and 5).

The data were plotted on log-log paper and exhibited a high degree of correlation:

$r = 0.88$ 26 m

$r = 0.97$ 64 m

A linear regression on the data yielded the following fit:

$$\log_{10} T_{SUN} = A \log_{10} T_{SUNOP} + B \qquad (15)$$

where

ANT	A	B
26-m	1.052	-0.043
64-m	1.148	-0.141

Some rearranging yields the following expressions,

$$T_{SUN} = (0.91)\, T_{SUNOP}^{(1.05)} \qquad 26 \text{ m} \qquad (16a)$$

$$T_{SUN} = (0.72)\, T_{SUNOP}^{(1.15)} \qquad 64 \text{ m} \qquad (16b)$$

These equations enable a user to estimate a T_{SUN} value from a readily obtainable T_{SUNOP}. It is interesting to note the departure of the data from the slope 1 line. This is probably due to maser gain variation.

VI. Summary

As we have seen, it is possible to model *SNR* degradation as a function of *SEP* (due to increasing *SNT*) during solar conjunctions to a reasonable degree of accuracy. To do so, however, requires the introduction of an intermediate parameter that depends only on the *SEP* angle, since the *SNR* degradation depends on both the SEP and antenna elevation angles. From Eq. (6) it was seen that T_{SUN} is a reasonable choice for this modelling parameter.

In addition, from a theoretical standpoint, it was seen that the explicit expression for T_{SUN} was dependent on the physical interpretation of the Sun-signal-system interaction. In this study, the point of view taken is that the solar effects are treated as a noise source.

From measured degraded *SNR* data, a T_{SUN} vs *SEP* data base was constructed using the procedure of Section II. This data base was divided into two groups: 26-m data and 64-m data. These were treated as independent data. A curve fit of the data provided a functional relationship between T_{SUN} and *SEP*.

What we now have is a model for *SNR* degradation as a function of *SEP*. The only inputs required are T_Z (a pretrack measurement), antenna elevation angle, symbol bit rate, and antenna size. The complete model is:

$$\Delta SNR \text{ (dB)} = 10 \log_{10} \left(\frac{T_Z + T_{EL} + T_{SUN}}{T_Z + T_{EL}} \right)$$

$$T_{EL} = A' \exp - B' (EL)$$

$$T_{SUN} = A \exp \left\{ \frac{B}{SEP + C} \right\}$$

The assumptions made in developing this model have been, admittedly, oversimplified.

In reducing the data, effects due to the weather and the quadrapod structure have been neglected. However, the most important improvements probably lie in the area of Sun-signal-system interpretation. An understanding of how the Sun actually affects the signal and system during inferior conjunction will, undoubtedly, be one of the more interesting approaches to building a better model.

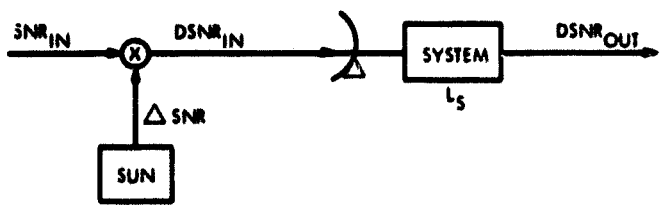

Fig. 1. Sun-signal-system interpretation

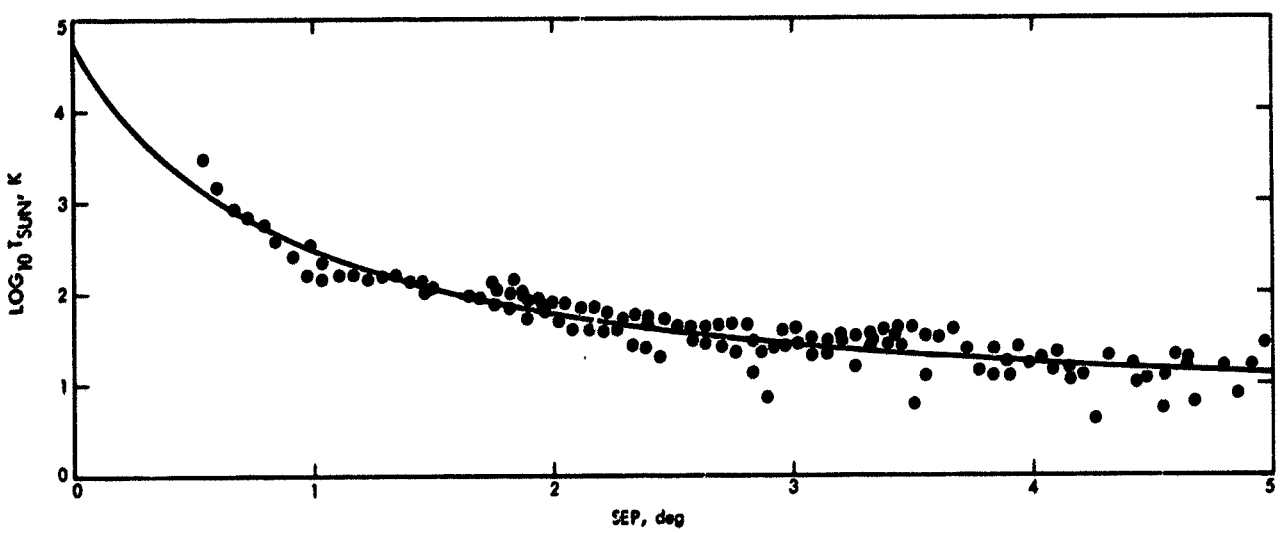

Fig. 2. Helios 1 and 2, T_{SUN} vs SEP, 26-m-antenna data

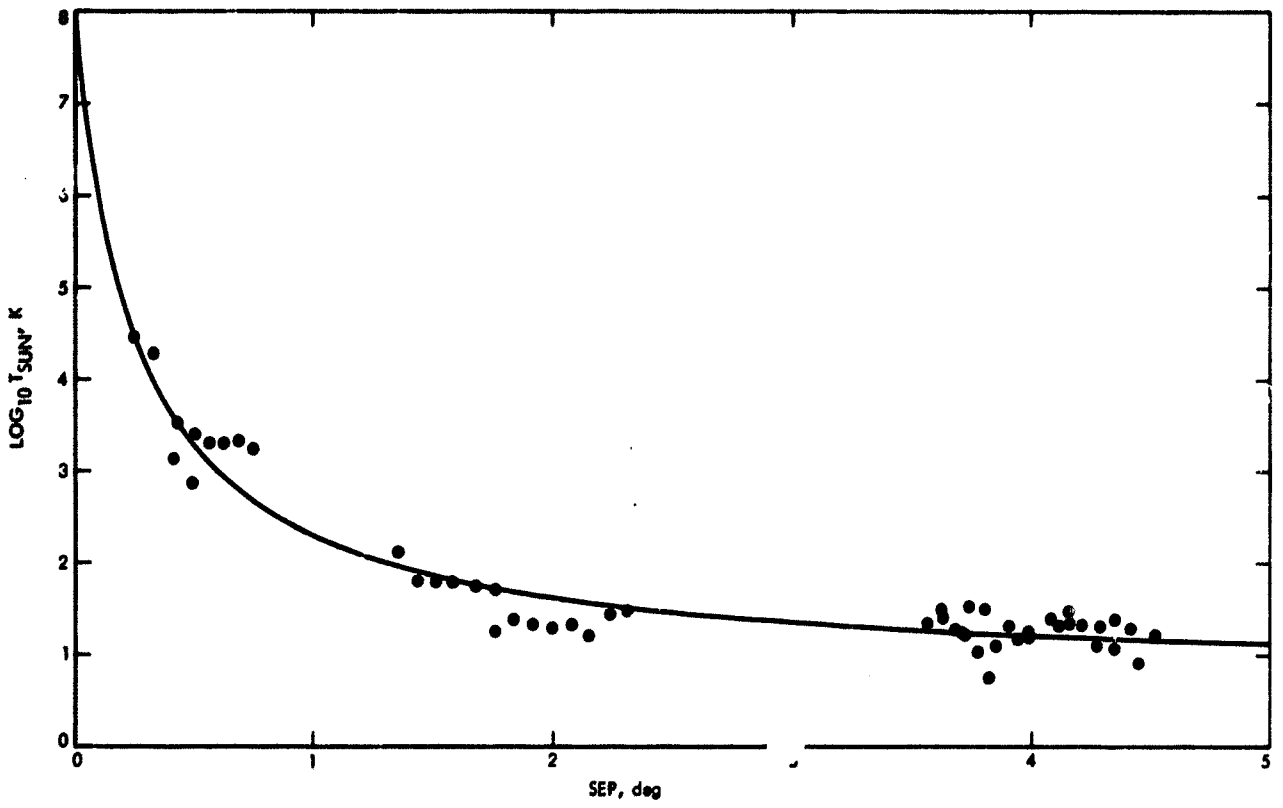

Fig. 3. Helios 1 and 2, T_{SUN} vs *SEP*, 64-m-antenna data

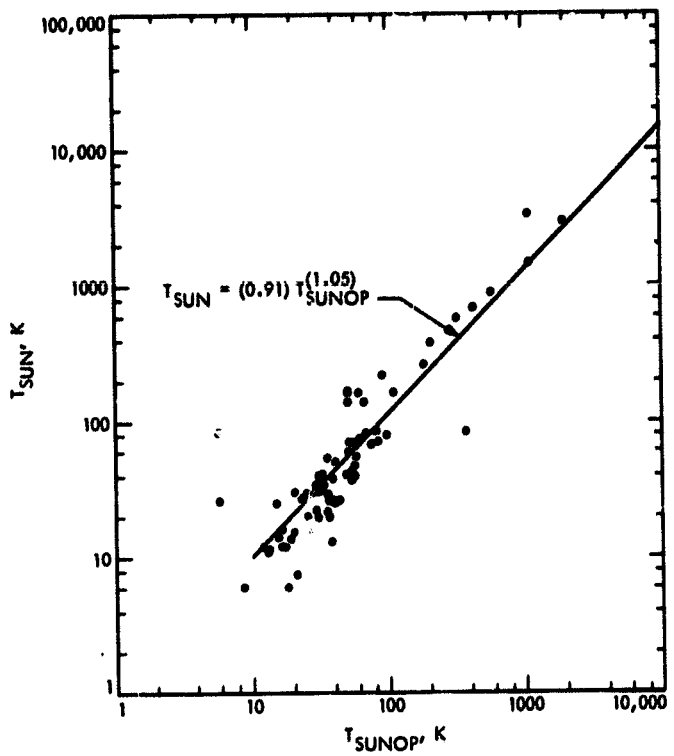

Fig. 4. Helios 1 and 2, T_{SUN} vs T_{SUNOP} 26-m-antenna data

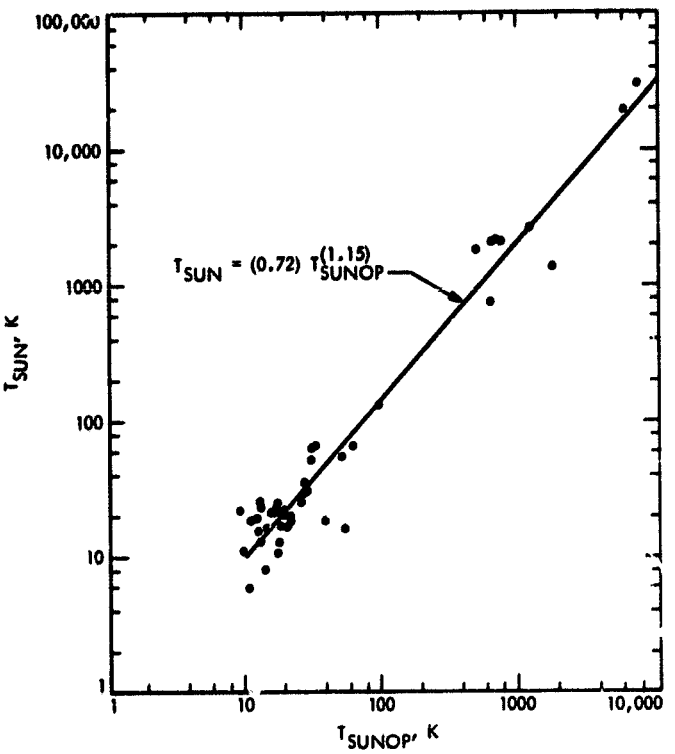

Fig. 5. Helios 1 and 2, T_{SUN} vs T_{SUNOP} 64-m-antenna data

Appendix A

Elevation Correction Coefficients

26-m antenna	64-m antenna
$A' = 29.91$	$A' = 25.90$
$B' = 0.051$	$B' = 0.066$

Appendix B

SNR_{IN} Equation Derivation

To obtain Eq. (11), start with Eq. (1):

$$SNR = \frac{ST_S}{kT}$$

Expressing *SNR* in dB write

$$10 \log SNR = 10 \log \frac{ST_S}{kT}$$

$$SNR \text{ (dB)} = 10 \log S + 10 \log T_S - 10 \log k - 10 \log T$$

Now, put $10 \log S$, data power in dBm, in a more useful form. We know:

$$\frac{S_C}{S_T} = \cos^2 \phi \qquad \text{and} \qquad \frac{S_D}{S_T} = \sin^2 \phi$$

where

S_D = data power
S_C = carrier power
S_T = total power
ϕ = modulation index

$$\frac{S_D}{S_C} = \tan^2 \phi \qquad \text{or} \qquad S_D = S_C \tan^2 \phi$$

Expressing S_D in dBm:

$$10 \log S_D = 10 \log S_C + 20 \log \tan \phi$$

$$S_D \text{ (dBm)} = S_C \text{ (dBm)} + 20 \log \tan \phi$$

$$SNR \text{ (dB)} = S_C \text{ (dBm)} + 20 \log \tan \phi$$

$$+ 10 \log T_S - 10 \log k - 10 \log T$$

Appendix C

T_{SUN} vs SEP

26-m-antenna data					
SEP	T_{SUN}	*SEP*	T_{SUN}	*SEP*	T_{SUN}
0.54	2948.67	2.45	20.27	4.04	19.02
0.60	1468.44	2.46	53.16	4.08	13.96
0.67	863.26	2.51	43.19	4.10	21.71
0.73	692.40	2.57	41.93	4.15	10.99
0.79	565.20	2.58	30.87	4.15	14.75
0.85	373.77	2.63	42.97	4.21	12.25
0.91	260.41	2.64	26.92	4.26	4.10
0.97	163.63	2.69	45.02	4.31	20.02
0.98	341.03	2.70	26.03	4.41	16.21
1.04	141.46	2.75	46.56	4.43	10.35
1.04	221.87	2.77	22.44	4.47	11.56
1.10	157.51	2.81	45.95	4.54	12.10
1.16	158.10	2.83	13.65	4.54	5.14
1.22	141.18	2.84	28.52	4.59	20.48
1.28	162.62	2.87	22.75	4.60	13.52
1.34	155.88	2.89	7.17	4.64	15.58
1.40	138.73	2.92	25.65	4.64	18.21
1.46	135.01	2.95	38.19	4.67	6.06
1.46	108.61	2.97	26.51	4.73	13.67
1.49	109.52	3.01	41.03	4.79	14.98
1.64	94.44	3.02	28.78	4.85	7.53
1.70	92.37	3.07	31.61	4.91	15.38
1.74	78.86	3.08	20.82	4.97	28.52
1.76	110.58	3.14	22.65		
1.77	98.94	3.14	29.72		
1.82	68.40	3.20	34.13		
1.82	102.81	3.20	30.77		
1.83	140.07	3.20	34.13		
1.87	102.97	3.26	34.23		
1.88	95.15	3.26	15.52		
1.88	98.43	3.32	26.21		
1.90	55.68	3.32	35.95		
1.90	84.11	3.33	30.60		
1.94	85.77	3.38	39.53		
1.96	73.19	3.40	26.51		
1.97	63.77	3.43	34.07		
1.99	82.22	3.44	40.42		
2.02	48.20	3.45	25.91		
2.05	76.63	3.45	25.91		
2.08	40.39	3.50	40.61		
2.11	68.52	3.50	5.96		
2.15	41.97	3.55	11.99		
2.17	70.36	3.55	33.81		
2.21	37.55	3.61	32.69		
2.23	60.29	3.67	37.42		
2.27	40.99	3.73	23.33		
2.29	53.32	3.77	13.63		
2.33	26.87	3.83	24.45		
2.34	56.00	3.84	11.82		
2.39	24.93	3.88	17.79		
2.40	53.90	3.90	11.90		
2.40	45.21	3.93	25.56		
		3.98	16.61		

64-m-antenna data			
SEP	T_{SUN}	*SEP*	T_{SUN}
0.24	29126.79	3.62	25.50
0.32	18968.85	3.67	18.99
0.41	1352.23	3.70	18.17
0.43	3328.34	3.73	16.83
0.49	740.89	3.73	34.41
0.50	2577.77	3.77	10.59
0.56	2035.71	3.79	31.57
0.62	2035.72	3.82	5.79
0.68	2125.27	3.85	12.85
0.74	1788.51	3.90	20.69
1.35	128.59	3.93	14.96
1.43	64.33	3.98	18.16
1.51	64.70	4.00	16.43
1.59	63.26	4.07	25.08
1.67	54.60	4.11	21.76
1.75	51.76	4.15	30.10
1.75	17.95	4.15	22.56
1.83	25.39	4.21	21.52
1.91	22.02	4.27	12.69
1.99	19.81	4.28	21.03
2.07	21.59	4.35	11.88
2.15	15.97	4.35	24.58
2.23	28.40	4.41	19.49
2.30	30.35	4.44	7.90
3.55	21.58	4.52	16.61
3.61	31.10		

DSN Research and Technology Support

E. B. Jackson
Radio Frequency and Microwave Subsystems Section

The activities of the Venus Station (DSS 13) and the Microwave Test Facility (MTF) during the period October 11, 1976, through February 13, 1977, are discussed and progress noted.

A significant effort on implementation of equipment for the planned conversion of DSS 13 to unattended operation is discussed. The Receiver and Microwave Subsystem are near completion, and the new feedcone and position encoders have been implemented onto the 26-m antenna. Support of the 400-kW X-band radar, located at DSS 14, is reported, and the activities of the DSN High Power Transmitter Maintenance Facility (HPTMF), located at DSS 13 and MTF, are discussed. The successful completion of the first series of observations planned for VLBI validation is reported and significant station maintenance activities are briefly covered.

Clock synchronization transmissions to DSS 43 and DSS 63 are reported, and an evaluation of any pointing errors in the new 26-m antenna position transducer are made. Extensive tracking support for various Advanced Systems Development and Ground Based Radio Science activities is reported. In particular, VLBI observations for DSN platform parameters, interplanetary scintillation of signals from the Viking spacecraft at small SEP angles, planetary radio astronomy, radio frequency interference analysis, and geo-stationary satellite radar cross section experiments were supported and are discussed.

I. Introduction

The activities of the Development Support Group, in operating the Venus Station (DSS 13) and the Microwave Test Facility (MTF) during the period October 11, 1976, through February 13, 1977, are discussed.

II. Unattended Operation, DSS 13

A. Receiver and Microwave Subsystem Automation

The receiver front ends have been installed into the electronics room of the DSS 13 26-m antenna. Interfacing with the maser has been accomplished and operation has been verified with temporary cabling. The microcontroller for control of the waveguide switching has been installed and operation verified. The modified PDS feedcone, now identified as the S-band Venus unattended (SVU) feedcone, has been installed onto the 26-m antenna. Inasmuch as this is a 64-m feedcone, a special adapter ring was necessary to physically mount this cone and fill the open space on the antenna surface which was left bare.

B. Transmitter Subsystem Automation

In anticipation of the future automation of the uplink, additional wiring was added to the transmitter remote control

cabinet (located in the Operations and Data Processing building) and documentation updated as necessary. The temperature and pressure transducers, with which operation of the transmitter cooling system will be monitored, have been tested and the results made available to the design engineers.

C. Antenna Subsystem Automation

The original position encoders with which the 26-m antenna was equipped have been removed and replaced with a new design transducer which provides 20-bit (1 part in 1,048,576) resolution. These new transducers have been temporarily interfaced with the station SDS-930 digital computer to provide an interim tracking and conical scanning capability pending complete implementation of a new antenna control and pointing computer.

D. 26-m Antenna Pointing System Evaluation

The introduction of a new position transducer into the 26-m antenna subsystem required evaluation of any pointing errors which might be present. Using an automatic boresighting computer program called SCOUR (*S*can and *CO*rrect *U*sing *R*eceiver), 22 hours of pointing evaluation were performed using radio sources as targets. An initial series of observations resulted in a nominal azimuth offset of +0.150 deg and an elevation offset of -0.015 deg. The transducer was adjusted to remove this offset and a new series of observations have commenced.

The new antenna control and pointing computer, a MODCOMP, has been installed and interfaced with the servo system, but software checkout has not yet been accomplished. This checkout is being slowed by an intermittent problem which has cropped up with the new encoders. Although several successful tracks have been performed with the new encoders and the SDS-930, a problem has recently surfaced wherein the encoders exhibit a "jump" in indication. Readjustment of the coarse and fine synchro-/resolvers is in progress to correct this problem.

III. X-band Radar, 8495 MHz, 400 kW

In support of a major effort to realize a reliable 400-kW X-band radar, significant testing and on-site support at DSS 14 has been provided by the Development Support Group. Testing included full power testing, on an expedited basis, of two VA949J klystrons (S/N 33R1 and 32R2) at the 200-kW power level. On-site support included trouble shooting and repair of the buffer amplifier, as well as disassembly and reassembly of the final amplifier(s) and transportation by JPL aircraft of the defective klystrons to and from the vendor for repair.

IV. Deep Space Network High Power Transmitter Maintenance Facility (DSN HPTMF)

The protective circuits (arc and body current detectors) with which the DSN high power transmitters are equipped must act very rapidly (within microseconds) when a fault condition develops. Extensive measurement of the "time to perform" of the spare and installed detectors was performed at DSS 13. Additionally, three arc detectors, two photon generators, one filament power monitor and various logic cards which had failed in service were repaired and operation verified at the HPTMF.

Other testing activities included acceptance class testing of three DSN 20 kW (5K70SG) klystrons and delivery of them, as needed, to DSN Logistics Facility for shipment to the stations.

V. VLBI Validation

In support of the implementation of VLBI into the DSN as an operational technique, several demonstrations of short and long baseline length determination are planned. DSS 13 will play an active role in this series of demonstrations and additional equipment was necessary.

For Experiment 1, the data gathering technique required utilization of an SDS-920 digital computer, with which DSS 13 is not equipped. A computer, previously used at DSS 12 as the TCP, was installed at DSS 13 by station personnel and checked out using the special program required for VLBI data collection. A wide band (40-MHz instantaneous bandwidth) maser was also a requirement, and a development maser, which is also tunable from 2270 to 2388 MHz, was installed and interfaced with station receivers.

With this new equipment, and with a special receiver furnished by the Validation Project, DSS 13 successfully supported Experiment 1, Run 1 and Experiment 1, Run 3 for a total time of 22.5 hr. The first run was made using the old feedcone, and the last run was made using the new SVU feedcone described previously (*DSN Progress Report 42-36*, pp. 153-156). With the completion of Experiment 1, the SDS-920 computer is no longer needed and will be disposed of through appropriate channels.

VI. Station Maintenance

During the last month of use of the old 26-m feedcone, additional maintenance was required on the maser refrigerator, but installation of the new tunable wideband maser and over-

haul of the associated maser compressor has apparently produced a reliable system, as no problems have been experienced since that installation.

The 1.2-MW, 70-kV dc Power Supply used with the high-power transmitter developed excessive ripple in the output voltage. Investigation revealed that one or more of the solid-state rectifier assemblies had failed. Baseline performance under test conditions was ascertained for the spare assemblies and a complete replacement was made. The transformer and rectifier tanks were cleaned, the insulating oil was filtered, and the system was restored to service. Wiring changes were made in the over current and phase unbalance protective circuits. Extensive phase voltage and current measurements were also made for future reference in performance evaluation.

The data collection systems of the Faraday rotation and solar and microwave monitoring equipment failed in several areas, but all assemblies have now been repaired and data collection on both punched paper tape (Faraday rotation) and magnetic tape (solar and microwave and Faraday rotation) is now being performed.

VII. Clock Synchronization System

Although troubled by problems at the receiving stations, and, on one occasion, by a transmitter problem a total of 29 transmissions were made as scheduled by DSN Scheduling. Of these, 12 transmissions were made to the DSS 43 complex and 17 were made to the DSS 63 complex, for a total of 29 hr of reception and correlation.

The electrical power input to the control system was interrupted by a failure of one phase of the incoming three-phase power. The connecting lug on the input to the circuit breaker broke and the line came into contact with the panel case. The ground current overheated and melted the safety ground wire and the resulting smoke activated the smoke detectors. The fire department responded in a timely fashion and the station electrician repaired the damage and restored the system to service. No planned testing or transmissions were affected.

VIII. DSN Platform Parameters

VLBI promises to be useful for spacecraft navigation, if a suitable set of calibrated radio sources can be developed. Determination of the flux density and position of this set of radio sources is one of the tasks underway in this Advanced Systems Development experiment. In support of this survey of radio sources, DSS 13 provided 67.75 hr of VLBI observing in conjunction with either DSS 43 or DSS 63. Approximately 330 source observations were made during this reporting time.

IX. USAF Satellite Radar Cross Section

By letter agreement between OTDA and USAF, a series of radar observations of a geo-stationary satellite were made. Using the 400 kW S-band transmitter at DSS 14, the target was illuminated. By frequency shifting the transmitter every round trip light time, reception of the reflected signal at DSS 13 was possible. The received signal was microwaved to DSS 14 for analysis and recording. This project is now complete and DSS 13 provided 12.25 hr of observing during this period.

X. Planetary Radio Astronomy

On a time-available basis DSS 13 provides support to this experiment from the "Ground Based Radio Science Plan." The radiation received from Jupiter at 2295 MHz is measured and its variability determined. A number of radio sources are used as calibrators for this program. A total of 35.25 hr of observing were accomplished during this period, using the 26-m antenna and both RCP and LCP, at an observing frequency of 2295 MHz.

XI. Pulsar Rotation Constancy

Also on a time-available basis, DSS 13 observes pulsars in support of this experiment from the "Ground Based Radio Science Plan." The data collected include pulse rate, pulse-to-pulse spacing, pulse power, and pulse shape. These measurements are made at 2388 MHz, with the 26-m antenna adjusted for LCP. During this period, 48.5 hr of pulsar tracking was performed. These data are normally taken as part of the DSN automation test bed activities. However, at present, data will be taken in the manual mode until the automation test bed is reconfigured in June 1977.

XII. Radio Frequency Interference

With the increase in utilization of S-band, the potentiality for interference with the DSN grows more probable. In support of a program to learn more about this problem, DSS 13 provides observations in special circumstances which might produce interference to the DSN radio frequency systems. A large-scale USAF exercise, which involved extensive utilization of electronic countermeasures, provided such a special circumstance. DSS 13 performed 9 hours of observing, and observed interference from this exercise in the band 2290 to 2300 MHz.

XIII. Interplanetary Scintillation

In support of the Viking science project, DSS 13 performed tracking of the Viking spacecraft as the Sun-Earth-Probe (SEP) angle went through a minimum. The received signals, which were received using a predicted frequency technique and a digital controlled oscillator, had passed through the interplanetary media and, in particular, had passed through varying amounts of the solar corona. The signals were microwaved to DSS 14, which was also observing, for real-time spectral analysis and recording. Four days of spaced observations were provided by DSS 13 for a total of 25.75 hr of observing.

Cost Reduction Potential of the DSN Data Base

M. McKenzie
TDA Planning

The cost of the DSN data base can be reduced by computerizing and unifying the current multiplicity of separate manual, computer, and hybrid data bases. Savings would accrue from eliminating all manual system costs, increasing efficiency in data base implementation and maintenance-and-operation, and increasing data accuracy. By applying a simple mathematical savings model to current data base costs, this study estimates the probable range of net ten-year savings. The minimum net savings, under the assumptions of the study, is calculated as $7.5 million.

I. Introduction

The evolving technology and methodology in data bases have now reached the point at which the DSN can properly consider unifying its approach to specification and control of the operational DSN data base. The DSN is currently using computers in most of the separate data bases. Now the technology exists for a unified DSN data base that optimally splits functions between hardware, software, and people to maximize service to the end user within life-cycle cost constraints. These productivity improvements can arise from a reduction in both paperwork and data errors, not to mention the provision of much more timely access to the data required for Operations, Operations Support, and DSN Management. It is the purpose of this article to conservatively estimate the cost saving potential of this unified approach to the DSN data base.

The evolving Configuration Control and Audit (CCA) Assembly proposes to combine all the DSN distended data bases under one structured, though decentralized, computer system. Designed to minimize redundant data, reduce operating costs, and increase productivity (Ref. 1), the CCA Assembly would have a structured data base and user terminals at each DSN complex (Goldstone, Australia, and Spain). A JPL master data base would be in weekly communication with each through existing GCF high-speed, two-way transmission links. The data base structure is planned as a standardized, cross-referenced, hierarchical tree of files such that all users input data according to a standard format at an on-line terminal (Ref. 2). Integrity of the input is the responsibility of the respective complex.

The question addressed by this study is then: given the present data base structure and work load, what would be the life cycle savings (or disavings) accompanying conversion to such a structured computerized data base? The savings model, called DBSAVE and expanded in Appendix B, addresses this

problem and estimates the net ten-year savings likely to result from the DSN data base structuring and unification.

II. Data Base Savings Model — DBSAVE

The present DSN data base structure can be characterized as follows:

(1) Manual data base systems.

(2) Computerized data base systems, composed of:

(a) Pure computer time.

(b) Manual input to computer.

The present total DSN data base yearly costs (CT1) can also be divided into the categories shown in Table 1.

Hypothetically, the conversion of this structure to one unified computerized system can be viewed as a two-step process. First, all manual systems (any manual gathering, storing, filing, and updating of data) are converted to computer. There is an efficiency ratio (call it EFF1) of time as employed in the old manual data base system to time as used in the new computerized system. When applied to the present manual data base system costs, EFF1 will give rise to the savings (or disavings) of step 1. Call these savings SAV1. At this point, all data is now on computer, but the various computerized data base systems are nonrelated.

Next, all the now computerized data systems are unified under one structured system. Again, there is an efficiency ratio between the old computer systems and the structured computer system. This ratio may well differ for the two computer data base system components — computer time and manual input. So these are treated separately with:

EFF2: the efficiency ratio of computer time as used in a nonstructured computer system to that as used in the unified computer system.

EFF3: the efficiency ratio of manual input time as used in a nonstructured computer system to that as used in the unified computer system.

Applying these efficiency ratios to the proper computer component costs (including the extra loads derived from step 1) results in the step 2 savings (or disavings) SAV2 and SAV3.

Thus, the data flow for model DBSAVE can be visualized as shown in Fig. 1.

This two-step model of the data base conversion process is not altogether hypothetical. Many older manual data bases were converted to separate computer systems, and now will be unified under the CCA Assembly. The model fits the current structure of the DSN data base, the final system toward which the CCA is aimed, and is not an unreasonable description of the intermediate process.

In addition to savings SAV1, SAV2, and SAV3, are the yearly savings, called ERSAVE, derived from the increased accuracy of the DSN data base. The total gross yearly savings (SAVTOT) from the two-step process are then simply:

$$SAVTOT = SAV1 + SAV2 + SAV3 + ERSAVE$$

The net ten-year savings (NETSAV) are:

$$NETSAV = (SAVTOT*10) - (\text{ten-year costs of data base conversion})$$

Each component of the SAVTOT and NETSAV calculations is further explained in the following sections.

A. Section SAV1

SAV1 is derived from the elimination of all manual data base costs, by converting manual systems to computer. Obviously, the savings will be the difference between the original manual data base costs and the new computer costs from this added work load. The new computer costs will depend on the relative efficiency of the manual to computer systems, EFF1.

The value for EFF1 is not precisely known, so EFF1 is parameterized in DBSAVE as a 1 X 4 vector with four possible values. There is no restriction, within the model, on the maximum or minimum value of the EFF1 elements. These are delegated to the choice of the user. Letting A be a 1 X 4 vector with each element equal to 1, the first savings are:

$$SAV1 = CM1 - (EFF1*CM1) = (A - EFF1) * CM1$$

Four possible SAV1 values, either positive or negative, are thus calculated.

B. Section LOAD

Step 2 converts all computer systems, including those derived in step 1, to the unified computer data base. First it is necessary, however, to calculate the extra computer system costs derived from the earlier manual to computer data base conversion. This extra cost, called CTC2, is calculated:

$$CTC2 = EFF1 * CM1$$

As CTC2 depends on EFF1, it is also a 1 X 4 vector.

C. Section SAV2

Some portion of this load, CTC2, is pure computer time. This portion is likely to vary for different data bases. A good average value is the ratio of present computer time costs to total computer data base costs, or CCC1/CTC1. Though the computer time and manual input portions may not be exactly averageable over work units, any discrepancy from the chosen average can be absorbed in the variables EFF2 and EFF3.

Thus, the extra computer time costs, CCC2, from the manual system to computer conversion, are:

$$CCC2 = (CCC1/CTC1) * CTC2 \qquad (1 \times 4 \text{ vector})$$

Now the total computer time costs, CCC3, to be converted to the unified computer system, must be the sum of the manual-converted costs plus present costs, or:

$$CCC3 = (CCC1 * A) + CCC2 \qquad (1 \times 4 \text{ vector})$$

(The A vector is necessary to conform the scalar CCC1).

The total computer time can now be converted to the unified system. EFF2, the nonsystematic-to-systematic computer time ratio, is parameterized as a 4×1 vector. (The vector directions are chosen so that in the final NETSAV $4 \times 4 \times 4$ matrix, each EFF parameter will vary in a different direction). Again, there are no size restrictions within the model placed on the EFF2 values.

Thus, the savings (positive or negative) from the conversion of computer time to the structured computer system are:

$$SAV2 = CCC3 - (EFF2 * CCC3)$$

$$= (B - EFF2) * CCC3 \qquad (4 \times 4 \text{ vector})$$

where B is a 4×1 vector with all elements equal to 1.

D. Section SAV3

This section is symmetric to Section SAV2. The same equations are used, with manual input to computer substituted for computer time. Thus the extra manual input to computer costs, from step 1, is:

$$CMC2 = (CMC1/CTC1) * CTC2$$

The total manual input to computer costs is:

$$CMC3 = (CMC1 * B) + CMC2$$

Therefore the savings (positive or negative) from the conversion of manual input to the structured computer system are:

$$SAV3 = (B - EFF3) * CMC3 \qquad (4 \times 4 \text{ vector})$$

E. Section SAVTOT

As earlier stated:

$$SAVTOT = SAV1 + SAV2 + SAV3 + ERSAVE$$

For conformity, the SAV matrices are extended to three dimensions (I, J, K) so that the three efficiency ratio parameters vary along different axes. Specifically, EFF1 of SAV1 varies along the K axis, EFF2 of SAV2 varies along J, and EFF3 of SAV3 varies along I. ERSAVE must be a $4 \times 4 \times 4$ matrix with each element equal to the ERSAVE value.

F. Section NETSAV

This final section calculates the estimated ten-year net savings of the unified computerized data base system. First, the values of the two quantifiable system costs – IMPL and MO – are prompted from the program user. IMPL is the estimated implementation cost of the unified system. MO is the estimated yearly maintenance and operations cost for the system.

The ten-year estimated cost, then, is:

$$COST = IMPL + (MO * 10)$$

To conform to the SAVTOT matrix, COSTS is the proper $4 \times 4 \times 4$ matrix, with each element equal to COST. Then,

$$NETSAV = (SAVTOT * 10) - COSTS$$

III. Values of Constants and Variables

A. Value of Constants

The values of the constants for the model were determined through interviews with the cognizant individuals of forty WAD 76-1 work units likely to include major data base functions. These were both in-house and M&O units. Of these, twenty-one did have noticeable data base costs. The results of the interviews are shown in Table 2. The values for the constants in DBSAVE are given in Table 3. The values in Table 3, it should be noted, are "ballpark" figures. The information solicited in the interviews was often not obvious from the Work Authorization Document. So, though the data represent information gained from knowledgable personnel, they are necessarily somewhat "gut-level" in nature.

There are other effects, however, which would tend to offset inaccuracies. First, it is reasonable to assume that any errors are randomly distributed, thus having a self-canceling effect. Also, very importantly, all the relevant work units were undoubtedly not found during the survey. This would downbias the final savings figures, if anything.

B. Value of ERSAVE

The yearly savings due to the increased accuracy of the DSN data base, ERSAVE, are assigned the value of $877k/yr. Based on industry-accepted error rates and current cost of the data base, the estimated present cost of DSN data base errors is $975k/yr (in 1976 dollars) (Ref. 3). Under the final system this figure will be reduced by a factor of ten (Ref. 4). Thus:

$$\text{ERSAVE} = (\$975/\text{k}) * (0.9) = \$877\text{k/yr}$$

C. Values of Variables

The values for the efficiency ratio vectors were chosen as:

$$\text{EFF1} = (0.5, 0.75, 0.825, 0.95)$$

$$\text{EFF2} = (0.1, 0.55, 0.605, 1.0)$$

$$\text{EFF3} = (0.3, 0.65, 0.715, 1.0)$$

In justification of these values, they are first of all *averages* over all data bases. For instance, though EFF1 is possibly greater than one for a very small data base, over all data base work the average will be less than one. In substantiation of this assertion are the results of the first phase of the Goldstone Facility Maintenance computerized data base system. F. R. Maiocco and J. P. Hume report "the following improvements in the Work Control Center's efficiency have been achieved:"

(1) "Report preparation time, which took from 2 to 4 weeks [under the manual system], has been significantly reduced to basically computer access time."

(2) "Computation errors are basically non-existant and the accuracy of the reports is dependent upon the accuracy of the data input to data files."

(3) "Expanded capability exists in energy reporting not previously available in the manual recording system (Ref. 7)."

Thus, the likely range of EFF1 is conservatively selected as 0.5 to 0.95. The second EFF1 element, 0.75, is simply the midrange value. The third element of each efficiency vector is 10% greater than the second element, for use later in sensitivity tests. For EFF1, this test value is 0.825.

The values chosen for EFF2 and EFF3 are not otherwise substantiated. The assumption is simply made that computer time and manual input time will not be less efficient under the structured, computer data base system, than under an unstructured system. It is believed that this is the case; however, there exists no data in the literature to test the assumption. Evaluation of the first phase of the CCA Assembly will hopefully provide solid evidence, one way or the other. Until then, the results of this study must be viewed with this assumption in mind.

Thus, the range of EEF2 was chosen as 0.1 to 1.0, and EFF3 as 0.3 to 1.0. Again the second elements are midrange values, and third elements are test values.

D. Values of Structured Data Base System Costs

The CCA Assembly system costs are estimated in Table 4, which are the costs for the CCA Assembly only. All other data base costs are encompassed in the model's cost efficiency calculations.

IV. Computer Output of the Model

A. Savings Estimates

This output is shown in Fig. 2.

Note that in reading the computer output of a three-dimensional matrix (I, J, K), the K axis varies most rapidly, then the J, and lastly the I. For example, the corresponding three-dimensional elements for the first six rows of matrix output are:

(1, 1, 1)	(1, 1, 2)	(1, 1, 3)	(1, 1, 4)
(1, 2, 1)	(1, 2, 2)	(1, 2, 3)	(1, 2, 4)
(1, 3, 1)	(1, 3, 2)	(1, 3, 3)	(1, 3, 4)
(1, 4, 1)	(1, 4, 2)	(1, 4, 3)	(1, 4, 4)
(2, 1, 1)	(2, 1, 2)	(2, 1, 3)	(2, 1, 4)
(2, 2, 1)	(2, 2, 2)	(2, 2, 3)	(2, 2, 4)

B. Output Evaluation

1. **Sensitivity.** Before even examining the estimated net savings, the sensitivity of the model must be checked. The computer program for the savings model provides tests of the sensitivity of the savings estimates with respect to changes in variables and constants. The method used is fully explained in Appendix C and results are given in Appendix D.

The sensitivity test results are very encouraging. If the EFF1 value is increased 10% from midrange, the estimated net

savings decreases by only 4%. For a 10% increase in the variable EFF2, NETSAV decreases only 2%, and likewise only 4% for EFF3. Even when all three are increased by 10%, NETSAV decreases by 11%. There are, therefore, no "blow up" points in the results with respect to the variables.

The NETSAV sensitivity with respect to constants is also quite acceptable. At the most, NETSAV increases by 5% when the CM1 constant is increased by 10%.

Thus, the net savings calculations are not highly sensitive to changes in variables, or errors in constants.

2. Nonquantifiable costs and savings. The ten-year costs of the proposed system are seen as $1,967k. There are other costs, however, which could not be quantified. For example, some personnel involved in the data base work may need additional training. There is some cost of data inaccessability when one of the computers is temporarily down. Finally, there may be a temporary cost of maintaining constant output during the period of transition to the unified system.

Hopefully, the nebulous costs are minor and/or are offset by corresponding qualitative savings. For instance, the external savings from the increased system accuracy could not be quantified. Also, substantial expected savings from decreased turnaround time were omitted. Finally, the potential use of the increased data capacity of the system could not be included in the model.

3. Quantitative savings. In any case, the quantitative savings results are clear. In general, NETSAV varies linearly with each variable, yet nonlinearly with respect to all three variables. It varies such that at the lower savings range, greater then linear increases in NETSAV result from linear decreases in variables. (See the graphs in Appendix A.) This means that at the minimum range of possible net savings, the region most important in a policy decision, greater than linear gains in NETSAV result from a slight decrease in estimated EFF values. This result, too, is encouraging.

This nonlinearity points out that the previous sensitivity results are limited to the assumptions under which they were made. In other words, since the tests dealt with the midrange of the NETSAV curve, it is here that the results apply. Until a more exact study is required – one dealing in specific values rather than variables – the tests performed here are sufficient.

Finally, in magnitude, the net ten-year estimated savings range from $7,584.8k to $24,620.2k. Therefore, even in the least savings case, where the manual system to computer system efficiency ratio equals 0.95 and the other efficiency ratios are unity, the estimated net ten-year savings are still $7.5 million. At the other extreme is an estimated $24 million savings.

Thus, if the assumptions made in this study are valid, substantial savings are clearly possible – the DSN data base does indeed have a strong potential for cost reduction.

References

1. A. I. Bryan, private communication.
2. For more information on the current status of the Configuration Control and Audit Assembly, see A. I. Bryan, "A Distributed Data Base Management Capability for the Deep Space Network," *JPL Deep Space Network Progress Report 42-33*, Jet Propulsion Laboratory, Pasadena, Calif., June 15, 1976.
3. E. C. Posner, private communication.
4. E. C. Posner, private communication.
5. F. R. Maiocco and J. P. Hume, "Computerizing Goldstone Facility Maintenance Data for Management Decisions," *JPL Deep Space Network Progress Report 42-32*, p. 313, Jet Propulsion Laboratory, Pasadena, Calif., April 15, 1976.
6. E. C. Posner, private communication. This estimates the one-time cost, with reference to the CCA Assembly, in converting manual data bases to computer.
7. E. C. Posner, private communication.

Table 1. DSN data base yearly cost categories

Category	Name of constant in model
Cost of total manual data base, including overhead	CM1
Cost of total computer data base	CTC1
Cost of computer time of computer data base	CCC1
Cost of manual input to computer data base	CMC1

Table 2. Value of constants

JPL work unit No.	Computer time cost per year, $k	Manual input cost per year, $k	Total computer cost per year, $k	Total manual data base cost per year, $k
12-10-02	45.0	0.0	45.0	0.0
12-30-01	3.0	3.0	3.0	96.3
12-30-03	0.0	0.0	0.0	2.6
13-31-01	62.0	6.5	68.5	0.0
13-31-04	0.0	0.0	0.0	193.0
13-41-04	0.0	0.0	0.0	2.4
13-41-06	0.0	0.0	0.0	3.0
13-41-07	0.0	0.0	0.0	4.6
31-10-55	9.3	26.0	35.3	0.0
31-20-90	8.0	14.0	22.0	0.0
43-20-04	2.2	0.0	2.2	34.2
43-20-09	18.0	44.0	62.0	0.0
44-10-01	3.0	0.0	3.0	7.0
44-10-02[a]	0.5	4.0	4.5	4.5
44-30-01	27.0	195.0	222.0	0.0
Subtotal 1:	178.0	289.5	467.5	347.6
Goldstone work units: No.				
11-10-01	2.0	11.6	13.6	68.0
11-10-02	0.0	0.0	0.0	93.0
11-11-02	0.0	0.0	0.0	59.2
11-11-04	0.0	0.0	0.0	50.1
11-12-05[b]	0.0	0.0	0.0	120.0
11-12-10	0.0	2.0	2.0	55.0
Subtotal 2:	2.0	13.6	15.6	445.3
Overseas station costs estimated as twice the applicable Goldstone costs				
Subtotal 3:	4.0	27.2	31.2	770.6
Total	184k/yr	330.3k/yr	514.3k/yr	1563.5k/yr

[a]This is a new unit. The cost values are estimated as half the unit's budget, split evenly between manual data base costs and computer data base costs.

[b]Only half of this unit's costs are applicable to overseas stations.

Table 3. Constants in DBSAVE

Meaning of the constant	Value, $k	Constant name
Cost of total DSN data base	2077.8	CT1
Cost of total computer data base	514.3	CTC1
Cost of computer time of computer data base	184.0	CCC1
Cost of manual input to computer data base	330.3	CMC1
Cost of total manual data base (including overhead)	1563.5	CM1

Table 4. CCA Assembly system costs

Cost explanation	Value	Model name
Implementation costs (from WAD 76-2)		IMPL
Station configuration control audit engineering	$488k	
Station configuration control audit equipment	$879k	
CCA Assembly costs distributed in operations accounts (Ref. 6)	$100k	
Total	$1467k	
Maintenance and operations costs (Ref. 7)	$50k/yr	MO
0.5 manyear (JPL)		
1.0 manyear (contractor)		
$5k for parts		

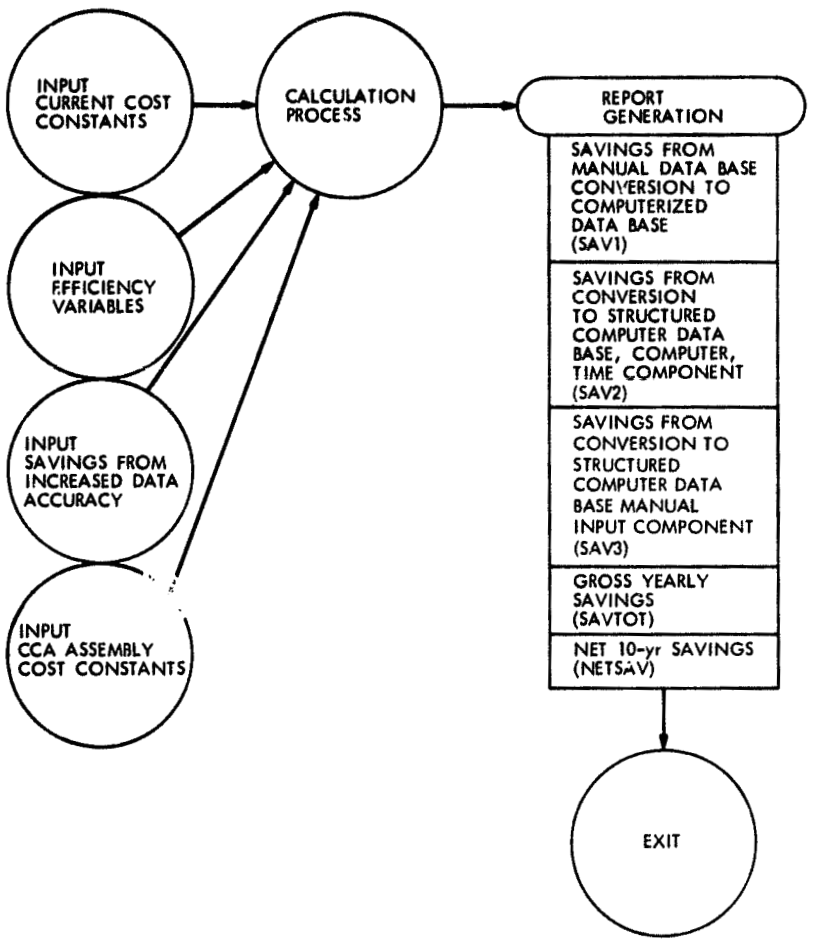

Fig. 1. Data flow for model DBSAVE

```
>RUN
CT1: 2077.0
CTC1: 514.3
CCC1: 124.0
CNC1: 330.3
CN1: 1563.5
ERSAVE: 877
ENTER EFF1: .5
ENTER EFF1: .75
ENTER EFF1: .825
ENTER EFF1: .95
ENTER EFF2: .1
ENTER EFF2: .55
ENTER EFF2: .605
ENTER EFF2: 1.0
ENTER EFF3: .3
ENTER EFF3: .65
ENTER EFF3: .715
ENTER EFF3: 1.0

SAVINGS CALCULATIONS

SAV1 IN $K:     731.7     399.9     273.6      79.2

SAV2 IN $K:
     417.3     543.2     580.9     643.9
     208.7     271.6     290.5     321.9
     104.2     238.4     255.0     282.6
       0.0       0.0       0.0       0.0

SAV3 IN $K:
     562.7     756.4     811.1     899.0
     291.3     379.2     405.5     449.5
     227.2     308.8     330.2     366.0
       0.0       0.0       0.0       0.0

SAV3 IN $K:
     562.7     756.4     811.1     899.0
     562.7     756.4     811.1     899.0
     562.7     756.4     811.1     899.0
     562.7     756.4     811.1     899.0
     291.3     379.2     405.5     449.5
     291.3     379.2     405.5     449.5
     291.3     379.2     405.5     449.5
     291.3     379.2     405.5     449.5
     227.2     308.8     330.2     366.0
     227.2     308.8     330.2     366.0
     227.2     308.8     330.2     366.0
     227.2     308.8     330.2     366.0
       0.0       0.0       0.0       0.0
       0.0       0.0       0.0       0.0
       0.0       0.0       0.0       0.0
       0.0       0.0       0.0       0.0
```

Fig. 2. Savings estimates

```
SAVTOT IN $K:
EFF1 VARIES WITH K, EFF2 J, EFF3 I
      2650.7      2569.4      2542.6      2498.0
      2450.1      2297.8      2252.2      2176.1
      2424.6      2264.6      2216.7      2136.7
      2241.4      2026.3      1961.7      1854.1
      2367.4      2190.2      2137.1      2048.5
      2158.7      1918.7      1846.6      1726.6
      2132.2      1885.5      1811.1      1687.2
      1950.1      1647.1      1556.2      1404.7
      2313.3      2119.8      2061.8      1965.0
      2104.6      1848.2      1771.3      1643.1
      2079.1      1815.0      1735.8      1603.8
      1896.0      1576.6      1480.8      1321.2
      2076.1      1811.0      1731.5      1599.0
      1867.4      1539.5      1441.1      1277.1
      1841.9      1506.3      1405.6      1237.8
      1658.7      1267.9      1150.6       955.2

IMPL: 1467
 NO: 50

TOTAL 10 YEAR COSTS IN $K:     1967.0

NET 10 YEAR SAVINGS IN $K:
     24620.2     23727.3     23459.4     23012.9
     22533.6     21011.4     20554.7     19793.6
     22278.6     20679.5     20199.7     19400.2
     20447.1     18295.5     17650.1     16574.3
     21706.9     19935.4     19403.9     18518.1
     19620.4     17219.5     16499.3     15298.8
     19365.3     16887.6     16144.2     14905.4
     17533.8     14503.6     13594.6     12079.5
     21165.9     19231.2     18650.8     17683.4
     19079.3     16515.3     15746.1     14464.1
     18824.3     16183.4     15391.1     14070.6
     16992.7     13799.4     12841.4     11244.8
     18793.7     16143.5     15348.4     14023.4
     16707.1     13427.6     12443.8     10804.1
     16452.1     13095.7     12088.8     10410.6
     14620.5     10711.7      9539.1      7584.8
```

Fig. 2 (contd)

Appendix A

Graphs

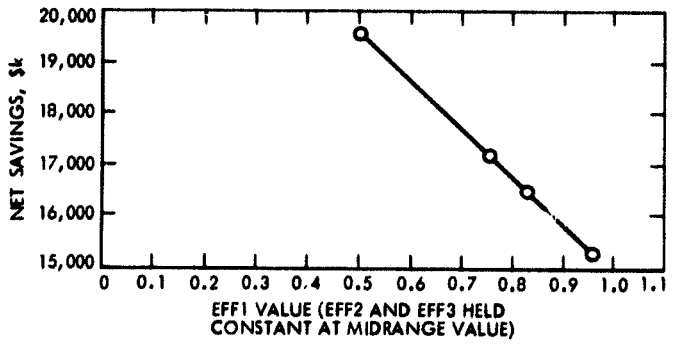

Fig. A-1. NETSAV vs EFF1

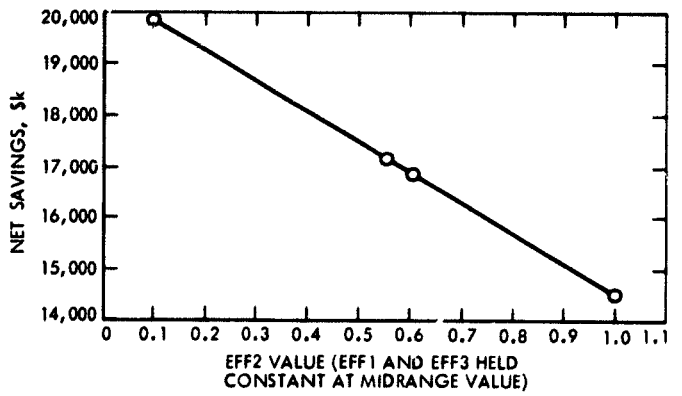

Fig. A-2. NETSAV vs EFF2

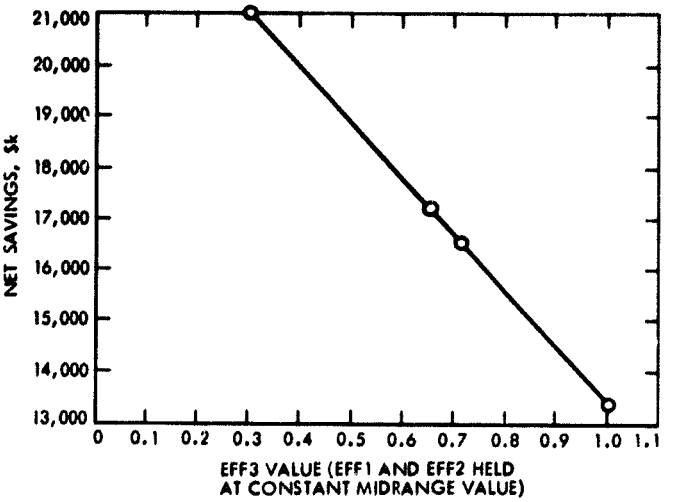

Fig. A-3. NETSAV vs EFF3

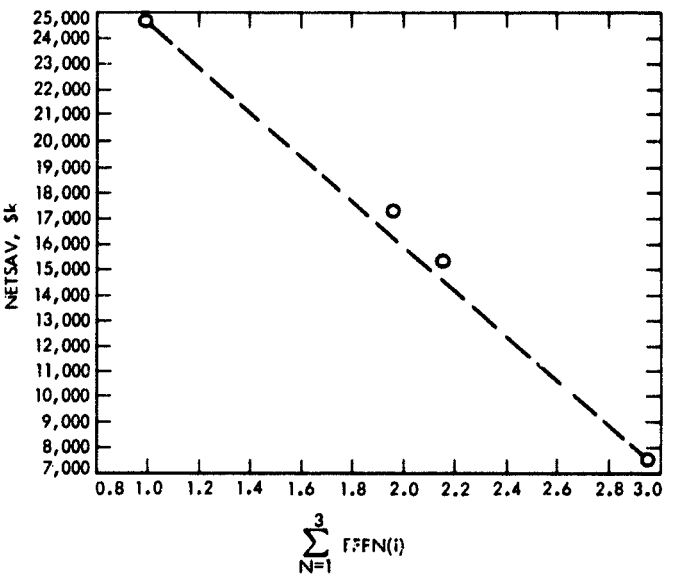

Fig. A-4. NETSAV vs $\sum_{N=1}^{3}$ EFFN (*i*), where *i* = 1 to 4. A graph of the four-dimensional NETSAV is impossible. This graph captures in two dimensions how NETSAV varies with all three parameters.

Appendix B

Program DBSAVE — Subprograms Initialize and Savings

The program DBSAVE is implemented in the DSN standard nonreal-time language MBASIC. Following top-down construction procedure, the program is divided into subprograms within which each statement is identified with a module number.

The first subprogram, Initialize, declares and prompts from the program user the values of all primary constants and variables. The second, subprogram Savings, calculates the range of possible ten-year net savings accompanying the unified computer data base system. Sensitivity, the last subprogram, calculates the degree to which the savings results would change with specified changes in the input constants and variables. The flowcharts follow.

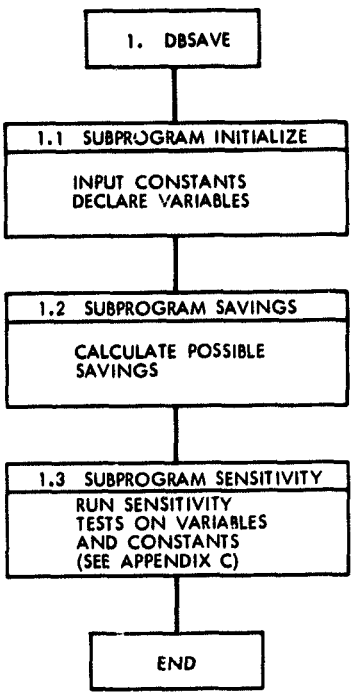

Fig. B-1. DBSAVE

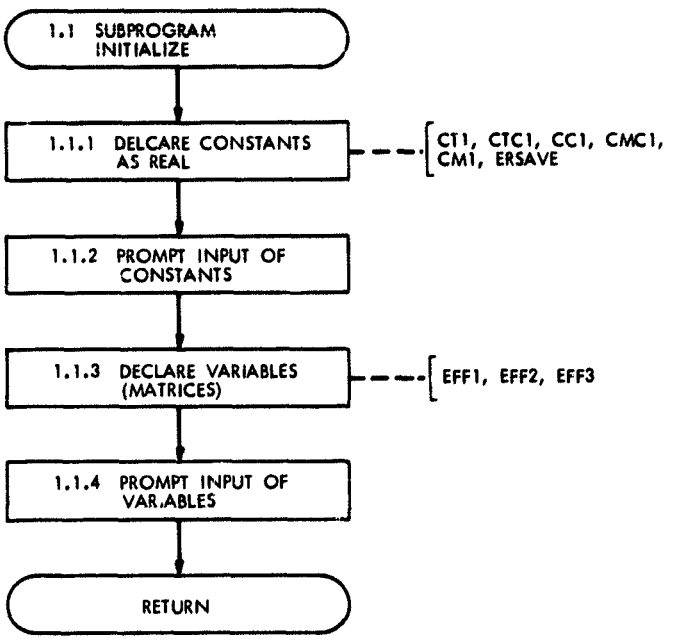

Fig. B-2. Subprogram Initialize

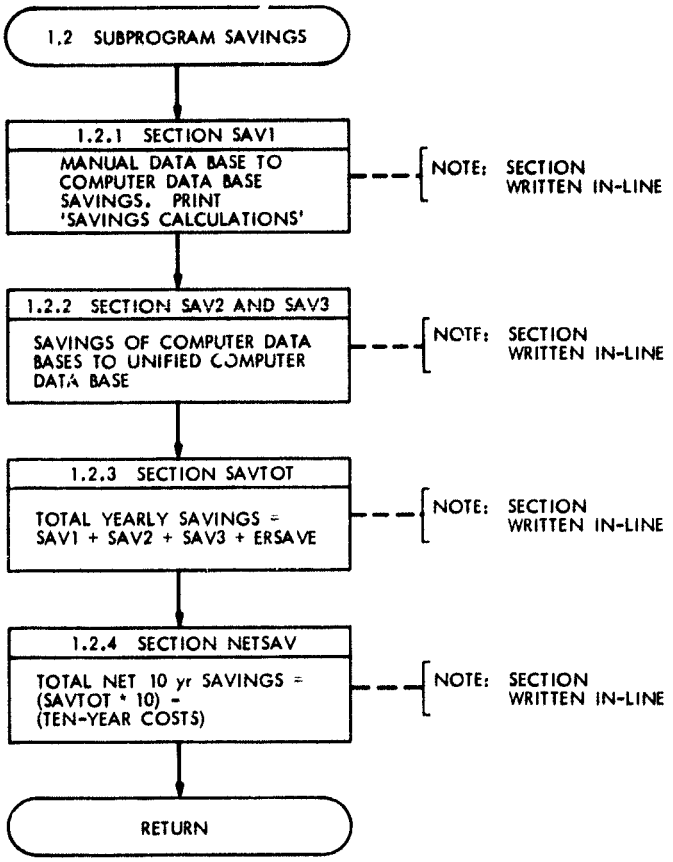

Fig. B-3. Subprogram Savings

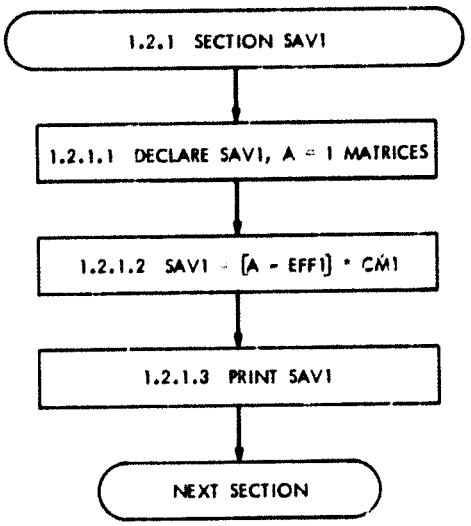

Fig. B-4. Section SAV1

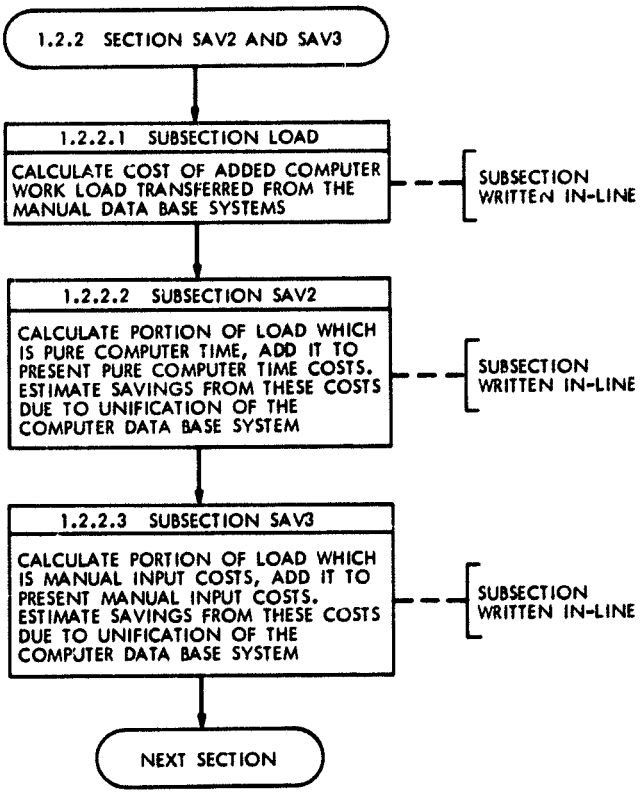

Fig. B-5. Section SAV2 and SAV3

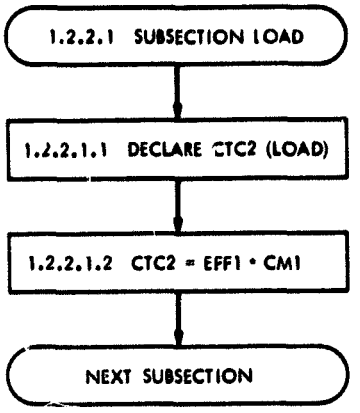

Fig. B-6. Subsection LOAD

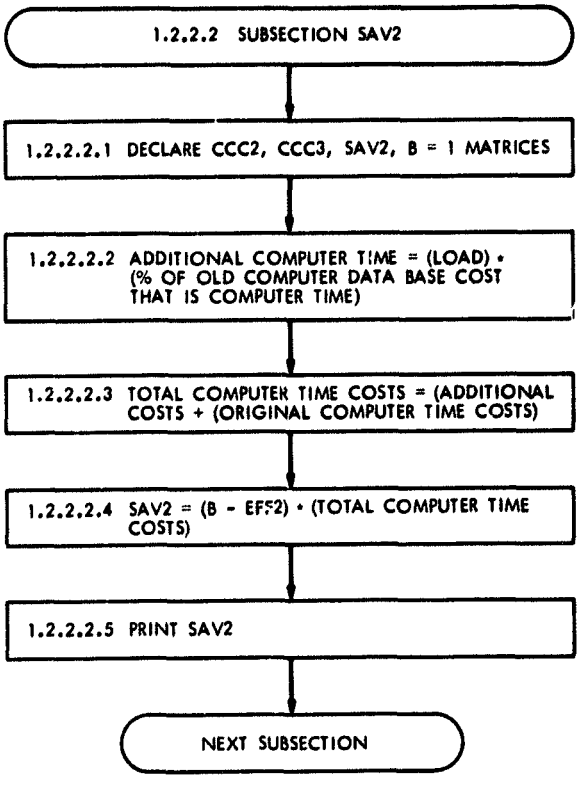

Fig. B-7. Subsection SAV2

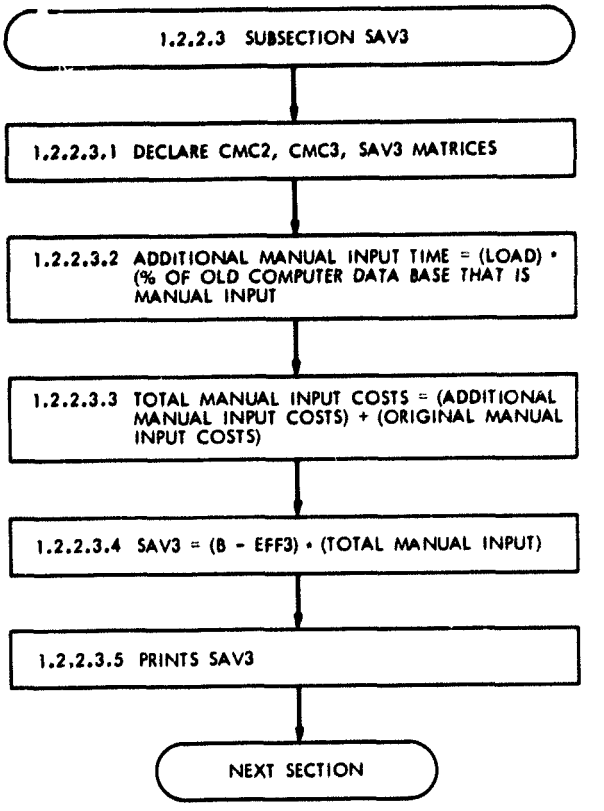

Fig. B-8. Subsection SAV3

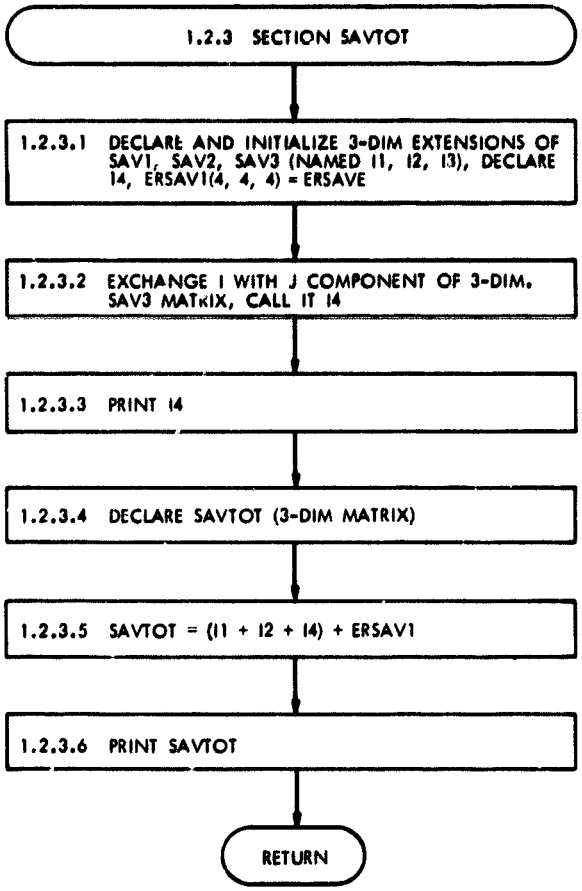

Fig. B-9. Section SAVTOT

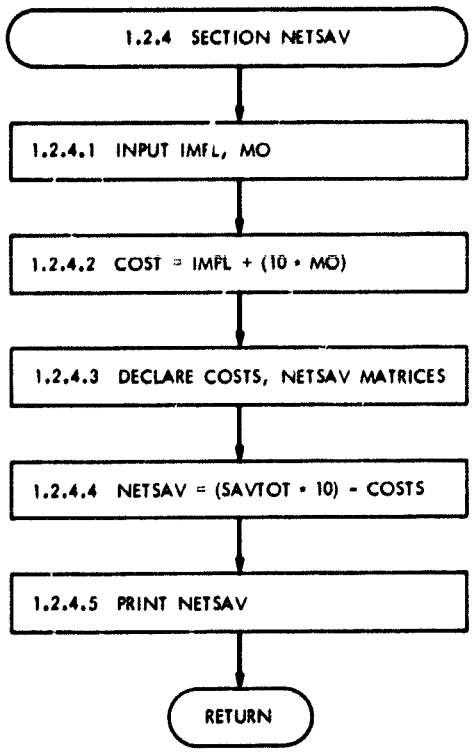

Fig. B-10. Section NETSAV

Appendix C

Program DBSAVE — Subprogram SENSITIVITY

The NETSAV value is clearly dependent upon the chosen value of the three efficiency ratios. The value of these ratios is not known. Yet, it would be useful to know, given three assumed values, the percent change in net savings due to a 10% change in the variables. This is the calculation of section Sensitivity: Variables.

The NETSAV matrix would also vary with different values of constants. This is doubly important since values of the constants depend on ballpark figures. The percent change in net savings due to a specified percent change in constants is the calculation of section Sensitivity: Constants.

Thus, subprogram Sensitivity is organized as shown in Fig. C-1.

I. Section Sensitivity: Variables

The goal is to calculate the percent change of NETSAV with respect to each of the variables, and then the percent change with respect to all three. This calculation is extremely easy if a trick is used in the input values of the variables. Specifically, for this study, the variable values were chosen such that:

$$\frac{\text{EFF}N(3) - \text{EFF}N(2)}{\text{EFF}N(2)} = 10\% \qquad (\text{for } N = 1, 2, 3)$$

or, the third element in each efficiency vector is 10% greater than the value of the second element. The necessary NETSAV calculations are then included in the NETSAV matrix.

With this format for the vector values, the percent change of NETSAV with respect to EFF1, is:

```
DTLDE1 = (NETSAV(2, 2, 3) - NETSAV(2, 2, 2))/NETSAV(2, 2, 2)
```

Here, both EFF2 and EFF3 are held constant at their midrange values, EFF2(2) and EFF3(2), and EFF1 is varied 10%. Likewise, the other two percent changes are:

```
DTLDE2 = (NETSAV(2, 3, 2) - NETSAV(2, 2, 2))/NETSAV(2, 2, 2)

DTLDE3 = (NETSAV(3, 2, 2) - NETSAV(2, 2, 2))/NETSAV(2, 2, 2)
```

For the NETSAV percent change with respect to all three, the variables are changed 10% together, or

```
DTLDE = (NETSAV(3, 3, 3) - NETSAV(2, 2, 2))/NETSAV(2, 2, 2)
```

The flowchart for this section is given in Fig. C-2.

II. Section Sensitivity: Constants

Again, we want to calculate the percent change in net savings with respect to each constant. No easy trick will help in this section. Instead, the constant in question is increased a specified percent, and the net savings is then recalculated. For this study, the percent error factor, called ER, was chosen as 0.1, or 10%. The corresponding multiplier for the constants, ERR, is equal to 1 + ER, or 1.1.

For the percent change of NETSAV with respect to the constant CM1, the procedure is as follows. The NETSAV calculation is first stated in one equation:

```
NETSAV = ((1 - EFF1) * CM1
       + (1 - EFF2) * (CCC1 + CCC1/CTC1 * EFF1 * CM1)
       + (1 - EFF3) * (CMC1 + CMC1/CTC1 * EFF1 * CM1)
       + ERSAVE) * 10 - COST
```

Next, the constant, CM1, is multiplied by 1.1, or ERR; the variables are held at their midrange values; and the new NETSAV value, called DELSV1, is:

```
DELSV1 = ((1-EFF1(1,2))*CM1*ERR
       +(1-EFF2(2,1))*(CCC1+CCC1/CTC1*EFF1(1,2)*CM1*ERR)
       +(1-EFF3(2,1))*(CMC1+CMC1/CTC1*EFF1(1,2)*CM1*ERR)
       +ERSAVE)*10-COST
```

The percent change of NETSAV with respect to CM1, then, is:

```
DTDCM1 = (DELSV1 - NETSAV(2,2,2))/NETSAV(2,2,2)
```

The other percent changes — DTDCCC, DTDCTC, and DTDCMC — are calculated similarly. The flowchart and equations are given in Fig. C-3.

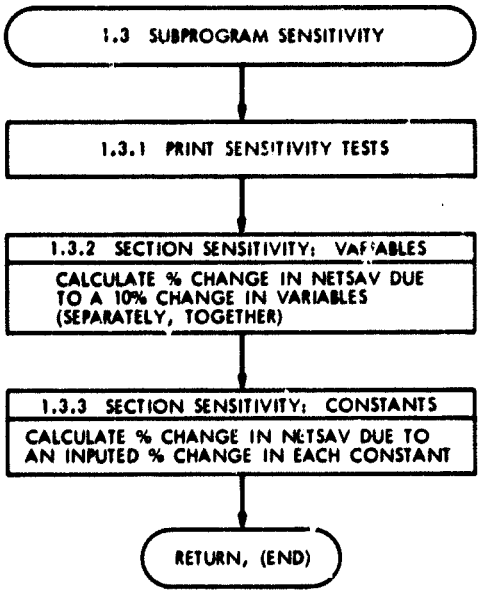

Fig. C-1. Subprogram Sensitivity

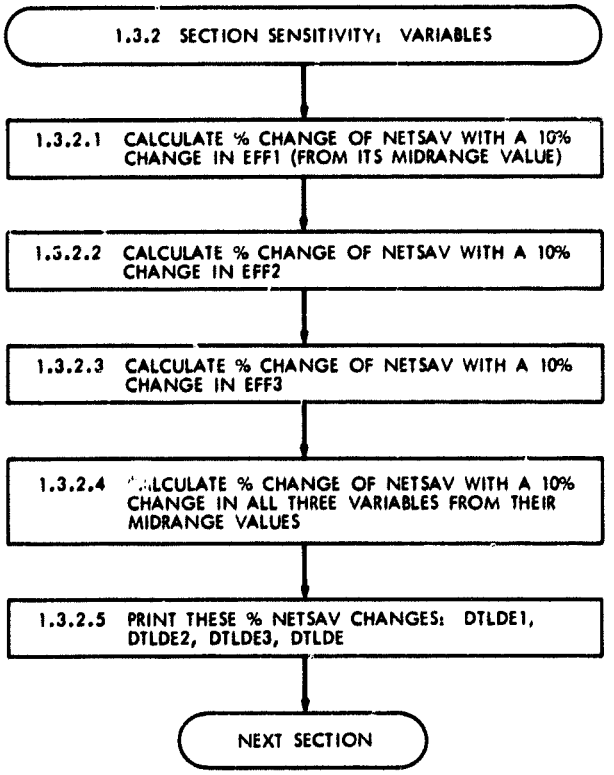

Fig. C-2. Section Sensitivity: Variables

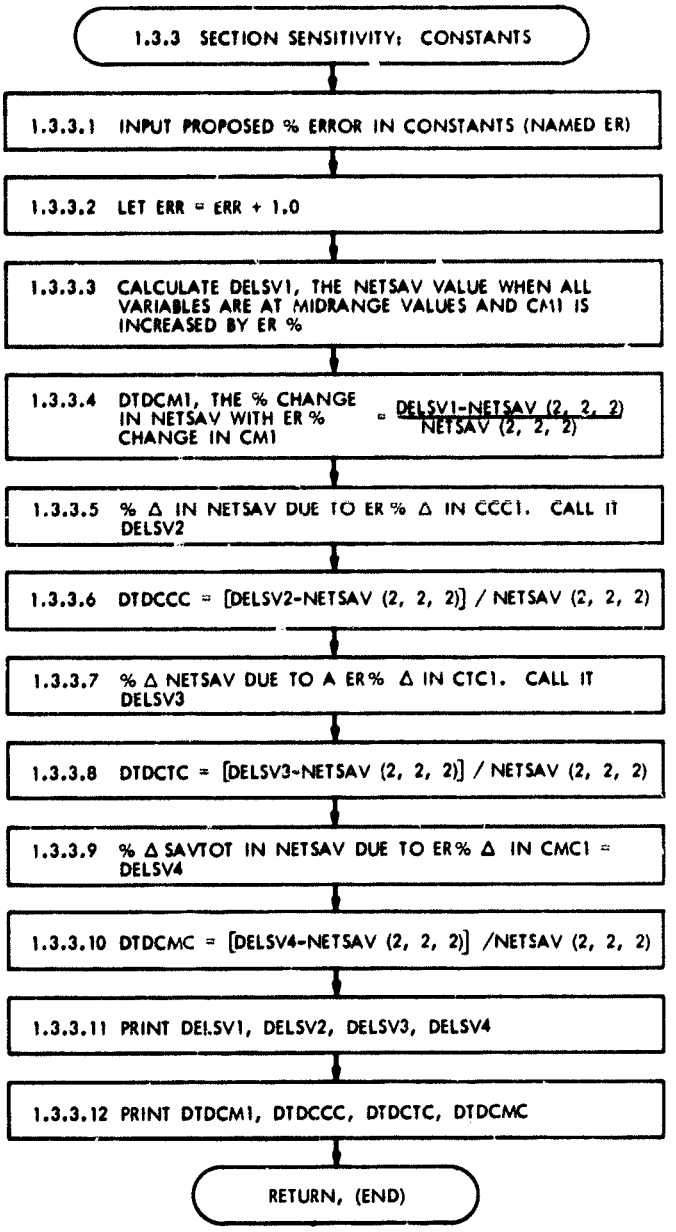

Fig. C-3. Section Sensitivity: Constants

Appendix D

Sensitivity Results

```
SENSITIVITY TESTS

DTLDE1=  -0.04
DTLDE2=  -0.02
DTLDE3=  -0.04
DTLDE=   -0.11

ERROR IN CONSTANTS : .1

DELSU1 IN $K=     18062.8
DELSU2 IN $K=     17491.1
DELSU3 IN $K=     16808.3
DELSU4 IN $K=     17598.7


DTDCM1=   0.05
DTDCCC=   0.02
DTDCTC=  -0.02
DTDCMC=   0.02

>EXIT
```


NASA—JPL—Coml., L.A., Calif.